

**Regularizations as subgrid models  
for turbulent flows**

by

**Jonathan Pietarila Graham**

B.S. (Hon), Oklahoma State University, 1993

M.S., University of Colorado, 2005

A thesis submitted to the  
Faculty of the Graduate School of the  
University of Colorado in partial fulfillment  
of the requirements for the degree of  
Doctor of Philosophy  
Department of Applied Mathematics

2007

This thesis entitled:  
Regularizations as subgrid models for turbulent flows  
written by Jonathan Pietarila Graham  
has been approved for the Department of Applied Mathematics

---

Annick Pouquet

---

Keith Julien

Date \_\_\_\_\_

The final copy of this thesis has been examined by the signatories, and we find that both the content and the form meet acceptable presentation standards of scholarly work in the above mentioned discipline.

Pietarila Graham, Jonathan (Ph.D., Applied Mathematics)

Regularizations as subgrid models for turbulent flows

Thesis directed by Affiliate Professor Annick Pouquet

As the implementation of numerical modeling of geophysical and astrophysical flows exceeds technological limits and since truncation of the omitted scales removes important physics, a closure (e.g., subgrid (subfilter) modeling) is required. This thesis examines the use of regularizations as subgrid models for turbulent flows. Two related goals are their application (to extend what can be achieved with numerical modeling) and to gain understanding of turbulence (how regularizations alter the flow, which properties they retain). Four regularization models are compared to direct numerical simulations (DNS); exact subfilter scalings are derived and subfilter scale properties are explored numerically. Particular attention is given to intermittency, an essential feature of turbulence and a departure from self-similarity.

The Lagrangian-averaged magnetohydrodynamic alpha (LAMHD- $\alpha$ ) model is applied to magnetofluids. The Lagrangian-averaged Navier-Stokes alpha (LANS- $\alpha$ ) model and the Leray- $\alpha$  and Clark- $\alpha$  models (truncations of the subfilter-scale stress of LANS- $\alpha$ ) are applied to nonconducting flows. Clark- $\alpha$  is associated with the first term of a Taylor expansion of the subfilter-scale stress. Leray- $\alpha$  and LANS- $\alpha$  represent advection by a smoothed velocity in an Eulerian and a Lagrangian sense, respectively.

Both Lagrangian-averaged models are found to reproduce the intermittency properties, such as the cancellation exponent, of the DNS. Exact scaling laws, analogous to the Kármán-Howarth equation, are derived for Leray- $\alpha$  and Clark- $\alpha$ . Leray- $\alpha$  results in an excessive reduction of the nonlinearity of the flow. Clark- $\alpha$  reproduces the large-scale energy spectrum of the DNS but exhibits increased intermittency at subfilter scales. This effect is reduced in LANS- $\alpha$ , likely due to its conservation of circulation.

This conservation results from Taylor’s frozen-in turbulence hypothesis in LANS- $\alpha$ ’s derivation which also leads to the presence of “rigid bodies” (no internal degrees of freedom (*dof*) nor contributions to the energy cascade) at subfilter scales. Consequently, the energy spectrum scales as the wavenumber at subfilter scales.

I identify the shortcomings and promising features of regularizations as subgrid models of turbulence. They reproduce high-order statistics of turbulence, but the reduction in *dof* is rather modest. No model preserves best all properties of the flow and further studies are necessary, e.g., through coupling to Large Eddy Simulations.

## Dedication

To Anna.

## Acknowledgements

There are a lot of people who have made this all possible. Pablo Mininni has been my patient mentor throughout this work. He never tired of giving me repeated lectures on turbulence theory as my understanding of this field grew. Annick Pouquet, my advisor, has been instrumental both in my development as a scientist and in my awareness of how things really work in this industry. My committee members, Harvey Segur, Keith Julien, and Bengt Fornberg, performed the mostly thankless job of reading every word, learning about my work, and providing valuable input. The other members of our group provided both the social context of my work, endless political discussions, and good professional role models: Duane Rossenber, Aim Fournier, Jai Sukhatme, Alex Alexakis, and Ed Lee. My fellow students provided lecture notes, study groups, and company for the shared misery that is prelims: Cory Ahrens, José Garcia, Maribeth Ocamou, Matt Reynolds, Ian Grooms, Ben Jamroz... Hundreds of administrative details had to be handled and I was always too frazzled to be of much use. Therefore, I am indebted to Liz Rothney, Silvia Gentile, Susan Pryor, Betty Thorson, and Karen Hawley.

Family and friends have widely been neglected in support of my education. Hopefully, I can now begin remembering how to be a human being. In the meantime, maybe birthday cards won't be quite so late anymore. Anna, I have been studying the entire time we have known each other. Now, finally, we can have time to start doing all those things we've been wanting to do. Thank you for always brightening up my life.

## Contents

### Chapter

<b>1</b>	Introduction	1
1.1	Motivation . . . . .	1
1.2	Dissertation overview . . . . .	3
<b>2</b>	Fluid Turbulence	4
2.1	Equations of motion . . . . .	4
2.2	Ideal invariants . . . . .	8
2.2.1	Energy . . . . .	8
2.2.2	Momentum . . . . .	10
2.2.3	Helicity . . . . .	11
2.2.4	Kelvin’s circulation theorem . . . . .	13
2.3	Energy spectrum and scale-by-scale energy budget . . . . .	13
2.4	Kármán and Howarth, 1938 . . . . .	17
2.5	Kolmogorov, 1941 . . . . .	22
2.6	Phenomenology . . . . .	29
2.7	Extensions to Magnetohydrodynamics (MHD) . . . . .	30
2.8	Beyond K41 . . . . .	32
2.8.1	Nonlocality . . . . .	32
2.8.2	Intermittency . . . . .	35

<b>3</b>	<b>Subgrid modeling</b>	<b>40</b>
3.1	Large eddy simulations (LES)	41
3.1.1	The eddy-viscosity of Smagorinsky	42
3.1.2	Dynamic model	44
3.1.3	Similarity model	46
3.1.4	Leonard tensor-diffusivity (Clark) model	46
3.1.5	Spectral eddy-viscosity	50
3.1.6	Hyperviscosity	51
3.1.7	Intermittency	51
3.1.8	MHD LES	52
3.2	Four regularization subgrid models	55
3.2.1	Clark- $\alpha$	56
3.2.2	Leray- $\alpha$	62
3.2.3	LANS- $\alpha$	65
3.2.4	Comparisons between LANS- $\alpha$ , Leray- $\alpha$ , Clark- $\alpha$ , and LES	71
3.2.5	LAMHD- $\alpha$	73
<b>4</b>	<b>Regularized MHD</b>	<b>83</b>
4.1	2D MHD	84
4.2	The cancellation exponent	86
4.3	Computation	88
4.4	Forced simulations	89
4.4.1	Numerical results for intermittency and scaling anomaly	90
4.4.2	Cancellation statistics	101
4.5	Decaying simulations	105
4.5.1	Flow visualizations	110
4.5.2	Numerical results for intermittency and scaling anomaly	110



4.5.3	Cancellation statistics . . . . .	113
4.6	Discussion and outlook . . . . .	116
<b>5</b>	LANS- $\alpha$ scaling . . . . .	121
5.1	Introduction . . . . .	122
5.2	Technique . . . . .	123
5.3	Inertial range scaling of LANS- $\alpha$ . . . . .	125
5.3.1	$l^3$ scaling of third-order structure function derived from the Kármán-Howarth theorem for LANS- $\alpha$ . . . . .	125
5.3.2	Subdominance of the $k^{-1}$ energy spectrum and rigid-body motions . . . . .	129
5.4	Resolution requirements for grid-independent LANS- $\alpha$ solutions: Size of attractor . . . . .	135
5.5	Can LANS- $\alpha$ be considered as a Large Eddy Simulation? . . . . .	142
5.5.1	Free parameter $\alpha$ and quality of the $\alpha$ -LES . . . . .	145
5.5.2	Numerical savings from employing LANS- $\alpha$ . . . . .	151
5.6	LANS- $\alpha$ at very high Reynolds number . . . . .	152
5.7	Conclusions . . . . .	158
<b>6</b>	Three regularization models of Navier-Stokes . . . . .	163
6.1	Introduction . . . . .	164
6.2	Three regularization models . . . . .	165
6.2.1	Kármán-Howarth equation for Clark- $\alpha$ . . . . .	165
6.2.2	Kármán-Howarth equation for Leray- $\alpha$ . . . . .	168
6.2.3	LANS- $\alpha$ . . . . .	169
6.3	Numerical study . . . . .	170
6.4	Discussion of computational gains . . . . .	178
6.5	Conclusions . . . . .	183

<b>7</b>	<b>Conclusion and future research problems</b>	<b>186</b>
7.1	Review of key results . . . . .	186
7.2	Future research . . . . .	189
7.3	Final remarks . . . . .	192
	 <b>Bibliography</b>	 <b>193</b>
	 <b>Appendix</b>	
<b>A</b>	<b>Required identities</b>	<b>211</b>

## Tables

### Table

3.1	Summary of LAMHD- $\alpha$ subgrid modeling results . . . . .	82
4.1	Relative scaling exponents computed from DNS runs (forced turbulence)	99

## Figures

### Figure

2.1	Leonardo da Vinci's illustration of the swirling flow of turbulence. . . .	5
2.2	Example of an omni-directional spectral energy density . . . . .	16
2.3	Illustration of the scale-by-scale energy budget equation . . . . .	18
2.4	Example of flux versus wavenumber . . . . .	24
2.5	Kolmogorov's four-fifths law . . . . .	25
2.6	Kolmogorov's five-thirds law . . . . .	28
2.7	Demonstration of the bottleneck. . . . .	34
2.8	Example of a spatially intermittent signal. . . . .	36
2.9	Example of scale dependence for increments of an intermittent signal. .	38
2.10	Anomalous scaling of structure function exponents. . . . .	39
4.1	Averaged spectra: magnetic and kinetic energy (forced turbulence) . . .	91
4.2	Compensated third-order, mixed structure function versus length (forced turbulence) . . . . .	95
4.3	Third-order structure functions for $\mathbf{z}^+$ (forced turbulence) . . . . .	96
4.4	Eighth-order structure functions for $\mathbf{z}^+$ (forced turbulence) . . . . .	97
4.5	Structure function scaling exponent for $\mathbf{z}^+$ versus order (forced turbulence)	100
4.6	Structure function scaling exponents for $\mathbf{z}^-$ , $\mathbf{v}$ and $\mathbf{b}$ versus order (forced turbulence) . . . . .	102

4.7	Partition function $\chi(l)$ averaged in time for $j_z$ (forced turbulence) . . .	104
4.8	Time evolution of magnetic and kinetic energies (freely decaying turbulence)	107
4.9	Time evolution of mean square current and mean square vorticity (freely decaying turbulence) . . . . .	108
4.10	Averaged spectra (freely decaying turbulence) . . . . .	109
4.11	2D stream function and vector potential (freely decaying turbulence) . .	111
4.12	2D electric current and vorticity (freely decaying turbulence) . . . . .	112
4.13	Scaling exponent for $z^+$ versus order (freely decaying turbulence) . . . .	114
4.14	Partition function $\chi(l)$ (freely decaying turbulence) . . . . .	115
4.15	Time history of cancellation exponent and magnetic dissipation (freely decaying turbulence) . . . . .	117
4.16	Partition function for predictive LAMHD- $\alpha$ run (freely decaying turbu- lence) . . . . .	117
5.1	Third-order longitudinal structure function of the smoothed velocity field versus length for large $\alpha$ LANS- $\alpha$ . . . . .	128
5.2	Spectral energy density versus wavenumber for large- $\alpha$ LANS- $\alpha$ . . .	130
5.3	Two-dimensional slice of the cubed longitudinal increment . . . . .	133
5.4	Pdfs of cubed longitudinal increment . . . . .	134
5.5	Coexistent energy spectra: $k^{-1}$ and $k^1$ . . . . .	136
5.6	Plots for $Re \approx 500$ simulations demonstrating convergence to the grid- independent LANS- $\alpha$ solution . . . . .	138
5.7	$Re \approx 670$ simulations: linear resolution of $\alpha$ -model simulations versus $\alpha^{-1}$ , convergence results . . . . .	140
5.8	Scaling with $Re$ of $dof$ for LANS- $\alpha$ . . . . .	141
5.9	Plot of $Re \approx 670$ simulations demonstrating optimal $\alpha$ -LES . . . . .	144

5.10	Plots for $Re \approx 670$ simulations: Average error versus simulation resolution and versus increasing filter width . . . . .	146
5.11	Plot of errors of grid-independent solutions compared to DNS versus ratio of $\alpha$ to the forcing scale, Taylor scale, and dissipation scale. . . . .	147
5.12	Compensated averaged grid-independent energy spectra for DNS and LANS- $\alpha$ holding the ratio of Taylor scale to $\alpha$ nearly constant . . . . .	149
5.13	Energy flux for three DNS with $Re \approx 3300$ , $Re \approx 670$ , and $Re \approx 500$ and Energy flux at $Re \approx 3300$ for both DNS and $\alpha$ -model runs . . . . .	150
5.14	Averaged compensated energy spectra, $Re \approx 3300$ . . . . .	153
5.15	3D volume rendering of enstrophy density . . . . .	155
5.16	Compensated 3rd-order structure function versus length $l$ . . . . .	157
5.17	Structure function scaling exponent versus order . . . . .	159
6.1	Time evolution of dissipation . . . . .	172
6.2	Averaged compensated spectra . . . . .	173
6.3	3D volume rendering of the enstrophy density . . . . .	177
6.4	Kármán-Howarth scaling . . . . .	179
6.5	Normalized structure function scaling exponent versus order . . . . .	180

## Chapter 1

### Introduction

When I meet God, I am going to ask him two questions: Why relativity?  
And why turbulence? I really believe he will have an answer to the first.  
-Werner Heisenberg<sup>1</sup>

#### 1.1 Motivation

By and large, the solved partial differential equations of theoretical physics are either linear or based on “small” perturbations to linearized problems. That is, the principle of superposition (the whole is equal to the sum of its parts, loosely speaking) is applicable. This is the case for quantum mechanics and for classical physics (optics, electricity and magnetism, the heat equation) although recent advances in these fields have stressed the nonlinear character of these topics (e.g., for nonlinear optics [187, 70]). For linear problems, whether algebraic equations, ordinary differential equations (ODEs), or partial differential equations (PDEs), and for finite dimensional systems of ODEs (as often encountered in classical mechanics) we have a large chest of tools, as well as rigorous mathematics, developed over the centuries. For a fully nonlinear PDE—such that no obvious small expansion parameter is available for traditional asymptotic approaches—we have only a very small number of tools. It is just this kind of nonlinear problems we must address, however, if we are to continue to advance our understanding of the physical world around us. For example, remarkable progress in nonlinear science has been

---

<sup>1</sup> According to an apocryphal story [255].

achieved in the understanding of low-dimensional chaotic systems (such as the Lorenz attractor) and of the dynamics of solitons (as for the nonlinear Schrödinger equation and for shallow water – the Korteweg-de Vries equation). These two fields, however, cover but a small portion of the parameter space available to nonlinear problems.

This dissertation focuses on one particular nonlinear problem, incompressible fluid turbulence: we are interested in the fluid flow equations, Navier-Stokes and the magnetohydrodynamic (MHD) equations, in the regime where the nonlinear terms dominate. That is, the Reynolds number  $Re$  (the ratio of the nonlinearities to the dissipation) is large, as can be the case in geophysical and astrophysical flows. In this regime, the fluid motion is turbulent. Turbulence is just what its colloquial meaning implies: it is the swirls in the rising smoke from an extinguished match, the reason for a bumpy ride in a commercial airliner, and the invisible eddies behind a car that cause drag. Turbulence is also one of the last unsolved problems of classical physics. This is, of course, because the vast machinery of linear theory does not apply.

In fact, for the Navier-Stokes equations, we have no theorem guaranteeing the existence and uniqueness of strong (smooth) solutions [80]. This poses quite a stumbling block: if the solutions are not smooth, much of what we do (for instance, solve the equations numerically) may not apply, and if the solutions are not unique, what good does it do to solve them in the first place? This problem of existence and uniqueness of regular solutions was included in David Hilbert's famous lecture about open mathematical problems on August 8, 1900, at the second International Congress of Mathematicians in Paris. At the turn of this century, the Clay Mathematics Institute (CMI) identified it as still one of the most important open questions in mathematics and is offering a one million dollar prize for a solution. This dissertation makes no open attempt at the solution of this problem. Instead, we employ one of our few remaining tools: when a problem is too difficult, consider a simpler problem.<sup>2</sup> Consequently, we examine regularizations of

---

<sup>2</sup> That is, simplify the problem until you can do something with it and try to work your way back



fluid flow equations. That is, we consider instead of a Navier-Stokes flow, equations for which there are proofs of the existence and uniqueness of smooth solutions and which possess a free model parameter. In the limit of this parameter going to zero, we recover the Navier-Stokes (or MHD) equations. From the regularization, we then have a system of equations with a greater assurance of computability (and, often, a reduced computation cost) and, hopefully, a system which will be more yielding to analysis. The focus of this dissertation is on the numerical and sometimes phenomenological. How these regularizations are similar to (and different from) the original fluid equations can help us learn more about fluid turbulence. And, in the meantime, anything we can learn about a highly nonlinear problem is a step towards enriching our understanding of nonlinear science and mathematics.

## 1.2 Dissertation overview

This thesis addresses two main questions. Firstly, can a regularization as a sub-grid model, especially for MHD, reproduce the turbulence (scaling laws, high-order statistics, etc.) of the original fluid equations. That is, can their numerical solutions be used in lieu of fully-resolved direct numerical simulations (DNS) of the fluid equations to answer scientific questions that depend on higher-order statistics and deviations from self-similarity? Secondly, what are the small-scale properties (scalings) of the regularizations studied and their effects on using the regularizations as subgrid models? A more general question is: can we learn more about turbulence through either approach? To answer these questions, we conduct numerical simulations. We compare the models both for their ability to reproduce the predictions of turbulence theory (energy spectra, scalings of moments of increments, etc.) and to reproduce the strong, impulsive (intermittent) events that are the hallmark of turbulence.

---

from there.

## Chapter 2

### Fluid Turbulence

Big whorls have little whorls that feed on their velocity, and little whorls  
have lesser whorls, and so on to viscosity.

-Lewis Fry Richardson [210]

With this rhyme (adapted from Jonathan Swift), Lewis Richardson coined the term 'turbulent cascade.' He envisioned that turbulent flow consists of eddies (swirls) of all available sizes (see Fig. 2.1) and that eddies of any given size break up to form eddies of a slightly smaller size (the so-called local cascade).<sup>1</sup> Through the nonlinearity of fluid flow, all of these eddies of different sizes may (potentially) interact with one another. It is this that makes the analysis (and computation) of fluid flow so difficult. Consequently, there is today no universal 'theory of turbulence,' but in this chapter we briefly review the history of progress towards such a theory focusing on the topics most relevant to the results presented in later chapters.

#### 2.1 Equations of motion

First derived in 1822, the Navier-Stokes equations, named after Claude-Louis Navier and George Gabriel Stokes, govern the time evolution of a fluid. Under the assumptions that the fluid is incompressible and Newtonian the equations are

$$\partial_t \mathbf{v} + \mathbf{v} \cdot \nabla \mathbf{v} = -\nabla P + \mathcal{F} + \nu \nabla^2 \mathbf{v} \quad (2.1a)$$

---

<sup>1</sup> Energy is observed to be transferred from large to small scales, the cascade is one hypothesis of how this might occur.



Figure 2.1: Leonardo da Vinci's illustration of the swirling flow of turbulence. (The Royal Collection ©2004, Her Majesty Queen Elizabeth II.) Taken from <http://www.maths.monash.edu.au/~jjm/jjmsph.shtml>.

$$\nabla \cdot \mathbf{v} = 0 \quad (2.1b)$$

where  $\mathbf{v}$  is the three-dimensional (3D) fluid velocity field,  $P$  is the pressure divided by density,<sup>2</sup>  $\nu$  the kinematic viscosity, and  $\mathcal{F}$  an arbitrary external force. Physically, they result from the continuum hypothesis applied to Newton's second law of motion and by taking the limit of infinite sound speed (i.e., incompressibility). Mathematically, they are the starting point of our discussion. The advection term,  $\mathbf{v} \cdot \nabla \mathbf{v}$ , is the source of nonlinearity in the problem. A measurement of nonlinearity, the Reynolds number,  $Re$ , was proposed by Osborne Reynolds in 1883 for his experiments in pipe flows. It is a dimensionless quantity often used to estimate the strength of the nonlinear term,  $\mathbf{v} \cdot \nabla \mathbf{v}$ , compared to the dissipative term,  $\nu \nabla^2 \mathbf{v}$ . From dimensional analysis<sup>3</sup> of the ratio between these two we arrive at

$$\frac{([V]^2[L]^{-1})}{\nu[L]^2[V]} \sim Re \equiv \frac{v_{r.m.s.}L}{\nu} \quad (2.2)$$

where  $L$  is some characteristic length scale in the problem and  $v_{r.m.s.}$  is the root-mean-square (*r.m.s.*) velocity. When  $Re$  is large the ensuing complicated and irregular dynamics (usually chaotic) calls for a statistical description based on averaging over regions of space, intervals of time, or ensembles.

The term magnetohydrodynamics (MHD) was first coined by Hannes Alfvén in 1942. The MHD equations govern the time evolution of an electrically conductive (and, in our case, resistive and incompressible) fluid. We add a Lorentz forcing term to the Navier-Stokes equations and include Maxwell's equations for electrodynamics. The additional assumptions are that there is no creation nor loss of particles, no pair productions, nor recombinations, that the (single) fluid has a constant conductivity and we take the limit that the speed of light is infinite so that the displacement current can be

---

<sup>2</sup> Given an initially uniform density field, conservation of mass and incompressibility lead to a constant uniform density, which has been divided out from all terms.

<sup>3</sup> The symbol,  $\sim$ , is used to denote quantities that have the same dimension. This is distinct from the symbol,  $\propto$ , which indicates that two quantities are the same to within a constant of proportionality. Also,  $[L]$  denotes the dimension of length,  $[T]$  of time, and  $[V] \equiv [L]/[T]$  of velocity.

neglected. We then have,

$$\partial_t \mathbf{v} + \mathbf{v} \cdot \nabla \mathbf{v} = -\nabla P + \mathbf{j} \times \mathbf{b} + \mathcal{F} + \nu \nabla^2 \mathbf{v} \quad (2.3a)$$

$$\nabla \cdot \mathbf{v} = 0 \quad (2.3b)$$

$$\partial_t \mathbf{b} + \mathbf{v} \cdot \nabla \mathbf{b} = \mathbf{b} \cdot \nabla \mathbf{v} + \eta \nabla^2 \mathbf{v} \quad (2.3c)$$

$$\nabla \cdot \mathbf{b} = 0 \quad (2.3d)$$

where  $\mathbf{b}$  is the 3D magnetic induction,<sup>4</sup>  $\mathbf{j} = \mu \nabla \times \mathbf{b}$  is the current,  $\mu$  is the magnetic permeability and  $\eta$  the magnetic diffusivity. The MHD equations were derived as early as 1950 by George Keith Batchelor who continued work began by Hartmann and Lazarus in 1937 [10]. Batchelor also noted that in the limit of infinite conductivity magnetic lines of force are “frozen-in” to the fluid motions. In 1950, for  $\eta < \nu$ , he was among the first to postulate the kinematic dynamo [10]. That is, that turbulent fluid motions could amplify a small magnetic disturbance. We notice a similarity between the two sets of equations, Eqs. (2.1) and (2.3), in that they both possess an advective operator  $\partial_t + \mathbf{v} \cdot \nabla$  and a dissipative operator  $\nabla^2$ . We thus define a magnetic Reynolds number,

$$Re_M \equiv \frac{v_{r.m.s.} L}{\eta}. \quad (2.4)$$

The additional non-linear terms,  $\mathbf{b} \cdot \nabla \mathbf{v}$  and  $\mu(\nabla \times \mathbf{b}) \times \mathbf{b}$ , represent the physics of the rotation and stretching of magnetic field lines by the fluid motions and the tension in the magnetic field lines tending to contract and accelerate the fluid [10]. Chandrasekhar hypothesized that “the inclusion of electromagnetic forces does not introduce any essential difficulty which is not already present in our understanding of ordinary turbulence” [50]. Adopting this viewpoint, we treat MHD and Navier-Stokes as parallel subtopics of incompressible fluid turbulence. Note, however, that we do not imply the Navier-Stokes

---

<sup>4</sup> Actually, the magnetic induction is given by  $\mathbf{B} = \mu \mathbf{H}$  where  $\mathbf{H}$  is the magnetic field and  $\mu$  is the permeability. The MHD equations as presented here are in Alfvénic units,  $\mathbf{b} = \mathbf{B} / \sqrt{\rho \mu}$  where  $\rho$  is the uniform constant mass density. Nevertheless, hereafter  $\mathbf{b}$  is referred to as the magnetic field.

and MHD fluids behave in identical ways; for example, unlike incompressible Navier-Stokes, incompressible MHD supports waves, leading to possibly different dynamics involving the interactions between turbulent eddies and waves.

## 2.2 Ideal invariants

### 2.2.1 Energy

The dissipation rate of total energy in a flow was first derived by Geoffrey Ingram Taylor in 1935 [226]. Our analysis of Navier-Stokes begins with identifying this and other ideal invariants, i.e., quantities that are invariant in the absence of external forcing and dissipation. For simplicity, we employ the Einstein summation notation wherein (2.1) is written as

$$\partial_t v_i + v_j \partial_j v_i = -\partial_i P + \mathcal{F}_i + \nu \partial_{jj} v_i \quad (2.5a)$$

$$\partial_j v_j = 0. \quad (2.5b)$$

Next, we take the dot product of the first equation with  $v_i$  from the left and integrate over the entire spatial domain, which we denote by  $\langle \cdot \rangle$ :<sup>5</sup>

$$\langle v_i \partial_t v_i \rangle + \langle v_j v_i \partial_j v_i \rangle = -\langle v_i \partial_i P \rangle + \langle v_i \mathcal{F}_i \rangle + \nu \langle v_i \partial_{jj} v_i \rangle. \quad (2.6)$$

As the kinetic energy of a solid body is given by

$$E_K = \frac{1}{2} m v^2, \quad (2.7)$$

we define the total (kinetic) energy<sup>6</sup> (per unit mass) for our fluid as

$$E \equiv \left\langle \frac{1}{2} |\mathbf{v}|^2 \right\rangle. \quad (2.8)$$

---

<sup>5</sup> Technically, we take  $\langle \cdot \rangle$  to represent an “ensemble average” over many different realizations of the flow but, under the assumption of homogeneity, this can be shown to be equivalent to a spatial average.

<sup>6</sup> For an incompressible fluid with constant density, the kinetic energy is the only energy in the system and it is conventional to drop “kinetic” both in the terminology and from the symbol  $E_K$  [80]. Note that  $\mathcal{F}$  is an external force and cannot contribute to an internal potential energy.

We see that the first term in Eq. (2.6) is the time derivative of the total energy,  $\langle v_i \partial_t v_i \rangle = dE/dt$ , under the assumptions necessary for the Lebesgue dominated convergence theorem.<sup>7</sup> To simplify Eq. (2.6) we develop identities for the integrals of a gradient, a divergence, and an advection-like term over the entire domain. From the divergence theorem we have

$$\int_V \nabla \cdot \mathbf{f} dV = \int_{\partial V} \mathbf{f} \cdot d\mathbf{S} \quad (2.9)$$

for a vector field, and

$$\int_V \nabla f dV = \int_{\partial V} f d\mathbf{S} \quad (2.10)$$

for a scalar field. Both of these are zero for periodic boundary conditions, an infinite domain for which we insist  $\lim_{x \rightarrow \pm\infty} f_{(i)} = 0$ , or if the fields are zero on the boundary. Hereafter, we assume that one of these three conditions holds. For an advection-like term, we integrate by parts

$$\langle v_j \partial_j \phi \rangle = \langle \partial_j (\phi v_j) \rangle - \langle \phi \partial_j v_j \rangle. \quad (2.11)$$

Since the first term is the integral of a divergence and since  $\mathbf{v}$  is incompressible, the entire expression is identically zero. Removing all such terms from Eq. (2.6) and noting that  $\langle v_j v_i \partial_j v_i \rangle = \langle v_j \partial_j (v_i)^2 \rangle / 2$  we are left with

$$\frac{dE}{dt} = \langle v_i \mathcal{F}_i \rangle + \nu \langle v_i \partial_{jj} v_i \rangle. \quad (2.12)$$

Thus, total energy is our first invariant (in the absence of forcing and dissipation).

The curl of the velocity is the vorticity,  $\boldsymbol{\omega} \equiv \nabla \times \mathbf{v}$ , which is a measure of the local rotation of a fluid element. In summation notation  $\omega_i = \epsilon_{ijl} \partial_j v_l$ , where  $\epsilon_{ijl}$  is the Levi-Civita pseudotensor. We define the (total) enstrophy,

$$\Omega \equiv \left\langle \frac{1}{2} |\boldsymbol{\omega}|^2 \right\rangle \quad (2.13)$$

---

<sup>7</sup> Specifically, we assume that the energy is finite at each instant of time and that the time derivative of  $v^2(\mathbf{x}, t)$  is bounded above by a non-negative integrable function for all time.

and note that

$$\Omega = \frac{1}{2} \langle \epsilon_{ijl} \partial_j v_l \epsilon_{imn} \partial_m v_n \rangle = \frac{1}{2} \langle (\partial_j v_l)^2 \rangle, \quad (2.14)$$

where we have used the contracted epsilon identity,  $\epsilon_{ijl} \epsilon_{imn} = \delta_{jm} \delta_{ln} - \delta_{jn} \delta_{lm}$ , and  $\langle \partial_j (\partial_l v_l v_j) \rangle = 0$ . Finally, after integrating by parts  $\langle v_i \partial_{jj} v_i \rangle = \langle \partial_j (v_i \partial_j v_i) \rangle - \langle (\partial_j v_i)^2 \rangle = -2\Omega$ , Eq. (2.12) becomes

$$\frac{dE}{dt} = -2\nu\Omega + \langle v_i \mathcal{F}_i \rangle. \quad (2.15)$$

We define the total energy dissipation rate (per unit mass)

$$\varepsilon \equiv 2\nu\Omega \quad (2.16)$$

which is the dissipation into heat due to internal fluid friction. It plays a central role in turbulence theory. Under the assumption of a statistical steady-state we have  $dE/dt \approx 0$  and, consequently,

$$\varepsilon \approx \langle v_i \mathcal{F}_i \rangle. \quad (2.17)$$

That is, the energy injection rate and the dissipation rate must be approximately<sup>8</sup> the same for a statistical steady state.

### 2.2.2 Momentum

Another conserved quantity easily compared to that of a single object is momentum. Integrating Navier-Stokes, Eq. (2.5a), over the entire domain we find,

$$\langle \partial_t v_i \rangle + \langle \partial_j (v_i v_j) \rangle = -\langle \partial_i P \rangle + \langle \mathcal{F}_i \rangle + \nu \langle \partial_j (\partial_j v_i) \rangle. \quad (2.18)$$

By eliminating the integral of all gradients and divergences, we find  $\langle \partial_t v_i \rangle = \langle \mathcal{F}_i \rangle$  which we can, by Lebesgue dominated convergence, transform into

$$\frac{d}{dt} \langle \mathbf{v} \rangle = \langle \mathcal{F} \rangle. \quad (2.19)$$

That is, the time rate of change of the total momentum is equal to the total of the externally applied forces. Momentum is thus our second ideal invariant.

---

<sup>8</sup> The symbol,  $\approx$  represents “approximately equal” which we will take to loosely mean “equivalent to one significant figure” (see, e.g. [241]).



### 2.2.3 Helicity

For our third invariant, we first develop the vorticity equation for the time evolution of  $\omega_i$ . To do this we return to conventional vector notation and take the curl of Eq. (2.1). As the curl is a linear operator, we have

$$\nabla \times \partial_t \mathbf{v} + \nabla \times (\mathbf{v} \cdot \nabla \mathbf{v}) = -\nabla \times \nabla P + \nabla \times \mathcal{F} + \nabla \times \nu \nabla^2 \mathbf{v} \quad (2.20)$$

Assuming the velocity field has continuous second partial derivatives, Clairaut's theorem allows us to interchange the order of differentiation,

$$\nabla \times \partial_t \mathbf{v} = \partial_t \nabla \times \mathbf{v} = \partial_t \boldsymbol{\omega} \quad (2.21)$$

and

$$\nabla \times \nabla^2 \mathbf{v} = \nabla^2 \nabla \times \mathbf{v} = \nabla^2 \boldsymbol{\omega}. \quad (2.22)$$

Next, we employ that the curl of a gradient is zero,

$$\nabla \times \nabla P = 0. \quad (2.23)$$

This leaves us with the curl of the nonlinear term. Using the identity,  $\mathbf{v} \times (\nabla \times \mathbf{v}) = \frac{1}{2} \nabla v^2 - \mathbf{v} \cdot \nabla \mathbf{v}$ :

$$\nabla \times (\mathbf{v} \cdot \nabla \mathbf{v}) = \nabla \times \left( \frac{1}{2} \nabla v^2 - \mathbf{v} \times \boldsymbol{\omega} \right) = -\nabla \times (\mathbf{v} \times \boldsymbol{\omega}) = -(\boldsymbol{\omega} \cdot \nabla) \mathbf{v} + \boldsymbol{\omega} \nabla \cdot \mathbf{v} - \mathbf{v} \nabla \cdot \boldsymbol{\omega} + (\mathbf{v} \cdot \nabla) \boldsymbol{\omega}. \quad (2.24)$$

Here we used again that the curl of a gradient is zero and the familiar vector identity for the curl of a cross product. Now using that the flow is incompressible, Eq. (2.1b), and that the divergence of a curl is zero:

$$\nabla \times (\mathbf{v} \cdot \nabla \mathbf{v}) = -(\boldsymbol{\omega} \cdot \nabla) \mathbf{v} + (\mathbf{v} \cdot \nabla) \boldsymbol{\omega}. \quad (2.25)$$

Finally, we obtain the vorticity equation by combining Eqs. (2.20), (2.21), (2.22), (2.23), and (2.25):

$$\partial_t \boldsymbol{\omega} + \mathbf{v} \cdot \nabla \boldsymbol{\omega} = \boldsymbol{\omega} \cdot \nabla \mathbf{v} + \nabla \times \mathcal{F} + \nu \nabla^2 \boldsymbol{\omega}. \quad (2.26)$$

Now returning to summation notation, the vorticity equation becomes

$$\partial_t \omega_i + v_j \partial_j \omega_i = \omega_j \partial_j v_i + \epsilon_{ijl} \partial_j \mathcal{F}_l + \nu \partial_{jj} \omega_i. \quad (2.27)$$

We define the (total) helicity

$$H \equiv \left\langle \frac{1}{2} \mathbf{v} \cdot \boldsymbol{\omega} \right\rangle \quad (2.28)$$

and note that  $\partial_t(v_i \omega_i) = \omega_i \partial_t v_i + v_i \partial_t \omega_i$ . Therefore, we multiply Eq. (2.27) with  $v_i$  and add Eq. (2.5) multiplied with  $\omega_i$  and integrate over the domain, to obtain

$$\begin{aligned} \langle \partial_t(v_i \omega_i) + \omega_i v_j \partial_j v_i + v_i v_j \partial_j \omega_i \rangle &= \langle v_i \omega_j \partial_j v_i - \omega_i \partial_i P + v_i \epsilon_{ijl} \partial_j \mathcal{F}_l + \omega_i \mathcal{F}_i \rangle \\ &\quad + \nu \langle (v_i \partial_{jj} \omega_i + \omega_i \partial_{jj} v_i) \rangle. \end{aligned} \quad (2.29)$$

We define what could be called the total vortical helicity [80],

$$H_\omega \equiv \left\langle \frac{1}{2} \boldsymbol{\omega} \cdot (\nabla \times \boldsymbol{\omega}) \right\rangle \quad (2.30)$$

and note that

$$H_\omega = \frac{1}{2} \langle (\partial_j v_l)(\partial_j \omega_l) \rangle. \quad (2.31)$$

Integrating by parts yields,

$$\langle v_i \partial_{jj} \omega_i \rangle = \langle \partial_j(v_i \partial_j \omega_i) \rangle - \langle (\partial_j v_i)(\partial_j \omega_i) \rangle = -2H_\omega. \quad (2.32)$$

We have the same result upon interchanging  $v_i$  and  $\omega_i$ . Note that  $\mathbf{v} \cdot (\nabla \times \mathcal{F}) = \nabla \cdot (\mathcal{F} \times \mathbf{v}) + \mathcal{F} \cdot \boldsymbol{\omega}$ . Finally, Eq. (2.29) becomes, after eliminating all advection-like terms and dividing by two,

$$\frac{dH}{dt} = -2\nu H_\omega + \langle \omega_i \mathcal{F}_i \rangle. \quad (2.33)$$

This is the third invariant, first shown by J.-J Moreau [183] and H. K. Moffatt [175] (see, e.g., the review given by Ref. [176]).

### 2.2.4 Kelvin's circulation theorem

In 1869, William Thomson, 1st Baron Kelvin, proved that in the absence of rotational body forces (such as  $\mathbf{j} \times \mathbf{b}$ ) and dissipation, the circulation around a material loop is conserved. By a material loop (or material surface) we mean one that moves along with the fluid. We begin by considering the change in flux of vorticity through a material surface,  $S_m$  in a time  $\delta t$ :

$$\delta \int_{S_m} \boldsymbol{\omega} \cdot d\mathbf{S} = \delta t \int_{S_m} \frac{\partial \boldsymbol{\omega}}{\partial t} \cdot d\mathbf{S} + \oint_{S_m} \boldsymbol{\omega} \cdot \delta \mathbf{S}. \quad (2.34)$$

We also have  $\delta \mathbf{S} = (\mathbf{v} \times d\mathbf{l})\delta t$  where  $d\mathbf{l}$  is the line element of the curve  $\gamma_m$  bounding  $S_m$ . Application of this in Eq. (2.34) and taking the limit as  $\delta t$  goes to zero,

$$\frac{d}{dt} \int_{S_m} \boldsymbol{\omega} \cdot d\mathbf{S} = \int_{S_m} \frac{\partial \boldsymbol{\omega}}{\partial t} \cdot d\mathbf{S} - \oint_{\gamma_m} \mathbf{v} \times \boldsymbol{\omega} \cdot d\mathbf{l}. \quad (2.35)$$

Applying Stokes' integral theorem, we arrive at the kinematic equation (see, e.g., [66]),

$$\frac{d}{dt} \int_{S_m} \boldsymbol{\omega} \cdot d\mathbf{S} = \int_{S_m} \left[ \frac{\partial \boldsymbol{\omega}}{\partial t} - \nabla \times (\mathbf{v} \times \boldsymbol{\omega}) \right] \cdot d\mathbf{S}. \quad (2.36)$$

Another application of Stokes' theorem identifies this as the time rate of change of the circulation  $\Gamma \equiv \oint_{\gamma_m} \mathbf{v} \cdot d\mathbf{l}$ ,

$$\frac{d}{dt} \int_{S_m} \boldsymbol{\omega} \cdot d\mathbf{S} = \frac{d}{dt} \int_{S_m} \nabla \times \mathbf{v} \cdot d\mathbf{S} = \frac{d}{dt} \oint_{\gamma_m} \mathbf{v} \cdot d\mathbf{l} = \frac{d}{dt} \Gamma. \quad (2.37)$$

Finally, after substituting the vorticity equation into Eq. (2.36), we arrive at Kelvin's circulation theorem

$$\frac{d}{dt} \Gamma = \int_{S_m} [\nabla \times \mathcal{F} + \nu \nabla^2 \boldsymbol{\omega}] \cdot d\mathbf{S}. \quad (2.38)$$

That is, circulation is conserved in the absence of dissipation and rotational body forces.

## 2.3 Energy spectrum and scale-by-scale energy budget

The turbulent energy spectrum was first introduced by Simmons and Salter in 1938 [215]. The proof of its relation to the total energy through Parseval's theorem

was given by Rayleigh.<sup>9</sup> We now present a version of this proof. We utilize the Fourier transform  $\mathfrak{F}$  and its associated inverse transform  $\mathfrak{F}^{-1}$ . In 1D,

$$\mathfrak{F}[f(x)] \equiv \hat{f}(k) = \int_{-\infty}^{\infty} f(x) e^{-ikx} dx \quad (2.39)$$

and

$$\mathfrak{F}^{-1}[\hat{f}(k)] = \frac{1}{2\pi} \int_{-\infty}^{\infty} \hat{f}(k) e^{ikx} dk. \quad (2.40)$$

If the hypotheses of the Riemann-Lebesgue lemma<sup>10</sup> (or Dirichlet's theorem)<sup>11</sup> are satisfied, then  $\mathfrak{F}^{-1}[\hat{f}(k)] = f(x)$ . In 3D we apply the 1D transform thrice in succession. For  $v_i$  continuous, real-valued, and satisfying either the hypotheses of Riemann-Lebesgue or Dirichlet, Parseval's theorem guarantees

$$\frac{1}{2} \langle |\mathbf{v}|^2 \rangle = \frac{1}{2} \int \left( \frac{1}{2\pi} \right)^3 \hat{v}_i^*(\mathbf{k}) \cdot \hat{v}_i(\mathbf{k}) d\mathbf{k} \quad (2.41)$$

where  $(\cdot)^*$  indicates complex conjugation. The integrand in this expression is the spectral energy density,  $E(\mathbf{k}) \equiv \frac{1}{2} \left( \frac{1}{2\pi} \right)^3 \hat{v}_i^*(\mathbf{k}) \cdot \hat{v}_i(\mathbf{k})$ , from which the omni-directional spectral energy density,  $E(k)$ , may be obtained from the relation

$$E = \int_0^\infty \oint E(\mathbf{k}) d\sigma dk = \int_0^\infty E(k) dk \quad (2.42)$$

where  $\oint d\sigma$  represents integration over the surface of the sphere. Therefore,

$$E(k) = \left( \frac{1}{2\pi} \right)^2 k^2 \hat{v}_i^*(\mathbf{k}) \cdot \hat{v}_i(\mathbf{k}). \quad (2.43)$$

An example of an energy spectrum from a computation in a  $1024^3$  periodic box ( $Re \approx 3300$ , see [2]) is shown in Fig. 2.2.<sup>12</sup> This computation is used for all further figures in this chapter.

---

<sup>9</sup> This proof is attributed to Rayleigh in 1938 by Taylor [227]. It is unclear whether this refers to John William Strutt (1842-1919), Lord Rayleigh and some more general result or to Robert John Strutt (1875-1947), 4th Baron Rayleigh.

<sup>10</sup> That is,  $f(x)$  and its derivative are piecewise continuous on every finite interval,  $f$  is absolutely integrable, and  $f$  is continuous.

<sup>11</sup> Which applies when  $f(x)$  is periodic and continuous.

<sup>12</sup> Note that by  $N^3$  we imply a (generally pseudospectral) 3D uniform grid of  $N$  points in each direction.

The convolution<sup>13</sup> theorem,

$$\mathfrak{F}[f \otimes g] = \hat{f}(k)\hat{g}(k), \quad (2.44a)$$

$$\mathfrak{F}[fg] = \left(\frac{1}{2\pi}\right)^3 \hat{f} \otimes \hat{g}, \quad (2.44b)$$

for square-integrable functions  $f$  and  $g$  is another result of Fourier transforms that we require.

Following [76] we can derive the spectral energy balance equation in steps similar to the conservation of energy derivation. We first take the Fourier transform of Navier-Stokes, Eq. (2.5a),

$$\partial_t \hat{v}_i(\mathbf{k}) + \mathfrak{F}[v_j \partial_j v_i](\mathbf{k}) = -ik_i \hat{P}(\mathbf{k}) + \hat{\mathcal{F}}_i(\mathbf{k}) - \nu k^2 \hat{v}_i(\mathbf{k}) \quad (2.45)$$

where we have applied integration by parts as needed. From the convolution theorem, (2.44b), we have

$$\mathfrak{F}[v_j \partial_j v_i](\mathbf{k}) = \frac{i}{(2\pi)^3} \int \hat{v}_j(\mathbf{k} - \mathbf{q}) q_j \hat{v}_i(\mathbf{q}) d\mathbf{q}. \quad (2.46)$$

Multiplying Eq. (2.45) by  $\hat{v}_i^*(\mathbf{k})$  and substituting Eq. (2.46) we find,

$$\begin{aligned} \frac{1}{2} \partial_t (\hat{v}_i^*(\mathbf{k}) \hat{v}_i(\mathbf{k})) = & -\frac{i}{(2\pi)^3} \hat{v}_i^*(\mathbf{k}) \int_{\mathbf{k}=\mathbf{p}+\mathbf{q}} \hat{v}_j(\mathbf{p}) q_j \hat{v}_i(\mathbf{q}) d\mathbf{q} - i \hat{v}_i^*(\mathbf{k}) k_i \hat{P}(\mathbf{k}) + \\ & \hat{v}_i^*(\mathbf{k}) \hat{\mathcal{F}}_i(\mathbf{k}) - \nu k^2 \hat{v}_i^*(\mathbf{k}) \hat{v}_i(\mathbf{k}). \end{aligned} \quad (2.47)$$

This is the time evolution of the spectral energy density,  $(2\pi)^3 \partial_t E(\mathbf{k})$ . Integrating over all values of  $\mathbf{k}$ , we recover the energy budget equation, Eq. (2.15). From this relation between Eqs. (2.15) and (2.47) we may note three things. Firstly, the pressure term in Eq. (2.47) must vanish as it does not appear in Eq. (2.15). (This can also be seen more clearly by Eq. (2.67) in the Fourier transform of Eq. (2.47), Eq. (2.68).) Secondly, we may identify the dissipation rate density,

$$(2\pi)^3 \varepsilon(\mathbf{k}) = \nu k^2 \hat{v}_i^*(\mathbf{k}) \hat{v}_i(\mathbf{k}) \quad (2.48)$$

---

<sup>13</sup> The convolution of two functions is defined by  $[f \otimes g](y) \equiv \int f(x)g(y-x)dx$ .

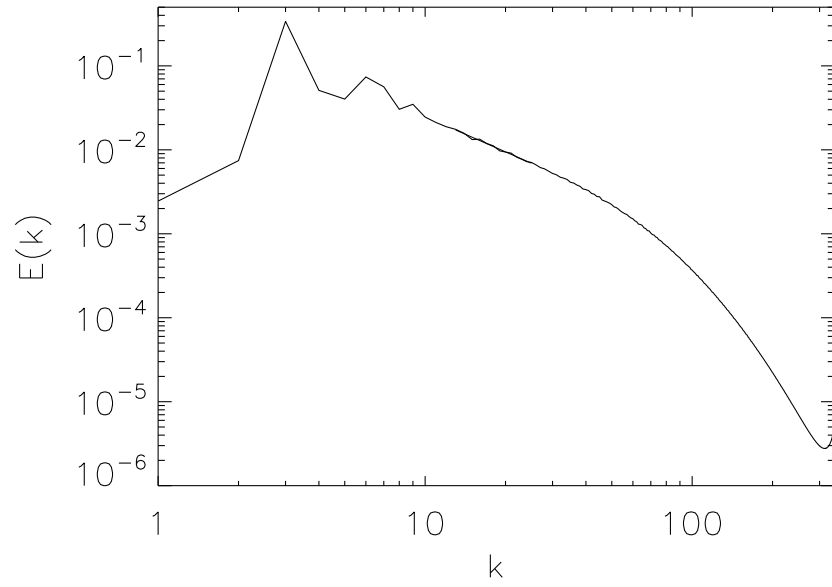


Figure 2.2: Example of an omni-directional spectral energy density,  $E(k)$ , versus wavenumber,  $k$  plotted in log-log coordinates. The bumps at  $k = 3$  and  $6$  are due to the forcing and its first harmonic. Details of this computation (used for all further figures in this chapter) are given in Ref. [2].

where  $\varepsilon = \int_0^\infty \oint \varepsilon(\mathbf{k}) d\sigma dk$ . Thirdly, the triadic transfer,

$$T(\mathbf{k}) \equiv \frac{i}{(2\pi)^6} \hat{v}_i^*(\mathbf{k}) \int_{\mathbf{k}=\mathbf{p}+\mathbf{q}} \hat{v}_j(\mathbf{p}) q_j \hat{v}_i(\mathbf{q}) d\mathbf{q}, \quad (2.49)$$

which exchanges energy between different wavenumbers, cannot change the total energy as the equivalent to Eq. (2.49) in Eq. (2.15) was shown to give zero contribution. That is,

$$\int_0^\infty \oint T(\mathbf{k}) d\sigma dk = 0. \quad (2.50)$$

Next, we define the cumulative energy,

$$\mathfrak{E}_K \equiv \int_0^K \oint E(\mathbf{k}) d\sigma dk, \quad (2.51)$$

the flux through wavenumber  $K$ ,

$$\Pi_K \equiv - \int_0^K \oint T(\mathbf{k}) d\sigma dk, \quad (2.52)$$

the cumulative energy injection,

$$\mathfrak{f}_K \equiv \frac{1}{(2\pi)^3} \int_0^K \oint \hat{v}_i^*(\mathbf{k}) \hat{\mathcal{F}}_i(\mathbf{k}) d\sigma dk, \quad (2.53)$$

and the cumulative energy dissipation,

$$2\nu\Omega_K \equiv \frac{2\nu}{(2\pi)^3} \int_0^K \oint k^2 \hat{v}_i^*(\mathbf{k}) \hat{v}_i(\mathbf{k}) d\sigma dk. \quad (2.54)$$

From Eq. (2.47), we then arrive at the scale-by-scale energy budget equation [80]

$$\partial_t \mathfrak{E}_K + \Pi_K = \mathfrak{f}_K - 2\nu\Omega_K. \quad (2.55)$$

This equation may be more easily understood from a pictorial representation, Fig. 2.3.

## 2.4 Kármán and Howarth, 1938

In 1921, G. I. Taylor introduced the two-point correlation tensor,  $\mathcal{Q}_{ij}(\mathbf{r}) \equiv \langle v_i(\mathbf{x}) v_j(\mathbf{x} + \mathbf{r}) \rangle$ , and in 1938 recognized its connection to the energy spectrum: that

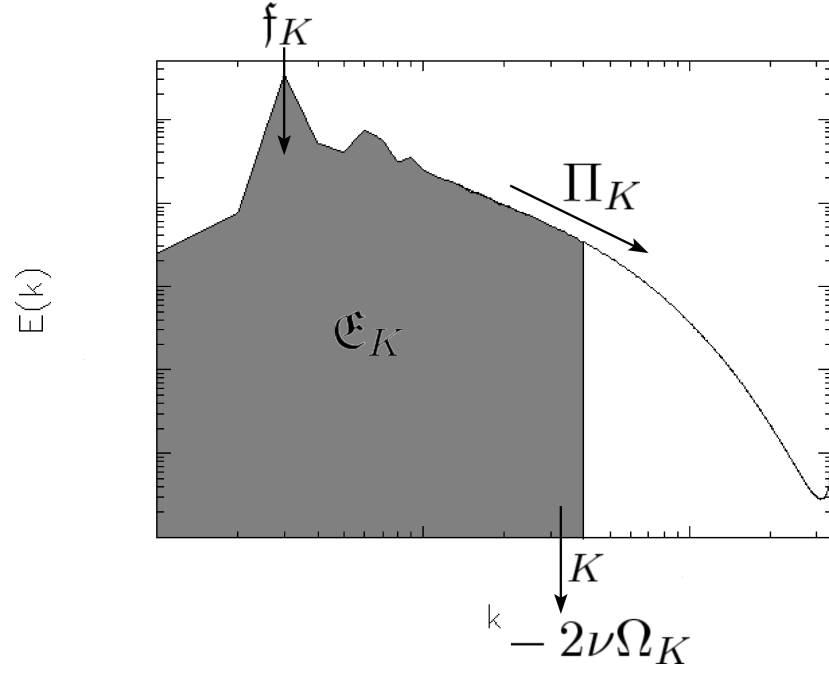


Figure 2.3: Illustration of the scale-by-scale energy budget equation, Eq. (2.55). The gray area represents the cumulative energy,  $\mathfrak{E}_K$ , the time derivative of which is given by the flux of energy to wavenumbers greater than  $K$ ,  $-\Pi_K$ , plus the injection of energy up to wavenumber  $K$ ,  $\mathfrak{f}_K$ , minus energy loss to dissipation from all scales up to  $K$ ,  $2\nu\Omega_K$ .



they “are, in fact, Fourier transforms of one another” [227]. This follows directly from the convolution theorem, Eq. (2.44a). Therefore,

$$\widehat{\mathcal{Q}_{ii}(\mathbf{r})} = 2(2\pi)^3 E(\mathbf{k}). \quad (2.56)$$

If  $\mathcal{Q}_{ij}(\mathbf{r})$  is large, there are eddies which span  $|\mathbf{r}|$  and, if zero, the motions at  $\mathbf{x}$  and  $\mathbf{x}' \equiv \mathbf{x} + \mathbf{r}$  are independent. In 1935, Taylor introduced the concept of homogeneous and isotropic turbulence [226]. Homogeneity is the assumption that mean properties do not vary with position. Isotropy implies the independence of direction as well (all velocity moments are invariant under rotation). In 1938, Kármán and Howarth [68] derived from the Navier-Stokes equations an exact law relating the time derivative of the two-point correlation with the divergence of the third-order correlation. This result is significant in that experimentally verifiable scalings follow from it.

We review that important result here, but for the sake of simplicity, we consider the case without viscous dissipation,  $\nu = 0$ , and without any external forcing,  $\mathcal{F} = 0$ . These terms can be added at any point in the derivation. As we seek to employ the result at scales far away from both the forcing and the dissipation, we do not need these terms. We denote  $\mathbf{v}' \equiv \mathbf{v}(\mathbf{x}', t)$  and compute the ingredients of the time derivative of  $\mathcal{Q}_{ij} = \langle v_i v'_j \rangle$ . Navier-Stokes, Eq. (2.5a), may be rewritten at  $\mathbf{x}$  and  $\mathbf{x}'$  as

$$\partial_t v_i + \partial_m (v_i v'_m + P \delta_{im}) = 0, \quad (2.57a)$$

$$\partial_t v'_j + \partial'_m (v'_j v'_m + P' \delta_{jm}) = 0. \quad (2.57b)$$

Multiplying Eq. (2.57a) by  $v'_j$  and Eq. (2.57b) by  $v_i$  and integrating yields

$$\langle v'_j \partial_t v_i \rangle = - \langle \partial_m (v_i v'_j v'_m + P v'_j \delta_{im}) \rangle, \quad (2.58a)$$

$$\langle v_i \partial_t v'_j \rangle = - \langle \partial'_m (v_i v'_j v'_m + P' v_i \delta_{jm}) \rangle. \quad (2.58b)$$

As averages and differentiation permute,<sup>14</sup> by the chain rule  $(\partial/\partial r_m \langle \cdot \rangle = -\partial/\partial x_m \langle \cdot \rangle)$

---

<sup>14</sup> Again invoking the assumptions necessary for Lebesgue dominated convergence (see Section 2.2.1).

we have,

$$-\partial_m \langle v_i v'_j v_m \rangle = + \frac{\partial}{\partial r_m} \langle (v_i v'_j v_m) \rangle. \quad (2.59)$$

For Eq. (2.58b), we replace  $\mathbf{r}$  with  $-\mathbf{r}$  so that the chain rule now yields  $\partial/\partial r_m = -\partial/\partial x'_m$  and

$$-\partial'_m \langle v_i v'_j v'_m \rangle = + \frac{\partial}{\partial r_m} \langle (v_i(\mathbf{x}) v_j(\mathbf{x} - \mathbf{r}) v_m(\mathbf{x} - \mathbf{r})) \rangle. \quad (2.60)$$

After noting that  $\langle (v_i(\mathbf{x}) v_j(\mathbf{x} - \mathbf{r}) v_m(\mathbf{x} - \mathbf{r})) \rangle = \langle (v_i(\mathbf{x}') v_j(\mathbf{x}) v_m(\mathbf{x})) \rangle$ , we may combine Eqs. (2.58a) and (2.58b) to find

$$\partial_t \langle v_i v'_j \rangle = \frac{\partial}{\partial r_m} \langle v_i v'_j v_m + v'_i v_j v_m \rangle + \frac{\partial}{\partial r_m} \langle P v'_j \delta_{im} - P' v_i \delta_{jm} \rangle. \quad (2.61)$$

We define the third-order correlation tensors

$$\mathcal{T}_{ijm} = \langle (v_i v'_j + v_j v'_i) v_m \rangle, \quad (2.62)$$

$$\Pi_{ijm} = \langle P v'_j \delta_{im} - P' v_i \delta_{jm} \rangle. \quad (2.63)$$

To see that  $\langle P v'_j \rangle$  vanishes we rotate into the coordinate frame such that  $\mathbf{r} = (|\mathbf{r}|, 0, 0)$ .

We denote by  $w'_j$  the components of  $v'_j$  in this coordinate frame. As the pressure at point  $\mathbf{x}$  can affect only the component of velocity along  $\mathbf{r}$  at point  $\mathbf{x}'$ , we have that  $\langle P w'_j \rangle = 0$  (no correlation) for  $j = 2$  or  $3$ . We may then write

$$\langle P w'_1 \rangle = f(r). \quad (2.64)$$

From incompressibility, Eq. (2.1b), along with our usual boundary conditions (introduced in Section 2.2) we have that

$$\nabla \cdot \langle P v'_j \rangle = 0. \quad (2.65)$$

Transforming to spherical coordinates, we see that

$$\frac{\partial}{\partial r} [r^2 \sin \theta f(r)] = 0 \quad (2.66)$$

for which the solution is  $f = c/r^2$ . Demanding regularity at the origin we have  $f = 0$  and, hence,  $\langle Pw'_j \rangle = 0 \forall j$  and

$$\langle Pv'_j \rangle = 0 \forall j. \quad (2.67)$$

Finally,  $\Pi_{ijm}$  vanishes and we obtain

$$\partial_t \mathcal{Q}_{ij} = \frac{\partial}{\partial r_m} \mathcal{T}_{ijm}. \quad (2.68)$$

This is the Kármán-Howarth equation and the Fourier transform of the spectral energy balance, Eq. (2.47). This may appear at first as a “solution” to the problem of Navier-Stokes in that we have an expression for the time evolution of the second-order correlation and, hence the energy spectrum. In fact, the expression is not closed as the third-order correlation is dependent on the fourth-order correlation and so on and so forth. This is the so-called closure problem.

Recalling the association between the second-order correlation and the energy spectrum, Eq. (2.56), and employing Eqs. (2.47) and (2.48), we have that

$$\partial_t \widehat{\mathcal{Q}}_{ii} = \partial_t 2(2\pi)^3 E(\mathbf{k}) = -2(2\pi)^3 \varepsilon(\mathbf{k}). \quad (2.69)$$

Applying the inverse Fourier transform to this yields that the time derivative of the two-point correlation tensor is proportional to the dissipation rate,<sup>15</sup>

$$\partial_t \mathcal{Q}_{ii}(\mathbf{r}) = -2\hat{\varepsilon}(\mathbf{r}). \quad (2.70)$$

To see the importance of this fact, we must consider another statistic employed in turbulence theory, the structure functions. These are the moments of the velocity increments,

$$\delta \mathbf{v}(\mathbf{r}) \equiv \mathbf{v}(\mathbf{x}') - \mathbf{v}(\mathbf{x}). \quad (2.71)$$

For the present analysis, it is sufficient to show the relation between the divergence of a third-order structure function to that of the third order correlation tensor  $\mathcal{T}_{iim}$ . First

---

<sup>15</sup> Here we define  $\hat{\varepsilon}(\mathbf{r}) \equiv \nu \langle \omega_i(\mathbf{x}) \omega_i(\mathbf{x} + \mathbf{r}) \rangle$ . We assume we may take the limit as  $r$  goes to zero for which we find  $\varepsilon = \hat{\varepsilon}$  (see Section 2.5 and Ref. [80] for further discussion on assumptions involving limits in turbulence theory).

we note that

$$\langle (\delta v_i)^2 \delta v_m \rangle = -2 \langle v_i v'_i v'_m \rangle + \langle (v_i)^2 v'_m \rangle - \langle (v'_i)^2 v_m \rangle + 2 \langle v_i v'_i v_m \rangle \quad (2.72)$$

where two terms have been dropped due to homogeneity. From incompressibility we have  $\partial(v'_i)^2 v_m / \partial r_m = 0$  and homogeneity yields

$$\frac{\partial}{\partial r_m} - 2 \langle v_i v'_i v'_m \rangle = \frac{\partial}{\partial r_m} + 2 \langle v'_i v_i v_m \rangle \quad (2.73)$$

as previously demonstrated. Therefore, we find

$$\frac{\partial}{\partial r_m} \langle (\delta v_i)^2 \delta v_m \rangle = 2 \frac{\partial}{\partial r_m} \mathcal{T}_{im}. \quad (2.74)$$

Combining Eqs. (2.68), (2.70), and (2.74), we find the Kármán-Howarth-Monin relation

$$\varepsilon = -\frac{1}{4} \nabla_m \cdot \langle |\delta \mathbf{v}_i|^2 \delta \mathbf{v}_m \rangle \quad (2.75)$$

which applies to homogeneous solutions to Navier-Stokes (isotropy is not required) [80]. Curiously, this relation was not found until 1975 by Monin and Yaglom [180]. This is the anisotropic generalization of Kolmogorov's celebrated four-fifths law, to which we turn now before addressing its significance.

## 2.5 Kolmogorov, 1941

Andrei Nikolævich Kolmogorov's 1941 theory [131, 130, 129] (K41 hereafter) begins from the assumption of an inertial range. As forcing is assumed to occur at much larger scales and dissipation at much smaller scales, the dynamics is dominated by the inertia terms ( $d\mathbf{v}/dt = 0$ ). This idea was first proposed in 1922 by Lewis Fry Richardson who envisioned a process whereby large eddies break up into smaller eddies and viscous stresses are negligible (the process is driven by inertia). The inertial range follows from taking the following limits applied to the scale-by-scale energy budget equation, Eq. (2.55). First we assume that the limit as time goes to infinity exists. This yields

stationarity (the statistics of the velocity field are independent of time) and, thus,

$$\lim_{t \rightarrow \infty} \partial_t \mathfrak{E}_K = 0. \quad (2.76)$$

We then find that the flux, injection and dissipation of energy are all equal and in particular,

$$\Pi_K = \varepsilon. \quad (2.77)$$

That is, the flux of energy across scales in the inertial range is constant and equal to the dissipation rate. Where Eq. (2.77) holds is the conjectured inertial range. An example from the  $Re \approx 3300$  computation used for our examples is shown in Fig. 2.4. This prediction has been verified, for example, recently in a computation of incompressible homogeneous Navier-Stokes turbulence in a  $2048^3$  periodic box computed on the Earth Simulator by Kaneda et al. [126]. Next we take the limit of zero viscosity (infinite Reynolds number) so that we may, *a priori*, ignore dissipation, and the limit of  $r$  going to zero so that we may ignore the forcing term. Consequently, we may employ our “inertial-range” Kármán-Howarth equation, Eq. (2.68). Finally, Kolmogorov employed the Kármán-Howarth theory of isotropic tensors [68] which results in the Kármán-Howarth theorem and directly from that (note the relation between  $\Pi_K$  and  $\mathcal{T}_{iik}$ ) found

$$\langle \delta v_{\parallel}^3 \rangle = -\frac{4}{5} \epsilon r, \quad (2.78)$$

where  $\delta v_{\parallel}(\mathbf{r}) \equiv \delta \mathbf{v}(\mathbf{r}) \cdot \mathbf{r} / r$  is the longitudinal velocity increment. This is the Kolmogorov four-fifths law. This result is exact, non-trivial, and experimentally verifiable. As such, it marks the first major step towards a theory of turbulence. It has been empirically verified, for instance, in the analysis of atmospheric turbulent boundary layer data at  $R_{\lambda} \simeq O(10^4)$  with an inertial range broader than three decades [234] (for numerical confirmation, see, e.g., [261]). In Fig. 2.5 we show an example confirmation (of the  $r^1$  scaling) from the computation described in [2] (see Ref. [6] for a generalization including transverse components and Ref. [260] for the passive tracer).

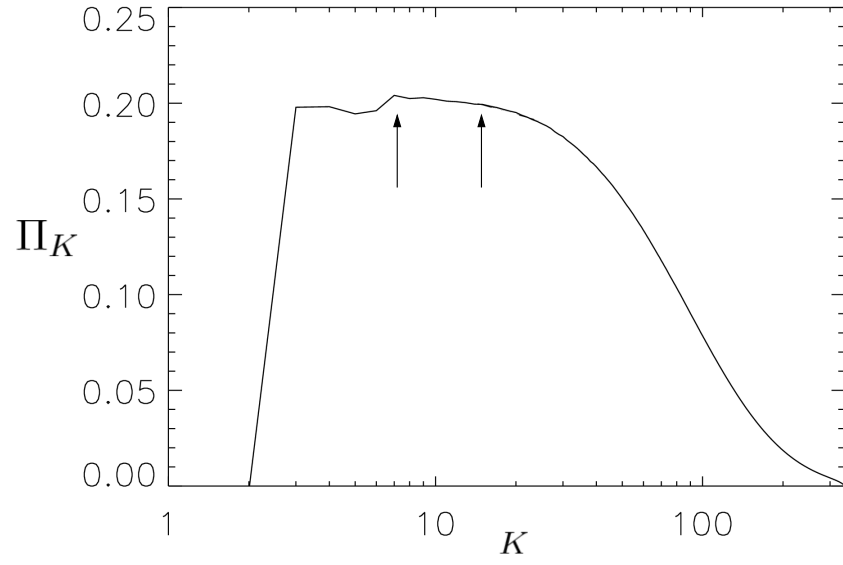


Figure 2.4: Example of flux,  $\Pi_K$ , versus wavenumber,  $K$ . The approximate inertial range where the flux is constant and equal to  $\varepsilon$  is indicated by arrows. The feature from  $k = 3$  to  $k \approx 6$  is again due to the forcing. Details of the computation are given in Ref. [2].

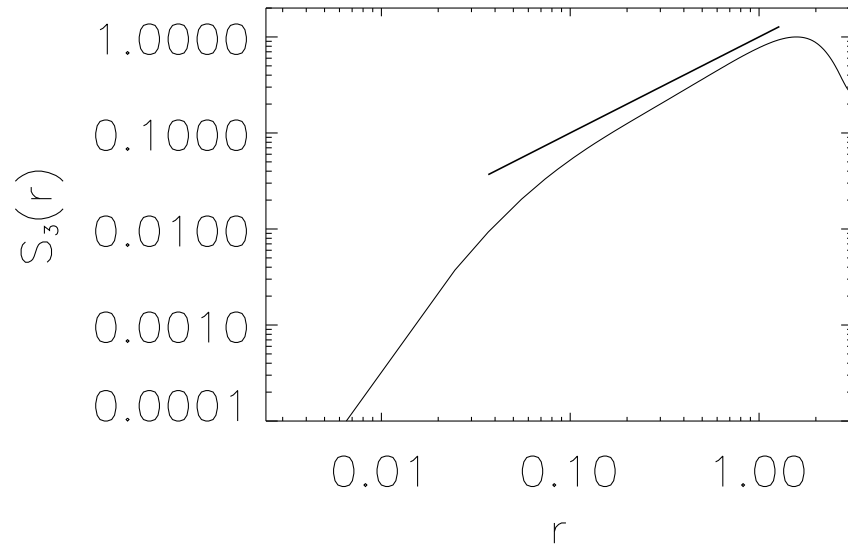


Figure 2.5: Kolmogorov's four-fifths law:  $S_3(r) = \langle \delta(v_{\parallel}(r))^3 \rangle$  versus  $r$  in log-log. The straight line indicates a slope of 1 consistent with the four-fifths law. Details of the computation are given in Ref. [2]. See Ref. [261] for an example of confirmation of the 4/5 coefficient.

K41 theory assumes a finite positive dissipation in the limit of infinite  $Re$  (zero viscosity). This is the previously empirically determined law of finite dissipation which is supported by many experimental (and computational) results [222, 230, 80]. For example, using a  $4096^3$  computation ( $R_\lambda = 1200$ ) it is suggested that the normalized mean energy dissipation rate  $D \equiv \langle \epsilon \rangle L / (E^{3/2})$  tends to a constant as  $\nu \rightarrow 0$  [126]. It is also the case that K41 implicitly assumes there are finite-time singularities for the Euler equations (Navier-Stokes with  $\nu = 0$ ). This is because the absence of finite-time singularities for Euler means that [80]

$$\lim_{\nu \rightarrow 0} \epsilon = 0, \quad (2.79)$$

because a smooth field has finite gradients. This is a violation of the (empirical) law of finite dissipation. The theory is also dependent on the order of the limits taken (if the limit of  $r$  going to zero is taken before the limit of zero viscosity, we find  $\langle \delta v_\parallel^3 \rangle \propto r^3$  [80]). Nonetheless, the theory is valuable to the degree to which it agrees with experiment, observation, and computation.

The next assumption in K41 is that of scale-invariance (self-similarity). “Scale invariance means that certain features of the flow remain the same in different scales of motion. Such a symmetry can be interpreted as a particularly simple relationship between small and large scales” [162]. In particular, Kolmogorov assumed that the velocity increments are self-similar:

$$\langle \delta \mathbf{v}(\lambda \mathbf{r}) \rangle = \lambda^h \langle \delta \mathbf{v}(\mathbf{r}) \rangle \quad (2.80)$$

which we apply to the longitudinal structure functions,

$$S_p(\mathbf{r}) \equiv \langle (\delta v_\parallel(\mathbf{r}))^p \rangle. \quad (2.81)$$

From this we may infer that

$$S_p \propto r^{ph}. \quad (2.82)$$



The last assumption in K41 is that of universality, that some statistical properties of turbulence are the same regardless of the forcing, the boundary conditions, or what fluid is flowing. Namely, he proposed

$$S_p = C_p \varepsilon^{ph} r^{ph}, \quad (2.83)$$

where  $C_p$  is a dimensionless, universal constant for all turbulent flows. From the four-fifths law, Eq. (2.78), we have that  $h = 1/3$  (and  $C_3 = -4/5$ ). From this determination of the scaling constants, we can find verification of K41 theory by comparison with the empirical two-thirds law,  $\langle (\delta v(r))^3 \rangle \propto r^{2/3}$  [80, 188]. Taking Eq. (2.83) with  $p = 2$  (and given that  $h = 1/3$ ), we find Kolmogorov's and Obukhov's [189, 190] two-thirds law

$$S_2(\mathbf{r}) \equiv \langle (\delta v_{\parallel}(\mathbf{r}))^2 \rangle \propto r^{2/3}. \quad (2.84)$$

This is our second experimentally verified prediction of K41 theory (to within small intermittency corrections, see Section 2.8.2).

Next, we observe the connection between the second-order structure function and the two-point correlation tensor,

$$S_2 \equiv \langle (v'_i - v_i)^2 \rangle = 4E - 2Q_{ii}, \quad (2.85)$$

which is now directly related to the energy spectrum through Eq. (2.56). Therefore, we have

$$S_2 = 4E - 4(2\pi)^3 \mathfrak{F}^{-1}[E(\mathbf{k})]. \quad (2.86)$$

Under the assumption that the energy spectrum is a power law,  $E(k) \propto k^{-n}$  with  $1 < n < 3$ , it can be shown [80] that  $S_2 \propto r^{n-1}$ . Using this with the two-thirds law yields Kolmogorov's five-thirds law (hereafter the K41 energy spectrum),

$$E(k) \propto \varepsilon^{2/3} k^{-5/3} \quad (2.87)$$

where  $\varepsilon^{2/3}$  yields the correct dimensions. This is the final and most famous prediction of the K41 theory. It has been confirmed in numerous fluid experiments, in numerical

calculations, and even in astrophysical phenomena and other applications far exceeding the hypotheses used to derive it [97, 48, 158, 18]. We close this section by showing as an example a computational spectrum compared to the K41 scaling in Fig. 2.6.

## 2.6 Phenomenology

Phenomenology is a broader, less rigorous approach to turbulence theory that essentially amounts to dimensional analysis. For instance, following Obukhov [189, 190] and Kraichnan [134] we denote the root-mean-square (*r.m.s.*) velocity for an eddy of size  $k^{-1}$  as  $V_k$ ,

$$V_k = \left( \frac{1}{D} \int_D |\mathbf{v}_k|^2 d^3x \right)^{1/2} \quad (2.88)$$

where  $\mathbf{v}_k$  denotes, e.g., a bandpass filtered velocity with the bandpass centered at wavenumber  $k$ . From dimensional analysis we conclude that the corresponding turnover time,  $\mathbf{t}_k$ , for an eddy of size  $k^{-1}$  is

$$\mathbf{t}_k \propto 1/(kV_k). \quad (2.89)$$

Similarly, we relate the *r.m.s.* velocity  $V_k$  to the spectral energy density  $E(k)$  by

$$V_k \sim \left( \int E(k) dk \right)^{1/2} \sim (kE(k))^{1/2} \quad (2.90)$$

Then, the total energy dissipation rate,  $\varepsilon$  must also then be related to the spectral energy density by  $\varepsilon \equiv dE/dt \sim E/\mathbf{t}_k$  or,

$$\varepsilon \sim (\mathbf{t}_k)^{-1} \int E(k) dk \sim k^2 V_k E(k) \sim k^{5/2} E(k)^{3/2}. \quad (2.91)$$

This yields the K41 energy spectrum,

$$E(k) \sim (\varepsilon)^{2/3} k^{-5/3}. \quad (2.92)$$

Ignoring forcing (which is assumed to take place at large scales) in the energy dissipation relation, Eq. (2.15), noting that for dissipation the large wavenumbers dominate,

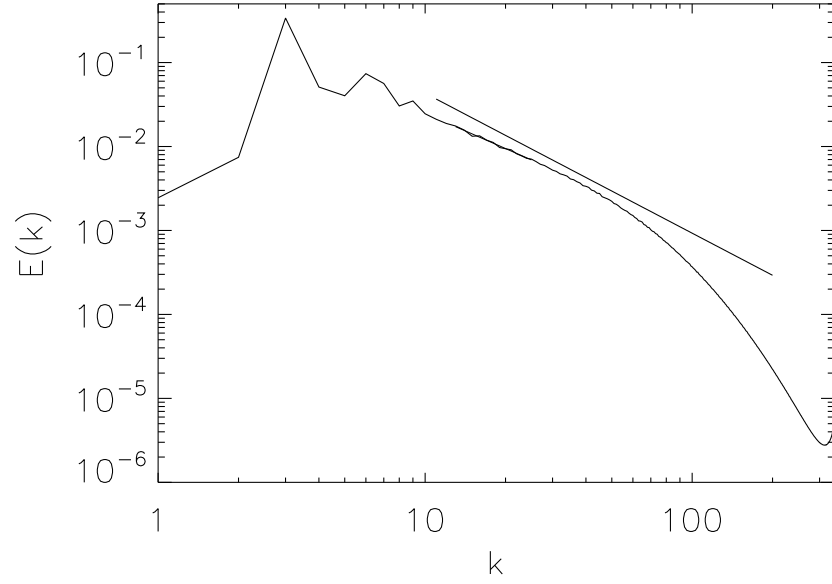


Figure 2.6: Kolmogorov’s five-thirds law:  $E(k)$ , versus wavenumber,  $k$  plotted in log-log. The straight line indicates a  $k^{-5/3}$  scaling. Note that this scaling is only reproduced in the relatively small inertial range (shown in Fig. 2.4). At higher wavenumber a shallower spectrum is observed (to be discussed in Section 2.8.1). Details of the computation are given in Ref. [2]. As a rule of thumb, an order of magnitude in wavenumbers is needed to resolve each of the dissipation, this shallower (or “bottleneck” spectrum), and between the forcing and the inertial range; this leaves only a very small inertial range at a resolution of  $1024^3$  [103].

and inserting the K41 energy spectrum we can estimate the Kolmogorov dissipation wavenumber  $k_\eta$  by

$$\frac{\varepsilon}{\nu} \propto \int^{k_\eta} k^2 E(k) dk \sim \int^{k_\eta} k^2 \varepsilon^{2/3} k^{-5/3} dk \sim \varepsilon^{2/3} (k_\eta)^{4/3}. \quad (2.93)$$

Then we have,

$$k_\eta \sim \left( \frac{\varepsilon}{\nu^3} \right)^{1/4}. \quad (2.94)$$

This estimate has been found to predict accurately the necessary resolution for numerical computation of turbulent Navier-Stokes solutions and allows a heuristic counting of the degrees of freedom (*dof*). We note that  $Re \propto \nu^{-1}$  and that  $dof \propto (Lk_\eta)^3$  to estimate,

$$dof \propto Re^{9/4}. \quad (2.95)$$

## 2.7 Extensions to Magnetohydrodynamics (MHD)

In 1951, Subrahmanyan Chandrasekhar extended the theory of homogeneous isotropic turbulence to MHD [50, 51]. He derived the (ideal) conservation of total energy,

$$\frac{dE_T}{dt} = -2\nu\Omega - 2\eta\Omega_M \quad (2.96)$$

(where  $E_T = \langle v^2 + b^2 \rangle / 2$  and  $\Omega_M = \langle j^2 \rangle / 2$ ) of cross helicity,

$$\frac{dH_C}{dt} = -\frac{1}{2}(\nu + \eta) \langle \boldsymbol{\omega} \cdot \mathbf{j} \rangle \quad (2.97)$$

(where  $H_C = \langle \mathbf{v} \cdot \mathbf{b} \rangle / 2$ ) and the time evolution of the correlation tensors  $\langle u_i u'_j \rangle$  and  $\langle b_i b'_j \rangle$  for the MHD equations, Eqs. (2.3). In 3D magnetic helicity is also an ideal invariant,

$$\frac{dH_M}{dt} = -\eta \langle \mathbf{b} \cdot \mathbf{j} \rangle \quad (2.98)$$

where  $H_M = \langle \mathbf{a} \cdot \mathbf{b} \rangle$  and  $\mathbf{a}$  is the vector magnetic potential,  $\mathbf{b} = \nabla \times \mathbf{a}$ . In 2D, the mean square magnetic vector potential is instead an ideal invariant,

$$\frac{d\mathcal{A}}{dt} = -2\eta E_M \quad (2.99)$$

where  $\mathcal{A} = \langle a^2 \rangle$  and  $E_M = \langle b^2 \rangle / 2$  is the magnetic energy. Other ideal invariants are as in Navier-Stokes: mass, momentum, and angular momentum.

The MHD equations, Eqs. (2.3), can be written using the Elsässer variables,  $\mathbf{z}^\pm = \mathbf{v} \pm \mathbf{b}$ :

$$\partial_t \mathbf{z}^\pm + \mathbf{z}^\mp \cdot \nabla \mathbf{z}^\pm = -\nabla P_* + \nu_+ \nabla^2 \mathbf{z}^\pm + \nu_- \nabla^2 \mathbf{z}^\mp \quad (2.100)$$

where  $P_* = P + b^2/2$  is the total pressure and  $\nu_\pm = (\nu \pm \eta)/2$ . In terms of these variables the total energy is given by  $E_T = \langle \mathbf{z}^\pm \cdot \mathbf{z}^\mp \rangle$ . Politano and Pouquet [201, 204] have extended the Kármán-Howarth theorem to the MHD case using these variables. The equivalent of Kolmogorov's four-fifths law for MHD is

$$\langle \delta z_\parallel^\mp |\delta z^\pm|^2 \rangle = -\frac{4}{d} \varepsilon^\pm r, \quad (2.101)$$

where  $d$  is the number of space dimensions and  $\varepsilon^\pm = -\partial_t E^\pm$  where  $E^\pm = \langle (z^\pm)^2 \rangle / 2$ . Again this is an exact relation for the third-order (mixed) structure function.

The phenomenological derivation of the K41 energy spectrum (see Section 2.6) is also valid for MHD (in Eqs. (2.3) the magnetic field has the same units as the velocity field and the dimensional arguments are unchanged). However, unlike Navier-Stokes, incompressible MHD supports wave perturbations. This can be seen by linearizing the MHD equations in the presence of a uniform magnetic field  $B_0$  (see, e.g., [66, 194]). These transverse disturbances are Alfvén waves. They take the form  $\mathbf{v} = \pm \mathbf{b}$  and travel along the magnetic field lines of  $B_0$ . In fact, as  $\mathbf{v} = \pm \mathbf{b}$  implies that  $\mathbf{z}^\mp = 0$  identically, we can see that these waves are solutions of the nonlinear MHD equations, Eqs. (2.100) as the nonlinear term is always zero in these cases. Because of these waves a second phenomenology, introduced by Iroshnikov and by Kraichnan [125, 133] (hereafter, the IK model), is possible. In the IK model the plus and minus Alfvén waves can only interact when they collide along field lines (along which they travel in opposite directions). The characteristic time for an Alfvén wave is  $\mathbf{t}_A \sim (kB_0)^{-1}$ . If this is less than a turnover

time, Eq. (2.89), the effective transfer time  $\mathfrak{t}_T$  is increased,

$$\mathfrak{t}_T \sim \frac{\mathfrak{t}_k^2}{\mathfrak{t}_A}. \quad (2.102)$$

Now, the total energy dissipation rate,  $\varepsilon$  is related to the spectral energy density by  $\varepsilon \equiv dE_T/dt \sim E_T/\mathfrak{t}_T$  or,

$$\varepsilon \sim (\mathfrak{t}_T)^{-1} \int E_T(k) dk \sim \frac{k^2 V_k^2}{B_0} E_T(k) \sim k^3 B_0^{-1} E_T(k)^2. \quad (2.103)$$

This yields the IK energy spectrum,

$$E_T(k) \sim (\varepsilon B_0)^{1/2} k^{-3/2}. \quad (2.104)$$

The debate about which scaling, K41 or IK, is correct and under what conditions is still open. One consequence is that in IK theory, the longitudinal structure functions are predicted to follow the self-similar scaling:  $S_p \propto r^{p/4}$ .

## 2.8 Beyond K41

### 2.8.1 Nonlocality

In this section we address problems with K41 theory. The problems arise from two assumptions: self-similarity and (spectral) locality. Locality is a concept that began with the Richardson cascade. It is the idea that an eddy of a given size cannot interact with (be distorted by) eddies of a far greater size (which vary little at its scale) nor with eddies of a far lesser size (which act as incoherent ensembles) [80]. This is an implicit assumption in K41 in that we neglect forcing (assumed to be at far greater scales) and dissipation (at far lesser scales) in the inertial range. It is also a fundamental assumption in K41 phenomenology. Finally, when the large scales are inhomogeneous and/or anisotropic, the idea that small scales restore isotropy and homogeneity is based strongly on the assumption of local interactions between scales.

It has been discovered that nonlinear triadic transfer, Eq. (2.49), is local at each scale but occurs through nonlocal interactions [2, 169]. In fact, several forcing schemes

were tried for 3D periodic boundary conditions and even in the case of an isotropic random forcing, the energy cascades with a fixed step ( $\delta k = k' - k$  where energy is transferred from wavenumber  $k$  to  $k'$ ) proportional to the forcing wave number. This constitutes a breakdown of the assumption of self-similarity which would dictate the step size to vary as a power law of  $k'$ . Indeed, these strong nonlocal interactions are responsible for a non-negligible fraction of the total flux ( $\approx 20\%$ , though the fraction decreases slowly as  $Re$  increases). It was also determined that both local and nonlocal interactions can give a K41 spectrum while nonlocal interactions give rise to intermittency (an exception to the assumption of self-similarity to be discussed shortly) [2, 169]. It was further determined that the so-called bottleneck<sup>16</sup> in the energy spectrum (see Fig. 2.7) is due to depletion of energy transfer from local interactions which are inhibited because of numerical and/or viscous cut off in wave number and the nonlocal triads become dominant (without nonlocal interactions, there is no bottleneck and reduced intermittency [106]). Based on these results, for turbulent flows in astrophysics and geophysics, there could be persistence of anisotropies in the small scales because of nonlocal interactions. In that case, the theory of homogeneous isotropic turbulence would be of less generality.

For MHD, the departure from locality is even more pronounced. Energy transfer has been studied in the kinematic (or linear) dynamo regime and in the steady-state regime for the case of constant forcing for 3D periodic boundary conditions [3, 168]. Long-range interactions in Fourier space were found for transfer from the velocity field to the magnetic field while locality of transfer was found for magnetic energy to magnetic energy and for kinetic energy to kinetic energy (corresponding to advection). In the steady-state regime, a small-scale magnetic field receives the same amount of energy from all larger scales of the velocity field in the inertial range. Furthermore, this non-

---

<sup>16</sup> The “bottleneck” or “spectral bump” is a bulge of the energy spectrum at the end of the inertial  $k^{-5/3}$  range and before the exponentially decreasing dissipation range (see, e.g., [139]).

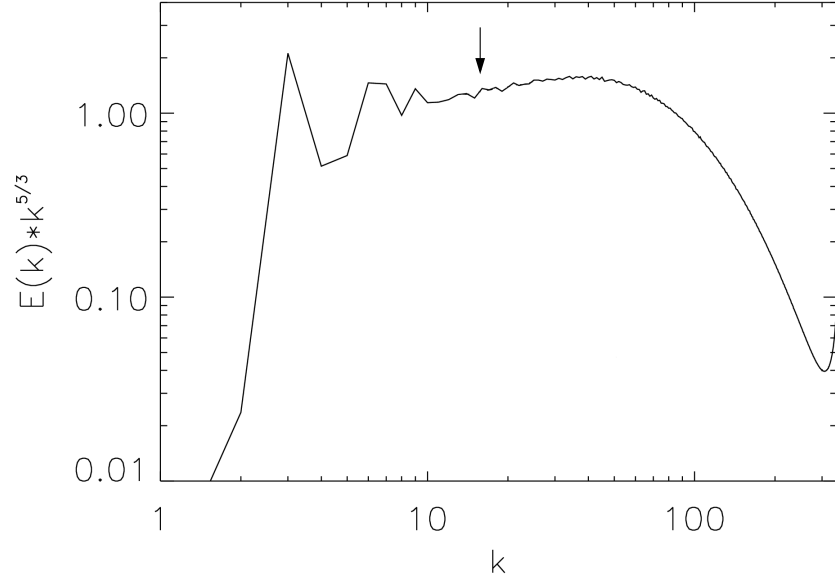


Figure 2.7: Spectra compensated by  $k^{5/3}$  so that a K41 spectrum appears flat. The arrow indicates the beginning of the so-called bottleneck where a shallower spectrum ( $\approx k^{-4/3}$ ) is observed (see, e.g., [139]). The bottleneck appears in both computation and experimental/observational results. It is in contradiction with K41 theory and drastically reduces the extent of an observable K41 inertial range. Computation on a  $1024^3$  grid,  $Re \approx 3300$  [2].



local transfer amounted to 20% of all energy transferred to that scale (the other 80% came from local magnetic-magnetic transfers) at the Reynolds number of the study,  $R_\lambda \sim 750$ .<sup>17</sup> It was suggested that this nonlocality of the energy transfer is a general feature of mechanically forced MHD turbulence though different forcings might produce different (nonlocal) transfers. For the kinematic dynamo regime, at scales down to the peak of the magnetic energy spectrum, input directly from the large-scale kinetic energy to magnetic energy dominates while for smaller scales is not as important as the direct cascade of magnetic energy. This puts the assumptions of small-scale homogeneity and isotropy at even greater risk for geophysical MHD (the core of the Earth) and astrophysical applications than for Navier-Stokes applications.

### 2.8.2 Intermittency

An intermittent signal is a signal that exhibits a “burstiness” or “spottiness” (see Fig. 2.8). The increments,  $\delta \mathbf{f}(\mathbf{r}) \equiv \mathbf{f}(\mathbf{x} + \mathbf{r}) - \mathbf{f}(\mathbf{x})$ , have a different behavior whether  $r \equiv |\mathbf{r}|$  is (i) larger (or smaller) than a “typical” relative quiescence length between bursts and whether  $r$  is (ii) larger (or smaller) than a “typical” burst length. Because of this critical behavior with scale, the average of the velocity increments taken at these different scales cannot satisfy Kolmogorov’s assumption of their self-similarity:  $\langle \delta \mathbf{v}(\lambda r) \rangle = \lambda^h \langle \delta \mathbf{v}(r) \rangle$  (see Fig. 2.9). Consequently, the K41 prediction for the structure functions ( $p \neq 3$ ),

$$S_p \propto r^{\zeta_p}, \quad (2.105a)$$

$$\zeta_p = p/3, \quad (2.105b)$$

does not hold. For  $p = 2$  this has consequences for the  $k^{-5/3}$  K41 energy spectrum. In fact, for the Earth simulator computation [126], it was found that  $\zeta_2 = 2/3 + \mu_r$  with  $\mu_r = 0.067$ . At the same time, the correction to the energy spectrum  $E(k) \propto k^{-(5/3+\mu_k)}$

---

<sup>17</sup> The Taylor Reynolds number,  $R_\lambda \equiv v_{r.m.s} \lambda / \nu$ , is based on the Taylor microscale,  $\lambda \equiv 2\pi \sqrt{\langle v^2 \rangle / \langle \omega^2 \rangle}$ , and is frequently used as it is more easily determined for experiments.

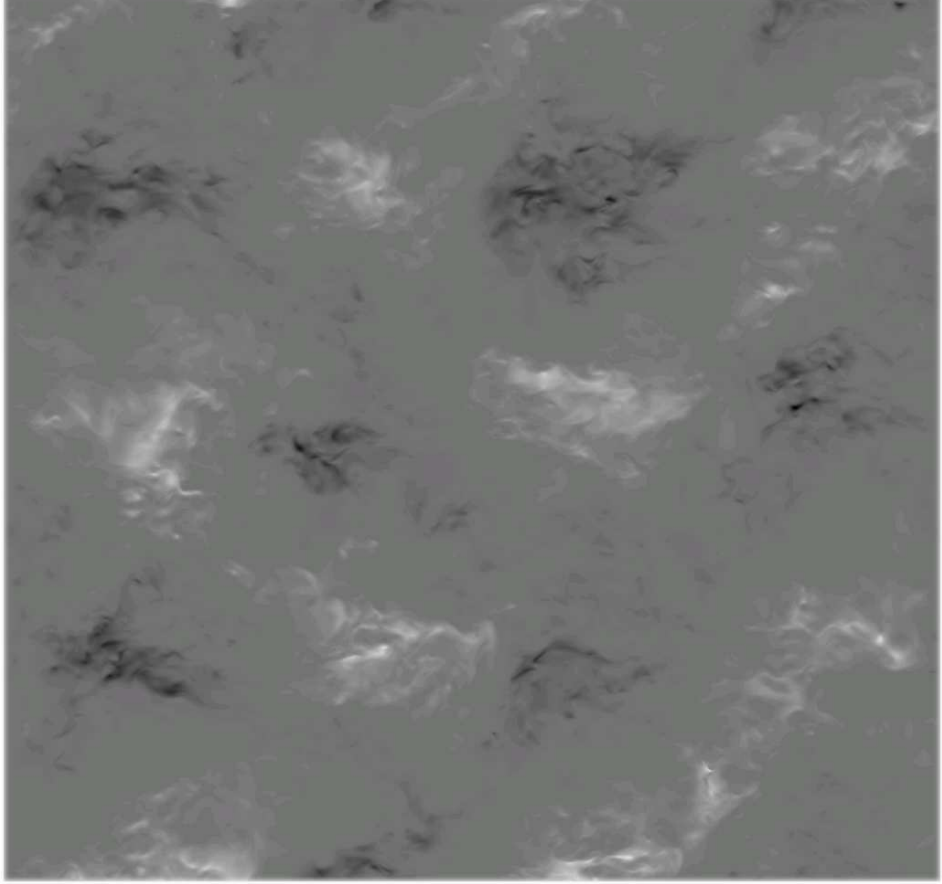


Figure 2.8: Example of a spatially intermittent signal. The “bursty” patches (black and white) are surrounded by a more quiescent background of gray. The data is a 2D slice of  $(v_x)^3$  (corresponding to energy transfer, since dimensionally,  $\varepsilon \sim v^3/l$ ) from the  $Re \approx 3300$  computation used for illustrations in this chapter. Details of the computation are given in Ref. [2].

was found to be  $\mu_k = 0.1$  (it should be the case that  $\mu_k = \mu_r$  and the difference between the two measurements was attributed to the short width of the inertial range). For observations of the atmospheric turbulent boundary layer, the Kolmogorov constant,  $C_2$  in Eq. (2.83), was found to be a function of  $R_\lambda$  and was affected by large-scale anisotropy [234]. Thus, the assumptions of both self-similarity and universality are contradicted.

The intermittency corrections to K41 for the high-order ( $p > 4$ ) structure functions are even larger than for the energy spectrum corrections. How the scaling exponents,  $\zeta_p$ , of these differ from the K41 prediction, the so-called anomalous scaling, is a useful measure of intermittency. The structure functions at numerically achievable Reynolds numbers exhibit a very small inertial range (see Fig. 2.5). In fact, the amount of data used in calculating  $S_p(r)$  determines the highest order for which we can even observe a scaling in the inertial range. Above this order, the assumption of self-similarity allows us to fit a scaling law to our data in any event. But in the absence of sufficient statistics, such a fit can be poor and the error bars rather large (see Fig. 2.10). As the four-fifths law is exact, it can be used to compute more accurate anomalous scaling exponents of structure functions of higher order. Due to cancellation problems (linked with having limited statistics), absolute values are often employed; we also find linear scaling in this case, *viz.*:

$$L(r) \equiv \langle |\delta v_\parallel|^3 \rangle \propto r. \quad (2.106)$$

Accordingly we determine the relative scaling exponents,  $\xi_p$ ,

$$S_p(r) \propto [L(r)]^{\xi_p} \quad (2.107)$$

and note that

$$\xi_p = \frac{\zeta_p}{\zeta_3}. \quad (2.108)$$

This is the Extended Self-Similarity (ESS) hypothesis [12, 13, 14, 15] which is found to apply to a much wider scaling range than the inertial range. Here, the scaling range

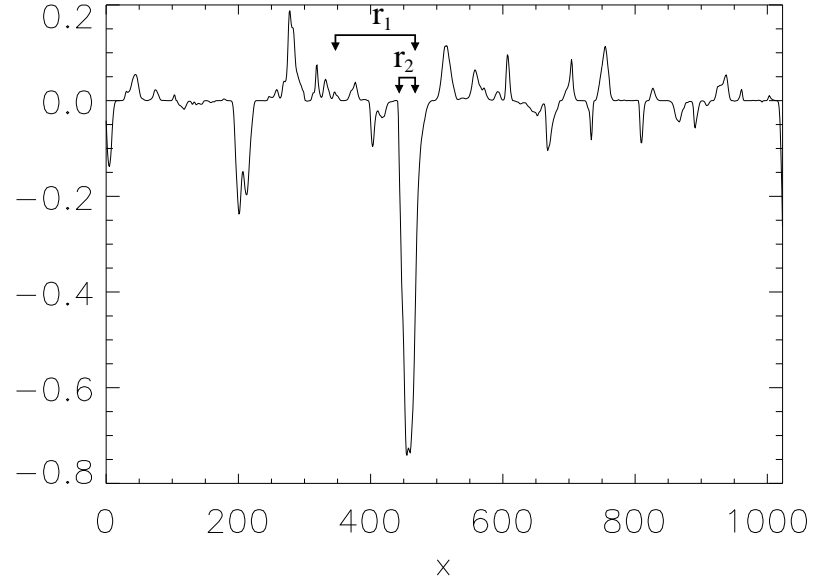


Figure 2.9: Example of scale dependence for increments of an intermittent signal: 1D slice of Fig. 2.8. Increments taken with  $r$  larger ( $r_1$ ), or smaller ( $r_2$ ), than a typical burst length behave differently when averaged over the entire signal and cannot satisfy Kolmogorov's assumption of the self-similarity of velocity increments,  $\langle \delta \mathbf{v}(\lambda r) \rangle = \lambda^h \langle \delta \mathbf{v}(r) \rangle$ .

is determined by the observed scaling for low orders and a chief benefit is increased statistics to compute more accurate exponents at higher order (again, see Fig. 2.10).

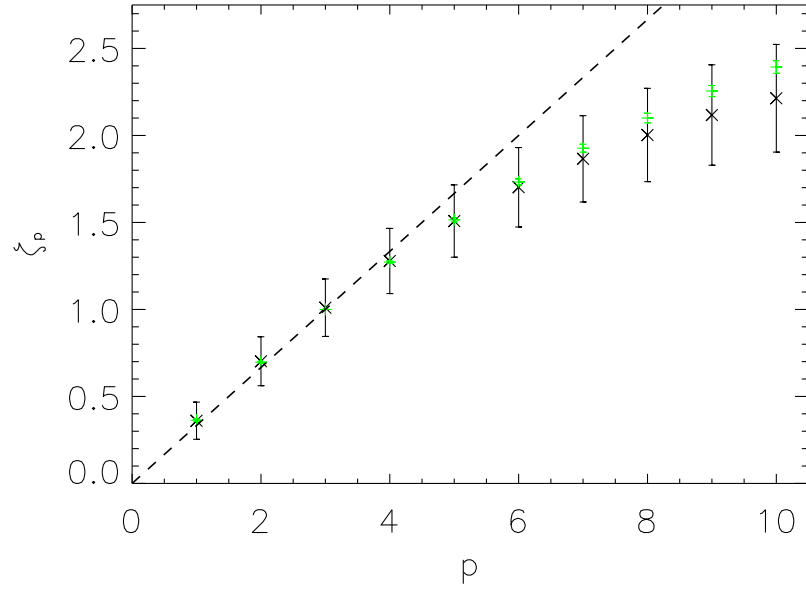


Figure 2.10: Anomalous scaling of structure function exponents:  $\zeta_p$  versus  $p$  from a  $Re \approx 3300$  numerical simulation [2]. Black X's correspond to results calculated from the inertial range and green pluses to results from utilizing the ESS hypothesis which allows for a more precise determination as can be seen from the error bars. The K41 prediction, Eqs. (2.105), is shown as a dashed line.

## Chapter 3

### Subgrid modeling

Nonlinearities prevail in turbulent flows when the Reynolds number,  $Re$ , is large [80]. For geophysical flows, the Reynolds number is often larger than  $10^8$  and for some astrophysical flows  $Re \sim 10^{18}$  is not unreasonable. The number of degrees of freedom (*dof*) in the flow increases as  $Re^{9/4}$  for  $Re \gg 1$  in the Kolmogorov framework (see Section 2.6). Such a huge number of *dof* make direct numerical simulations (DNS) infeasible on any existing or projected computer for decades to come. Because of this intractability, simulations are always carried out in a region of parameter space far from the observed values either with (a) an unphysical lack of scale separation between the energy-containing, inertial, and dissipative ranges while empirically parameterizing the missing physics or (b) a study of the processes at much smaller length scales and often with periodic boundaries (unphysical at large scales but often used under the hypothesis of homogeneity of turbulent flows). Clearly, modeling of unresolved small scales is necessary. Two main approaches to do this have been developed over the years. The first approach to handle the unresolved small scales is Large Eddy Simulations (LES, see [162, 211]). They are widely used in engineering, in atmospheric sciences, and to a lesser extent in astrophysics. However, in the LES approach, the Reynolds number is not known. Instead, one attempts modeling the behavior of the flow in the limit of very large  $Re$ . A different approach is to use modeling tools that allow for a larger Reynolds number than what a DNS would give on a given grid, by using a variety of

techniques that can be viewed as filtering on the small scales. However, intermittency is included explicitly in neither approach. It is not clear whether the overall statistics of the flow at large scale is affected by the omission of small-scale intermittency, and if so, how intermittency should be incorporated [46, 197, 196].

A rather novel approach to modeling of turbulent flows is regularization modeling employed as a LES (albeit with a known  $Re$ ) [58, 88, 89, 114, 60, 90]. Unlike other subgrid closures which normally employ eddy-viscosity concepts and modify the dissipative processes, this approach modifies the spectral distribution of energy. Existence and uniqueness of smooth solutions can be rigorously proven as well as the fact that the subgrid model recovers the Navier-Stokes equations in the limit of the filter width going to zero, unlike many LES (e.g. eddy-viscosity). Their robust analytical properties ensure computability of solutions. We show in Section 3.1.5 that eddy-viscosity models (on which many LES are based) can be related to an assumption of a  $k^{-5/3}$  spectrum. For this reason, they are not suitable for transitional flows<sup>1</sup> nor easily extendible to MHD where there is more than one field and some controversy has arisen regarding the power law (see Section 2.7) for the total energy spectrum (there are power law corrections to Navier-Stokes due to intermittency as well, see Section 2.8.2). In this chapter, we present a brief review of LES and regularization subgrid modeling.

### 3.1 Large eddy simulations (LES)

LES is the modeling of a turbulent flow with more degrees of freedom than are computable by truncating the number of scales that are represented. We spatially low-bandpass filter the Navier-Stokes equations, Eqs. (2.5), with a filter,  $L : \mathbf{z} \rightarrow \bar{\mathbf{z}}$ , where  $\bar{\mathbf{z}}$  ( $\mathbf{z}$ ) denotes the filtered (unfiltered) field and  $\mathbf{z}'$  ( $\mathbf{z} = \bar{\mathbf{z}} + \mathbf{z}'$ ) the high spatial frequency fluctuations. By convention we define  $u_i \equiv \bar{v}_i$ . As proposed by Leonard, we employ a convolution filter and let  $\bar{G}(\mathbf{r})$  be the convolution kernel,  $[Lz](\mathbf{r}) = \int \bar{G}(\mathbf{r} - \mathbf{r}') z(\mathbf{r}') d^3 \mathbf{r}'$

---

<sup>1</sup> By transitional flow we imply transition between a laminar state and fully developed turbulence.



[143]. Filtering Eqs. (2.5) yields

$$\partial_t u_i + \partial_j(u_j u_i) + \partial_i \bar{p} + \partial_j \bar{\tau}_{ij} = \nu \partial_{jj} u_i \quad (3.1)$$

where  $\bar{\tau}_{ij} = \overline{v_i v_j} - \bar{v}_i \bar{v}_j$  is the turbulent stress tensor. This stress is similar to the forces on a pipe that contains a turbulent flow in that it represents the forces on a resolution element due to the turbulent motions contained inside it. The turbulent stress tensor  $\bar{\tau}_{ij}$  is often called the subgrid-scale (SGS) stress tensor.<sup>2</sup> As the unfiltered fields are not available some approximate model (hence the term subgrid modeling) must be made for  $\bar{\tau}_{ij}$ . This is again the problem of closure which we first discussed in Section 2.4. In this section we review briefly the major LES subgrid models and their performance.

To gage this performance, two types of tests are typically performed. The first are *a priori* validations that compare the exact  $\bar{\tau}_{ij}$  for a given filter calculated from a DNS to the approximation for the turbulent stress tensor that the model would produce with the filtered exact solution. Following Clark et al. [63], these tests are correlations,  $\rho$ , for the subgrid stress,  $\bar{\tau}_{ij}$ , the subgrid forcing,  $\partial_j \bar{\tau}_{ij}$ , or the subgrid dissipation,  $u_i \partial_j \bar{\tau}_{ij}$ . These tests are of limited predictive power, however, as the effects of modeling errors to the temporal evolution are neglected [211]. Comparisons between filtered DNS data and real LES runs (*a posteriori* tests) are far more valuable in ascertaining the usefulness of a model. As has been pointed out, however, “*a posteriori* tests typically do not provide much insight into the detailed physics of models and the reasons that they do or do not work” [162].

### 3.1.1 The eddy-viscosity of Smagorinsky

By analogy with momentum transfer from molecular motion in a fluid causing molecular (kinematic) viscosity, Boussinesq postulated in 1877 that the momentum transfer caused by turbulent eddies can be modeled with an eddy viscosity [47, 138,

---

<sup>2</sup> Sub-filter-scale would be more appropriate.

29]. From Newton's empirical law of viscosity, we have that shear stress is directly proportional to fluid distortion,

$$\tau_{ij} = -\nu(\partial_j v_i + \partial_i v_j). \quad (3.2)$$

In 1963, Smagorinsky applied eddy-viscosity as an LES [216, 147]:

$$\bar{\tau}_{ij} - \frac{1}{3}\bar{\tau}_{kk}\delta_{ij} = -2\nu_T\bar{S}_{ij} \quad (3.3)$$

where  $\bar{S}_{ij} = (\partial_j \bar{v}_i + \partial_i \bar{v}_j)/2$  is the resolved strain-rate tensor and  $\nu_T$  is called eddy viscosity. The  $\frac{1}{3}\delta_{ij}$  assures that (in the absence of shear) the stress tensor is isotropic with its trace equal to negative two times the subgrid scale kinetic energy [148]. The eddy viscosity is assumed to be of the form

$$\nu_T = (C_S \bar{\Delta})^2 |\bar{S}| \quad (3.4)$$

where  $|\bar{S}| = (2\bar{S}_{ij}\bar{S}_{ij})^{1/2}$  is the magnitude of the resolved strain-rate tensor,  $C_S$  is the Smagorinsky constant ( $\approx 0.2$  for isotropic homogeneous turbulence [162]), and  $\bar{\Delta}$  is the filter width. This is a reasonable first-approach to subgrid modeling and makes possible computation at resolutions at least an order of magnitude smaller than would otherwise be possible. But, unlike the molecular case, for turbulence there is no clear separation of scales and Eq. (3.3) cannot be true if eddies are larger than the scale of the curvature of the velocity field [138]. In addition, the model is completely dissipative and, therefore, can provide no “backscatter” or energy transferred from the subfilter scales to the resolved scale [162]. Furthermore, the eigenvectors of  $\bar{S}_{ij}$  and  $\bar{\tau}_{ij}$  are rarely aligned which invalidates a central assumption of the model [63, 162]. The *a priori* correlations are  $\rho(\bar{\tau}_{ij}, \bar{\tau}_{ij}^{smag}) \sim 0$  to 0.25,  $\rho(\partial_j \bar{\tau}_{ij}, \partial_j \bar{\tau}_{ij}^{smag}) \sim 0.4$  and for the local SGS dissipation rate  $\rho(u_i \partial_j \bar{\tau}_{ij}, u_i \partial_j \bar{\tau}_{ij}^{smag}) \sim 0.5$  to 0.7 [162]. Thus, the Smagorinsky model is poorly correlated with the turbulent stress tensor. While the SGS dissipation rate correlation is quite good, in transition to turbulence it predicts excessive damping (inhibits the transition) [198, 199] and has excessive dissipation near solid walls and

in laminar flow with large gradients [90]. Smagorinsky is solely dissipative and cannot represent normal stress effects in sheared turbulent flows [177]. Overall, the performance can be summarized as the “eddy viscosity model does not adequately capture the proper physics of SGS turbulence” [162].

### 3.1.2 Dynamic model

To address problems near solid walls and with transitional regimes as well as the absence of backscatter, a dynamic eddy-viscosity model was introduced [85]. It utilizes an algebraic identity between the turbulent stress tensors for two different filter widths called “Germano’s identity” [84]. As usual, we obtain filtered LES fields by use of a convolution filter:

$$\bar{f}(x) = \int \bar{G}(x - x')f(x')dx'. \quad (3.5)$$

We also employ a coarser “test” filter:

$$\tilde{f}(x) = \int \tilde{G}(x - x')f(x')dx'. \quad (3.6)$$

Consider a doubly-filtered field:

$$\tilde{\tilde{f}}(x) = \int \tilde{G}(x - x')\bar{f}(x')dx', \quad (3.7)$$

or

$$\tilde{\tilde{f}}(x) = \int \tilde{G}(x - x') \int \bar{G}(x' - y)f(y)dydx'. \quad (3.8)$$

under Fubini’s theorem,<sup>3</sup>

$$\tilde{\tilde{f}}(x) = \int \int \tilde{G}(x - x')\bar{G}(x' - y)dx'f(y)dy. \quad (3.9)$$

Now, let  $x - x' = -z'$  and we find

$$\tilde{\tilde{f}}(x) = \int f(y) \int \tilde{G}(-z')\bar{G}(z' - (y - x))dz'dy. \quad (3.10)$$

---

<sup>3</sup> For a finite domain (as used in computation), the assumptions for Fubini’s theorem are satisfied if  $f$ ,  $\bar{G}$ , and  $\tilde{G}$  are bounded, measurable functions (which, in general, they are).

So we can now identify the kernel for doubly-filtered fields (assuming symmetric filters,  $G(-z') = G(z')$ ) as

$$\tilde{\tilde{G}}(x - y) = \int \tilde{G}((x - y) - z') \bar{G}(z') dz' \quad (3.11)$$

where we employed  $h \otimes g = g \otimes h$ . As usual the sub-filter scale stress is  $\bar{\tau}_{ij} = \overline{\bar{v}_i \bar{v}_j} - \bar{v}_i \bar{v}_j$  and the sub-test scale (STS) stress tensor is  $T_{ij} = \widetilde{\bar{v}_i \bar{v}_j} - \tilde{\bar{v}}_i \tilde{\bar{v}}_j$ . We define the resolved turbulent stress as

$$\mathfrak{L}_{ij} = \widetilde{\bar{v}_i \bar{v}_j} - \tilde{\bar{v}}_i \tilde{\bar{v}}_j \quad (3.12)$$

which represents the stresses from the “small” resolved scales (those intermediate to the two filter widths,  $\bar{\Delta}$  and  $\tilde{\Delta}$ ). This quantity can be completely determined from the LES as it uses only the filtered velocity,  $\bar{\mathbf{v}}$ . Germano’s identity is easily derived,

$$\begin{aligned} \mathfrak{L}_{ij} &= \widetilde{\bar{v}_i \bar{v}_j} - \widetilde{\bar{v}_i \bar{v}_j} + \widetilde{\bar{v}_i \bar{v}_j} - \tilde{\bar{v}}_i \tilde{\bar{v}}_j \\ &= T_{ij} - \tilde{\tau}_{ij}, \end{aligned} \quad (3.13)$$

and can be used to determine the Smagorinsky constant  $C_S$  as a function of time and space for any flow. Assuming eddy-viscosity, Eqs. (3.3) and (3.4), approximates the stress at both filter widths, we have

$$\bar{\tau}_{ij} - \frac{1}{3} \bar{\tau}_{kk} \delta_{ij} \approx m_{ij}, \quad (3.14)$$

where

$$m_{ij} = -2 (C_S \bar{\Delta})^2 |\bar{S}| \bar{S}_{ij}, \quad (3.15)$$

and

$$T_{ij} - \frac{1}{3} T_{kk} \delta_{ij} \approx M_{ij}, \quad (3.16)$$

where

$$M_{ij} = -2 (C_S \tilde{\Delta})^2 |\tilde{S}| \tilde{S}_{ij}. \quad (3.17)$$

From which we obtain

$$\mathfrak{L}_{ij} - \frac{1}{3} \delta_{ij} \mathfrak{L}_{kk} = -2 C_S^2 \left( \tilde{\Delta}^2 |\tilde{S}| \tilde{S}_{ij} - \bar{\Delta}^2 \widetilde{|\bar{S}| \bar{S}_{ij}} \right). \quad (3.18)$$

Here we have assumed the SGS stress is self-similar for the scales  $\bar{\Delta}$  and  $\tilde{\Delta}$  (this can be problematic for intermittent flows). As Eq. (3.18) represents five equations with a single unknown, the system is over-determined. The error can be minimized by a standard least-squares approach as first recognized by Lilly [148]. This model represents a step forward as the *a posteriori* results for the dynamic Smagorinsky model are improved over those of Smagorinsky alone. Unfortunately, the method can be destabilizing in numerical simulations [162].

### 3.1.3 Similarity model

Bardina et al (1980) employ the assumption of self-similarity almost literally. That is, they assume that

$$\bar{\tau}_{ij} = C_{sim} \mathfrak{L}_{ij}. \quad (3.19)$$

This model performs very well in *a priori* tests:  $\rho(\tau_{ij}^{DNS}, \tau_{ij}) \sim 0.8$  (somewhat lower for SGS force and dissipation) and it is able to produce backscatter. However, the similarity model has inadequate dissipation and unrealistically high levels of small scale fluctuations and, therefore, it produces inaccurate results in *a posteriori* testing. For this reason, it is often used with additional dissipation supplied from coarsening the grid or in mixed models with a Smagorinsky term (i.e.,  $\bar{\tau}_{ij}$  is given by Eq. (3.3) *plus* Eq. (3.19)). Finally, when employed in mixed models with a Smagorinsky term and dynamic determination of both constants, it performs better in *a posteriori* tests than all other eddy-viscosity-type LES [162].

### 3.1.4 Leonard tensor-diffusivity (Clark) model

The Leonard tensor-diffusivity model [143] (*aka* the Clark model [63]) has an interesting history. The model itself is easily written,

$$T_{ij} = \gamma \partial_k u_i \partial_k u_j \quad (3.20)$$

where the constant  $\gamma$  is determined by which tensor  $T_{ij}$  we are actually trying to model, as we now discuss. Leonard originally proposed it to model the now-called Leonard term,  $L_{ij}$ , where

$$\begin{aligned}\bar{\tau}_{ij} &= \overline{v_i v_j} - \overline{\bar{v}_i \bar{v}_j} + \overline{\bar{v}_i \bar{v}_j} - \bar{v}_i \bar{v}_j \\ &= \overline{\bar{v}_i v'_j} + \overline{\bar{v}_i v'_j} + \overline{v'_i v'_j} + \overline{\bar{v}_i \bar{v}_j} - \bar{v}_i \bar{v}_j \\ &= C_{ij} + R_{ij} + L_{ij},\end{aligned}\tag{3.21}$$

and where  $C_{ij}$  is the cross-stress tensor,

$$C_{ij} = \overline{\bar{v}_i v'_j} + \overline{\bar{v}_i v'_j},\tag{3.22}$$

$R_{ij}$  is the subgrid-scale Reynolds stress tensor,

$$R_{ij} = \overline{v'_i v'_j},\tag{3.23}$$

and, finally, the Leonard term is

$$L_{ij} = \overline{\bar{v}_i \bar{v}_j} - \bar{v}_i \bar{v}_j,\tag{3.24}$$

(see [63, 143]). When employing a Reynolds operator (a filter that is a linear projector with the following properties:  $\overline{\bar{z}} = \bar{z}$ ,  $\overline{z'} = 0$  and  $\overline{\bar{z}z} = \bar{z}\bar{z}$ , see [211]) we have identically

$$L_{ij} = C_{ij} = 0.\tag{3.25}$$

Clark suggested employing the Leonard model to model  $\bar{\tau}_{ij}$  but did not do so himself and rather named a separate model after himself for the cross term,

$$C_{ij} \sim \bar{v}_i \nabla^2 \bar{v}_j + \bar{v}_j \nabla^2 \bar{v}_i.\tag{3.26}$$

This model never received much attention. Instead, crediting Clark with the suggestion to use the Leonard model for the turbulent stress tensor, many authors refer to the Leonard model as the Clark model.

Under the name of nonlinear or gradient model, the Leonard model has also been used in conjunction with the dynamic similarity model to avoid the expense of a second filtering. Here, we determine the similarity constant  $C_{sim}$  with

$$C_{sim}\mathfrak{L}_{ij} \approx C_{nl}\bar{\Delta}^2\partial_k\bar{v}_i\partial_k\bar{v}_j \quad (3.27)$$

where, typically,  $C_{nl} = 1/12$ . In combination with a Smagorinsky term such a dynamic model performs nearly as well in *a posteriori* tests as the mixed dynamic similarity model (which employs the second filtering) [162]. Such a model, however, does not predict the correct behavior near walls [150].

As first demonstrated in Ref. [43], the Leonard tensor-diffusivity model, Eq. (3.20), is the first term of the reconstruction series for the turbulent sub-filter stress for all symmetric filters that have a nonzero second moment. Next, we recount this proof. Assume the Fourier transform of the convolution filter kernel  $\hat{\hat{G}}(k)$  is  $C^\infty$  and that two fields  $a(x)$  and  $b(x)$  have Fourier transforms and are  $C^\infty$  (for simplicity we begin in 1D).

**Theorem 1** (Generalized commutator for symmetric filters and products:

$$\overline{ab} - \bar{a}\bar{b} = \bar{\Delta}^2\partial_x\bar{a}\partial_x\bar{b} + \mathcal{O}(\bar{\Delta}^3)). \quad \text{We begin with the assumption,}$$

$$\overline{ab} = \sum_{r,s=0}^{\infty} c_{rs}\partial_x^r\bar{a}\partial_x^s\bar{b}. \quad (3.28)$$

Taking the Fourier transform of this relation and making repeated use of the Convolution Theorem, Eqs. (2.44), we find

$$\hat{\hat{G}}(k) \int dq \hat{a}(q)\hat{b}(k-q) = \sum_{r,s=0}^{\infty} c_{rs} \int dq (iq)^r \hat{\hat{G}}(q)\hat{a}(q)(i(k-q))^s \hat{\hat{G}}(k-q)\hat{b}(k-q). \quad (3.29)$$

Invoking Lebesgue dominated convergence, we commute integration and summation and note that Eq. (3.29) must be true for all  $a(x)$ ,  $b(x)$  and  $q$ . Therefore, it must be the case that

$$\hat{\hat{G}}(k) = \sum_{r,s=0}^{\infty} c_{rs} (iq)^r \hat{\hat{G}}(q)(i(k-q))^s \hat{\hat{G}}(k-q). \quad (3.30)$$

The assumed expansion Eq. (3.28) is valid if and only if

$$F(\phi, \psi) \equiv \sum_{r,s=0}^{\infty} c_{rs} \phi^r \psi^s \quad (3.31)$$

is a real and bounded function (unbounded derivatives of  $a(x)$  or  $b(x)$  would still be a problem). Through the change of variables  $q = -i\phi$ ,  $k - q = -i\psi$  in Eq. (3.30) we find that

$$F(\phi, \psi) = \frac{\hat{\hat{G}}(-i(\phi + \psi))}{\hat{\hat{G}}(-i\phi)\hat{\hat{G}}(-i\psi)}. \quad (3.32)$$

Since  $\hat{\hat{G}}(k)$  is assumed symmetric,  $F$  is real (invariant under  $i \rightarrow -i$ ) and the assumed expansion Eq. (3.28) is valid. Furthermore,  $F$  is the generating function for the expansion. Assuming  $\hat{\hat{G}}(k)$  is normalized and symmetric we have that  $\hat{\hat{G}}(0) = 1$  and  $d\hat{\hat{G}}/dk(0) = 0$ . Then the first terms in the Taylor expansion of  $F$  are

$$F(\phi, \psi) = 1 - \frac{d^2 \hat{\hat{G}}(k)}{dk^2}|_{k=0} \phi \psi + \dots \quad (3.33)$$

We define the filter width  $\bar{\Delta}$  by noting the relation

$$\frac{d^2 \hat{\hat{G}}(k)}{dk^2}|_{k=0} = - \int_{-\infty}^{\infty} x^2 \bar{G} x dx \equiv \bar{\Delta}^2. \quad (3.34)$$

Substitution into Eq. (3.28) yields

$$\overline{ab} - \bar{a}\bar{b} = \bar{\Delta}^2 \partial_x \bar{a} \partial_x \bar{b}. \quad (3.35)$$

Extrapolation to 3D follows assuming that the filter is taken as a product of 1D filters and assuming an isotropic expansion:

$$\overline{a_i b_j} = \sum_{r,s=0}^{\infty} c_{rs} \partial_k^r \bar{a}_i \partial_k^s \bar{b}_j. \quad (3.36)$$

The resulting generating function is then

$$F(\phi, \psi) = \frac{\hat{\hat{G}}(-i(\phi + \psi))}{\hat{\hat{G}}(-i\phi)\hat{\hat{G}}(-i\psi)} = \sum_{r,s=0}^{\infty} c_{rs} \phi_k^r \psi_k^s. \quad (3.37)$$

This approximation of the subgrid stress, Eq. (3.35), is then generic [256, 43]. In a priori testing, it reconstructs a significant fraction ( $> 90\%$  but not all) of the subgrid



stress, provides for local backscatter along the stretching directions while remaining globally dissipative, and possesses a better reconstruction of the subgrid stress than the similarity model. In *a posteriori* testing the Leonard tensor-diffusivity model required additional dissipation (a dynamic Smagorinsky term) to achieve reasonable gains in computation speed for 3D periodic flows and for channel flows [256].

### 3.1.5 Spectral eddy-viscosity

This method of LES is used in conjunction with pseudospectral calculation where derivatives are taken in Fourier space and the nonlinear term,  $\mathbf{v} \cdot \nabla \mathbf{v}$  is calculated in real space. We begin with the time evolution of the spectral energy density Eq. (2.47),

$$\partial_t E(\mathbf{k}, t) + T(\mathbf{k}, t) = \frac{1}{(2\pi)^3} \hat{v}_i^*(\mathbf{k}, t) \hat{\mathcal{F}}_i(\mathbf{k}, t) - 2\nu k^2 E(\mathbf{k}, t), \quad (3.38)$$

where  $T(\mathbf{k}, t)$  is given by Eq. (2.49). In this form, subgrid modeling amounts to specifying the portion of the transfer  $T(\mathbf{k})$  for which  $p$  and/or  $q$  is larger than the truncation wavenumber  $k_c$ , i.e.  $T(k|k_c)$ . Assuming a  $k^{-5/3}$  subgrid spectral range Kraichnan [135] calculated

$$T(k|k_c) = 2\nu_e k^2 E(\mathbf{k}). \quad (3.39)$$

This has the same form as the viscous dissipation in Eq. (2.48) and can then be recognized as an eddy-viscosity. To complete the derivation of the model, taking the limit  $k \rightarrow 0$ , assuming a  $k^{-5/3}$  spectrum, and applying an eddy-damped quasi-normal Markovian closure (EDQNM, see, e.g., [208]. EDQNM is a contracted description of Navier-Stokes dynamics, (a closure) involving only the energy spectrum which is compatible with K41 theory [80]), it is found that [61]

$$\nu_e = C_{SE} E(k_c)^{1/2} k_c^{-1/2} \quad (3.40)$$

where the constant of proportionality,  $C_{SE}$  is been chosen to recover the Kolmogorov constant.

### 3.1.6 Hyperviscosity

Though technically not a LES, increasing the order of the viscous operator (to  $(\nabla^2)^n$  for  $n > 1$ ) has been used to shorten the dissipative range [9, 161, 160, 193, 27, 101]. This method is known to introduce an enhanced bottleneck [23, 21, 101].<sup>4</sup> It also raises some difficulties in assigning a meaningful Reynolds number. It has been shown to reproduce the energy spectrum of high  $Re$  homogeneous and isotropic turbulence [101] (though wavenumbers must be scaled to match the results to a DNS—with such an analysis even Smagorinsky eddy-viscosity can be shown to reproduce the spectrum [103]). Finally, it must be noted that hyperviscosity is not a universally valid approximation (e.g., in MHD when magnetic helicity is finite in a closed or fully periodic box [33]).

### 3.1.7 Intermittency

Only a very few studies of the intermittency of LES have been made [141]. One of them studies *a priori* the intermittency of several LES [46]. Using a  $256^3$  DNS ( $R_\lambda \approx 150$ ), first the scaling of the SGS dissipation rate was compared to the scaling of the longitudinal structure functions and was found to be comparable, if slightly more intermittent. Next, the SGS dissipation was used to make *a priori* estimates of the intermittency of several LES: Smagorinsky eddy-viscosity, constant eddy-viscosity (where a global average replaces  $|\bar{S}|$  in Eq. (3.4)), the similarity model, spectral eddy-viscosity, the dynamic model, the clipped dynamic model (where all negative eddy-viscosities are zeroed), and a volume-averaged dynamic model (with a single eddy-viscosity for the entire domain) [46]. Though  $R_\lambda \approx 150$  was somewhat insufficient for a determination of third-order scaling, the ESS hypothesis was employed to arrive at more precise estimates. Up to  $p = 4$  all models successfully reproduced the scaling of the DNS. At higher order several of the models exhibited reduced intermittency as listed here from least intermittent to most intermittent: the constant eddy-viscosity model, spectral

---

<sup>4</sup> Also note that the operator is globally dissipative but can be locally anti-dissipative.

eddy-viscosity, the volume-averaged dynamic model, and the Smagorinsky model. The similarity model performed fairly well (e.g., the error in the exponent for  $p = 7$  was less than 7%). Finally, the dynamic and clipped dynamic models were excessively intermittent. In models not capturing intermittency properly, the question arises whether the overall statistics of the flow at large scales are affected by the absence of intermittency; and if so, how intermittency should be incorporated.

Intermittency has been studied also for the case of hyperviscosity (which is known to cause an enhanced bottleneck) and which corrupts the scaling of the larger scales for structure functions of order 2 and higher [101]. Despite this, the anomalous scaling of the structure function exponents was found to agree with a model of She and L  v  que [214] over the remaining scaling range.

### 3.1.8 MHD LES

Just as for the Navier-Stokes case, we spatially low-bandpass filter the MHD equations, Eqs. (2.3), with a convolution filter  $L : \mathbf{z} \rightarrow \bar{\mathbf{z}}$  which yields

$$\partial_t \bar{v}_i + \partial_j (\bar{v}_i \bar{v}_j) + \partial_i \bar{\pi} - \partial_j (\bar{b}_i \bar{b}_j) - \nu \partial_{jj} \bar{v}_i + \partial_j \bar{\tau}_{ij} = 0 \quad (3.41a)$$

$$\partial_t \bar{b}_i + \bar{v}_j \partial_j \bar{b}_i - \bar{b}_j \partial_j \bar{v}_i - \eta \partial_{jj} \bar{b}_i + \partial_j \bar{\tau}_{ij}^b = 0 \quad (3.41b)$$

$$\partial_i \bar{v}_i = \partial_i \bar{b}_i = \partial_i v_i = \partial_i b_i = 0 \quad (3.41c)$$

where  $\pi = P + \frac{1}{2}|\mathbf{b}|^2$ . The Reynolds (turbulent) SGS stress tensor,

$$\bar{\tau}_{ij} = \overline{v_i v_j} - \bar{v}_i \bar{v}_j - (\overline{b_i b_j} - \bar{b}_i \bar{b}_j), \quad (3.42)$$

and the turbulent electromotive-force (emf) stress tensor,

$$\bar{\tau}_{ij}^b = \overline{b_i v_j} - \bar{b}_i \bar{v}_j - (\overline{v_i b_j} - \bar{v}_i \bar{b}_j), \quad (3.43)$$

represent the closure problem.

Modeling of MHD flows is still under development (see [207, 262]). As we have seen, most LES for hydrodynamic turbulence are based upon eddy-viscosity concepts, which can be related to a known power law of the energy spectrum, or upon self-similarity. For MHD, the locality of interactions in Fourier space is not necessarily valid [3, 168] (a contradiction of self-similarity (see Section 2.8.1)) and the general expression of the energy spectrum is not known. Furthermore, purely dissipative models are clearly inadequate as they ignore the (important) exchange of energy at subfilter scales between the velocity and magnetic fields. Furthermore, spectral eddy-viscosity concepts should not be applied as the kinetic energy is not a conserved quantity and the power laws are not clear. Additional difficulties arise from the fact that MHD has several regimes depending on the relative strengths of the magnetic and velocity fields, the ratios of the several invariants, and whether mechanical or magnetic energy is injected into the flow. For these reasons, the physicality of parameters is an even greater problem than for Navier-Stokes.

Based on the similarity between the viscous and diffusive terms in the MHD equations, the concept of eddy-viscosity (see Section 3.1.1) has been extended to eddy-resistivity [229]. Here we assume the magnetic rotation is directly proportional to the magnetic distortion,

$$\bar{\tau}_{ij}^b = -2\eta_T \bar{J}_{ij} \quad (3.44)$$

where the resolved magnetic-rotation tensor is given by  $\bar{J}_{ij} = (\partial_j \bar{b}_i - \partial_i \bar{b}_j)/2$  and  $\eta_T$  is called eddy resistivity. The eddy resistivity is assumed to be of the form

$$\eta_T = C_R \bar{\Delta}^2 |\bar{J}| \quad (3.45)$$

where  $|\bar{J}| = (2\bar{J}_{ij}\bar{J}_{ij})^{1/2}$  is the magnitude of the resolved magnetic-rotation tensor,  $C_R$  is a constant, and  $\bar{\Delta}$  is the filter width. The constant  $C_R$  can be determined, for example, by imposing a  $k^{-5/3}$  magnetic energy spectrum [229] (which is a questionable assumption given that the magnetic energy is not a conserved quantity and the general expression of

even the total energy is not known) or by employing the dynamic procedure (see Section 3.1.2) [1]. The former method has not been tested *a posteriori* but it does succeed in imposing the chosen energy spectrum. The latter method is initially excessively dissipative and the magnetic energy spectrum was reduced across a wide range of scales. Eddy-viscosity and eddy-resistivity MHD LES are also known to suppress small-scale dynamo action [103].

The use of eddy-viscosity and eddy-resistivity for MHD make little sense when compared with the MHD SGS and turbulent emf stress tensors, Eqs. (3.42) and (3.43), in that the first includes both the velocity and magnetic fields and the second includes interactions between the two. For this reason an extension of the Leonard tensor-diffusivity model (see Section 3.1.4) to MHD as well as a new cross-helicity model for MHD were introduced [185]. Leonard tensor-diffusivity (Clark) extended to MHD yields

$$\bar{\tau}_{ij}^C \propto \partial_k \bar{v}_i \partial_k \bar{v}_j - \partial_k \bar{b}_i \partial_k \bar{b}_j \quad (3.46)$$

$$\bar{\tau}_{ij}^b \propto \partial_k \bar{b}_i \partial_k \bar{v}_j - \partial_k \bar{v}_i \partial_k \bar{b}_j. \quad (3.47)$$

The cross-helicity model was designed to model better the exchange between kinetic and magnetic energies and to relate dissipation to the relative scrambling between the two fields [185],

$$\nu_T = C \bar{\Delta}^2 ((\partial_j \bar{v}_i + \partial_i \bar{v}_j)(\partial_j \bar{b}_i + \partial_i \bar{b}_j)/2)^{1/2} \quad (3.48a)$$

$$\eta_T = D \bar{\Delta}^2 \text{sgn}(\mathbf{j} \cdot \boldsymbol{\omega}) |\mathbf{j} \cdot \boldsymbol{\omega}|^{1/2}. \quad (3.48b)$$

Thus, the cross-helicity model belongs to a class of LES for MHD which assume some degree of alignment between the kinetic and electromagnetic fields [152, 185].

MHD LES at a resolution of  $64^3$  were compared to a  $512^3$  DNS for dynamic versions of eddy-resistivity, tensor-diffusivity, and cross-helicity [185]. The eddy-viscosity/eddy-resistivity based models were unable to induce any inverse cascade from the sub-grid scales while tensor-diffusivity undesirably altered the resolved-scale MHD dynamics.

Only the cross-helicity model reproduced well the time evolution of the energies and the magnetic helicity. All others had excessive dissipation during the critical start phase immediately after the LES is switched on, showed excessive sub-grid dissipation of magnetic energy and a deficit of magnetic to kinetic energy transfer. The cross-helicity model also fitted the energy spectra best, although the tensor-diffusivity also matched well the magnetic energy spectrum. The mechanism by which the cross-helicity functions, however, is to underestimate the SGS magnetic diffusion while over estimating the SGS transfer to the velocity field and the SGS kinetic dissipation. Finally, the probability distribution functions (*pdfs*) of the Elsässer-field increments in all models had a tendency to Gaussianize statistics at the smallest resolved scales (i.e., they reduced the intermittency) [185].

Other MHD LES also exist for restricted application.<sup>5</sup> One model is for nonhelical, statistically stationary MHD, assuming  $k^{-5/3}$  for both the kinetic and magnetic spectrum as well as a specified ratio of energy between the two fields [264]. It does not model interactions between the velocity and magnetic fields. There are also LES for low magnetic Reynolds number that only model the subfilter scales of the velocity field [206, 128, 205]. Though technically not an LES, there are also hyper-resistive models for MHD which require rescaling of the length (wavenumber) scales to a known DNS [103]. They are, however, known to change the saturation amplitude of the large scale magnetic field in helical dynamos [33, 102].

### 3.2 Four regularization subgrid models

The idea has been recently proposed [89, 90] of using regularizations of the nonlinear terms in fluid equations to provide a systematic approach to deriving subgrid closures for numerical simulations of turbulent flows. In this way, instead of phenomenologically

---

<sup>5</sup> In the field of plasma physics LES are, generally, not needed due to the existence of reduced MHD equations for the geometries of interest (see, e.g., [224]).

creating a subgrid model, we *derive* one through the combination of a regularization, a filter, and the formal inverse of that filter which, together, imply a subgrid closure. Advantages include that, by construction, regularization results in a systems of equations with guaranteed unique, smooth solutions and characterized by an attractor of finite dimensions. This has favorable consequences for the computability of the solution compared to the Navier-Stokes equations. Moreover, the momentum-conservation structure of the equations is retained. It is important, however, to recall that though regularizations can be interpreted in terms of implied subgrid models, they are an alternative to LES. While the LES approach, philosophically, is to reduce drastically the *dof* computed and try to do the best we can, our approach here is to make sure we recover the full system (in the limit of zero filter width) and then to see how far we can reduce the *dof*. In this section, we review the four regularization subgrid models studied in later chapters.

### 3.2.1 Clark- $\alpha$

It has been shown [256, 43] that for all symmetric filters that have a nonzero second moment, the first term of the reconstruction series for the turbulent sub-filter stress  $\bar{\tau}_{ij}$  in Eq. (3.1) is

$$\bar{\tau}_{ij} = -\frac{d^2 \hat{\hat{G}}}{dk^2} \Big|_{k=0} \partial_m u_i \partial_m u_j + \dots \quad (3.49)$$

where  $\hat{\hat{G}}(k)$  is the Fourier transform of the convolution kernel. This approximation of the subgrid stress is then generic and is known as the Leonard tensor-diffusivity model or, often, the Clark model (see Section 3.1.4). This model, however, does not conserve energy in the non-viscous limit. Cao, Holm, and Titi developed a related (conservative) subgrid model which they dubbed Clark- $\alpha$  [42]. The Clark- $\alpha$  model is [42]

$$\partial_t v_i + \mathcal{H} \partial_j (u_j u_i) + \partial_i p + \alpha^2 \partial_j (\partial_m u_i \partial_m u_j) = \nu \partial_{jj} v_i. \quad (3.50)$$

Here the filter is the inverse of a Helmholtz operator,  $L = \mathcal{H}^{-1} = (1 - \alpha^2 \nabla^2)^{-1}$ . Using  $\mathbf{v} = \mathcal{H}\mathbf{u}$  this can be rewritten

$$\mathcal{H}(\partial_t u_i + u_j \partial_j u_i - \nu \partial_{jj} u_i) + \partial_i p + \alpha^2 \partial_j \tau_{ij}^C = 0, \quad (3.51)$$

where

$$\tau_{ij}^C = \partial_m u_i \partial_m u_j. \quad (3.52)$$

Note we have assumed the filter commutes with differentiation which, for our filter, is true by Clairaut's theorem (assuming  $\mathbf{v}$  sufficiently smooth). By comparison with the subgrid equation, Eq. (3.1), we can see that the subgrid stress tensor,  $\bar{\tau}_{ij}^C = \mathcal{H}^{-1} \alpha^2 \tau_{ij}^C$ , is

$$\bar{\tau}_{ij}^C = \mathcal{H}^{-1} \alpha^2 (\partial_m u_i \partial_m u_j) = \alpha^2 (\partial_m u_i \partial_m u_j) + \mathcal{O}(\alpha^4). \quad (3.53)$$

For  $L = \mathcal{H}^{-1}$ , we note that  $\hat{G} = (1 + \alpha^2 k^2)^{-1}$  which implies that the turbulent sub-filter stress tensor for the tensor-diffusivity model given by Eq. (3.49) is

$$\bar{\tau}_{ij} = 2\alpha^2 (\partial_m u_i \partial_m u_j) + \dots \quad (3.54)$$

which is proportional to that of Clark- $\alpha$  to second order in  $\alpha$ . Hence, the *a priori* tests of [256] should apply to Clark- $\alpha$ .

### 3.2.1.1 Energy conservation

To derive the energy conservation of Clark- $\alpha$ , we take the dot product of  $\mathbf{u}$  with the vector representation of Eq. (3.50) and integrate over the domain to obtain

$$\begin{aligned} & \underbrace{\langle \mathbf{u} \cdot \partial_t \mathbf{v} \rangle}_{\text{(A)}} + \underbrace{\langle \mathbf{u} \cdot \mathcal{H}\mathbf{u} \cdot \nabla \mathbf{u} \rangle}_{\text{(B)}} + \underbrace{\langle \mathbf{u} \cdot \nabla p \rangle}_{\text{(C)}} - \underbrace{\langle \mathbf{u} \cdot \nu \nabla^2 \mathbf{v} \rangle}_{\text{(D)}} + \underbrace{\langle \mathbf{u} \cdot \alpha^2 \nabla \cdot (\nabla \mathbf{u} \cdot \nabla \mathbf{u}^T) \rangle}_{\text{(E)}} \\ & = 0. \end{aligned} \quad (3.55)$$



We consider the five terms one at a time. For term **(A)**, as the Helmholtz operator,  $\mathcal{H} = (1 - \alpha^2 \nabla^2)$ , is Hermitian, we have

$$\int dx^3 \mathbf{u} \cdot \partial_t \mathbf{v} = \frac{1}{2} \frac{d}{dt} \int dx^3 \mathbf{u} \cdot \mathbf{v} = \frac{1}{2} \frac{d}{dt} \langle \mathbf{u} \cdot \mathbf{v} \rangle. \quad (3.56)$$

Term **(B)** becomes

$$\mathbf{u} \cdot (1 - \alpha^2 \nabla^2) \mathbf{u} \cdot \nabla \mathbf{u} = \mathbf{u} \cdot \mathbf{u} \cdot \nabla \mathbf{u} - \alpha^2 \mathbf{u} \cdot \nabla^2 (\mathbf{u} \cdot \nabla \mathbf{u}). \quad (3.57)$$

The first term is like the term that shows up in the Navier-Stokes equation (albeit smoothed, see Section 2.2) and, therefore, similarly vanishes. The second term is handled alongside term **(E)**. Term **(C)** is an advection term with  $\mathbf{u}$  and does not contribute to the integral with suitable boundary conditions (see Section 2.2). This takes us to term **(D)** which is  $-\mathbf{u} \cdot \nu \nabla^2 \mathbf{v}$ , or (dropping  $-\nu$  and integrating by parts with respect to (w.r.t.)  $l$ )

$$u_j \partial_l^l v_j = \partial_l (u_j \partial^l v_j) - (\partial_l u_j) (\partial_l v_j). \quad (3.58)$$

The divergence term contributes nothing. Consider the curls of the two fields,

$$(\nabla \times \mathbf{u})_i = \varepsilon_{ijl} \partial_j u_l,$$

$$\text{and } (\nabla \times \mathbf{v})_i = \varepsilon_{imn} \partial_m v_n. \quad (3.59)$$

Their dot product is

$$\varepsilon_{ijl} \partial_j u_l \varepsilon_{imn} \partial_m v_n = (\delta_{jm} \delta_{ln} - \delta_{jn} \delta_{lm}) \partial_j u_l \partial_m v_n \quad (3.60)$$

$$= (\partial_m u_n) (\partial_m v_n) - (\partial_n u_m) (\partial_m v_n). \quad (3.61)$$

But if we integrate the last term by parts w.r.t.  $n$ , we find

$$(\partial_n u_m) (\partial_m v_n) = \partial_n (u_m \partial_m v_n) - u_m \partial_m (\partial_n v_n), \quad (3.62)$$

which are a divergence and advection term, respectively, and yield no contribution to the integral. Therefore,  $-\mathbf{u} \cdot \nu \nabla^2 \mathbf{v}$  is equivalent to  $\nu (\nabla \times \mathbf{u}) \cdot (\nabla \times \mathbf{v}) = \nu \langle \bar{\omega} \cdot \omega \rangle$  where  $\omega = \nabla \times \mathbf{v}$  and  $\bar{\omega} = \nabla \times \mathbf{u}$ .

This leaves us with term **(E)** and the deferred term:

$$-\alpha^2 \mathbf{u} \cdot \nabla^2 (\mathbf{u} \cdot \nabla \mathbf{u}) + \alpha^2 \mathbf{u} \cdot \nabla \cdot (\nabla \mathbf{u} \cdot \nabla \mathbf{u}^T), \quad (3.63)$$

or

$$\alpha^2 (-u_j \partial_l^l (u_m \partial^m u_j) + u_j \partial_m (\partial_l u_j \partial^l u^m)). \quad (3.64)$$

Expanding the last term of (3.64), we find

$$\partial_m (\partial_l u_j \partial^l u^m) = (\partial_l u_j) \cdot 0 + (\partial^l u_m) (\partial_l^m u_j). \quad (3.65)$$

Then, integration by parts w.r.t.  $l$  yields

$$(\partial^l u_m) (\partial_l (\partial^m u_j)) = \partial_l (\partial^l u_m \partial^m u_j) - \partial^m u_j \partial_l^l u_m, \quad (3.66)$$

and again yields,

$$\partial^l u_m \partial^m u_j = \partial^l (u_m \partial^m u_j) - u_m \partial_l^m u_j. \quad (3.67)$$

Thus, Eq. (3.64) becomes

$$\alpha^2 u_j (-\partial_l^l (u_m \partial^m u_j) + \partial_l^l (u_m \partial^m u_j) - \partial_l (u_m \partial_l^m u_j) - \partial^m u_j \partial_l^l u_m). \quad (3.68)$$

Integrating the first remaining term by parts w.r.t.  $l$ , we find

$$-\alpha^2 u_j \partial_l (u_m \partial_l^m u_j) = -\alpha^2 \partial_l (u_j u_m \partial_l^m u_j) + \alpha^2 (\partial_l u_j) u_m \partial^m (\partial^l u^j) \quad (3.69)$$

$$= -\alpha^2 \partial_l (u_j u_m \partial_l^m u_j) + \frac{\alpha^2}{2} u_m \partial^m (\partial_l u_j)^2, \quad (3.70)$$

which as a divergence and an advection contributes nothing to the integral. All this leaves is, after multiple integration by parts,

$$-\alpha^2 u_j \partial^m u_j \partial_l^l u_m = -\frac{\alpha^2}{2} \partial^m (u_j)^2 \partial_l^l u_m \quad (3.71)$$

$$= -\frac{\alpha^2}{2} \partial_l (\partial^m (u_j)^2 \partial_l^l u_m) + \frac{\alpha^2}{2} \partial^l u_m \partial_l^m (u_j)^2 \quad (3.72)$$

$$= \frac{\alpha^2}{2} \partial^l (u_m \partial_l^m (u_j)^2) - \frac{\alpha^2}{2} u_m \partial^m \partial_l^l (u_j)^2 = 0, \quad (3.73)$$

where we have made use of the fact that divergences and advections make no contribution. Therefore, Clark- $\alpha$  conserves energy in the  $H_\alpha^1(u)$  norm instead of the  $L^2(v)$  norm:

$$\frac{dE_\alpha}{dt} = -2\nu\Omega_\alpha, \quad (3.74)$$

where energy is expressed as:

$$E_\alpha = \frac{1}{2} \langle |\mathbf{u}|^2 + \alpha^2 |\nabla \mathbf{u}|^2 \rangle = \frac{1}{2} \langle (\mathbf{u} - \alpha^2 \nabla^2 \mathbf{u}) \cdot \mathbf{u} \rangle = \frac{1}{2} \langle \mathbf{v} \cdot \mathbf{u} \rangle, \quad (3.75)$$

and

$$\Omega_\alpha = \frac{1}{2} \langle \boldsymbol{\omega} \cdot \bar{\boldsymbol{\omega}} \rangle. \quad (3.76)$$

### 3.2.1.2 Computation

Equation (3.50) is not efficient for computation. So, we employ the identities,

$$\nabla \cdot (\nabla \mathbf{u} \cdot \nabla \mathbf{u}^T) = \frac{1}{2} [\nabla^2 (\mathbf{u} \cdot \nabla \mathbf{u}) - \mathbf{u} \cdot \nabla (\nabla^2 \mathbf{u}) - (\nabla^2 \mathbf{u}) \cdot \nabla \mathbf{u}], \quad (3.77)$$

and

$$\mathbf{A} \cdot \nabla \mathbf{B} + \mathbf{B} \cdot \nabla \mathbf{A} = \nabla (\mathbf{A} \cdot \mathbf{B}) + (\nabla \times \mathbf{B}) \times \mathbf{A} + (\nabla \times \mathbf{A}) \times \mathbf{B}. \quad (3.78)$$

The latter identity provides the relations

$$\mathbf{u} \cdot \nabla \mathbf{u} = \bar{\boldsymbol{\omega}} \times \mathbf{u}, \quad (3.79)$$

and

$$\mathbf{u} \cdot \nabla (\nabla^2 \mathbf{u}) + (\nabla^2 \mathbf{u}) \cdot \nabla \mathbf{u} = \nabla (\mathbf{u} \cdot (\nabla^2 \mathbf{u})) + (\nabla^2 \bar{\boldsymbol{\omega}}) \times \mathbf{u} + \bar{\boldsymbol{\omega}} \times (\nabla^2 \mathbf{u}) \quad (3.80)$$

where divergence terms have been neglected and are absorbed into the pressure term.

Then, we find

$$\partial_t \mathbf{v} + (1 - \frac{1}{2} \alpha^2 \nabla^2) (\bar{\boldsymbol{\omega}} \times \mathbf{u}) + \nabla \mathcal{P} - \nu \nabla^2 \mathbf{v} - \frac{1}{2} \alpha^2 [(\nabla^2 \bar{\boldsymbol{\omega}}) \times \mathbf{u} + \bar{\boldsymbol{\omega}} \times (\nabla^2 \mathbf{u})] = 0. \quad (3.81)$$

This form is more efficient for computation.

### 3.2.1.3 Regularity, dimensionality, and phenomenological energy spectrum

The global well-posedness of the Clark– $\alpha$  model and the existence and uniqueness of its solutions have been demonstrated [42]. Provided the forcing term belongs to the appropriate class of regularity, the solution instantaneously becomes analytic. An upper bound for the Hausdorff,  $d_H$ , and fractal,  $d_F$ , dimensions of the global attractor is given by

$$d_H \leq d_F \leq C \left( \frac{L}{\alpha} \right)^{3/4} \left( \frac{L}{\eta_K^C} \right)^3$$

where  $L$  is the integral length scale (or domain size) and  $\eta_K^C$  is the Kolmogorov dissipation length scale corresponding to the Clark– $\alpha$  model [42].

We review here the dimensional analysis derivation of the spectrum which follows scaling ideas originally due to Kraichnan [134] and which is developed more fully in Ref. [42]. Examining the nonlinear terms in Eq. (3.50), it is not entirely clear which of three possible scales for the average velocity for an eddy of size  $k^{-1}$ ,

$$U_k^{(0)} = \left( \frac{1}{D} \int_D |\mathbf{v}_k|^2 d^3x \right)^{1/2}, \quad (3.82)$$

$$U_k^{(1)} = \left( \frac{1}{D} \int_D \mathbf{u}_k \cdot \mathbf{v}_k d^3x \right)^{1/2}, \quad (3.83)$$

or

$$U_k^{(2)} = \left( \frac{1}{D} \int_D |\mathbf{u}_k|^2 d^3x \right)^{1/2} \quad (3.84)$$

should result. Therefore, the corresponding turnover time,  $\mathbf{t}_k$ , for such an eddy is

$$\mathbf{t}_k^{(n)} \propto 1/(kU_k^{(n)}). \quad (3.85)$$

We define the (omnidirectional) spectral energy density,  $E_\alpha(k)$ , from the relation

$$E_\alpha = \int_0^\infty \oint E_\alpha(\mathbf{k}) d\sigma d\mathbf{k} = \int_0^\infty E_\alpha(k) dk. \quad (3.86)$$

Since,  $\mathbf{u}_k \cdot \mathbf{u}_k = \mathbf{u}_k \cdot \mathbf{v}_k / (1 + \alpha^2 k^2) = E_\alpha(k) / (1 + \alpha^2 k^2)$ , we have

$$U_k^{(n)} \propto \left( \int E_\alpha(k) (1 + \alpha^2 k^2)^{(1-n)} dk \right)^{1/2} \sim \left( k E_\alpha(k) (1 + \alpha^2 k^2)^{(1-n)} \right)^{1/2} \quad (3.87)$$

Then, the total energy dissipation rate,  $\varepsilon_\alpha^C$  is related to the spectral energy density by

$$\varepsilon_\alpha^C \sim (\mathbf{t}_k^{(n)})^{-1} \int E_\alpha^C(k) dk \sim k^2 U_k^{(n)} E_\alpha^C(k) \sim k^{5/2} E_\alpha^C(k)^{3/2} (1 + \alpha^2 k^2)^{(1-n)/2}, \quad (3.88)$$

which yields, finally, the predicted energy spectra for Clark- $\alpha$ ,  $E_\alpha^C(k)$ ,

$$E_\alpha^C(k) \sim (\varepsilon_\alpha^C)^{2/3} k^{-5/3} (1 + \alpha^2 k^2)^{(n-1)/3}. \quad (3.89)$$

For scales much larger than  $\alpha$  ( $\alpha k \ll 1$ ) the Kolmogorov scaling for Navier-stokes is recovered,

$$E_\alpha^C(k) \sim (\varepsilon_\alpha^C)^{2/3} k^{-5/3}, \quad (3.90)$$

whereas for scales much smaller ( $\alpha k \gg 1$ ), the spectrum becomes

$$E_\alpha^C(k) \sim (\varepsilon_\alpha^C)^{2/3} \alpha^{2(n-1)/3} k^{(2n-7)/3}. \quad (3.91)$$

Based on these arguments we can only constrain the Clark- $\alpha$  sub-filter scale spectrum to be between  $k^{-1}$  and  $k^{-7/3}$ .

### 3.2.2 Leray- $\alpha$

One of the earliest regularization models was the Leray model, which Leray used to prove the existence (but not smoothness) of solutions to the Navier-Stokes equations in  $\mathbb{R}^n$ ,  $n=2,3$  [144]. Geurts and Holm [88, 89, 90] began using this model with (a three-point invertible approximation of) an inverse-Helmholtz-operator filter. Later it was dubbed Leray- $\alpha$  and an upper bound for the dimension of the global attractor was established [60]. The global existence and uniqueness of regular solutions for the Leray model is a classical result [144].

The Leray model is

$$\partial_t v_i + \partial_j (u_j v_i) + \partial_i \mathcal{P} = \nu \partial_{jj} v_i \quad \partial_i v_i = 0, \quad (3.92)$$

where the flow is advected by a smoothed velocity,  $\mathbf{u}$ . By comparison with Eq. (3.1) we see that we can derive the subgrid stress using the Leray regularization and a filter  $L$ :  $\bar{\tau}_{ij}^L = L(L(v_j)v_i) - L(v_j)L(v_i) = L(u_j v_i) - u_j u_i$ . With  $L = \mathcal{H}^{-1}$ ,  $\mathbf{v} = \mathcal{H}\mathbf{u}$  and along with the identity Eq. (A.11), Eq. (3.92) becomes

$$\mathcal{H}(\partial_t u_i + u_j \partial_j u_i - \nu \partial_{jj} u_i) + \partial_j \mathcal{P}' + \alpha^2 \partial_j \tau_{ij}^L = 0, \quad (3.93)$$

where we have absorbed all pressure-like terms into  $\mathcal{P}'$  and we define

$$\tau_{ij}^L = \partial_m u_i \partial_m u_j + \partial_m u_i \partial_j u_m. \quad (3.94)$$

By comparison with the subgrid equation, Eq. (3.1), we can see that the subgrid stress tensor,  $\bar{\tau}_{ij}^L = \mathcal{H}^{-1} \alpha^2 \tau_{ij}^L$ , is given by

$$\bar{\tau}_{ij}^L = \mathcal{H}^{-1} \alpha^2 (\partial_m u_i \partial_m u_j + \partial_m u_i \partial_j u_m). \quad (3.95)$$

As has been previously noted [114], the subgrid stress of Clark- $\alpha$ , Eq. (3.53), is a truncation of the subgrid stress of Leray- $\alpha$ , Eq. (3.95).

### 3.2.2.1 Energy conservation

The Leray model differs from Navier-Stokes only in its second term  $u_j \partial_j v_i \neq v_j \partial_j v_i$ . Therefore, derivation of the conserved energy proceeds in the usual way (see Section 2.2). We take the product of  $v_i$  with Eq. (3.92) and integrate over the domain. We consider only the non-identical (compared to Navier-Stokes) term which becomes

$$v_i u_j \partial_j v_i = \frac{1}{2} u_j \partial_j (v_i)^2. \quad (3.96)$$

This advection-like term gives zero contribution (as did the Navier-Stokes's  $v_i v_j \partial_j v_i$  term) to the integral under the usual boundary conditions and we find the dissipation is unchanged. Then, the  $L^2(v)$  norm is the quadratic invariant to be identified with energy,

$$\frac{dE}{dt} = -2\nu\Omega, \quad (3.97)$$

where

$$E = \frac{1}{2} \langle |\mathbf{v}|^2 \rangle, \quad (3.98)$$

and

$$\Omega = \frac{1}{2} \langle |\boldsymbol{\omega}|^2 \rangle. \quad (3.99)$$

As was pointed out in [236], the incompressibility of the velocity field  $\mathbf{v}$  only implies a divergenceless filtered velocity  $\mathbf{u}$  under certain boundary conditions for Leray- $\alpha$ . When  $\partial_i u_i \neq 0$ , the energy is no longer conserved (helicity and Kelvin's theorem are not conserved for Leray- $\alpha$ ). In the following chapters, we employ periodic boundary conditions, for which  $\partial_i v_i = 0$  implies  $\partial_i u_i = 0$  and Leray- $\alpha$  conserves energy in the usual  $L^2(v)$  sense.

### 3.2.2.2 Dimensionality and phenomenological energy spectrum

Ref. [60] proved an upper bound for the Hausdorff,  $d_H$ , and fractal,  $d_F$ , dimensions of the global attractor

$$d_H \leq d_F \leq c \left( 1 + \frac{L}{\alpha} \right)^{9/14} \left( \frac{L}{\eta_K^L} \right)^{12/7}$$

where  $L$  is the integral length scale (or domain size) and  $\eta_K^L$  is the dissipation length scale associated with this model. As the number of degrees of freedom grows substantially less than cubically with the size of the domain, Leray- $\alpha$  might have great potential as a sub-grid scale large-eddy simulation model.

We review here the dimensional analysis derivation of the spectrum for Leray- $\alpha$  as we did for Clark- $\alpha$  in Section 3.2.1.3. This analysis is developed more fully in Ref. [60]. We argue again that there are three possible scales for the average velocity for an eddy of size  $k^{-1}$ , Eqs. (3.82), (3.83), and (3.84), with the turn-over time,  $\mathbf{t}_k^{(n)}$  given by Eq. (3.85). Since,  $u_k^2 = v_k^2 / (1 + \alpha^2 k^2)^2 = E(k) / (1 + \alpha^2 k^2)^2$ , we have

$$U_k^{(n)} \sim \left( \int E(k) (1 + \alpha^2 k^2)^{-n} dk \right)^{1/2} \sim (k E(k) (1 + \alpha^2 k^2)^{-n})^{1/2} \quad (3.100)$$

Then, the total energy dissipation rate,  $\varepsilon^L$  is related to the spectral energy density by

$$\varepsilon^L \sim (\mathfrak{t}_k^{(n)})^{-1} \int E(k) dk \sim k^2 U_k^{(n)} E(k) \sim k^{5/2} E(k)^{3/2} (1 + \alpha^2 k^2)^{-n/2}, \quad (3.101)$$

which yields, finally, the predicted energy spectra for Leray- $\alpha$ ,  $E^L(k)$ ,

$$E^L(k) \sim (\varepsilon^L)^{2/3} k^{-5/3} (1 + \alpha^2 k^2)^{n/3}. \quad (3.102)$$

For scales much larger than  $\alpha$  ( $\alpha k \ll 1$ ) the K41 spectrum is recovered, Eq. (2.87), and for scales much smaller ( $\alpha k \gg 1$ ) the spectrum is

$$E^L(k) \sim (\varepsilon^L)^{2/3} \alpha^{2n/3} k^{(2n-5)/3}. \quad (3.103)$$

Based on these arguments we can only constrain the Leray- $\alpha$  sub-filter scale spectrum to be between  $k^{-1/3}$  and  $k^{-5/3}$ .

### 3.2.2.3 Comparison to LES

Leray- $\alpha$  has been compared to a dynamic mixed (similarity plus eddy-viscosity) model and to DNS simulations on a grid of  $N^3 = 192^3$  in a doubly-periodic compressible channel flow domain for  $Re \approx 50$  in a turbulent mixing layer [88]. Leray- $\alpha$  was found to be better and cheaper than the dynamic-mixed model when comparing momentum thickness and the stream-wise kinetic energy spectrum. While Leray- $\alpha$  possessed both forward- and back-scatter, it, however, exhibited too little dissipation, and possessed a systematic error of a slight over-prediction of the large scales accompanied by a slight under-prediction of the small scales. In visual comparisons, the dynamic-mixed model had an excess of smoothing compared to Leray- $\alpha$ .

### 3.2.3 LANS- $\alpha$

The third regularization model we consider is the incompressible Lagrangian-averaged Navier-Stokes (LANS- $\alpha$ ,  $\alpha$ -model, or also the viscous Camassa-Holm equation [113, 55, 57, 58, 56, 77]). It can be derived, for instance, by temporal averaging



applied to Hamilton's principle (where Taylor's frozen-in turbulence hypothesis is applied as the closure, and also as the only approximation of the derivation) [112, 110, 108]. For this reason, the momentum-conservation structure of the equations is retained. For scales smaller than the filter width, LANS- $\alpha$  reduces the steepness of steep gradients of the Lagrangian mean velocity and limits how thin vortex tubes become as they are transported (the effect on larger length scales is negligible) [58]. LANS- $\alpha$  may also be derived from smoothing the transport velocity of a material loop in Kelvin's circulation theorem [77]. Consequently, there is no attenuation of resolved circulation, which is important for many engineering and geophysical flows where accurate prediction of circulation is highly desirable. An alternative interpretation of the  $\alpha$ -model is that it neglects fluctuations about the smoothed velocity field while leaving the source term, vorticity, alone [181]. The  $\alpha$ -model also describes an incompressible second-grade non-Newtonian fluid (under a modified dissipation) [77]. In this interpretation,  $\alpha$  is a material parameter which measures the elastic response of the fluid.

LANS- $\alpha$  is given by

$$\partial_t v_i + \partial_j(u_j v_i) + \partial_i \pi + v_j \partial_i u_j = \nu \partial_{jj} v_i, \quad \partial_i v_i = 0, \quad (3.104)$$

For LANS- $\alpha$ , the usual choice of filter is again  $L = \mathcal{H}^{-1}$ . With this filter,  $\mathbf{v} = \mathcal{H}\mathbf{u}$  and along with the identities Eqs. (A.5) and (A.11), Eq. (3.104) may be written

$$\mathcal{H}(\partial_t u_i + u_j \partial_j u_i - \nu \partial_{jj} u_i) + \partial_i \pi' + \alpha^2 \partial_j \tau_{ij}^\alpha = 0, \quad (3.105)$$

where we have absorbed all pressure-like terms into  $\pi'$  and defined

$$\begin{aligned} \tau_{ij}^\alpha = \partial_m u_i \partial_m u_j &+ \underbrace{\partial_m u_i \partial_j u_m}_{\text{drop for Clark-}\alpha} - \underbrace{\partial_i u_m \partial_j u_m}_{\text{drop for Clark-}\alpha \text{ \& Leray-}\alpha}. \end{aligned} \quad (3.106)$$

By comparison with the subgrid equation, Eq. (3.1), we can see that the subgrid stress tensor,  $\bar{\tau}_{ij}^\alpha = \mathcal{H}^{-1} \alpha^2 \tau_{ij}^\alpha$ , is given by

$$\bar{\tau}_{ij}^\alpha = \mathcal{H}^{-1} \alpha^2 (\partial_m u_i \partial_m u_j + \partial_m u_i \partial_j u_m - \partial_i u_m \partial_j u_m). \quad (3.107)$$

As has been previously noted [114], the subgrid stress of Leray- $\alpha$ , Eq. (3.95), is a truncation of the subgrid stress of LANS- $\alpha$ , Eq. (3.107). Like Clark- $\alpha$ , energy is conserved in the  $H_\alpha^1(u)$  norm instead of the  $L^2(v)$  norm. Additionally, LANS- $\alpha$  is the only model for neutral fluids of the three examined here (Clark- $\alpha$ , Leray- $\alpha$ , and LANS- $\alpha$ ) that conserves the helicity (and Kelvin's circulation theorem). This makes LANS- $\alpha$  suitable for a rotating frame of reference and buoyancy affects.

### 3.2.3.1 Regularity, dimensionality, and phenomenological energy spectrum

The global existence and uniqueness of regular solutions of LANS- $\alpha$  has been proven [78]. As both Clark- $\alpha$  and LANS- $\alpha$  conserve energy in the  $H_\alpha^1(u)$  norm, the phenomenological derivation of its energy spectrum closely follows that of Clark- $\alpha$  (see Section 3.2.1.3). In this case, however, it is known that  $U_k^{(2)}$  is the advection velocity for eddies of size  $k^{-1}$  (see [77]). The energy spectrum for scales smaller than  $\alpha$  is then

$$E_\alpha(k) \sim \varepsilon_\alpha^{2/3} \alpha^{2/3} k^{-1}. \quad (3.108)$$

LANS- $\alpha$ 's spectrum differs from the Navier-Stokes spectrum due to the fact that the fluid is advected by the smoothed velocity  $\mathbf{u}$  which does not directly correspond to the conserved energy  $E_\alpha$ . The spectrum may be used to estimate the degrees of freedom of the LANS- $\alpha$  attractor,  $dof_\alpha$ . For dissipation the large wavenumbers dominate and, therefore, combining the LANS- $\alpha$  energy balance Eq. (3.74) with its sub-filter scale energy spectrum Eq. (3.108) allows us to specify implicitly its dissipation wavenumber,  $k_\eta^\alpha$ , by

$$\frac{\varepsilon_\alpha}{\nu} \propto \int_{k_\eta^\alpha}^{k_\eta^\alpha} k^2 E_\alpha(k) dk \sim \int_{k_\eta^\alpha}^{k_\eta^\alpha} k^2 \varepsilon_\alpha^{2/3} \alpha^{2/3} k^{-1} dk \sim \varepsilon_\alpha^{2/3} \alpha^{2/3} (k_\eta^\alpha)^2. \quad (3.109)$$

Then we have,

$$k_\eta^\alpha \sim \frac{\varepsilon_\alpha^{1/6}}{\nu^{1/2} \alpha^{1/3}}. \quad (3.110)$$

Next,  $dof_\alpha \propto Lk_\eta^\alpha$  and  $Re \propto \nu^{-1}$ , lead to

$$dof_\alpha \propto \frac{1}{\alpha} Re^{3/2} \quad (3.111)$$

(for further details see [77]). A more rigorous bound was found for the fractal (Lyapunov) dimension,  $d_F$  [78]:

$$d_F \leq (dof_\alpha)^{3/2}. \quad (3.112)$$

### 3.2.3.2 LANS- $\alpha$ Kármán-Howarth theorem

The  $\alpha$ -model possesses a theorem corresponding to the Kármán-Howarth theorem for the Navier-Stokes equations [109]. As in Section 2.4, we use the short notation  $v_i \equiv v_i(\mathbf{x})$ ,  $u'_i \equiv u'_i(\mathbf{x}', t)$  and  $\mathbf{r} \equiv \mathbf{x}' - \mathbf{x}$ . In the statistically isotropic and homogeneous case, without external forces and with  $\nu = 0$ , taking the dot product of Eq. (3.104) with  $u'_j$  we can obtain the equation

$$\partial_t \mathcal{Q}^\alpha_{ij} = \frac{\partial}{\partial r^m} (\mathcal{T}^{\alpha m}_{ij} - \alpha^2 \mathcal{S}^{\alpha m}_{ij}). \quad (3.113)$$

The trace of this equation is the Fourier transform of the detailed energy balance for LANS- $\alpha$ .

$$\mathcal{Q}^\alpha_{ij} = \langle v_i u'_j + v_j u'_i \rangle \quad (3.114)$$

is the second-order correlation tensor while

$$\mathcal{T}^{\alpha m}_{ij} = \langle (v_i u'_j + v_j u'_i + v'_i u_j + v'_j u_i) u^m \rangle, \quad (3.115)$$

and

$$\mathcal{S}^{\alpha m}_{ij} = \langle (\partial_m u_l \partial_i u_l) u'_j + (\partial_m u_l \partial_j u_l) u'_i + (g_\alpha \otimes \tau^{\alpha' m}_j) v_i + (g_\alpha \otimes \tau^{\alpha' m}_i) v_j \rangle, \quad (3.116)$$

are the third-order correlation tensors for LANS- $\alpha$ . For  $\alpha = 0$  this reduces to the well-known relation derived by Kármán and Howarth, Eq. (2.68). Finally, LANS- $\alpha$

also possesses an analogue to the four-fifths law, Eq. (2.78), the two-fifteenths law for the LANS- $\alpha$  model,

$$-\frac{2}{15}\varepsilon_\alpha = T^\alpha - \alpha^2 S^\alpha, \quad (3.117)$$

where  $T^\alpha$  and  $S^\alpha$  are scalar functions that generate the isotropic  $\mathcal{T}_{ij}^{\alpha m}$  and  $\mathcal{S}_{ij}^{\alpha m}$  [109].

### 3.2.3.3 Subgrid modeling results

LANS- $\alpha$  has been compared to direct numerical simulations (DNS) of the Navier-Stokes equations (taken as true at a given Reynolds number) at modest Taylor Reynolds numbers ( $R_\lambda \approx 72$  [263],  $R_\lambda \approx 130$  [58], and  $R_\lambda \approx 300$  (in a highly symmetrized geometry) [60]). In Ref. [58], LANS- $\alpha$  results were compared to those of a  $384^3$  DNS in a periodic box ( $R_\lambda \approx 130$ ) forced in modes  $k < 2.5$  to keep the energy constant in time and the ratio in the shells consistent with  $k^{-5/3}$ . A factor of six reduction in linear resolution was achieved with the  $\alpha$ -model reproducing the large scale features: structures, energy spectra, and transfer spectra for  $k\alpha < 1$ . LANS- $\alpha$  suppressed the vortex stretching dynamics (especially for small scale vortices size less than  $\alpha$ ) but did not change the qualitative features of stretching physics. The vortex aspect ratio, however, did change. As  $\alpha$  was increased the ratio of vortex length/radius was decreased. The vorticity alignment phenomenon ( $\boldsymbol{\omega}$  aligns with the second eigenvector of the symmetric strain-rate tensor,  $S_{ij} = (\partial_j u_i + \partial_i u_j)/2$ ) was also studied. The  $\alpha$ -model reproduced this phenomenon, but with greater alignment with the direction of the maximum-eigenvalue eigenvector and less with the second eigenvector, which may be associated with the increased thickness of the vortex tubes [58]. The velocity increments (for the  $L^2(u)$  norm) reproduced the fundamental features with a reduction in intermittency.

LANS- $\alpha$  was compared to a  $256^3$  DNS in 3D isotropic turbulence under two different forcing functions (for  $R_\lambda \approx 80$  and 115); a comparison to a dynamic eddy-viscosity LES as well was made for decaying turbulence with initial conditions peaked at a low wavenumber (with  $R_\lambda \approx 70$ ) as well as at a moderate wavenumber (with

$R_\lambda \approx 220$ ) [177]. For the first forcing function case, energy was injected at  $k = 1$  at a constant rate ( $R_\lambda \approx 80$ ,  $Re \approx 400$ ). LANS- $\alpha$  solutions were computed at a resolution of  $96^3$  with  $\alpha = 1/8$  and  $1/16$  of the domain size. The second forcing was tailored to ensure  $k^{-5/3}$  at large scales ( $R_\lambda \approx 115$ ,  $Re \approx 350$ ). LANS- $\alpha$  solutions were computed at  $256^3$  (no resolution gain) with  $\alpha = 1/4$  and  $1/16$ . LANS- $\alpha$  reproduced the *pdf* of the dissipation rate  $\epsilon$  well and predicted backscatter and its probability distribution level. The alignment of the the second eigenvalue of turbulent stress tensor  $\bar{\tau}_{ij}$  with the vorticity  $\boldsymbol{\omega}$  was reduced in agreement with the findings of [58].

For decaying turbulence, a broad initial spectrum with a peak at high wave number  $k = 8$  ( $R_\lambda = 72$ ,  $192^3$  DNS) was used. A resolution at  $72^3$  was inadequate for LANS- $\alpha$ ,  $\alpha = 1/8$  and  $1/16$ . At this resolution LANS- $\alpha$  was more under-dissipative than the LES. When instead forcing with a peak at  $k = 3$  ( $R_\lambda = 220$ ,  $256^3$  DNS), a resolution of  $72^3$  was sufficient for early times but became under-resolved as the turbulence developed. LANS- $\alpha$  was preferable in that it demonstrated correct alignment between eigenvectors of the subgrid stress tensor and the eigenvectors of the resolved stress tensor and vorticity vector, but it did not reproduce the energy spectra as accurately as the LES at this resolution.<sup>6</sup>

A dynamic (and potentially anisotropic) LANS- $\alpha$  model has been devised which could be used for a wall-bounded flow [263]. The dynamic component was achieved with the same Germano identity used for other dynamic LES (see Section 3.1.2). Isotropic tests with  $\alpha$  varying with time and *a priori* anisotropic tests were made comparing to a  $128^3$  DNS of decaying turbulence with an initial  $R_\lambda = 72$  ( $Re = 300$ ). LANS- $\alpha$  and dynamic LANS- $\alpha$  solutions were computed at resolutions of  $64^3$  and  $48^3$ . The dynamic LANS- $\alpha$  was an improved estimate of the DNS compared to LANS- $\alpha$ . This was the case as well when compared to a  $128^3$  DNS of forced, isotropic turbulence (the forcing imposed  $k^{-5/3}$  at large scales) with  $R_\lambda = 415$  and the LANS- $\alpha$  solution was at  $48^3$

---

<sup>6</sup> Here, as usual, the DNS of the Navier-Stokes equations is taken as true at a given Reynolds number.

( $\alpha = 1/5$ ).

### 3.2.4 Comparisons between LANS- $\alpha$ , Leray- $\alpha$ , Clark- $\alpha$ , and LES

Both LANS- $\alpha$  and Leray- $\alpha$  have been compared to a dynamic mixed (similarity plus eddy-viscosity) model in a turbulent mixing shear layer [87, 89, 90]. The computation was compressible (but low Mach number) of a mixing layer ( $Re \approx 50$ ) with free-slip against the walls and 2D periodic boundary conditions in the perpendicular plane ( $192^3$  DNS). LES were computed at  $32^3$ ,  $64^3$ , and  $96^3$  with a filter width,  $\Delta = \frac{1}{16}th$  of the domain size ( $\Delta \approx 12\eta_K$ ).<sup>7</sup> An explicit top-hat filter was used to approximate the inverse of the Helmholtz operator in a second-order finite volume simulation. At  $Re \approx 50$  there was no discernible inertial range. The filter was kept fixed and the subgrid resolution was varied explicitly to separate the influence of the effects of numerical errors and access independently the quality with which the models captured physical features by considering the predictions of the (approximately) grid-independent solutions. Deviations from the filtered DNS for these solutions were then a direct measure of the deficiencies in the subgrid model and would also be found in the same way for other spatial discretization methods. Leray- $\alpha$  provided a slight under-prediction of the influence of the small scales while LANS- $\alpha$  corresponded more closely to the filtered DNS and both were better than the dynamic-mixed-similarity model (which yielded significant under-prediction of intermediate and smaller scales). Leray- $\alpha$  and the dynamic-mixed-similarity model were both under-dissipative. In fact, the dynamic-mixed-similarity model is often supplied with additional dissipation from using a coarser grid. Though Leray- $\alpha$  under-predicted the mixing rate, it was significantly better than the dynamic-mixed model (for streamwise turbulent intensity as well) albeit both slightly underestimated the streamwise turbulent intensity. Leray- $\alpha$  had a slight under-prediction of small scales and an over-prediction of large scales, but

---

<sup>7</sup> The Kolmogorov dissipation scale,  $\eta_K$ , is given by  $\eta_K = k_\eta^{-1}$  (see Section 2.6).

it also had significant forward and backscatter. Leray- $\alpha$  was also considerably cheaper than the dynamic model at the same resolution. LANS- $\alpha$  was the most accurate of the three models at proper subgrid resolution but the effects of numerical contamination can be strong enough to lose most of this potential. For LANS- $\alpha$ , under-resolution constitutes a source for strong numerical contamination which is more characteristic of spatial discretization than a measure of the quality of the subgrid model. With adequate resolution, LANS- $\alpha$  possessed insufficient dissipation (still, however, much better than Leray- $\alpha$  or the dynamic-mixed-similarity model), very good mixing rate and streamwise turbulent intensity. LANS- $\alpha$  also had much greater backscatter than Leray.

There was a trade-off between needed resolution and grid-independent accuracy for the three models. The dynamic-mixed-similarity model required the least resolution, then the Leray- $\alpha$  model, and LANS- $\alpha$  required the greatest resolution. The accuracies of the grid-independent solutions were from least to greatest: dynamic-mixed-similarity, Leray- $\alpha$ , and LANS- $\alpha$ . From the LES perspective the comparison is not as clear. For instance, at a resolution of  $32^3$  the dynamic-mixed model was comparable to Leray- $\alpha$  for the dissipation rate. Also at this resolution, LANS- $\alpha$  had as comparably a poor prediction for turbulent streamwise intensity as the dynamic-mixed model. At the same time, for the resolutions studied, Leray- $\alpha$  always had a better streamwise turbulent intensity than the dynamic model. Clearly LANS- $\alpha$  was the best approximation, but the improvement displays rather strong deterioration in cases where the resolution is not adequate. While LANS- $\alpha$  had the greatest grid-independent accuracy of the three models, it also required the greatest resolution. From the LES perspective, this could pose some limitations on the practical use and application of LANS- $\alpha$  for high  $Re$  cases.

A 1D analysis of the subgrid stress tensors for Leray- $\alpha$ , LANS- $\alpha$ , and Clark- $\alpha$  found that, for large scales, both Leray- $\alpha$  and LANS- $\alpha$  deviate markedly from the

exact closure problem [87, 90]. Leray- $\alpha$  was also found to have an extra order one term and the potential to exaggerate the larger scales. It was concluded that Clark- $\alpha$  should work better than Leray- $\alpha$  for the  $\mathcal{H}^{-1}$  filter and that of the top-hat,  $\mathcal{H}^{-1}$ , and the Gaussian filters only  $\mathcal{H}^{-1}$  should work very well for Clark- $\alpha$  [87, 90].

### 3.2.5 LAMHD- $\alpha$

Existing MHD LES are not generally applicable in that they possess at least one of the following shortcomings: they are solely dissipative neglecting interactions between  $\mathbf{v}$  and  $\mathbf{b}$ , they are only applicable to nonhelical flow, or they assume energy spectra scaling, low magnetic Reynolds number, or some degree of alignment between the fields (see Section 3.1.8). One model which may be more generally applicable is the Lagrangian-Averaged Magneto-Hydrodynamics alpha (LAMHD- $\alpha$  or the MHD- $\alpha$ ) model [110]. The LAMHD- $\alpha$  model is derived by Lagrangian averaging ordinary MHD along particle trajectories. Specifically, the LAMHD- $\alpha$  equations arise from Lagrangian-averaging Hamilton's principle for incompressible ideal MHD, after using a form of Taylor's hypothesis of frozen-in turbulent fluctuations in the Euler-Poincaré equation for barotropic MHD [113]. When Navier-Stokes viscosity  $\nu$  and diffusivity  $\eta$  are included in the standard fashion, the equations for the LAMHD- $\alpha$  model emerge as,

$$\partial_t v_i + u_j \partial_j v_i + \partial_i \tilde{\pi} - \bar{b}_j \partial_j b_i + v_j \partial_i u_j + \bar{b}_j \partial_i b_j = \nu \partial_{jj} v_i, \quad (3.118a)$$

$$\partial_t \bar{b}_i + u_j \partial_j \bar{b}_i - \bar{b}_j \partial_j u_i = \eta \partial_{jj} b_i, \quad (3.118b)$$

$$\partial_j u_j = 0, \quad \partial_j \bar{b}_j = 0 \quad (3.118c)$$

where  $\tilde{\pi}$  is the modified total pressure. In these equations, the over-bar denotes the smoothing obtained by inverting the Helmholtz relations,

$$\mathbf{v} = (1 - \alpha^2 \nabla^2) \bar{\mathbf{v}}, \quad \mathbf{b} = (1 - \alpha_M^2 \nabla^2) \bar{\mathbf{b}}. \quad (3.119)$$



with Dirichlet boundary conditions,  $\bar{\mathbf{v}} = 0$  and  $\bar{\mathbf{b}} = 0$  on the boundary. In the equations,  $\alpha$  and  $\alpha_M$  are two constant parameters:  $\alpha$  characterizes the correlation length between the instantaneous Lagrangian fluid trajectory and its mean (time average), and  $\alpha_M$  is its magnetic counterpart. These two parameters need not be equal, *ab initio*. The traditional MHD system is obtained by setting both  $\alpha = 0$  and  $\alpha_M = 0$ . Likewise, the LANS- $\alpha$  incompressible nonconducting fluid turbulence model is obtained by setting  $\bar{\mathbf{b}} = \mathbf{0}$ . These equations may also be obtained through a filtering approach [181, 173].

### 3.2.5.1 Conservations

The LAMHD- $\alpha$  system of equations, Eqs. (3.118), possesses the standard properties of a normal fluid theory. For example, the LAMHD- $\alpha$  system monotonically dissipates the positive total energy

$$E_T^\alpha = \frac{1}{2} \langle \bar{\mathbf{v}} \cdot \mathbf{v} + \bar{\mathbf{b}} \cdot \mathbf{b} \rangle, \quad (3.120)$$

according to

$$\frac{dE_T^\alpha}{dt} = -\nu \langle \boldsymbol{\omega} \cdot \bar{\boldsymbol{\omega}} \rangle - \eta \langle j^2 \rangle. \quad (3.121)$$

The Kelvin circulation theorem for the incompressible LAMHD- $\alpha$  motion equation (3.118a) involves both of the velocities,

$$\frac{d}{dt} \oint_{\Gamma(\bar{\mathbf{v}})} \mathbf{v} \cdot d\mathbf{x} = \oint_{\Gamma(\bar{\mathbf{v}})} (\mathbf{j} \times \bar{\mathbf{b}} + \nu \nabla^2 \mathbf{v}) \cdot d\mathbf{x}, \quad (3.122)$$

where  $\mathbf{j} = \nabla \times \mathbf{b}$ . Hence, the  $\mathbf{j} \times \bar{\mathbf{b}}$  force and viscous force can each generate circulation of  $\mathbf{v}$  around material loops moving with smoothed velocity  $\bar{\mathbf{v}}$ . This results by Stokes theorem in vorticity dynamics for  $\boldsymbol{\omega} = \nabla \times \mathbf{v}$  in the form

$$\frac{\partial \boldsymbol{\omega}}{\partial t} + \bar{\mathbf{v}} \cdot \nabla \boldsymbol{\omega} - \boldsymbol{\omega} \cdot \nabla \bar{\mathbf{v}} = \bar{\mathbf{b}} \cdot \nabla \mathbf{j} - \mathbf{j} \cdot \nabla \bar{\mathbf{b}} + \nu \Delta \boldsymbol{\omega}. \quad (3.123)$$

The linkages of the smooth magnetic field,  $\bar{\mathbf{b}}$ , with itself and with the vorticity,  $\boldsymbol{\omega}$ , are given respectively by the magnetic helicity,  $H_M^\alpha = \langle \bar{\mathbf{a}} \cdot \bar{\mathbf{b}} \rangle$ , and the cross helicity,

$H_C^\alpha = \langle \mathbf{v} \cdot \bar{\mathbf{b}} \rangle / 2$ . The densities for these linkages satisfy

$$\frac{\partial}{\partial t}(\bar{\mathbf{a}} \cdot \bar{\mathbf{b}}) + \nabla \cdot ((\bar{\mathbf{a}} \cdot \bar{\mathbf{b}}) \bar{\mathbf{v}}) = \eta (\mathbf{a} \cdot \bar{\mathbf{b}} + \bar{\mathbf{a}} \cdot \mathbf{b}), \quad (3.124)$$

in which  $\bar{\mathbf{b}} = \nabla \times \bar{\mathbf{a}}$  and  $\mathbf{b} = \nabla \times \mathbf{a}$ , and,

$$\frac{\partial}{\partial t}(\mathbf{v} \cdot \bar{\mathbf{b}}) + \nabla \cdot ((\mathbf{v} \cdot \bar{\mathbf{b}}) \bar{\mathbf{v}} + (\tilde{\pi} + \frac{1}{2}|\bar{\mathbf{b}}|^2)\bar{\mathbf{b}}) = \nu \bar{\mathbf{b}} \cdot \Delta \mathbf{v} + \eta \mathbf{v} \cdot \Delta \bar{\mathbf{b}}. \quad (3.125)$$

Thus, resistivity affects the helicity, while both resistivity and viscosity affect the cross helicity, and these linkages are both preserved by LAMHD- $\alpha$  in the ideal case. In 2D the mean square magnetic vector potential,  $\mathcal{A}^\alpha = \langle \bar{a}_z^2 \rangle$ , is conserved instead of  $H_M^\alpha$ :

$$\frac{d\mathcal{A}}{dt} = -2\eta E_M^\alpha \quad (3.126)$$

where  $E_M^\alpha = \langle \mathbf{b} \cdot \bar{\mathbf{b}} \rangle$  is the magnetic energy. Of course, these properties of energy, momentum, circulation and linkages for the LAMHD- $\alpha$  model all reduce to characteristics of normal MHD, when  $\alpha \rightarrow 0$  and  $\alpha_M \rightarrow 0$  (see Section 2.7).

We may recast LAMHD- $\alpha$  in MHD LES form by imposing  $\alpha_M = \alpha$ . Then,  $\mathbf{v} = \mathcal{H}\mathbf{u}$  and  $\mathbf{b} = \mathcal{H}\bar{\mathbf{b}}$ . Using the identities Eqs. (A.5) and (A.11), Eq. (3.118a) may be written

$$\mathcal{H}(\partial_t u_i + u_j \partial_j u_i - \bar{b}_j \partial_j \bar{b}_i - \nu \partial_{jj} u_i) + \partial_i \tilde{\pi}' + \alpha^2 \partial_j \tau_{ij}^\alpha = 0, \quad (3.127)$$

where we have absorbed all pressure-like terms into  $\tilde{\pi}'$  and defined

$$\tau_{ij}^\alpha = \partial_m u_i \partial_m u_j + \partial_m u_i \partial_j u_m - \partial_i u_m \partial_j u_m - \partial_m \bar{b}_i \partial_m \bar{b}_j - \partial_m \bar{b}_i \partial_j \bar{b}_m + \partial_i \bar{b}_m \partial_j \bar{b}_m. \quad (3.128)$$

By comparison with the subgrid equation, Eq. (3.41a), we can see that the subgrid stress tensor,  $\bar{\tau}_{ij}^\alpha = \mathcal{H}^{-1} \alpha^2 \tau_{ij}^\alpha$ , is given by

$$\bar{\tau}_{ij}^\alpha = \mathcal{H}^{-1} \alpha^2 (\partial_m u_i \partial_m u_j + \partial_m u_i \partial_j u_m - \partial_i u_m \partial_j u_m - \partial_m \bar{b}_i \partial_m \bar{b}_j - \partial_m \bar{b}_i \partial_j \bar{b}_m + \partial_i \bar{b}_m \partial_j \bar{b}_m). \quad (3.129)$$

Comparison of Eq. (3.118b) with Eq. (3.41b) allows us to identify the turbulent emf stress tensor,

$$\bar{\tau}_{ij}^{b\alpha} = \alpha^2 \partial_{jmm} \bar{b}_i. \quad (3.130)$$

Note that this is a hyper-resistive modification at scales small compared to  $\alpha$ .

### 3.2.5.2 LAMHD- $\alpha$ Kármán-Howarth theorem

In 1938, Kármán and Howarth [68] derived from the Navier-Stokes equations an exact law relating the time derivative of the two-point velocity correlation with the divergence of the third-order correlation function (see Section 2.4). Later, this result was generalized to the MHD case by Chandrasekhar [50], and recently written in terms of Elsässer variables (see Section 2.7). For LAMHD- $\alpha$  it was derived in Ref. [196], which we review here.

For the sake of simplicity, we consider the case  $\eta = \nu = 0$ , the dissipative terms can be added at any point in the derivation. Also, we use  $\alpha = \alpha_M$ . We start writing the LAMHD- $\alpha$  equations using the Elsässer variables

$$\mathbf{z}^\pm = \mathbf{v} \pm \mathbf{b}, \quad \bar{\mathbf{z}}^\pm = \bar{\mathbf{v}} \pm \bar{\mathbf{b}}. \quad (3.131)$$

Applying the Helmholtz operator to Eq. (3.118b), we obtain

$$(1 - \alpha^2 \nabla^2) (\partial_t \bar{\mathbf{b}} + \bar{\mathbf{v}} \cdot \nabla \bar{\mathbf{b}} - \bar{\mathbf{b}} \cdot \nabla \bar{\mathbf{v}}) = 0. \quad (3.132)$$

Now we add and subtract Eqs. (3.127) and (3.132). Using Eqs. (3.131) we obtain equations for the evolution of  $\bar{\mathbf{z}}^\pm$ ,

$$(1 - \alpha^2 \Delta) (\partial_t \bar{\mathbf{z}}^\pm + \bar{\mathbf{z}}^\mp \cdot \nabla \bar{\mathbf{z}}^\pm + \nabla \bar{\pi}) = -\alpha^2 \nabla \cdot \tau^\alpha, \quad (3.133)$$

where the stress tensor divergence  $\nabla \cdot \tau^\alpha$  in terms of the Elsässer variables is

$$\begin{aligned} \nabla \cdot \tau^\alpha = & \frac{1}{2} \nabla \cdot \left( \nabla \bar{\mathbf{z}}^+ \cdot \nabla \bar{\mathbf{z}}^- + \nabla \bar{\mathbf{z}}^+ \cdot \nabla \bar{\mathbf{z}}^{-T} - \nabla \bar{\mathbf{z}}^{+T} \cdot \nabla \bar{\mathbf{z}}^- \right. \\ & \left. + \nabla \bar{\mathbf{z}}^- \cdot \nabla \bar{\mathbf{z}}^+ + \nabla \bar{\mathbf{z}}^- \cdot \nabla \bar{\mathbf{z}}^{+T} - \nabla \bar{\mathbf{z}}^{-T} \cdot \nabla \bar{\mathbf{z}}^+ \right). \end{aligned} \quad (3.134)$$

We could repeat all the derivation to obtain an equation for the evolution of  $\mathbf{z}^\pm$  from Eqs. (3.118a) and (3.132). Instead, starting from Eq. (3.133), using Eqs. (3.119)

and (A.11) we obtain

$$\partial_t \mathbf{z}^\pm + \bar{\mathbf{z}}^\mp \cdot \nabla \mathbf{z}^\pm + \nabla \tilde{\pi} = \alpha^2 \nabla \cdot \varsigma^\pm \quad (3.135)$$

where

$$\begin{aligned} \varsigma^\pm = & \frac{1}{2} \left( \nabla \bar{\mathbf{z}}^\pm \cdot \nabla \bar{\mathbf{z}}^\mp + \nabla \bar{\mathbf{z}}^\pm \cdot \nabla \bar{\mathbf{z}}^{\mp T} + \nabla \bar{\mathbf{z}}^{\pm T} \cdot \nabla \bar{\mathbf{z}}^\mp \right. \\ & \left. - \nabla \bar{\mathbf{z}}^\mp \cdot \nabla \bar{\mathbf{z}}^\pm - \nabla \bar{\mathbf{z}}^\mp \cdot \nabla \bar{\mathbf{z}}^{\pm T} + \nabla \bar{\mathbf{z}}^{\mp T} \cdot \nabla \bar{\mathbf{z}}^\pm \right). \end{aligned} \quad (3.136)$$

Note that Eqs. (3.133) and (3.135) make explicit the fact that Alfvén waves  $\mathbf{v} = \pm \mathbf{b}$ ,  $\bar{\mathbf{v}} = \pm \bar{\mathbf{b}}$  are exact nonlinear solutions of the LAMHD- $\alpha$  equations. For an Alfvén wave either  $\mathbf{z}^+$  or  $\mathbf{z}^-$  (as well as the corresponding field  $\bar{\mathbf{z}}^\pm$ ) is zero. In this case, all nonlinear terms are zero and verification of the solution follows.

In Cartesian coordinates, we can write equations (3.133) and (3.135) in components

$$\partial_t z_i^\pm + \partial_m (z_i^\pm \bar{z}^{\mp m} + \tilde{\pi} \delta_i^m - \alpha^2 \varsigma_i^{\pm m}) = 0 \quad (3.137)$$

$$\partial_t \bar{z}_j^\pm + \partial'_m (\bar{z}_j^\pm \bar{z}'^{\mp m} + \tilde{\pi}' \delta_j^m + \alpha^2 g_\alpha \otimes \tau_j^{\alpha' m}) = 0, \quad (3.138)$$

the prime denotes that the variables are evaluated at  $\mathbf{x}'$ , and

$$g_\alpha = \frac{e^{-r/\alpha}}{4\pi\alpha^2 r} \quad (3.139)$$

is the Yukawa potential. The Green's function of the Helmholtz operator is given by

$$g_\alpha \otimes \tau_i^{\alpha' m} = \int g_\alpha (|\mathbf{x}' - \mathbf{x}|) \tau_i^{\alpha' m}(\mathbf{x}') d^3 x', \quad (3.140)$$

and the components of the stress tensors  $\tau^\alpha$  and  $\varsigma^\pm$  are

$$\begin{aligned} \tau_i^{\alpha' m} = & \frac{1}{2} \left( \partial_j \bar{z}_i^+ \partial^m \bar{z}^{-j} + \partial_j \bar{z}_i^+ \partial^j \bar{z}^{-m} - \partial_i \bar{z}_j^+ \partial^m \bar{z}^{-j} \right. \\ & \left. + \partial_j \bar{z}_i^- \partial^m \bar{z}^{+j} + \partial_j \bar{z}_i^- \partial^j \bar{z}^{+m} - \partial_i \bar{z}_j^- \partial^m \bar{z}^{+j} \right), \end{aligned} \quad (3.141)$$

$$\begin{aligned} \varsigma_i^{\pm m} = & \frac{1}{2} \left( \partial_j \bar{z}_i^\pm \partial^m \bar{z}^{\mp j} + \partial_j \bar{z}_i^\pm \partial^j \bar{z}^{\mp m} + \partial_i \bar{z}_j^\pm \partial^m \bar{z}^{\mp j} \right. \\ & \left. - \partial_j \bar{z}_i^\mp \partial^m \bar{z}^{\pm j} - \partial_j \bar{z}_i^\mp \partial^j \bar{z}^{\pm m} + \partial_i \bar{z}_j^\mp \partial^m \bar{z}^{\pm j} \right). \end{aligned} \quad (3.142)$$

Multiplying Eq. (3.137) by  $\bar{z}'_j{}^\pm$ , Eq. (3.138) by  $z_i^\pm$ , and adding the result yields

$$\begin{aligned} \partial_t \langle z_i^\pm \bar{z}'_j{}^\pm \rangle &= \frac{\partial}{\partial r^m} \langle (z_i^\pm \bar{z}'^{\mp m} - \alpha^2 \varsigma_i^{\pm m}) \bar{z}'_j{}^\pm \rangle + \frac{\partial}{\partial r^m} \langle \tilde{\pi} \bar{z}'_j{}^\pm \delta_i^m - \tilde{\pi}' z_i^\pm \delta_j^m \rangle \\ &\quad - \frac{\partial}{\partial r^m} \langle (\bar{z}'_j{}^\pm \bar{z}'^{\mp m} + \alpha^2 g_\alpha \otimes \tau^{\alpha m}_j) z_i^\pm \rangle, \end{aligned} \quad (3.143)$$

where we used homogeneity (see Section 2.4)

$$\frac{\partial}{\partial r^m} \langle \cdot \rangle = \frac{\partial}{\partial x'^m} \langle \cdot \rangle = -\frac{\partial}{\partial x^m} \langle \cdot \rangle. \quad (3.144)$$

Now, we can make the equation symmetric in the indices  $i, j$  by adding the equation for  $\partial_t \langle z_j^\pm \bar{z}'_i{}^\pm \rangle$ . Again, we use homogeneity (see Section 2.4)

$$\langle q_i \bar{q}'_j \bar{q}^m + q_j \bar{q}'_i \bar{q}^m \rangle = -\langle q'_i \bar{q}_j \bar{q}^m + q'_j \bar{q}_i \bar{q}^m \rangle, \quad (3.145)$$

and define the tensors

$$\mathcal{Q}_{ij}^\pm = \langle z_i^\pm \bar{z}'_j{}^\pm + z_j^\pm \bar{z}'_i{}^\pm \rangle, \quad (3.146)$$

$$\mathcal{T}_{ij}^{\pm m} = \langle (z_i^\pm \bar{z}'_j{}^\pm + z_j^\pm \bar{z}'_i{}^\pm + z'_i{}^\pm \bar{z}_j^\pm + z'_j{}^\pm \bar{z}_i^\pm) \bar{z}'^{\mp m} \rangle, \quad (3.147)$$

$$\Pi_{ij}^{\pm m} = \langle (\tilde{\pi} \bar{z}'_j{}^\pm - \tilde{\pi}' z_j^\pm) \delta_i^m + (\tilde{\pi} \bar{z}'_i{}^\pm - \tilde{\pi}' z_i^\pm) \delta_j^m \rangle, \quad (3.148)$$

$$\mathcal{S}_{ij}^{\pm m} = \langle \varsigma_i^m \bar{z}'_j{}^\pm + \varsigma_j^m \bar{z}'_i{}^\pm + g_\alpha \otimes \tau^{\alpha m}_j z_i^\pm + g_\alpha \otimes \tau^{\alpha m}_i z_j^\pm \rangle. \quad (3.149)$$

We can drop  $\Pi_{ij}^{\pm m}$  because the terms with the pressures  $\tilde{\pi}$  and  $\tilde{\pi}'$  vanish everywhere, as follows from the usual arguments of isotropy [68]. Finally we obtain

$$\partial_t \mathcal{Q}_{ij}^\pm = \frac{\partial}{\partial r^m} (\mathcal{T}_{ij}^{\pm m} - \alpha^2 \mathcal{S}_{ij}^{\pm m}). \quad (3.150)$$

This is the LAMHD- $\alpha$  version of Eq. (2.68) in Section 2.4. In the case  $\alpha = 0$  this equation is also a linear combination of Eqs. (43), (50), and (56) in Ref. [50]. More Kármán-Howarth equations can be written for different combinations of  $z^\pm$  and  $\bar{z}^\mp$ .

Since  $\mathcal{Q}_{ij}^\pm$  and  $\mathcal{T}_{ij}^{\pm m}$  are symmetric and divergence-free in their indices  $i$  and  $j$ ,  $\mathcal{S}_{ij}^{\pm m}$  must be symmetric and divergence-free in  $i$  and  $j$ . But the Elsässer variables

$\mathbf{z}^\pm$  are combinations of vectors and pseudovectors. Therefore,  $\mathcal{Q}^\pm$  is a combination of tensors and pseudotensors. We can define a tensor as

$$\mathcal{Q}^\alpha = \mathcal{Q}^\pm + \mathcal{Q}^\mp, \quad (3.151)$$

and a pseudotensor as  $\mathcal{Q}^\pm - \mathcal{Q}^\mp$ . We continue using only the tensor  $\mathcal{Q}^\alpha$ , the results can also be obtained for the pseudotensors using the expressions in [50]. We also define  $\mathcal{T}^\alpha = \mathcal{T}^\pm + \mathcal{T}^\mp$  and  $\mathcal{S}^\alpha = \mathcal{S}^\pm + \mathcal{S}^\mp$ .

Imposing isotropy and from incompressibility,  $\mathcal{Q}^\alpha$  can be written as [49]

$$\mathcal{Q}^\alpha_{ij} = \text{curl}(Q^\alpha r_l \epsilon_{ijl}) = -(d+1)Q^\alpha \delta_{ij} + r Q^{\alpha'} \left( \frac{r_i r_j}{r} - \delta_{ij} \right), \quad (3.152)$$

where the curl is taken with respect to the third index ( $j$ ),  $Q^\alpha = Q^\alpha(r, t)$  is a scalar function,  $\epsilon_{ijl}$  is the Levi-Civita pseudotensor, and  $d$  is the number of dimensions. Here,  $Q^{\alpha'} = \partial_r Q^\alpha$ .

In the same way, we can write

$$\begin{aligned} \mathcal{T}^{\alpha m}_{ij} &= \text{curl} \left[ T^\alpha \left( r_i \epsilon_{jml} r^l + r_j \epsilon_{iml} r^l \right) \right] \\ &= \frac{2}{r} T^{\alpha'} r_i r_j r^m - (r T^{\alpha'} + d T^\alpha) (r_i \delta_j^m + r_j \delta_i^m) + 2 T^\alpha \delta_{ij} r^m. \end{aligned} \quad (3.153)$$

The tensor  $\mathcal{S}^\alpha$  takes the same form with scalar function  $S^\alpha(r, t)$ . Note that  $\mathcal{S}^\alpha$  is the isotropic sub-filter scale stress tensor in the LES formulation of LAMHD- $\alpha$ .

Now we compute the divergence of these tensors. In three dimensions

$$\frac{\partial}{\partial r^m} \mathcal{T}^{\alpha m}_{ij} = \text{curl} \left[ (r T^{\alpha'} + 5 T^\alpha) \epsilon_{ijl} r^l \right], \quad (3.154)$$

and the divergence for  $\mathcal{S}^\alpha$  takes the same form. Replacing Eqs. (3.152) and (3.154) into Eq. (6.10) we finally obtain

**Theorem 2** (Kármán-Howarth Theorem for LAMHD- $\alpha$ ).

*The exact LAMHD- $\alpha$  model relation (6.10) for homogeneous isotropic statistics implies the isotropic tensor relation in three dimensions*

$$\frac{\partial Q^\alpha}{\partial t} = \left( r \frac{\partial}{\partial r} + 5 \right) ((T^\alpha)^2 - \alpha^2 S^\alpha), \quad (3.155)$$

and in  $d$  dimensions the general result is

$$\frac{\partial Q^\alpha}{\partial t} = \left[ r \frac{\partial}{\partial r} + (d+2) \right] ((T^\alpha)^2 - \alpha^2 S^\alpha). \quad (3.156)$$

This is the generalization of the Kármán-Howarth equation for LAMHD- $\alpha$  (two more equations can be written for different combinations of the tensors and pseudotensors), without the dissipation. When  $\mathbf{b} = 0$  this equation is also Eq. (3.16) in Ref. [109]. When  $\alpha = 0$ , this is equivalent to the Kármán-Howarth equation for the Elsässer variables as derived in Refs. [201, 204], or a combination of equations (49) and (53) in Ref. [50].

Therefore, all equations in Refs. [201, 204] follow for  $\alpha/r \ll 1$ . This result confirms that the  $\alpha$ -model preserves the properties of MHD for separations larger than  $r \sim \alpha$  as the scaling of structure functions and the relation between second and third order functions as given by the Kármán-Howarth equation hold.

**Corollary 1** (Kolmogorov Theorem for LAMHD- $\alpha$  ).

*Introducing the flux  $\partial_t Q^\alpha = -2\epsilon_\alpha/d$  with  $\epsilon_\alpha = \epsilon_\alpha^+ + \epsilon_\alpha^-$  (the energy injection rate for each Elsässer variable) in Eq. (3.156) and integrating in the inertial range yields*

$$-\frac{2}{d(d+2)}\epsilon_\alpha = (T^\alpha - \alpha^2 S^\alpha), \quad (3.157)$$

*where  $T^\alpha$  and  $S^\alpha$  are defined in equations (6.20) and (6.9).*

Note a multiplicative factor compared with the usual expression from Kolmogorov. It is related to the relation between autocorrelation functions and structure functions in isotropic turbulence in  $d$  dimensions. For  $\alpha/r \ll 1$  this equation reduces again to the MHD results. Note that structure and autocorrelation functions in LAMHD- $\alpha$  involve one unsmoothed field and one smoothed field if quantities are of second order, and two smoothed fields if quantities are of third order. In the following chapter, we use this convention and all structure functions for LAMHD- $\alpha$  are written as they follow from the expressions of the tensors  $\mathcal{Q}^\alpha$  and  $\mathcal{T}^\alpha$ .

### 3.2.5.3 Subgrid modeling results

LAMHD- $\alpha$  has been compared to DNS of 2D MHD for the properties of selective decay (the total energy decays rapidly relative to the mean square magnetic vector potential), dynamic alignment (the tendency of the velocity and magnetic fields to align), and direct and inverse cascades at Reynolds numbers up to  $R_\lambda \approx 1150$  [173]. The results of the study are summarized in Table 3.1. LAMHD- $\alpha$  recovered the main of features of the long wavelength behavior (such as the energy spectra up to wavenumbers  $\sim 2/\alpha$ ) whereas small-scaled detailed information (such as the location of structures) was lost. The time evolution of the energies were reproduced fairly well, while the time evolution of the cross-helicity and the phenomenon of dynamic alignment were only approximately recovered. Additionally, the inverse cascade of the mean square magnetic vector potential was present but reduced. Finally, non-Gaussian wings of the *pdfs* (e.g., for the current density) were found (but the tails did not completely reproduce those of the DNS). These are indicative of intermittency but are not as quantitative a measure of it as the structure functions studied in the next chapter.

LAMHD- $\alpha$  has also been compared to DNS of 3D MHD for the properties of selective decay (the total energy decays rapidly relative to the magnetic helicity), dynamic alignment, the inverse cascade of magnetic helicity, and the helical dynamo effect [172]. Again the principal large-scale features were recovered (the results of the study are summarized in Table 3.1). The degree of dynamic alignment was underestimated by LAMHD- $\alpha$  but the correct growth rate for the inverse cascade of magnetic helicity was recovered (albeit with a time lag). For the helical dynamo, the linear growth rate was close to the DNS and also the saturation levels and time of saturation were reproduced. 3D LAMHD- $\alpha$  simulation have been used to examine the onset of the non-helical (small-scale) dynamo instability when the magnetic Prandtl number ( $P_M = \nu/\eta$ ) is small [205], as occurs in liquid metals in the laboratory, in the liquid core of the Earth



and in the solar convection zone. LAMHD- $\alpha$  reproduced the general tendencies with a systematic trend to overestimate the threshold of critical magnetic Reynolds number for dynamo action at a given value of  $P_M$ . This may be related to the fact that the turbulent emf stress tensor of LAMHD- $\alpha$  contains only a hyper-resistive term and, thus, cannot model the SGS stretching of magnetic fields lines.

Table 3.1: Summary of LAMHD- $\alpha$  subgrid modeling results from previous studies in 2D and 3D. A plus indicates a very good reproduction of DNS properties, a check acceptable, followed by approximate and reduced in decreasing order of accurate reproduction (see text).

2D <sup>†</sup>	time evolution of energies	✓
	time evolution of cross-helicity	≈
	energy spectra	+
	dynamic alignment	≈
	<i>pdfs</i>	except tails
	inverse cascade of vector potential	<
3D <sup>‡</sup>	time evolution of energies	✓
	time evolution of magnetic helicity	≈
	energy spectra	✓
	dynamic alignment	<
	inverse cascade of magnetic helicity	<
	dynamo	✓

<sup>†</sup> Ref. [173]. <sup>‡</sup> Refs. [172, 205].

## Chapter 4

### Regularized MHD

In this chapter we explore the possibility of employing a regularization, the Lagrangian averaged magnetohydrodynamic (*LAMHD*– $\alpha$ ) model [110], as a MHD LES. As explained in the previous chapter subgrid modeling for turbulent MHD is still in its infancy. As *LAMHD*– $\alpha$  may be generally applicable to the many regimes of MHD, it might fill an important vacancy in the field of LES. Because of the importance of intermittency as a fundamental, or even defining property of turbulence, we seek to determine to what extent *LAMHD*– $\alpha$  exhibits intermittency.

We study the scaling laws resulting as a corollary of an extension of the Kármán-Howarth theorem to *LAMHD*– $\alpha$  (see Section 3.2.5.2) as well as the scaling of the longitudinal structure function exponents indicative of intermittency. Numerical simulations for a magnetic Prandtl number ( $P_M \equiv \nu/\eta$ ) equal to unity are presented both for freely decaying and for forced 2D MHD turbulence, solving directly the MHD equations, and employing the *LAMHD*– $\alpha$  equations at 1/2 and 1/4 resolution. We observe a linear scaling of the third-order structure function with length. The *LAMHD*– $\alpha$  equations also capture the anomalous scaling of the longitudinal structure function exponents (related to intermittency, see Section 2.8.2) up to order 8. Next, the statistics of sign cancellations of the current at small scales is studied using both the cancellation exponent and the fractal dimension of the structures. The *LAMHD*– $\alpha$  model is found to have the same scaling behavior between positive and negative contributions as the

DNS. It is also able to reproduce the time evolution of these quantities in free decaying turbulence. An independence of the cancellation exponent with the Reynolds numbers is observed at large  $Re$ .

#### 4.1 2D MHD

Intermittency is believed to be associated only with a forward cascade of energy; that is, the transfer of energy from larger scales to smaller scales, or, equivalently, from low wavenumbers to high wavenumbers. MHD presents an interesting property, namely that intermittency occurs both in 2D and in 3D. This is in contrast with the 2D neutral fluid case for which the conservation of vorticity leads to an inverse energy cascade to the large scales (and the selective decay of enstrophy); in the presence of a magnetic field, this conservation is broken by the Lorentz force and a direct energy cascade to small scales is recovered, rendering 2D-MHD a valid model for the 3D case, although topological properties (such as linkage and twisting of field lines) are absent. “Selective decay” refers to

turbulent processes in which one or more ideal invariants are dissipated rapidly relative to another, due to the transfer of the dissipated quantities to short wavelengths where the dissipation coefficients become effective.[173]

The system seeks a state where the dissipated quantity is as close to zero as can be for the surviving value of the nearly-conserved quantity. In 2D MHD with negligible cross helicity (the case we study),<sup>1</sup> the dissipated quantity is energy. For 2D Navier-Stokes, the dissipated quantity is enstrophy (which therefore must experience a direct cascade to smaller scales). Fjortoft’s theorem (see [146]) suggests such a direct cascade for enstrophy and an inverse cascade (to larger scales) for energy for the 2D Navier-Stokes case. We now apply the same argument for 2D MHD to illustrate its dynamics. In

---

<sup>1</sup> We use random phases for  $\mathbf{v}$  and  $\mathbf{b}$  either in the initial conditions or in the forcing. This implies negligible correlation between them and, hence, negligible cross helicity.

Fourier space we consider only three modes,  $k_1$ ,  $k_2 = 2k_1$ , and  $k_3 = 3k_1$ . We ask the question: “if energy leaves the mode at  $k_2$  does it move to smaller or larger scales?” Let  $E(k_i, t)$  and  $\mathcal{A}(k_i, t)$  be the energy and the mean square magnetic vector potential, respectively, in the mode  $k_i$  at time  $t$ . Defining the variation  $\delta E_i = E(k_i, t_2) - E(k_i, t_1)$ , we see that conservation of energy between times  $t_1$  and  $t_2$  implies

$$\delta E_1 + \delta E_2 + \delta E_3 = 0. \quad (4.1)$$

Similarly, conservation of mean square magnetic vector potential implies

$$\delta \mathcal{A}_1 + \delta \mathcal{A}_2 + \delta \mathcal{A}_3 = 0, \quad (4.2)$$

or, using  $k^2 \mathcal{A} \sim b^2$ ,

$$\frac{1}{k_1^2} \delta E_{M_1} + \frac{1}{k_2^2} \delta E_{M_2} + \frac{1}{k_3^2} \delta E_{M_3} = 0. \quad (4.3)$$

We assume the magnetic energy is some fraction of the total energy,  $E_M = CE$  ( $C = 1/2$  for equipartition). Using this and the relation between our modes, we find

$$36\delta E_1 + 9\delta E_2 + 4\delta E_3 = 0. \quad (4.4)$$

Solving (4.1) and (4.4) we find  $\delta E_1 = -\frac{5}{32}\delta E_2$  and  $\delta E_3 = -\frac{27}{32}\delta E_2$ . If energy moves away from the middle energy band ( $\delta E_2 < 0$ ), more of it goes to smaller scales ( $k_3$ ) than to larger scales ( $k_1$ ).<sup>2</sup> This suggests a direct cascade of energy. Conversely, for the mean square magnetic vector potential, we find  $\delta \mathcal{A}_1 = -\frac{5}{8}\delta \mathcal{A}_2$  and  $\delta \mathcal{A}_3 = -\frac{3}{8}\delta \mathcal{A}_2$  which suggests an inverse cascade (more energy goes from  $k_2$  to  $k_1$  than to  $k_3$ ). Given this inverse cascade of mean square vector magnetic potential, in a freely decaying run with negligible cross helicity, it is expected that  $\mathcal{A}$  cascades to larger scales where it dissipates slowly. As a result, the final state is expected to be dominated by magnetic energy.

---

<sup>2</sup> We could instead ask where energy leaving mode  $k_3$  goes and would, find again, that though energy moves to  $k_2$  ( $\delta E_2 > 0$ ) more energy moves to  $k_4 = 4k_1$ .

Since, from a numerical standpoint, much higher Reynolds numbers can be achieved in 2D, it is possible to reach an intermittent flow in 2D-MHD with adequate scale separation between the energy-containing range, the inertial range and the dissipation range. Our 2D MHD tests are able to exhibit a substantially larger Reynolds number (up to  $R_\lambda \sim 1500$ ) than the values listed for previous studies. This provides an ideal testing ground for models of turbulent MHD flows, such as they occur in geophysics and astrophysics: magnetic fields are observed in detail in the Earth and Sun environments, and are known to be dynamically important as well for the solar-terrestrial interactions (the so-called space weather), in the interstellar medium and in galaxies.

## 4.2 The cancellation exponent

All subgrid models introduce changes in the small scales in order to preserve the evolution of the large scales. It is often of interest to know the statistics of the small scales. It is also important to model properly the small scales because they have an effect on large scales. An example of this is eddy noise: the beating of two small scale eddies produces energy at the large scale, and this may affect the global long-time evolution of the flow. This is an issue that arises in global climate evolution and in solar-terrestrial interactions. Moreover, plasmas and conducting fluids generate thin and intense current sheets where magnetic reconnection takes place. In these regions, the magnetic field and the current rapidly change sign, and after reconnection magnetic energy is turned into mechanical and thermal energy. Reconnection events are known to take place in the earth's magnetopause [217] and magnetotail [20], the solar atmosphere [95], and the interplanetary medium [213]. Current sheets are strongly localized and intermittent. It is therefore important to preserve reliable statistics of these events in subgrid models of MHD turbulence. The statistics of sign cancellations of the current at small scales, due to these fast oscillations of the fields, is studied using the cancellation exponent,  $\kappa$ , which is linked to the fractal dimension of the structures (see [197] for references).

In order to measure fast oscillations in sign of a field on arbitrary small scales, the cancellation exponent was introduced [192, 235, 218]. The exponent is a measure of sign-singularity. We can define the signed measure for the current  $j_z(\mathbf{x})$  on a set  $Q(L)$  of size  $L$  as

$$\mu_i(l) = \int_{Q_i(l)} d\mathbf{x} j_z(\mathbf{x}) \Big/ \int_{Q(L)} d\mathbf{x} |j_z(\mathbf{x})| \quad (4.5)$$

where  $\{Q_i(l)\} \subset Q(L)$  is a hierarchy of disjoint subsets of size  $l$  covering  $Q(L)$ . The partition function  $\chi$  measures the cancellations at a given lengthscale  $l$ ,

$$\chi(l) = \sum_{Q_i(l)} |\mu_i(l)|. \quad (4.6)$$

Note that for noninteger  $L/l$  the subsets do not cover  $Q(L)$  and finite size box effects must be considered in the normalization of Eq. (4.5). In the limit of  $l \rightarrow 0$  there are no cancellations and we have  $\chi = 1$ . As  $l$  increases there are more and more cancellations and  $\chi$  decreases. We can study the scaling behavior of the cancellations by defining the cancellation exponent  $\kappa$ , where

$$\chi(l) \sim l^{-\kappa}. \quad (4.7)$$

Positive  $\kappa$  indicates fast changes in sign on small scales (in practice, a cut-off is always present at the dissipation scale). A totally smooth field has  $\kappa = 0$ . The exponent is also related with the fractal dimension  $D$  of the structures [218],

$$\kappa = (d - D)/2, \quad (4.8)$$

where  $d$  is the number of spatial dimensions of the system. In some circumstances, we are also interested in the cancellation exponent for the vorticity  $\omega_z$ . In that case the vorticity replaces the current in the definition of  $\mu_i(l)$  [Eq. (4.5)].

Under special assumptions, relations between the cancellation exponent and scaling exponents have been derived [235]. Positive cancellation exponent  $\kappa$  has been found in plasma experiments [192], direct simulations of MHD turbulence [218], in situ solar

wind observations [44], and solar photospheric active regions [219], where changes in the scaling were identified as preludes to solar flares.

### 4.3 Computation

To solve the MHD and LAMHD- $\alpha$  equations numerically we use a parallel pseudospectral code in a box with edge length  $2\pi$  as described in [173]. In 2D, the velocity and magnetic field are expressed as the curl of a scalar stream function  $\Psi$  and a one component vector potential  $a_z$ , respectively:

$$\mathbf{v} = \nabla \times (\Psi \hat{\mathbf{z}}), \quad \bar{\mathbf{v}} = \nabla \times (\bar{\Psi} \hat{\mathbf{z}}) \quad (4.9)$$

$$\mathbf{b} = \nabla \times (a_z \hat{\mathbf{z}}), \quad \bar{\mathbf{b}} = \nabla \times (\bar{a}_z \hat{\mathbf{z}}) \quad (4.10)$$

where  $\Psi = (1 - \alpha^2 \nabla^2) \bar{\Psi}$ ,  $a_z = (1 - \alpha_M^2 \nabla^2) \bar{a}_z$ , and where we have employed the familiar dimensionless Alfvénic units. In terms of these quantities, the 2D MHD equations may be expressed as

$$\partial_t \nabla^2 \Psi = [\Psi, \nabla^2 \Psi] - [a_z, \nabla^2 a_z] + \nu \nabla^2 \nabla^2 \Psi \quad (4.11)$$

$$\partial_t a_z = [\Psi, a_z] + \eta \nabla^2 a_z, \quad (4.12)$$

where

$$[F, G] = \partial_x F \partial_y G - \partial_x G \partial_y F \quad (4.13)$$

is the standard Poisson bracket. LAMHD- $\alpha$ , Eqs. (3.118a-3.118c), modifies this 2D structure by introducing smoothed variables as

$$\partial_t \nabla^2 \Psi = [\bar{\Psi}, \nabla^2 \Psi] - [\bar{a}_z, \nabla^2 a_z] + \nu \nabla^2 \nabla^2 \Psi \quad (4.14)$$

$$\partial_t \bar{a}_z = [\bar{\Psi}, \bar{a}_z] + \eta \nabla^2 a_z. \quad (4.15)$$

In the following sections we test the LAMHD- $\alpha$  model against a DNS of the MHD equations (for which  $\alpha = \alpha_M = 0$ ) for freely decaying turbulence with the same initial conditions, dissipation and time-stepping. We also test it for forced turbulence where we

have averaged statistics over 189 turnover times taken from 9 experiments with distinct seeds for the random forcing, resulting in a data set of  $\sim 2 \cdot 10^8$  points.

#### 4.4 Forced simulations

In this section we consider forced turbulence with  $\eta = \nu = 1.6 \times 10^{-4}$ . Four sets of simulations were carried out, one set of MHD fully-resolved simulations (DNS) with  $1024^2$  grid points, and three sets of LAMHD- $\alpha$  simulations, with  $512^2$  grid points and  $\alpha = \alpha_M = 6/512$ , with  $256^2$  grid points and  $\alpha = \alpha_M = 6/256$ , and with  $256^2$  grid points and  $\alpha = \alpha_M = 6/128$ .<sup>3</sup> Note that the  $256^2$  LAMHD- $\alpha$  simulation with  $\alpha = \alpha_M = 6/128$  could be carried out with a  $128^2$  spatial resolution (the choice  $\alpha = 2/k_{max}$  is conventional [173, 172, 113, 55, 57, 56]). Although it is common to reduce the spatial resolution even more in studies of the large scale components of the energy spectrum in LES of hydrodynamic turbulence, this cannot be done in this context since wide energy spectra and large amounts of spatial statistics are needed to compute the cancellation exponent properly (see e.g., [46] for a study of intermittency in LES).

Both the momentum and the vector potential equations were forced. The expressions of the external forces were loaded in the Fourier ring between  $k = 1$  and  $k = 2$ , and the phases were changed randomly with a correlation time  $\Delta t = 5 \times 10^{-2}$ . Averaged over space, the amplitudes of the external forces were held constant to  $F_M = 0.2$  in the vector potential equation, and  $F_K = 0.45$  in the momentum equation. The systems were evolved in time until reaching a turbulent steady state,<sup>4</sup> and then the simulations were extended for 21 turnover times. Over this time span, 21 snapshots of the fields from each run were used to compute the longitudinal increments. As previously mentioned, each set of simulations (DNS, and LAMHD- $\alpha$  with 2 different spatial resolutions) comprises

---

<sup>3</sup> A single turnover time for the  $1024^3$  DNS took 164 seconds on 32 IBM POWER4 1.3 GHz processors. By comparison the  $256^2$  LAMHD- $\alpha$  simulation took approximately 1/16 of the computational cost.

<sup>4</sup> A turbulent steady state is defined as the energy remaining approximately constant over several turnover times.



nine runs with the same viscosity and diffusivity but different series of random phases in the external forcing. We do this to have enough statistics to determine the scaling exponents up to eighth order with small error bars. The total number of points was  $\sim 2 \cdot 10^8$  for the DNS and  $\sim 1.2 \cdot 10^7$  points for the  $256^2$  LAMHD- $\alpha$  simulations.

During these intervals, the integral Reynolds number based on the *r.m.s.* velocity fluctuates around 2200. The normalized correlation coefficient between the velocity and the magnetic field is 20% with a standard deviation of 16% within the set of nine runs, and its unsigned counterpart  $2\langle |\mathbf{v} \cdot \mathbf{b}| \rangle / \langle |\mathbf{v}|^2 + |\mathbf{b}|^2 \rangle$ , is  $\sim 29\% \pm 12\%$ . The ratio of the integral scale to the Taylor scale computed on the *r.m.s.* fields fluctuates around 10 for all the simulations. The ratio of magnetic to kinetic energies is  $\sim 2$  for all runs. Finally, the Kolmogorov dissipation wavenumbers  $k_\nu = (\langle \omega^2 \rangle / \nu^2)^{1/4}$  and  $k_\eta = (\langle j^2 \rangle / \eta^2)^{1/4}$  both fluctuate around 330, i.e., at values substantially larger than the largest resolved wavenumbers  $k_\alpha \sim 1/\alpha$  in all LAMHD- $\alpha$  simulations, by virtue of the model.

Omni-directional spectra for magnetic and kinetic energies averaged over the 189 turnover times are shown in Fig. 4.1. All spectra display an inertial range, and the LAMHD- $\alpha$  simulations are able to capture the spectral behavior up to  $k \approx 1/\alpha$ . For  $k > 1/\alpha$ , theoretical arguments suggest a  $k^{-1}$  spectrum for the  $\alpha$ -model. To observe this spectrum, however, large values of  $\alpha$  would be required (see Chapter 5).

#### 4.4.1 Numerical results for intermittency and scaling anomaly

In this section, we compare intermittency of LAMHD- $\alpha$  to that of DNS of the MHD equations, regarded as true at a given Reynolds number. Intermittency is associated both with the presence of strong localized structures and with the existence of strong non-Gaussian wings in the probability distribution functions. The latter have been previously investigated in Ref. [173]. We concentrate here on the strong localized structures giving rise to deviations from self-similarity, which can be studied by examining high order statistical moments, such as the structure functions.

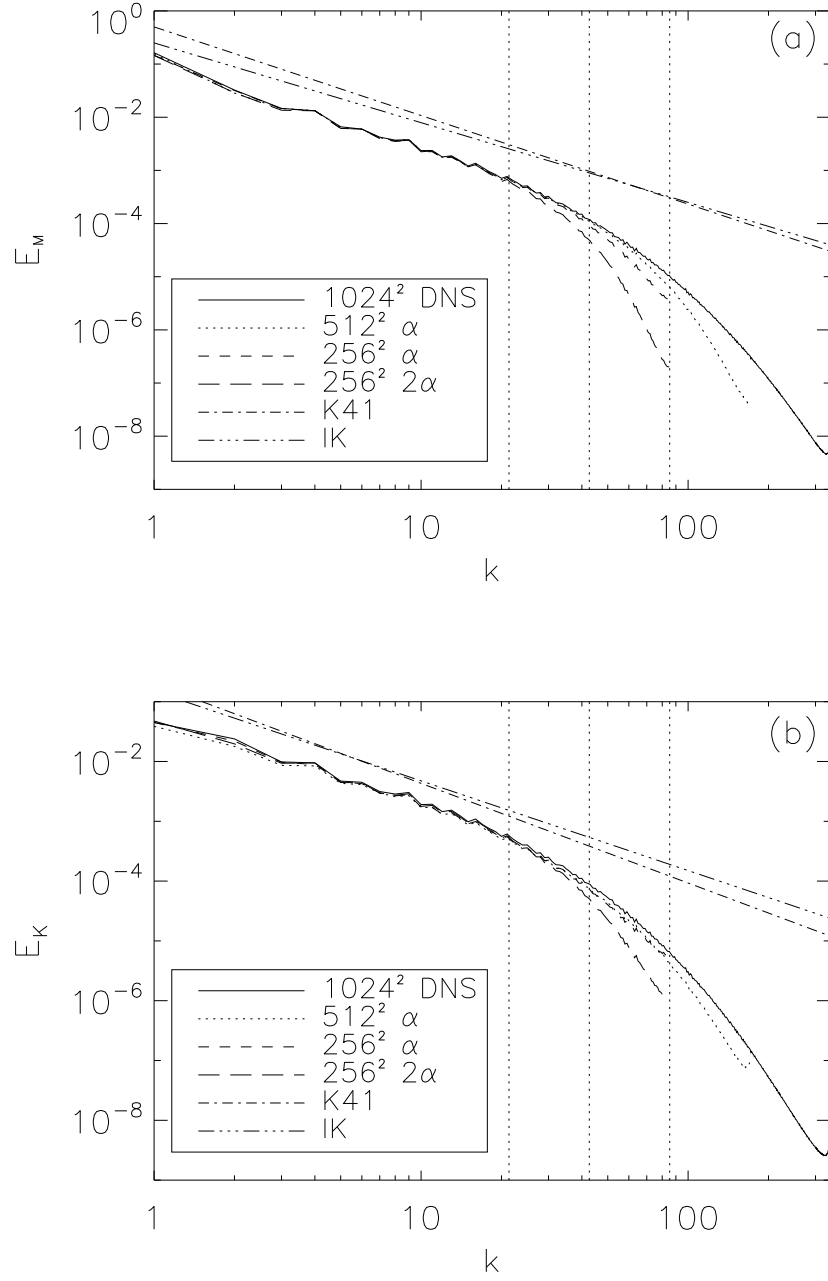


Figure 4.1: Spectra averaged over 189 turnover times.  $1024^2$  DNS is the solid line,  $512^2$  LAMHD- $\alpha$  is the dotted line,  $256^2$  LAMHD- $\alpha$  is the dashed line,  $256^2$  LAMHD- $\alpha$  with  $\alpha = \alpha_M = 6/128$  is the long-dashed line (hereafter indicated in figures as ' $256^2 2\alpha$ '),  $k^{-5/3}$  (K41) is the dash-dotted line, and  $k^{-3/2}$  (IK) is the dash-triple-dotted line; the K41 and IK slopes are shown for reference. The vertical lines indicate the wavenumbers corresponding to the lengths  $\alpha$  for all LAMHD- $\alpha$  simulations. Panel **(a)** is magnetic energy,  $E_M$ , versus wavenumber  $k$ , and panel **(b)** is kinetic energy,  $E_K$  vs.  $k$ .

The longitudinal structure function of a field  $\mathbf{f}$  is  $S_p^f(l) \equiv \langle |\delta f_{\parallel}|^p \rangle$  where  $\delta f_{\parallel} = (\mathbf{f}(\mathbf{x} + \mathbf{l}) - \mathbf{f}(\mathbf{x})) \cdot \mathbf{l}/l$  is the longitudinal increment of  $\mathbf{f}$  (see Section 2.5). In the inertial range between the large energy-containing scales and the small dissipative scales, the structure functions are assumed to vary in a self-similar manner,  $S_p^f(l) \propto l^{\zeta_p^f}$ . As previously mentioned, in isotropic and homogeneous turbulence the structure functions can be related to the correlation functions (see Section 2.5). K41 phenomenology predicts  $\zeta_p^v = p/3$ , while Iroshnikov and Kraichnan [125, 133] (hereafter, the IK model) gives  $\zeta_p^{\pm} = p/4$ . IK also leads to a shallower spectrum,  $E(K) \sim k^{-3/2}$  (dash-triple-dotted lines in Fig. 4.1), in the absence of significant velocity-magnetic field correlations. These two types of phenomenology differ by the taking into account in the latter case of the non-local interactions (in Fourier space) emanating from the propagation of Alfvén waves; it is worth mentioning here that the IK model also agrees with the isotropic limit of the weak turbulence theory for incompressible MHD [82]. The IK spectrum may also be recovered considering the anisotropy of MHD turbulence due to a large-scale guiding magnetic field from either externally applied fields or large-scale eddies. Under these conditions,  $E(K) \sim k^{-3/2}$  results from the scale-dependent dynamic alignment between  $\mathbf{v}$  and  $\mathbf{b}$  (see, [155, 26] and references therein). Note also that the She-Lévêque model of intermittency for MHD flows [200] recovers the intermittency as measured in direct numerical simulations both in 2D [200] and in 3D [22], but such models depend on two adjustable parameters and thus do not necessarily have a predictive power. The anomalous departure of the exponents  $\zeta_p$  from these linear scaling laws is a measure of intermittency-induced deviations from universality (see Section 2.8.2).

K41 theory predicts

$$S_p^v(l) \propto l^{\zeta_p^v}, \quad (4.16)$$

which follows from the assumption that the statistical properties of the field are self-

similar in the inertial range, which is identified here as the scales for which the relation

$$\zeta_3^v = 1 \quad (4.17)$$

holds. The existence of scaling (4.16) has been extensively verified for the hydrodynamic case. Starting from the assumption of self-similarity in the inertial range, we can then postulate the validity of Eq. (4.16) at arbitrarily high order,  $p$ . The Extended Self-Similarity (ESS) hypothesis (see Section 2.8.2) proposes the scaling

$$S_p^v(l) \propto [S_3^v(l)]^{\xi_p^v}, \quad (4.18)$$

which is found to apply to a much wider scaling range than the inertial range. Here, the scaling range is determined by the observed scaling for low orders and a chief benefit is increased statistics to compute more accurate exponents at high orders. For the case of MHD, Refs. [201, 204] propose to replace  $S_3^v(l)$  with the third-order, mixed structure functions. As in the ESS hypothesis, the third-order, mixed structure functions may provide better independent variables (as opposed to length  $l$ ) against which to determine the scaling exponents for MHD. From the KH theorem for an incompressible, non-helical MHD flow, Refs. [201, 204] derive

$$\langle \delta z_{\parallel}^{\mp}(\mathbf{l}) |\delta z^{\pm}(\mathbf{l})|^2 \rangle = -\frac{4}{d} \varepsilon^{\pm} l, \quad (4.19)$$

where  $|\delta z^{\pm}|^2 = (\delta z_{\parallel}^{\pm})^2 + (\delta z_{\perp}^{\pm})^2$ ,  $\delta z_{\perp}^{\pm}$  are the transverse increments,  $d$  is the space dimension,  $\varepsilon^+$  and  $\varepsilon^-$  are the energy dissipation rates for  $\frac{1}{2}(z^+)^2$  and  $\frac{1}{2}(z^-)^2$  respectively, and angle brackets indicate, as usual, spatial averages.

These results for the third-order structure functions are exact and can be used to compute more accurate anomalous scaling exponents of structure functions of higher order. Due to cancellation problems (linked with having limited statistics), absolute values are often employed. We also find linear scaling in this case, *viz.*:

$$L^{\pm}(l) \equiv \langle |\delta z_{\parallel}^{\mp}| |\delta z^{\pm}|^2 \rangle \propto l. \quad (4.20)$$

As follows from the expressions given in Section 3.2.5.2 and the invariants found for both MHD and  $LAMHD-\alpha$  [173, 107, 110, 108], when making comparisons between DNS and model runs, we substitute the  $H_\alpha^1$  norm,  $\langle ||u||_\alpha^2 \rangle = \langle |\mathbf{v} \cdot \bar{\mathbf{v}}| \rangle$  [113, 112], for the regular  $L^2$  norm,  $\langle |v|^2 \rangle = \langle |\mathbf{v} \cdot \mathbf{v}| \rangle$ , whenever we consider quantities for the  $LAMHD-\alpha$  model. The Kármán-Howarth theorem for  $LAMHD-\alpha$  (see Section 3.2.5.2) is essential to this study of intermittency in that it allows us to define the structure functions for  $LAMHD-\alpha$ ; it also identifies the flux relation that scales linearly with  $l$  for application in MHD of the ESS hypothesis. Accordingly we determine the relative scaling exponents,  $\xi_p^f$ , by using Eq. (4.20) for the third-order, mixed structure function,  $L^+(l) = \langle |\delta z_\parallel^-| |\delta z^+|^2 \rangle$  for MHD and  $L_\alpha^+(l) = \langle |\delta \bar{z}_\parallel^-| |\delta z^+|_\alpha^2 \rangle$  for  $LAMHD-\alpha$ ,

$$S_p^f(l) \propto [L_{(\alpha)}^+(l)]^{\xi_p^f}. \quad (4.21)$$

Figure 4.2 shows the third-order mixed structure function  $L_{(\alpha)}^+(l)/l$  as a function of  $l$ . We find, contrary to what is reported in [22], that Eq. (4.20) has an identifiable range of validity, as can be seen in the figure by comparison with the solid straight line denoting the computed slope  $L^+(l) \sim l^{0.99}$ . This range of validity is identified as the inertial range,  $2\pi/20 \leq l \leq 2\pi/10$ , and is indicated by dashed vertical lines. The  $LAMHD-\alpha$  runs display the same scaling as the MHD simulation, and departures are pronounced only for scales approaching and smaller than  $\alpha$  (for the  $256^2$  runs,  $\alpha \approx 0.15$  or  $0.29$  and for the  $512^2$  run,  $\alpha \approx 0.07$  as indicated by the arrows). Note that the results have been scaled by the mean value of  $L_{(\alpha)}^+(l)$ . As the average energies of the runs are disparate, this improves the ease of comparison. The same behavior is observed for  $L_{(\alpha)}^-(l)$ .

The scaling of the third-order structure function  $S_3^+$  versus  $L_{(\alpha)}^+$  for the Elsässer variable  $\mathbf{z}^+$  is shown in Fig. 4.3(a) as well as a compensated plot versus  $l$  in Fig. 4.3(b). We see very little contamination at scales larger than  $\alpha$ . This contrasts with hyperviscosity which is known to cause an enhanced bottleneck in Navier-Stokes turbulence,

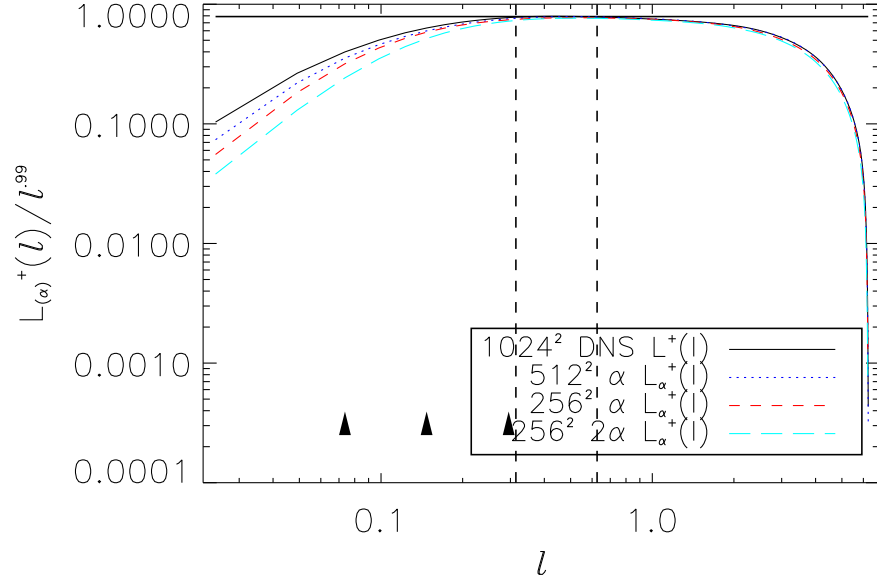


Figure 4.2: Third-order, mixed structure function,  $L_{(\alpha)}^+(l)/l^{0.99}$ , versus  $l$ , for forced runs of turbulence averaged over 189 turnover times. Results are scaled by the mean value of  $L_{(\alpha)}^+(l)$  for easier comparison.  $1024^2$  DNS is the black solid line,  $512^2$  LAMHD $-\alpha$  is the blue dotted line,  $256^2$  LAMHD $-\alpha$  is the red dashed line, and  $256^2$   $2\alpha$  is the cyan long-dashed line. The best fit to the DNS data,  $L^+ \sim l^{0.99}$ , is indicated by the solid straight line. The inertial range where this fit is made is indicated by dashed vertical lines and arrows indicate the lengths  $\alpha$  for the  $512^2$  and  $256^2$  simulations.

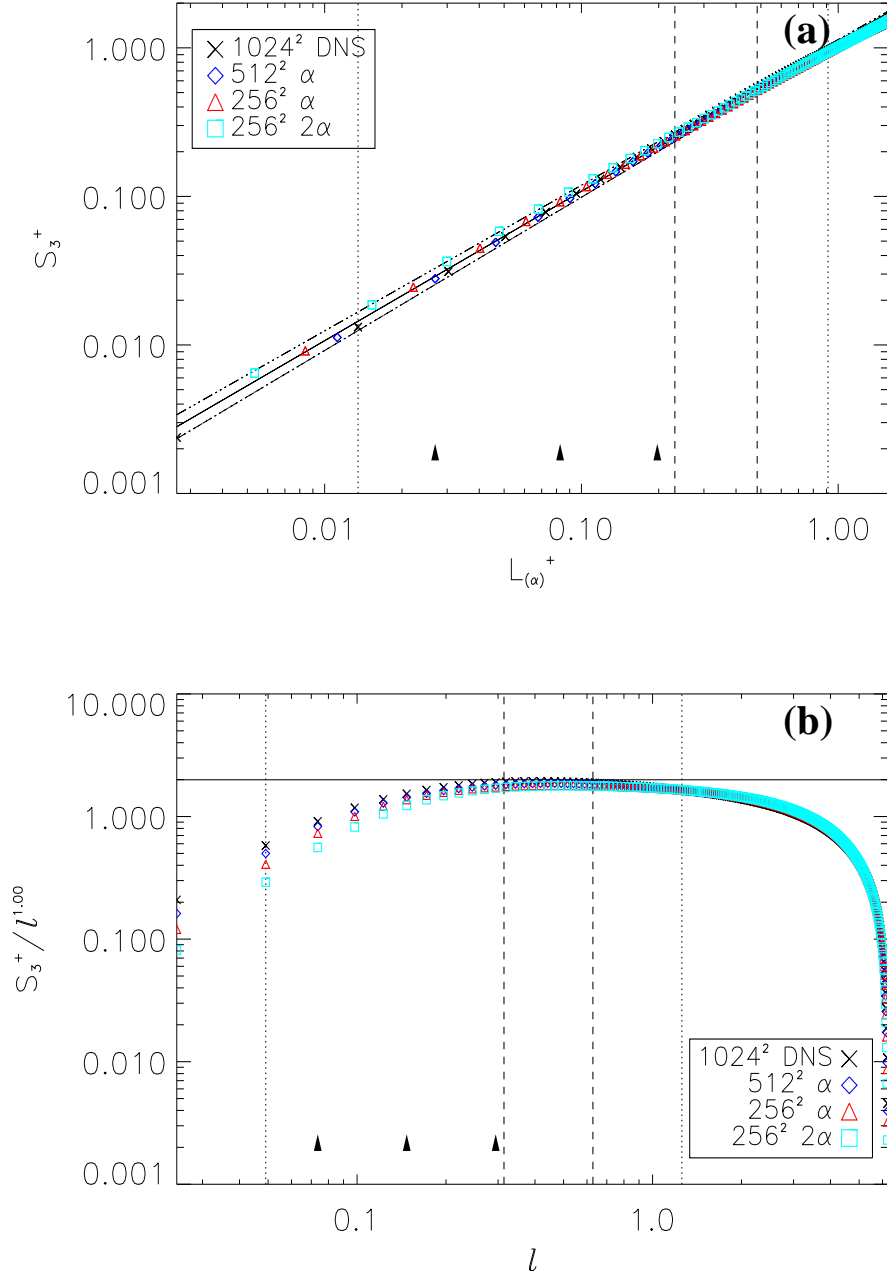


Figure 4.3: Third-order structure functions for  $z^+$ : Panel (a)  $S_3^+$  versus  $L_{(\alpha)}^+$  and panel (b)  $S_3^+ / l^{\zeta_3^+}$  versus  $l$ , computed over 189 turnover times. 1024<sup>2</sup> DNS are the black X's, 512<sup>2</sup> LAMHD- $\alpha$  are the blue diamonds, 256<sup>2</sup> LAMHD- $\alpha$  ( $\alpha = 6/256$ ) are red triangles, and 256<sup>2</sup> LAMHD- $\alpha$  ( $\alpha = 6/128$ ) are the cyan squares. The solid line corresponds to the best fit to the DNS data,  $S_3^+ = (L^+)^{1.01}$  (the dash-dotted lines represent the  $\sigma$  error). The ESS hypothesis range where this fit is made is indicated by dotted vertical lines and dashed vertical lines indicate the inertial range. Arrows indicate the several lengths  $\alpha$  used in the simulations.

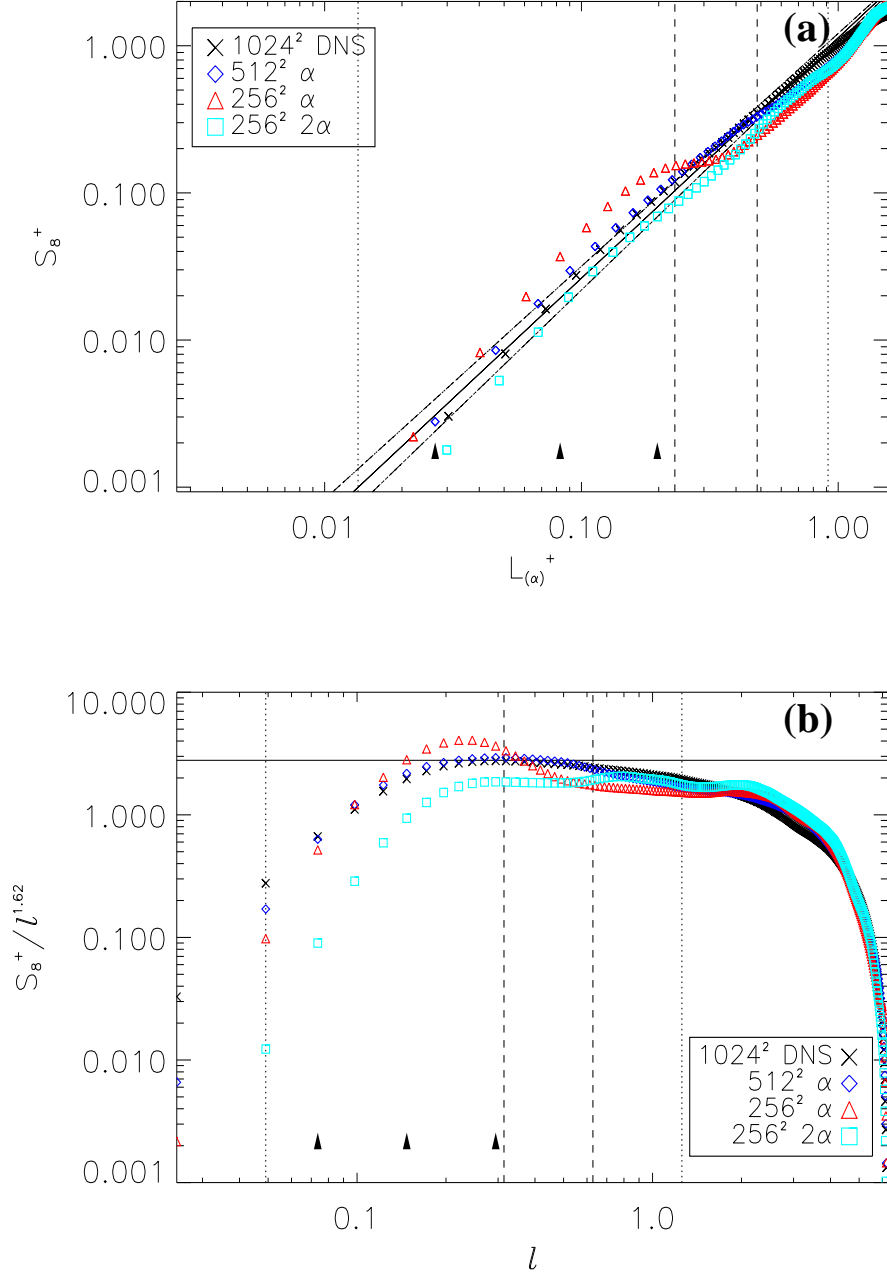


Figure 4.4: Eighth-order structure functions for  $z^+$ : Panel (a)  $S_8^+$  versus  $L_{(\alpha)}^+$  and panel (b)  $S_8^+ / l^{\zeta_8^+}$  versus  $l$ , computed over 189 turnover times. Labels are as in Fig. 4.3. The solid line corresponds to the best fit to the DNS data,  $S_8^+ = (L^+)^{1.63}$ . The ESS hypothesis range where this fit is made is indicated by dotted vertical lines and dashed vertical lines indicate the inertial range. Arrows indicate lengths  $\alpha$ .



which corrupts the scaling of the larger scales for structure functions of order two and higher [101]. The MHD case has not been studied in this context, and the presence of an inverse cascade of magnetic helicity might also exacerbate the problem.

The LAMHD- $\alpha$  simulations show similar scaling to what is found in DNS of MHD. A solid line indicates the best fit to the DNS data,  $\xi_3^+ = 1.01 \pm 0.08$  using the ESS hypothesis (the ESS scaling range is indicated by dotted vertical lines); note that all errors presented and shown in the figures correspond to the standard deviation,  $\sigma$ . The much smaller (compared to the ESS range) inertial range is indicated by dashed vertical lines and arrows indicate lengths  $\alpha$ . While in the  $1024^2$  DNS there is enough statistics to measure the scaling exponents  $\xi_p$  in the inertial range, when we use the LAMHD- $\alpha$  equations to reduce the computational cost, the amount of spatial statistics is drastically reduced (e.g., by a factor of 16 in the  $256^2$  runs). The ESS hypothesis allows us to extend the range where the  $\xi_p$  exponents are computed, giving a better estimation and smaller error bars. This is the main benefit of using the ESS hypothesis. As an example, in Fig. 4.4(a) we show the scaling of the eighth-order structure function  $S_8^+$  versus  $L_{(\alpha)}^+$  as well as a compensated plot versus  $l$  in Fig. 4.4(b). The ranges corresponding to the inertial range and ESS are also indicated. For the  $256^2$  runs, we cannot observe a scaling at this order. The error of a scaling computed from the assumption of self-similarity is excessively large (see Fig. 4.5(a)). From the ESS hypothesis a better estimation of the (postulated) scaling at order eight can be made (see Fig. 4.5(b)).

Figure 4.5 compares the scaling exponents,  $\xi_p^+$ , for the DNS runs and the three sets of LAMHD- $\alpha$  runs. Figure 4.5(a) is for exponents computed only over the inertial range. Notice that the LAMHD- $\alpha$  runs capture the scaling for the low-order moments ( $p \leq 4$ ). For higher-order moments (beginning at  $p = 5$ ), the drop in the scaling exponents for the  $256^2$  results (with  $\alpha = \alpha_M = 6/256$ ) and the large error bars are indicative of insufficient statistics. The advantages of ESS are clearly seen by comparison with Fig. 4.5(b), which shows the scaling exponents for all sets of runs employing the

ESS hypothesis. In both figures, the She-L  v  que (SL) formula [214] modified for the MHD case [200] is shown as a reference,

$$\frac{\xi_p}{\xi_3} = \frac{p}{6} + 1 - \left(\frac{1}{2}\right)^{p/3}. \quad (4.22)$$

From these results, we conclude that LAMHD- $\alpha$  captures the intermittency of the DNS runs up to and including the eighth-order moment (to within the errors of our statistics). By comparison with results for LES (see Section 2.8.2) we find that LAMHD- $\alpha$  recovers intermittency extremely well. LAMHD- $\alpha$  has less than a 3% error for  $p = 7$  at one-half resolution and a 6% error at one-quarter resolution. The best results for LES are a 7% error at  $p = 7$  and these are from overly-optimistic *a priori* tests.

Table 4.1: Relative scaling exponents (together with  $\sigma$  errors in computing the slope in parenthesis) computed from the 9 DNS runs over the inertial range,  $\xi$ , and utilizing the ESS hypothesis,  $\xi_{ESS}$ .

$p$	$\xi^+$	$\xi_{ESS}^+$	$\xi_{ESS}^-$	$\xi_{ESS}^v$	$\xi_{ESS}^B$
1	.43(03)	.43(02)	.42(01)	.37(02)	.43(01)
2	.75(04)	.76(02)	.76(01)	.67(03)	.76(01)
3	.99(05)	1.01(03)	1.01(01)	.92(03)	1.01(01)
4	1.16(05)	1.19(03)	1.20(01)	1.10(03)	1.16(01)
5	1.29(04)	1.34(03)	1.34(02)	1.25(03)	1.27(01)
6	1.37(03)	1.45(04)	1.45(03)	1.36(02)	1.33(02)
7	1.43(04)	1.55(04)	1.53(04)	1.44(04)	1.38(02)
8	1.46(07)	1.63(05)	1.60(05)	1.50(04)	1.43(03)

The anomalous scaling results for the DNS runs are shown in Table 4.1. Though our goal here is to test LAMHD- $\alpha$  against DNS, we remark briefly on the correspondence between our scaling exponents and other studies. In opposition to the findings of [202], we find  $\xi_3^\pm \sim 1$  but  $\xi_4^\pm > 1$ . We note, however, that the forcing in [202] was tailored to maintain at a constant level all Fourier modes with  $k = 1$  while our forcing is random with a constant amplitude between  $k = 1$  and  $k = 2$ . As can be seen from Table 4.1, our results for  $\xi_p^+$  are in good agreement with [22], for decaying turbulence, and with [94], for forced turbulence. As [22] suggests, the scaling exponents, as inertial

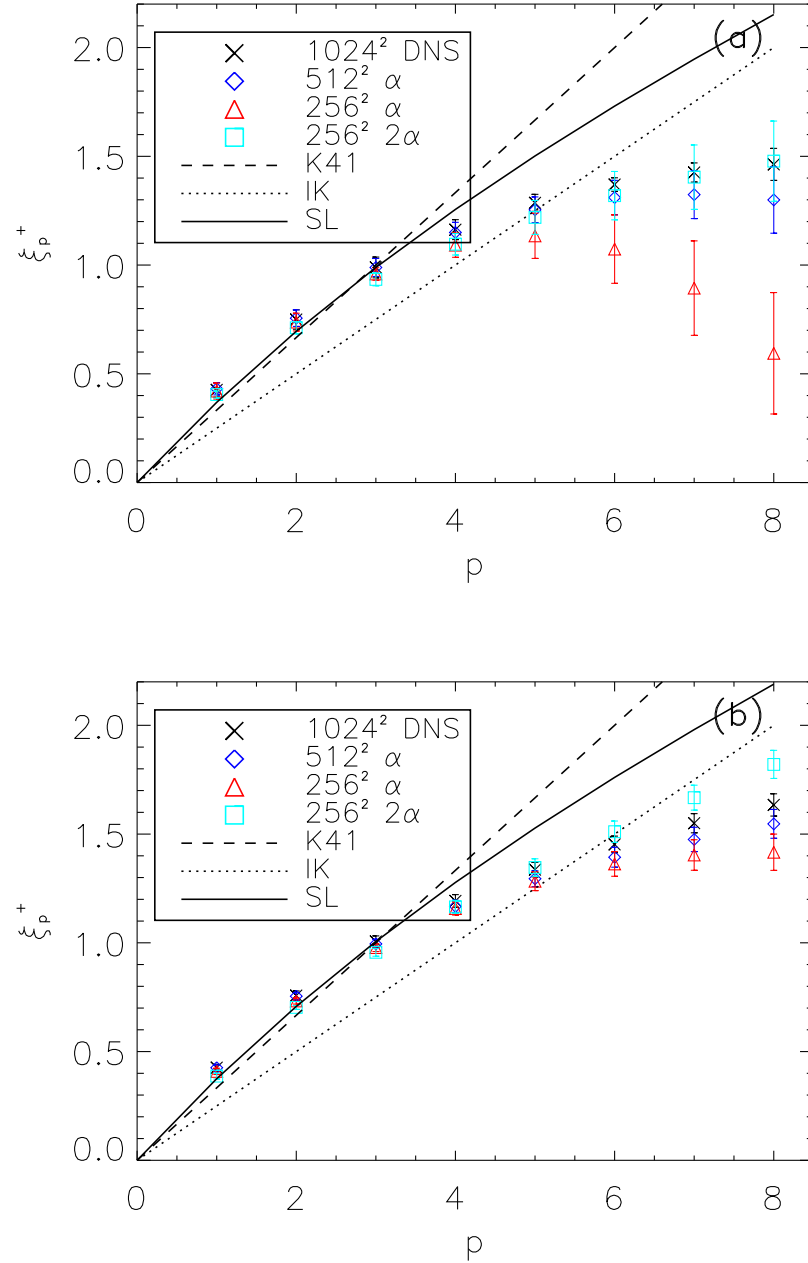


Figure 4.5: Structure function scaling exponent:  $\xi_p^+$  versus  $p$ , computed over 189 turnover times. Labels are as in Fig. 4.3. The dashed line indicates K41 scaling, dotted line indicates IK scaling, and the solid line is the prediction using the modified She-L  v  que formula (see text). Panel (a) is computed over the inertial range. Panel (b) is computed utilizing the ESS hypothesis.

range properties, may depend on the character of the driving due to non-local processes in the cascade dynamics connected with the Alfvén effect (see also [3, 168]); and as Ref. [202] points out, such an analysis can be sensitive to several parameters such as the ratio of kinetic to magnetic energy or the amount of correlation between the velocity and the magnetic fields.

Figure 4.6 shows the scaling exponents for the velocity and magnetic fields, as well as for the other Elsässer variable  $z^-$ . The anomalous scaling is again nearly matched by LAMHD- $\alpha$  up to and including eighth-order. The results from the MHD and LAMHD- $\alpha$  simulations are also in good agreement with Ref. [94]. Note that the magnetic field is more intermittent than the velocity field (in the sense that the scaling exponents deviate more from a straight line), as previously found in numerical simulations [202]. It may be related to the fact that in MHD, nonlinear interactions are more non-local (in Fourier space) than for neutral fluids [3, 168]. This well known feature of MHD turbulence is also properly captured by the LAMHD- $\alpha$  equations. The average (over all fields) of the  $3\sigma$  errors of the eighth order scaling exponent is 0.13 for the DNS on a  $1024^2$  grid; it is 0.15 and 0.16 for LAMHD- $\alpha$  on a  $512^2$  and  $256^2$  grid, respectively. To further test the convergence of our statistics, we reduced the amount of data used to compute the scaling exponents for the  $512^2$  runs by a factor of 4 (which gives the same amount of statistics than the  $256^2$  LAMHD runs) and determined an average  $3\sigma$  error of 0.17. While these results confirm our convergence as the amount of statistics is increased, they also highlight the rather low decrease in error with increased computational effort. Accordingly, the computational burden for more accurate determination of high-order statistics prohibits further analysis of the data.

#### 4.4.2 Cancellation statistics

To characterize the oscillating behavior and sign singularities in the flows obtained from the MHD and LAMHD- $\alpha$  simulations, we perform a signed measure analysis and

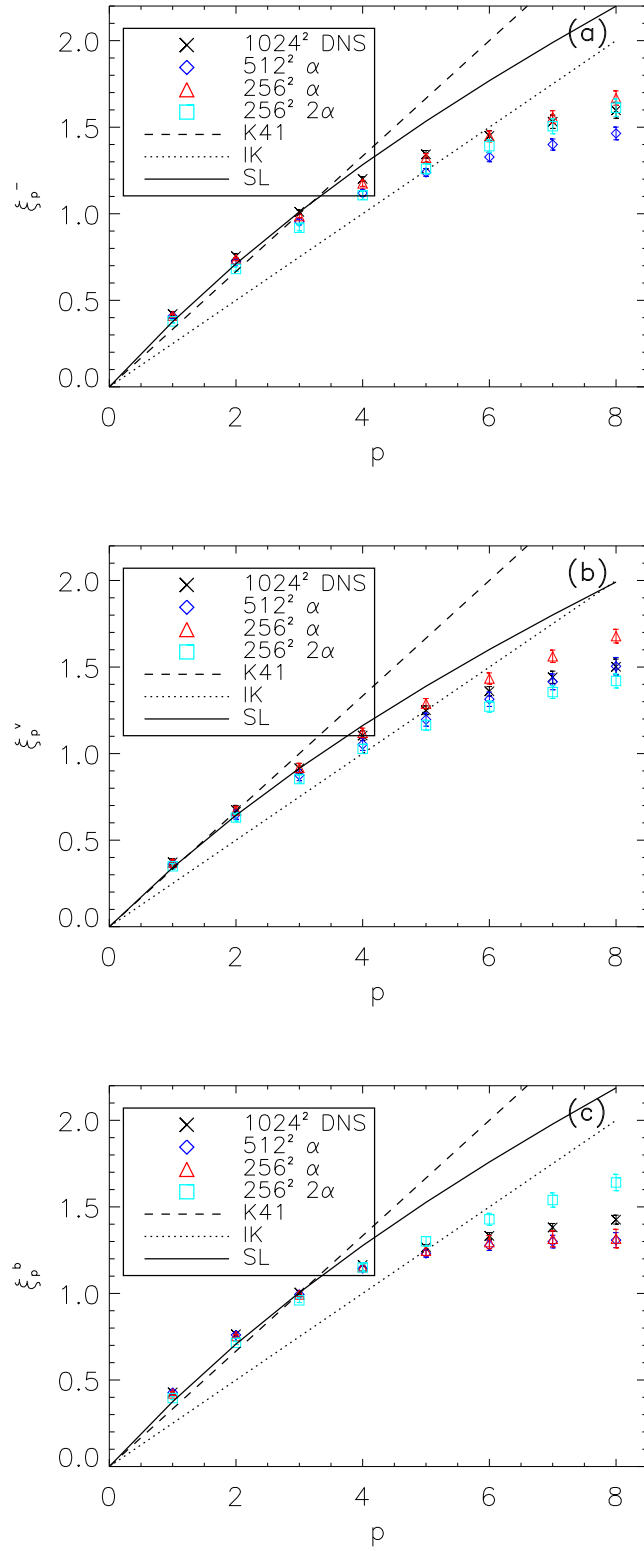


Figure 4.6: Structure function scaling exponent  $\xi_p$  versus  $p$  for  $z^-$  (panel (a)),  $v$  (panel (b)), and  $b$  (panel (c)). Labels are as in Figure 4.3.

compute the cancellation exponent  $\kappa$  for the current and for the vorticity. Following Eq. (4.7), its value is obtained by fitting  $\chi(l) = c(l/L)^{-\kappa}$  through the inertial range, where  $L = 2\pi$  is the length of the box, and  $c$  is a constant. The lengthscales in the inertial range used for this fit are obtained studying the scaling of the third-order mixed structure function.

Fig. 4.7 shows  $\chi(l)$ , Eq. (4.6), for three simulations ( $1024^2$  DNS,  $512^2$  LAMHD- $\alpha$  with  $\alpha = \alpha_M = 6/512$ , and  $256^2$  LAMHD- $\alpha$  with  $\alpha = \alpha_M = 6/256$ ), averaged using 11 snapshots of the current covering a total time span of 20 turnover times in a turbulent steady state (from a single run). A power law can be identified at intermediate scales, scales smaller than the forcing band but larger than the dissipation scale. Note that the two LAMHD- $\alpha$  simulations reproduce the same scaling as the DNS. As a result, the sign singularity and fractal structure are both well captured in the inertial range although the  $\alpha$ -model is known to give thicker structures at scales smaller than  $\alpha$  due to the introduction of the smoothing length [58, 173, 172]. The best fit for the current  $j_z$  using a power law in the inertial range gives  $\kappa = 0.50 \pm 0.17$  for the  $1024^2$  DNS,  $\kappa = 0.55 \pm 0.19$  for the  $512^2$  LAMHD- $\alpha$  simulation, and  $\kappa = 0.55 \pm 0.43$  for the  $256^2$  LAMHD- $\alpha$  simulation. Note that a value of  $\kappa = 0.50$  in the DNS gives a value of the fractal dimension,  $D = 1.00 \pm 0.34$ , close to the codimension of 1 corresponding to current sheets in MHD turbulence. For the vorticity, the cancellation exponent is  $\kappa = 0.73 \pm 0.16$  for the  $1024^2$  DNS,  $\kappa = 0.74 \pm 0.32$  for the  $512^2$  LAMHD- $\alpha$  simulation, and  $\kappa = 0.80 \pm 0.32$  for the  $256^2$  LAMHD- $\alpha$  simulation, giving a fractal dimension of  $D = 0.54$  for the DNS. The values obtained are compatible with the values of  $\kappa = 0.43 \pm 0.06$  and  $D = 1.14 \pm 0.12$  for the current, and  $\kappa = 0.69 \pm 0.12$  and  $D = 0.62 \pm 0.24$  for the vorticity obtained in Ref. [218] for forced direct numerical simulations of 2D MHD turbulence using a  $1024^2$  spatial grid and  $\eta = \nu = 8 \times 10^{-4}$ . Given the good agreement between DNS and LAMHD- $\alpha$  simulations, in the following sections we refer only to the cancellation exponent for the current density.

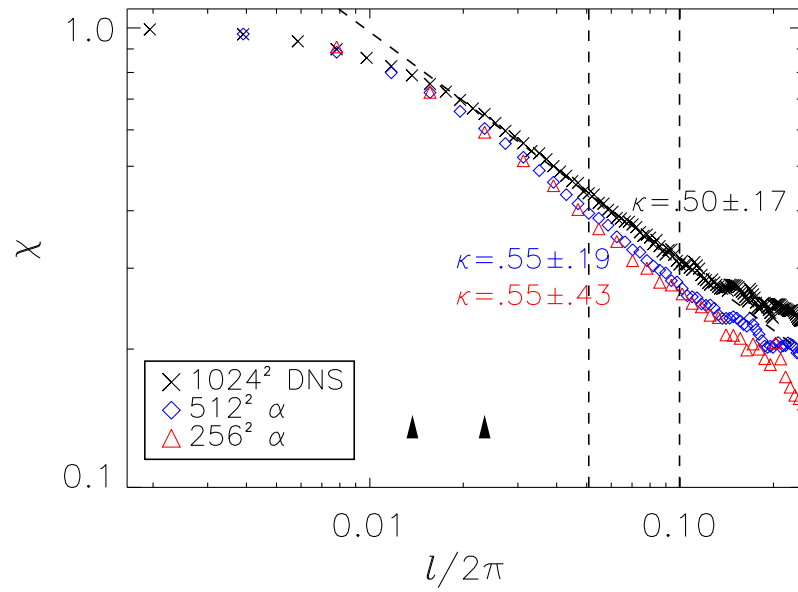


Figure 4.7:  $\chi(l)$  averaged in time for  $j_z$  in forced MHD turbulence. The X's correspond to the  $1024^2$  DNS, diamonds to the  $512^2$  LAMHD- $\alpha$  run, and triangles to the  $256^2$  LAMHD- $\alpha$  run. The dashed line indicates a slope of 0.50. The arrows indicate the lengths  $\alpha$  and the vertical dashed lines indicate the inertial range. Note that the slopes are of import, not the offsets.

## 4.5 Decaying simulations

In this subsection we discuss simulations of free decaying turbulence using both the MHD and the LAMHD- $\alpha$  equations. The results are similar to the ones presented in the previous subsection for forced turbulence. However, since no turbulent steady state can be defined in freely decaying runs, the amount of statistics is reduced as only a few snapshots of the velocity and magnetic field during the peak of mechanic and magnetic dissipation can be used to compute structure functions. To overcome this problem in part, we discuss simulations with higher spatial resolution than the ones presented in the forced case. The three simulations were started with the same initial conditions; initial velocity and magnetic fields. A  $2048^2$  DNS was made using  $\nu = \eta = 10^{-4}$ , as well as a  $1024^2$  LAMHD- $\alpha$  run with  $\alpha = \alpha_M = 6/1024$  and a  $512^2$  LAMHD- $\alpha$  run with  $\alpha = \alpha_M = 6/512$ .<sup>5</sup> The initial velocity and magnetic fields were loaded with random phases into the rings from  $k = 1$  to  $k = 3$  in Fourier space. The initial *r.m.s.* values of  $\mathbf{v}$  and  $\mathbf{b}$  are equal to unity. No external forces are applied and the system decays freely as a result of the dissipation. Under these conditions, the LAMHD- $\alpha$  equations have been shown to reproduce the time evolution of the magnetic and kinetic energy, as well as the evolution of the spectra and other statistical quantities (as was the lack of agreement between DNS and an under-resolved MHD simulation) [173]. For example, the evolution of magnetic,  $E_m$ , and kinetic,  $E_k$ , energies versus time for our runs is shown in Fig 4.8. The upper grouping of the lines are for magnetic energy, the green dotted line is for  $2048^2$  DNS, the blue dashed line and the red dash-triple-dotted line are for  $1024^2$  and  $512^2$  LAMHD- $\alpha$ , respectively. The lower grouping of lines are the kinetic energies, solid green for DNS, blue dash-dotted for  $1024^2$  alpha, and red long-dashed for  $512^2$  alpha. We see that the system is near (well within an order of magnitude of) equipartition and that the  $\alpha$ -model runs closely reproduce the time evolution of the

---

<sup>5</sup> A single turnover time for the  $2048^3$  DNS took 760 seconds on 32 IBM POWER4 1.3 GHz processors. By comparison the  $512^2$  LAMHD- $\alpha$  simulation took approximately 1/16 of the computational cost.



energy.

In Figure 4.9, the time evolution of the mean square current,  $\langle j^2 \rangle \sim \Omega_M$ , and mean square vorticity,  $\langle w^2 \rangle \sim \Omega$ , are shown. It is seen that the  $\alpha$ -model reproduces both the time of maximum dissipation and the order of magnitude of the dissipation. Next, we compare averaged spectra from  $t = 3$  up to  $t = 6$ , the time for which the energies are oscillating and prior to maximum dissipation (see Figure 4.9). We note that for large wavelength component behavior, up to  $\approx k_\alpha$ , both resolutions of the  $\alpha$ -model accurately reproduce the omni-directional spectra for the magnetic and kinetic energies as expected [173]<sup>6</sup> (see Figure 4.10). An inertial range can be identified for all simulations with an extent of approximately one decade in Fourier space, from  $k \approx 3$  up to  $k \approx 30$ . As [173] we also find that the spectral details at small scales are not accurate. Note that  $k_\alpha \equiv \frac{1}{\alpha} \approx 171$  for the  $1024^2$  run and  $k_\alpha \approx 85$  for the  $512^2$  run. These wavenumbers are indicated with vertical lines in the figures. As previously mentioned, for  $k > k_\alpha$  a steeper energy spectrum (compared to the spectrum for  $k < k_\alpha$ ) is predicted [77] and it is this very aspect of the  $\alpha$ -model that makes lower resolution simulations possible. Note, however, a marked better agreement (for  $k > 80$ ) with the DNS for the kinetic energy spectrum.

In the induction equation for the smoothed magnetic field, Eq. (3.118b), the Ohmic dissipation term is  $\eta \nabla^2 \mathbf{b} = \eta \nabla^2 \bar{\mathbf{b}} - \eta \alpha^2 \nabla^4 \bar{\mathbf{b}}$  and thus is hyper-viscosity-like (see Eq. (3.130)). This explains the faster drop in the magnetic energy spectrum. For this spectrum we note that for the  $512^2$  run, the spectrum is indistinguishable from the DNS up to  $k\alpha \approx 0.7$  and for  $1024^2$  up to  $\approx 0.6$ . As the smoothing is proportional to the square of  $k\alpha$ , neither of these values is surprising. For the kinetic spectrum on the other hand, the  $512^2$  remains indistinguishable beyond  $k\alpha = 1$  and the  $1024^2$  run only begins to deviate at  $k\alpha \approx 0.8$ . Both LAMHD- $\alpha$  spectra for kinetic and magnetic energy behave as expected and reproduce the large-scale spectra accurately.

---

<sup>6</sup> Reference [173] also finds that under-resolved MHD simulations have inaccurate spectra.

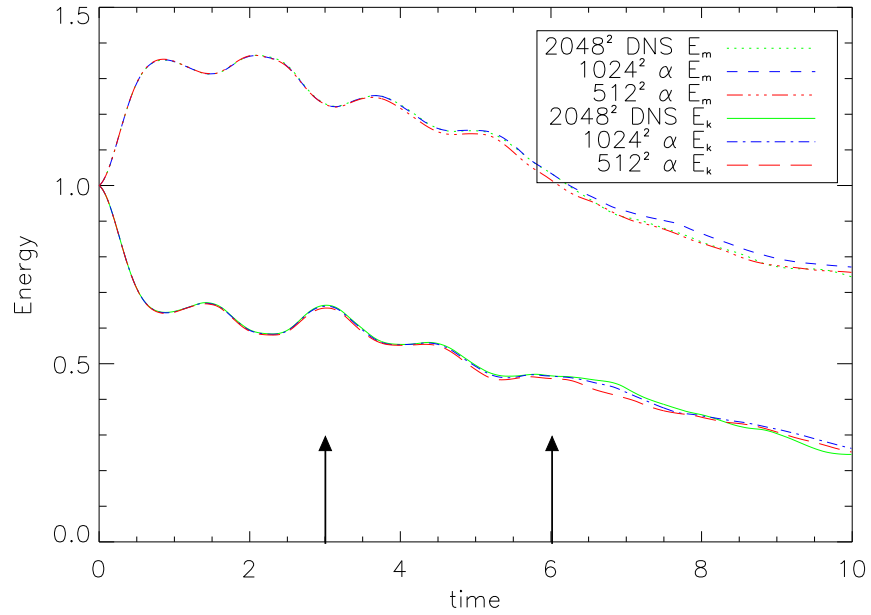


Figure 4.8: Magnetic,  $E_m(t)$ , and kinetic,  $E_k(t)$ , energies for freely decaying runs.  $E_m(t)$  for  $2048^2$  MHD is the green dotted line, for  $1024^2$  LAMHD- $\alpha$  is the blue dashed line, and for  $512^2$  LAMHD- $\alpha$  is the red dash-triple-dotted line.  $E_k(t)$  for  $2048^2$  MHD is the green solid line, for  $1024^2$   $\alpha$  is the blue dash-dot line, and for  $512^2$   $\alpha$  is the red long-dashes line. Note that the different solutions depart after the enstrophies have reached their peak (see Figure 4.9).

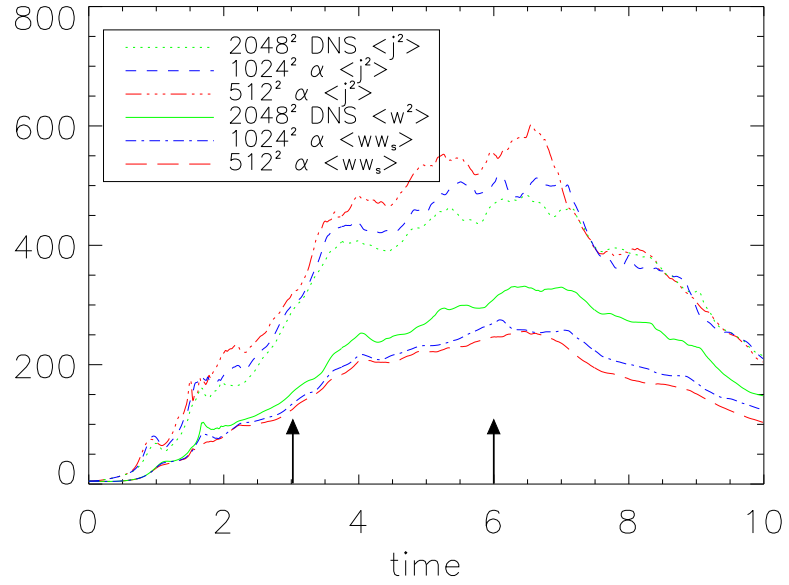


Figure 4.9: Mean square current,  $\langle j^2 \rangle$ , and mean square vorticity,  $\langle w^2 \rangle$ , for freely decaying.  $\langle j^2 \rangle$  for 2048<sup>2</sup> MHD is the green dotted line, for 1024<sup>2</sup> LAMHD- $\alpha$  is the blue dashed line, and for 512<sup>2</sup> LAMHD- $\alpha$  is the red dash-triple-dotted line.  $\langle w^2 \rangle$  for 2048<sup>2</sup> MHD is the green solid line, for 1024<sup>2</sup>  $\alpha$  is the blue dash-dot line, and for 512<sup>2</sup>  $\alpha$  is the red long-dashes line.

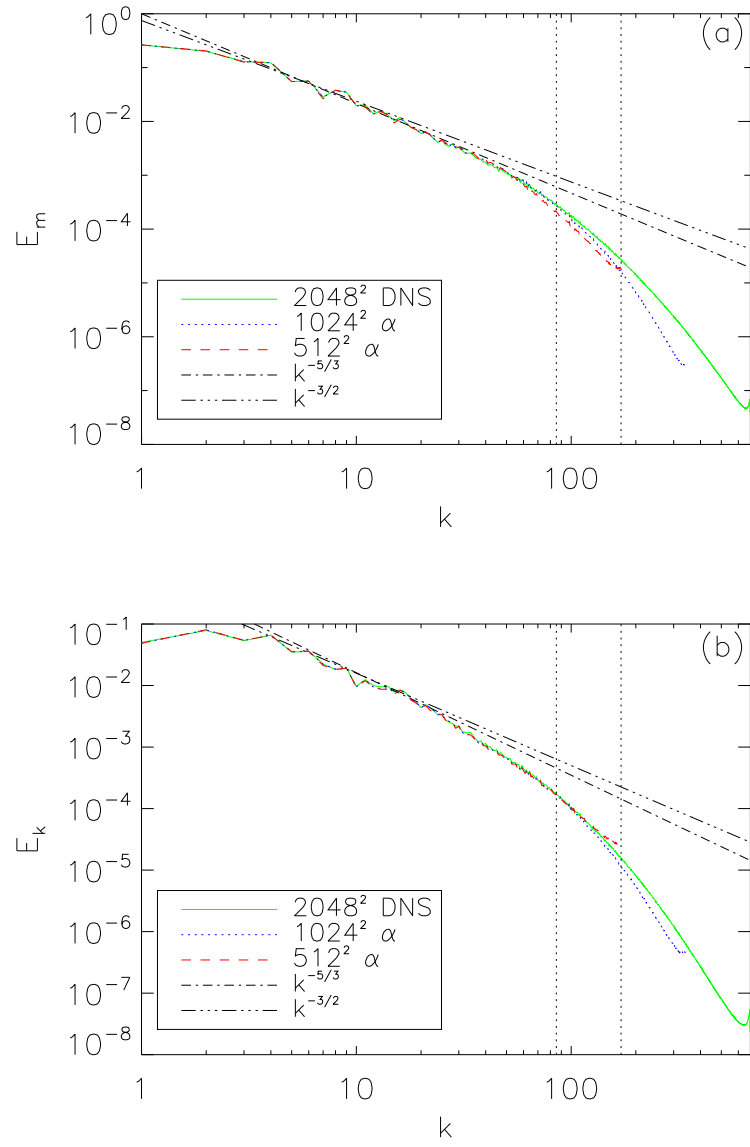


Figure 4.10: Spectra averaged from  $t = 3$  up to  $t = 6$  for freely decaying turbulence. 2048<sup>2</sup> MHD is the solid green line, 1024<sup>2</sup> LAMHD- $\alpha$  is the dotted blue line, 512<sup>2</sup> LAMHD- $\alpha$  is the dashed red line,  $k^{-5/3}$  (K41) is the dash-dot-dashed line, and  $k^{-3/2}$  (IK) is the dash-triple-dotted line. The K41 and IK slopes are shown as a reference. Vertical lines indicate the wavenumbers corresponding to the lengths  $\alpha$  for the 1024<sup>2</sup> and 512<sup>2</sup> simulations. Panel (a) is magnetic energy,  $E_m$ , versus  $k$  and panel (b) is kinetic energy,  $E_k$ , versus  $k$ .

#### 4.5.1 Flow visualizations

Plots of the stream function,  $\psi$ , and vector potential,  $a_z$ , for  $t = 4.5$  (shown in Figure 4.11), illustrate that the over-all structure of the DNS flow is preserved by LAMHD- $\alpha$ . In these plots bright yellow represents positive vector potential (or stream function) and counter-clockwise rotation of the magnetic field (velocity) while light pink represents negative values and clockwise rotations. Upon close enough inspection, some small-scale differences in the alpha model simulations can be discerned. The current (and hence the Ohmic dissipation) as well as the vorticity are shown in Figure 4.12. Here pink and white pixels indicate current (vorticity) coming out of the page while light blue and green pixels indicate current (vorticity) going into the page. The main feature of these plots are the (mostly pink) current sheets. The color scale masks all but the most strong negative current sheets. Small-scale differences are more easily observed in these plots as they emphasize more the small-scale features of the flow.

#### 4.5.2 Numerical results for intermittency and scaling anomaly

The magnetic and kinetic energy spectra between  $t = 3$  and  $t = 6$  in units of the eddy turnover time (over which the energy varies by less than 30%) display an inertial range with an extent of approximately one decade in Fourier space, from  $k \approx 3$  up to  $k \approx 30$  (see Fig. 4.10). As a result, one snapshot ( $t = 4.5$ ) of the fields in this range in time was used to compute the longitudinal structure functions. The Kolmogorov kinetic and magnetic dissipation wavenumbers  $k_\nu$  and  $k_\eta$  peaked at a value of 470, larger than the filtering wavenumber  $k_\alpha \sim 1/\alpha$  in both of the LAMHD- $\alpha$  simulations.

Both LAMHD- $\alpha$  runs preserve the scaling of the longitudinal structure function exponents observed in the DNS. As an example, Fig. 4.13 shows the  $\xi_p^+$  exponents for the  $z^+$  Elsässer variable for the DNS and LAMHD- $\alpha$  simulations using the ESS hypothesis. Note that the  $\xi_p^+$  exponents of the three simulations lie within the error bars,

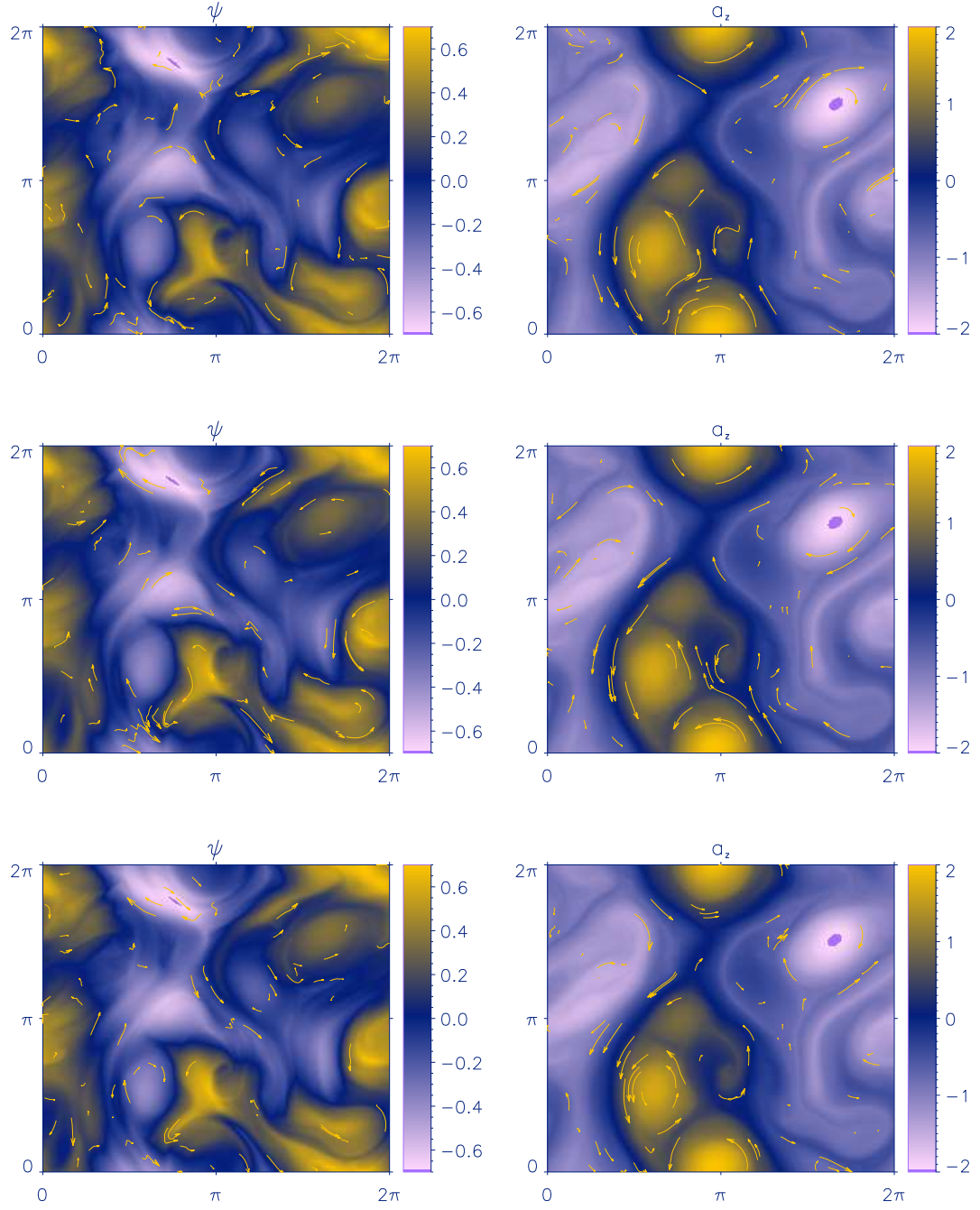


Figure 4.11: Stream function,  $\psi$ , and vector potential,  $a_z$  for freely decaying turbulence. Stream function is shown in the left column (super-imposed arrows show some velocity vectors). Vector potential is shown in the right column (super-imposed arrows show some magnetic field vectors). Snapshot is for  $t = 4.5$ . Yellow indicates positive vector potential (stream function) and counter-clockwise magnetic field (velocity) while light pink indicates negative values and clockwise flow. Top row is the  $2048^2$  DNS (MHD) run while the second and third rows are  $1024^2$  and  $512^2$  LAMHD- $\alpha$ , respectively.



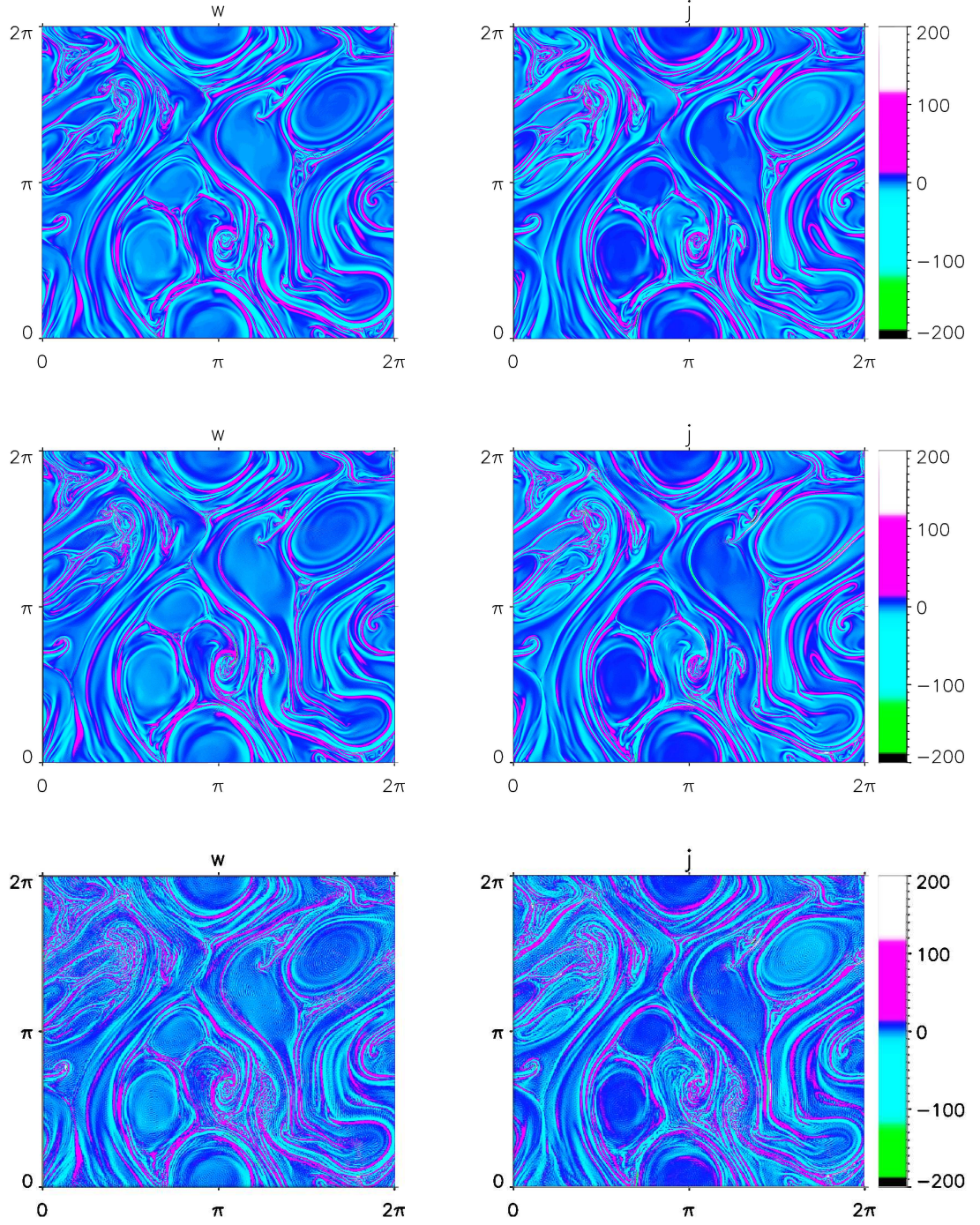


Figure 4.12: Electric current,  $j$ , and vorticity,  $w$ , for freely decaying turbulence. Vorticity is shown in the left column and current is shown in the right column. Snapshot is for  $t = 4.5$ . Pink/white indicates current/vorticity coming out of the page and light blue/green, into the page. Top row is the  $2048^2$  DNS (MHD) run while the second and third rows are  $1024^2$  and  $512^2$  LAMHD- $\alpha$ , respectively.

and the three simulations show departures from the self-similar K41 or IK scaling. For values of  $p$  larger than 6, effects associated with the limited amount of spatial statistics can be observed in all the runs.

### 4.5.3 Cancellation statistics

Fig. 4.14(a) shows  $\chi(l)$ , Eq. (4.6), for free decaying MHD turbulence. The evolution of the cancellation exponent as a function of time in the free decaying simulations is shown in Fig. 4.14(b). For these simulations, the cancellation exponent is computed between the lengthscales  $l \approx 20/2\pi$  and  $l \approx 70/2\pi$ , where a power law scaling in  $\chi(l)$  can be clearly identified from  $t = 2.5$  up to  $t = 10$ . At  $t = 0$  the cancellation exponent  $\kappa$  is zero, which corresponds to the smooth initial conditions. A gap between  $t = 0$  and  $t = 2.5$  is present where no clear scaling is observed. As time evolves,  $\kappa$  grows up to 0.75 at  $t \approx 8$ , as the system evolves from the initially smooth fields to a turbulent state with strong and localized current sheets. After this maximum, the exponent  $\kappa$  decays slowly in time. The maximum of  $\kappa$  takes place slightly later than the maximum of magnetic dissipation, as is also shown in Fig. 4.14(b). Note that the  $\alpha$ -model also captures the time evolution of the cancellation exponent in free decaying turbulence, as well as the fractal structure of the problem as time evolves.

In the three simulations the peak of magnetic dissipation takes place close to  $t \approx 6$ , just before the peak of the cancellation exponent  $\kappa$ . The observed slow decay of the cancellation exponent (compared with the mean square current) is related to the persistence of strong current sheets in the system for long times, even after the peak of magnetic dissipation. The system, instead of evolving fast to a smooth solution at every point in space, keeps dissipating energy in a few thin localized structures. The existence of these current sheets at late times can be more easily verified in simulations with smaller viscosity  $\nu$  and diffusivity  $\eta$ . While in the peak of magnetic dissipation the system is permeated by a large number of small current sheets, at late times only a few



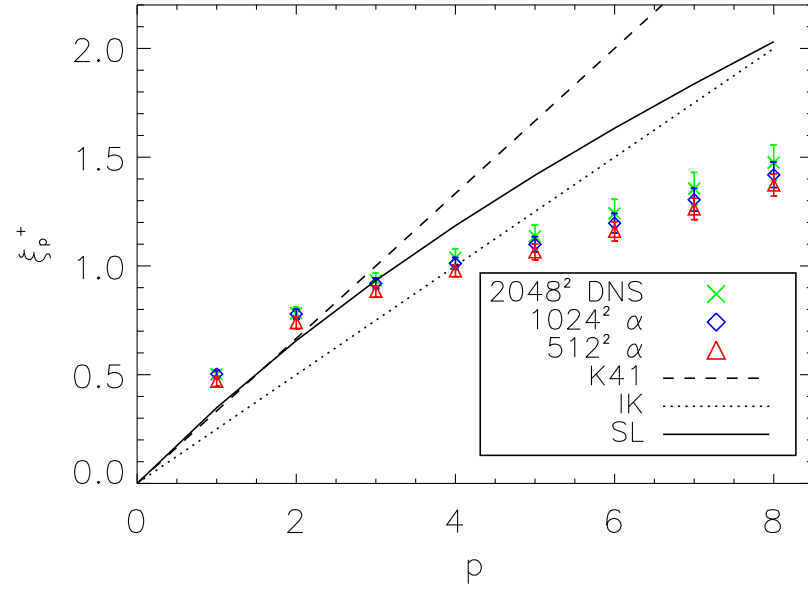


Figure 4.13: Scaling exponent  $\xi_p^+$  as a function of the order  $p$ , for the  $z^+$  Elsässer variable in simulations of freely-decaying turbulence. The DNS, the  $1024^2$  LAMHD- $\alpha$  run, and the  $512^2$  LAMHD- $\alpha$  run are denoted by green X's, blue diamonds, and red triangles respectively. The K41 scaling is the dashed line, the IK prediction is the dotted line, and the solid line corresponds to Eq. (4.22).

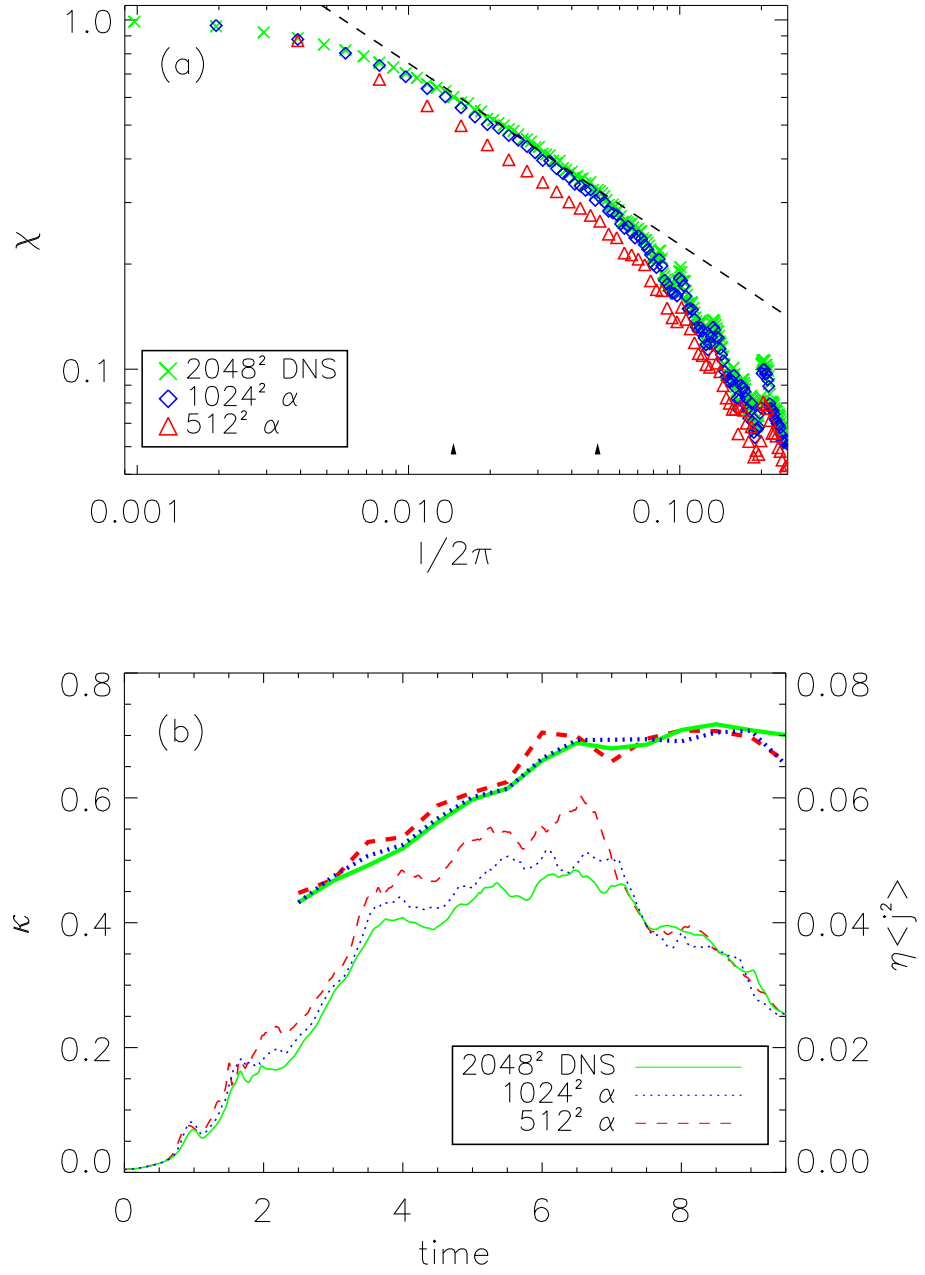


Figure 4.14: (a)  $\chi(l)$  at  $t = 4$  in the free decaying simulations. Labels are as in Fig. 4.13. The dashed line indicates a slope of 0.52 and the arrows indicate the inertial range. (b) time history of the cancellation exponent (thick lines) for the three runs, and of  $\eta \langle j_z^2 \rangle$ , where the brackets denote spatial average.

current sheets are observed isolated by large regions where the fields are smooth.

Given the good agreement between DNS and LAMHD- $\alpha$  as seen in the preceding figure, we can reliably explore with the model Reynolds numbers unattainable in a reasonable time with DNS. In this context, we show that the maximum values of  $\kappa$  obtained in the simulations seem to be insensitive to the Reynolds numbers within a given method (MHD or LAMHD- $\alpha$ ) once a turbulent state is reached. As an example, in Fig. 4.15 we give the time history of the cancellation exponent and the mean square current for a free decaying LAMHD- $\alpha$  simulation with  $\eta = \nu = 2 \times 10^{-5}$  up to  $t = 20$ . The initial conditions are the same as in the previously discussed simulations, and  $\alpha \approx 0.0033$ . It is worth noting that the time evolution of the magnetic dissipation in both decaying runs (Figs. 4.14(b) and 4.15) confirm previous results at lower Reynolds numbers [24, 203]: namely that the peak dissipation ( $t \sim 7$ ) is lower for higher Reynolds numbers, while for later times it is quite independent of the Reynolds values.

Fig. 4.16 shows  $\chi(l)$  for early and late times in the same simulation. At small scales, the slope of  $\chi$  always goes to zero, as can be expected since close to the dissipation lengthscale the fields are expected to be smooth. However, note that as time evolves the scaling of  $\chi$  with  $l$  drifts to smaller scales, and at  $t = 20$  a scaling can be observed up to  $l/L \approx 0.005$ . By virtue of the model the scaling is wider and the slope goes to zero faster than in the DNS due to the larger Reynolds number.

## 4.6 Discussion and outlook

Sufficient resolution for studying directly high Reynolds number flows as encountered in geophysics and astrophysics is today well beyond technological limits. Closures such as the LAMHD- $\alpha$  model can reduce the computational burden by reducing the resolution requirements. However, to be used as a model of hydrodynamic or magneto-hydrodynamic turbulence, or for applications in astrophysics and geophysics, detailed knowledge of the ability of the LANS- $\alpha$  or LAMHD- $\alpha$  equations to capture key fea-

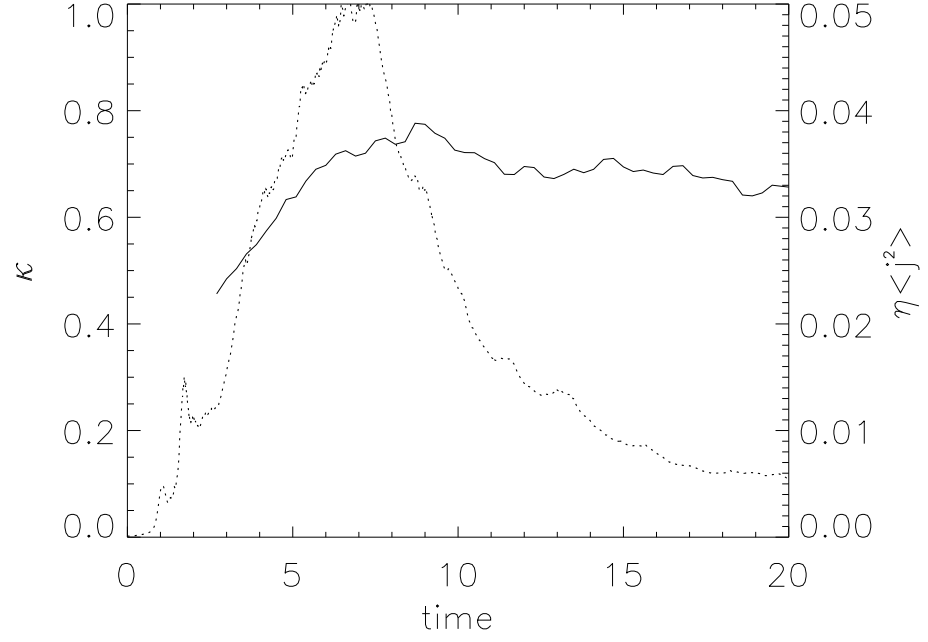


Figure 4.15: Time history of  $\kappa$  (solid line) and  $\eta \langle j_z^2 \rangle$  (dotted line), for a free decaying LAMHD- $\alpha$  simulation with  $\eta = \nu = 2 \times 10^{-5}$ .

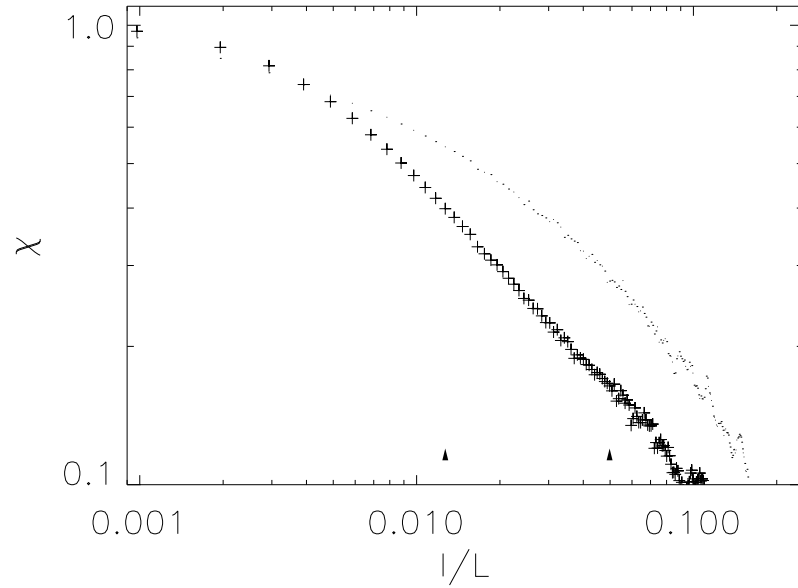


Figure 4.16:  $\chi(l)$  at  $t = 3$  (dots), and  $t = 20$  (pluses), for the free decaying LAMHD- $\alpha$  simulation with  $\eta = \nu = 2 \times 10^{-5}$ . The arrows indicate the inertial range.

tures of turbulent flows is required.

The LANS- $\alpha$  and LAMHD- $\alpha$  equations have been tested against direct numerical simulations in a variety of problems (see e.g. [56, 58] for neutral fluid studies and [173, 172, 205] for studies in conducting fluids). Most of these works compared the time evolution of ideal invariants for forced and free decaying turbulence, as well as the evolution of energy spectra. Also, some statistical comparisons were performed (e.g. studying the behavior of probability density functions). In this chapter, we applied more stringent tests to one of these models. Intermittency is a well known feature of turbulent flows, associated with the existence of strong events localized both in space and time. Intermittency can trigger large scale events, affect the transport coefficients, or give rise to corrections in the turbulent scaling. As a result, whether a model can capture the statistics of intermittent events is of utmost importance to model astrophysical or geophysical flows. The study of intermittency also requires computation of high order statistics, thereby extending previous comparisons between DNS and  $\alpha$ -models.

While LES often impose a particular regime and a power law [207, 262, 152, 1, 185, 229, 264, 206, 128], the LAMHD- $\alpha$  equations are shown to satisfy the general scalings satisfied by the MHD equations without any hypothesis about the scaling followed in the inertial range. The extension of the KH- $\alpha$  theorem to the LAMHD- $\alpha$  case (see Section 3.2.5.2) also allows us to define correlation and structure functions in the  $\alpha$ -model. With these functions, the analysis of anomalous scaling and intermittency can be performed. Numerical simulations were carried out both for freely decaying and for forced two dimensional MHD turbulence, solving directly the MHD equations, and employing the LAMHD- $\alpha$  equations at 1/2 and 1/4 resolution (a case equivalent to 1/8 of the DNS resolution was also considered for forced turbulence). In the forced runs, we have averaged statistics over 189 turn-over times (and up to  $\sim 2 \cdot 10^8$  points) to test if the LAMHD- $\alpha$  equations reproduces intermittent turbulent behavior. The scaling of the third-order structure function was tested and linear scaling with length (down

to length  $\alpha$ ) was observed, in good agreement with corollaries of the extended KH- $\alpha$  theorem and exact laws in MHD turbulence [201, 204]. The LAMHD- $\alpha$  equations also capture high-order statistics (up to and including order 8) and the anomalous scaling of the longitudinal structure function exponents, with a net gain in speed close to a factor of 16. For lower order structure functions, very little contamination of the scaling could be detected at scales larger than  $\alpha$ . On the other hand, for the highest computed order, fluctuations in the scaling are observed for the runs with the smallest resolution. Note that we would not expect any scaling to be preserved for  $\alpha$  so large that no inertial range remains.

Turbulence closures are never unique. The present case may owe its success not to its particular form, but rather to its general properties that it (1) preserves physical avenues of nonlinear energy exchange and (2) allows correct vortex stretching. These two properties derive from its origin via a Lagrangian-averaged Hamilton's principle. The derivation also identifies the appropriate dissipation for proper energy decay, which involves an enhanced resistivity, but not an enhanced viscosity. Together, the Navier-Stokes viscosity and the enhanced resistivity produce regularization (e.g., existence and uniqueness of strong solutions and their global attractor of finite Hausdorff dimension). In turn, the choices of viscosity and resistivity allow for the intermittency found here, which might have otherwise been suppressed.

The statistics of sign cancellation in MHD turbulence are related with intermittency and anomalous scaling of structure functions [235], inherently associated with the dynamics of the small scales, and as a result harder to model in truncations or closures of the MHD equations. For example, two-point closures of turbulence behave smoothly (they also have no information about physical structures since they deal only with energy spectra). A new result stemming from this study is that the LAMHD- $\alpha$  model, although it alters the small scales through filtering, it nevertheless preserves some statistical information concerning the small scales. It is able to reproduce the

scaling observed in forced MHD turbulence, as well as the time evolution of the cancellation exponent in free decaying simulations. It represents a valuable model for studies of MHD flows for example at low magnetic Prandtl number,  $P_M \equiv \nu/\eta$ , as encountered in the liquid core of the Earth or in the solar convection zone (see, e.g., [205]).

Relying on the fact that, contrary to neutral fluids, two dimensional MHD turbulence displays a direct cascade of energy and intermittency, we could show that the LAMHD- $\alpha$  equations reproduce intermittency features of turbulent flows and thus we postulate that these results will carry over to the three-dimensional case and thus these results could be also of relevance to the modeling of neutral fluids. Future challenges will include implementation of the LAMHD- $\alpha$  model in domains with boundaries and the study of intermittency for magnetic Prandtl numbers besides unity. The choices of boundary conditions may be expected to strongly influence the solution behavior. Of course, this matter is beyond the scope of this thesis.

## Chapter 5

### LANS- $\alpha$ scaling

In this chapter we compute solutions of the Lagrangian-Averaged Navier-Stokes  $\alpha$ -model (LANS- $\alpha$ ) for significantly higher Reynolds numbers (up to  $Re \approx 8300$ ) than have previously been accomplished. This allows sufficient separation of scales to observe a Navier-Stokes inertial range followed by a second inertial range specific to LANS- $\alpha$ . Both fully helical and non-helical flows are examined, up to Reynolds numbers of  $\sim 1300$ . The analysis of the third-order structure function scaling supports the predicted  $l^3$  scaling; it corresponds to a  $k^{-1}$  scaling of the energy spectrum for scales smaller than  $\alpha$ . The energy spectrum itself shows a different scaling which goes as  $k^1$ . This latter spectrum is consistent with the absence of stretching in the sub-filter scales due to the Taylor frozen-in hypothesis employed as a closure in the derivation of LANS- $\alpha$ . These two scalings are conjectured to coexist. The  $l^3$  ( $E(k) \sim k^{-1}$ ) scaling is subdominant to  $k^1$  in the energy spectrum, but the  $l^3$  scaling is responsible for the direct energy cascade, as no cascade can result from motions with no internal degrees of freedom. We demonstrate verification of the prediction for the size of the LANS- $\alpha$  attractor resulting from this scaling. From this, we give a methodology either for arriving at grid-independent solutions for LANS- $\alpha$ , or for obtaining a formulation of a Large Eddy Simulation (LES) optimal in the context of the alpha models. The fully-converged grid-independent LANS- $\alpha$  may not be the best approximation to a direct numerical simulation of the Navier-Stokes equations since the minimum error is a



balance between truncation errors and the approximation error due to using LANS- $\alpha$  instead of the primitive equations. Furthermore, the small-scale behavior of LANS- $\alpha$  contributes to a reduction of flux at constant energy, leading to a shallower energy spectrum for large  $\alpha$ . These small-scale features, however, do not preclude LANS- $\alpha$  to reproduce correctly the intermittency properties of the high Reynolds number flow.

## 5.1 Introduction

LANS- $\alpha$  and a related regularization, the Leray model, were contrasted with a dynamic eddy-viscosity model in a turbulent mixing shear layer ( $Re \approx 50$ ) [87, 90]. LANS- $\alpha$  was the most accurate of these three LES at proper subgrid resolution, but the effects of numerical contamination can be strong enough to lose most of this potential. This could pose some limitations on its practical use. Quantifying those limitations is one of the goals of this present work.

The  $\alpha$ -model also describes an incompressible second-grade non-Newtonian fluid (under a modified dissipation) [77]. In this interpretation,  $\alpha$  is a material parameter which measures the elastic response of the fluid. Either from this standpoint, from its status as a regularization of the Navier-Stokes equations, or, independently of any physically motivation, as a set of partial differential equations with proven unique regular solutions, we may analyze LANS- $\alpha$  without any LES considerations. Analyzing inertial-range scaling for LANS- $\alpha$  for moderate and large  $\alpha$ , as well as identifying different scalings at scales larger and smaller than  $\alpha$  is another of the goals of this work. In this context we also study the numerical resolution requirements to obtain well-resolved solutions of LANS- $\alpha$  (i.e., grid-independent solutions) which leads to a verification of the predictions of the size of the attractor in LANS- $\alpha$  [77, 91]. Section 6.3 presents the LANS- $\alpha$  model, our numerical experiments and technique. In Section 5.3 we analyze inertial-range scaling for LANS- $\alpha$ . In Section 5.4 we determine the numerical resolution requirements to obtain well-resolved solutions of LANS- $\alpha$ . In Section 5.5

we address the LES potential of LANS- $\alpha$  by comparing  $\alpha$ -model simulations to a  $256^3$  DNS ( $Re \approx 500$ ,  $R_\lambda \approx 300$ ),<sup>1</sup> a  $512^3$  DNS ( $Re \approx 670$ ,  $R_\lambda \approx 350$ ), a  $512^3$  DNS ( $Re \approx 1300$ ,  $R_\lambda \approx 490$ ),<sup>2</sup> a  $1024^3$  DNS ( $Re \approx 3300$ ,  $R_\lambda \approx 790$ ),<sup>3</sup> and a  $2048^3$  DNS ( $Re \approx 8300$ ,  $R_\lambda \approx 1300$ ).<sup>4</sup> (The  $Re \approx 3300$  simulation has been previously described in a study of the imprint of large-scale flows on local energy transfer [2, 169].) In Section 5.6, we compare and contrast in more detail LANS- $\alpha$  solutions with DNS at  $Re \approx 3300$ . Finally, in Section 5.7 we summarize our results, present our conclusion, and propose future directions of investigation.

## 5.2 Technique

We consider the incompressible Navier-Stokes equations for a fluid with constant density,

$$\begin{aligned} \partial_t v_i + v_j \partial_j v_i &= -\partial_i p + \nu \partial_{jj} v_i + F_i \\ \partial_i v_i &= 0, \end{aligned} \tag{5.1}$$

$$v_i = (1 - \alpha^2 \partial_{jj}) u_i, \tag{5.2}$$

where  $v_i$  denotes the component of the velocity field in the  $x_i$  direction,  $p$  the pressure divided by the density,  $\nu$  the kinematic viscosity, and  $F_i$  an external force that drives the turbulence (in all results, the time,  $t$ , is expressed in units of the eddy-turnover time). The LANS- $\alpha$  equations [113, 55, 57, 58, 56, 77] are given by

$$\begin{aligned} \partial_t v_i + u_j \partial_j v_i + v_j \partial_i u_j &= -\partial_i \pi + \nu \partial_{jj} v_i + F_i \\ \partial_i v_i &= \partial_i u_i = 0, \end{aligned} \tag{5.3}$$

---

<sup>1</sup> One turnover time took 8.3 minutes on 32 Opteron 2.2 GHz processors.

<sup>2</sup> One turnover time took 70 minutes on 96 Opteron 2.2 GHz processors.

<sup>3</sup> One turnover time took 15 hours on 256 IBM POWER4 1.3 GHz processors and the code sustained 0.12 TFLOPS.

<sup>4</sup> One turnover time took 9.4 hours on 2048 (2.6 GHz AMD Dual core) processors on a Cray XT3 and the code sustained 3 TFLOPS.

where  $u_i$  denotes the filtered component of the velocity field and  $\pi$  the modified pressure. Filtering is accomplished by the application of a normalized convolution filter  $L : f \mapsto \bar{f}$  where  $f$  is any scalar or vector field. By convention, we define  $u_i \equiv \bar{v}_i$ . We choose as our filter the inverse of a Helmholtz operator,  $L = \mathcal{H}^{-1} = (1 - \alpha^2 \partial_{kk})^{-1}$ . Therefore,  $\mathbf{u} = g_\alpha \otimes \mathbf{v}$  where  $g_\alpha$  is the Green's function for the Helmholtz operator,  $g_\alpha(r) = \exp(-r/\alpha)/(4\pi\alpha^2 r)$  (i.e., the well-known Yukawa potential), or in Fourier space,  $\hat{\mathbf{u}}(k) = \hat{\mathbf{v}}(k)/(1 + \alpha^2 k^2)$ .

We solve Eqs. (5.2) and (5.3) using a parallel pseudospectral code [81, 93] in a three-dimensional (3D) cube with periodic boundary conditions. In most of the runs, we employ a Taylor-Green forcing [228],

$$F = \begin{bmatrix} \sin k_0 x \cos k_0 y \cos k_0 z \\ -\cos k_0 x \sin k_0 y \cos k_0 z \\ 0 \end{bmatrix} \quad (5.4)$$

(generally, with  $k_0 = 2$ ), and employ dynamic control [174] to maintain a nearly constant energy with time. This expression Eq. (5.4) is not a solution of the Euler's equations, and as a result small scales are generated fast when the fluid is stirred with this forcing. That is, when substituted for  $\mathbf{v}$ , Eq. (5.4) does not solve the Euler's equations. Expanding the velocity response in time, the leading order will be proportional to the forcing and this motion rapidly excites smaller scale motions (see [228]). The resulting flow models the fluid between counter-rotating cylinders [30] and has been widely used to study turbulence, including studies in the context of the generation of magnetic fields through dynamo instability [205]. We also consider some runs with random and ABC [169] forcing. We define the Taylor microscale as  $\lambda = 2\pi\sqrt{\langle v^2 \rangle / \langle \omega^2 \rangle}$ , and the mean velocity fluctuation as  $v_{rms} = (2 \int_0^\infty E(k) dk)^{1/2}$ . The Taylor microscale Reynolds number is defined by  $R_\lambda = v_{rms} \lambda / \nu$  and the Reynolds number based on a unit length is  $Re = v_{rms} \cdot 1 / \nu$ .

### 5.3 Inertial range scaling of LANS- $\alpha$

#### 5.3.1 $l^3$ scaling of third-order structure function derived from the Kármán-Howarth theorem for LANS- $\alpha$

For LANS- $\alpha$ , the  $H_\alpha^1(u)$  norm is the quadratic invariant to be identified with the energy,

$$\frac{dE_\alpha}{dt} = -2\nu\Omega_\alpha, \quad (5.5)$$

where

$$E_\alpha = \frac{1}{D} \int_D \frac{1}{2} (\mathbf{u} - \alpha^2 \nabla^2 \mathbf{u}) \cdot \mathbf{u} d^3x = \frac{1}{D} \int_D \frac{1}{2} \mathbf{v} \cdot \mathbf{u} d^3x, \quad (5.6)$$

and

$$\Omega_\alpha = \frac{1}{D} \int_D \frac{1}{2} \boldsymbol{\omega} \cdot \bar{\boldsymbol{\omega}} d^3x. \quad (5.7)$$

As usual, we define the (omni-directional) spectral energy density,  $E_\alpha(k)$ , from the relation

$$E_\alpha = \int_0^\infty \oint E_\alpha(\mathbf{k}) d\sigma d\mathbf{k} = \int_0^\infty E_\alpha(k) dk \quad (5.8)$$

where  $\oint d\sigma$  represents integration over the surface of a sphere. The  $\alpha$ -model possesses a theorem corresponding to the Kármán-Howarth theorem for the Navier-Stokes equations and, as in the Navier-Stokes case, scaling of the inertial range energy spectra may be derived from it [109]. We summarize here the dimensional analysis argument for the LANS- $\alpha$  inertial range scaling that follows from this theorem, beginning from Equation (3.8) in Ref. [109]. We use the short notation  $v_i \equiv v_i(\mathbf{x})$ ,  $u'_i \equiv u'_i(\mathbf{x}', t)$  and  $\mathbf{r} \equiv \mathbf{x}' - \mathbf{x}$ . In the statistically isotropic and homogeneous case, without external forces and with  $\nu = 0$ , taking the dot product of Eq. (5.3) with  $u'_j$  we can obtain the equation

$$\partial_t \mathcal{Q}^\alpha_{ij} = \frac{\partial}{\partial r^m} (\mathcal{T}^{\alpha m}_{ij} - \alpha^2 \mathcal{S}^{\alpha m}_{ij}). \quad (5.9)$$

The trace of this equation is the Fourier transform of the detailed energy balance for LANS- $\alpha$ .

$$\mathcal{Q}^\alpha_{ij} = \langle v_i u'_j + v_j u'_i \rangle \quad (5.10)$$

is the second-order correlation tensor while

$$\mathcal{T}_{ij}^{\alpha m} = \left\langle (v_i u'_j + v_j u'_i + v'_i u_j + v'_j u_i) u^m \right\rangle, \quad (5.11)$$

and

$$\mathcal{S}_{ij}^{\alpha m} = \left\langle (\partial_m u_l \partial_i u_l) u'_j + (\partial_m u_l \partial_j u_l) u'_i + (g_\alpha \otimes \tau_j^m) v_i + (g_\alpha \otimes \tau_i^m) v_j \right\rangle, \quad (5.12)$$

are the third-order correlation tensors for LANS- $\alpha$  and  $\tau_i^j$  is the sub-filter scale stress tensor. For  $\alpha = 0$  this reduces to the well-known relation derived by Kármán and Howarth. The energy dissipation rate for LANS- $\alpha$ ,  $\varepsilon_\alpha$ , satisfies  $\varepsilon_\alpha \propto \partial_t \mathcal{Q}_{ij}^\alpha$ . By dimensional analysis in Eq. (5.9) we arrive at

$$\varepsilon_\alpha \sim \frac{1}{l} (v u^2 + \frac{\alpha^2}{l^2} u^3). \quad (5.13)$$

For large scales such that  $l \gg \alpha$ , the second right hand term is ignored,  $\mathbf{u} \approx \mathbf{v}$ ,  $\varepsilon_\alpha \approx \varepsilon$ , and we arrive at the scaling of the four-fifths law,  $\langle (\delta v_\parallel(l))^3 \rangle \sim \varepsilon l$  [80]. Here,  $\delta v_\parallel(l) \equiv [\mathbf{v}(\mathbf{x} + \mathbf{l}) - \mathbf{v}(\mathbf{x})] \cdot \mathbf{l}/l$  is the longitudinal increment of  $\mathbf{v}$ . The four-fifths law expresses that the third-order longitudinal structure function of  $\mathbf{v}$ ,  $S_3^v \equiv \langle (\delta v_\parallel)^3 \rangle$ , is given in the inertial range in terms of the mean energy dissipation per unit mass  $\varepsilon$  by

$$S_3^v = -\frac{4}{5} \varepsilon l, \quad (5.14)$$

or, equivalently, that the flux of energy across scales in the inertial range is constant. We also obtain the Kolmogorov 1941 [131, 130, 129] (hereafter, K41) energy spectrum,  $E(k)k \sim v^2 \sim \varepsilon^{2/3} l^{2/3}$ , or, equivalently,

$$E(k) \sim \varepsilon^{2/3} k^{-5/3}. \quad (5.15)$$

For small scales such that  $\eta_K \ll l \ll \alpha \ll l_F$ , however,  $v \sim \alpha^2 l^{-2} u$  and both right hand terms are equivalent in Eq. (5.13), and our scaling law becomes

$$S_3^u \equiv \langle (\delta u_\parallel(l))^3 \rangle \sim \varepsilon_\alpha \alpha^{-2} l^3. \quad (5.16)$$

With sufficient scale separation, both scalings, Eqs. (5.14) and (5.16), can be observed (see Fig. 5.16). Note that this scaling differs in a substantial way from the Kolmogorov scaling ( $\sim l$ ). For our small scale energy spectrum we then have

$$E_\alpha(k)k \sim uv \sim \varepsilon_\alpha^{2/3} \alpha^{2/3}, \quad (5.17)$$

where we used  $u \sim \alpha^{-2} l^2 v$ . The energy spectrum for scales smaller than  $\alpha$  is then

$$E_\alpha(k) \sim \varepsilon_\alpha^{2/3} \alpha^{2/3} k^{-1}. \quad (5.18)$$

This spectrum can also be derived from phenomenological arguments originally introduced by Kraichnan [134], and it differs from the Navier-Stokes spectrum due to the fact that the fluid is advected by the smoothed velocity  $\mathbf{u}$  which does not directly correspond to the conserved energy  $E_\alpha$  [77].

We test this prediction for LANS- $\alpha$  scaling at a resolution of  $256^3$  ( $\nu = 1.2 \cdot 10^{-4}$ ) by moving both the forcing ( $k_0 = 1$ ) and  $\alpha$  ( $k_\alpha \equiv 2\pi/\alpha = 3$ ) to large scales in order to increase the number of resolved scales for which  $k\alpha > 1$ . In so doing, we are assuming that the scaling for large  $\alpha$  is the same as for small  $\alpha$  and large  $k$  (for evidence to this effect, see [153]). Confirmation as given by Eq. (5.16) is presented in Fig. 5.1 where we plot  $S_3^u$  as a function of  $l$  (by convention, we plot  $S_3^u = \langle |\delta u_\parallel(l)|^3 \rangle$  to reduce cancellation in the statistics). The scales identified with an inertial range  $k \in [6, 10]$  are marked by vertical dashed lines and the predicted scaling,  $l^3$ , is indicated by a solid line. We fit a scaling exponent ( $S_3^u(l) \sim l^{\zeta_3^u}$ ) and find  $\zeta_3^u = 2.39 \pm .04$ . This is significantly steeper than the classical Kolmogorov scaling given by Eq. (5.14); it can thus be viewed as more consistent with the scaling given by Eq. (5.16). It is also more consistent with  $l^3$  than with other possible LANS- $\alpha$  scalings: under the assumption that the turnover time scale of eddies of size  $\sim l$  is determined by the unsmoothed velocity  $\mathbf{v}$ , we find  $S_3^u(l) \sim l^5$ , and if it is determined by  $\sqrt{\mathbf{v} \cdot \mathbf{u}}$ , we find  $S_3^u(l) \sim l^4$  (see, e.g., Refs. [153, 42, 60, 124]). The observed scaling corresponds to none of these cases,

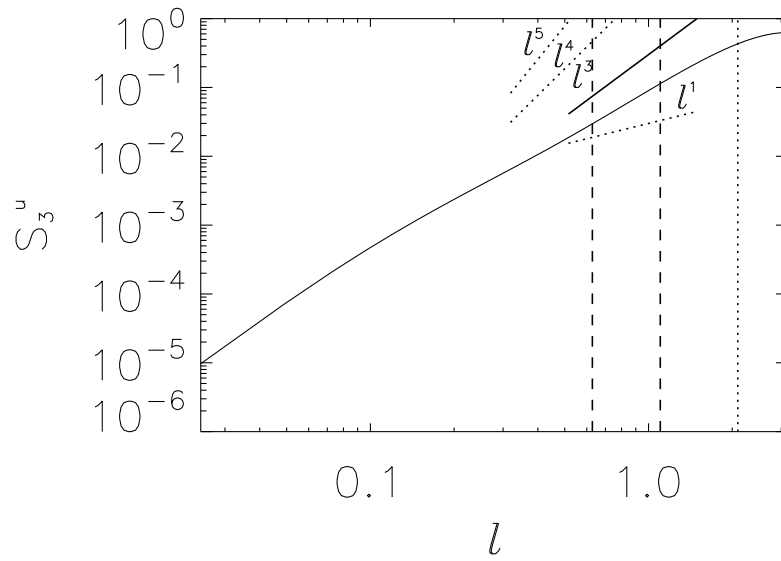


Figure 5.1: Third-order longitudinal structure function of the smoothed velocity field  $\mathbf{u}$ ,  $S_3^u$ , versus  $l$  for large  $\alpha$  LANS- $\alpha$  ( $\alpha = 2\pi/3$  indicated by the vertical dotted line). The scales identified with an inertial range are marked by vertical dashed lines and the scaling predicted by Eq. (5.16),  $l^3$ , is indicated by a solid line. The fitted scaling exponent  $\zeta_3^u$  ( $S_3^u(l) \sim l^{\zeta_3^u}$ ) is found to be  $\zeta_3^u = 2.39 \pm .04$ . This is more consistent with the scaling given by Eq. (5.16) than K41 scaling,  $l^1$  Eq. (5.14), or other proposed LANS- $\alpha$  scalings (indicated by dotted lines, see text).

and is actually closer to an evaluation of the turnover time  $t_l$  at the scale  $l$  given by  $t_l \sim l/u_l$  (with  $S_3^u(l) \sim l^3$ ). Note that for 2D LANS- $\alpha$ , however, it is the case that the scaling is determined by the unsmoothed velocity  $\mathbf{v}$  [153]. We note that this is one of many differences between the 2D and 3D cases (e.g., ideal invariants and cascades). Another difference, which we shall show in Section 5.6, is that in 2D vorticity structures decrease in scale as  $\alpha$  increases while in 3D there is a change in aspect ratio with structures getting both shorter and fatter. This may, in fact, be related to the shallower LANS- $\alpha$  energy spectrum for  $k\alpha > 1$  which we show in Section 5.6. While differences are observed between the scaling shown in Fig. 5.1 and Eq. (5.16), the error bars deny a K41 scaling (as well as the  $l^4$  and  $l^5$  scalings) at scales smaller than  $\alpha$ . We believe the discrepancy between the observed and predicted scaling can be due to lack of resolution to resolve properly the inertial range at sub-filter scales. We have less than a decade of inertial range and only  $256^3$  points for the statistics. As more computational resources become available, this scaling should be re-examined.

### 5.3.2 Subdominance of the $k^{-1}$ energy spectrum and rigid-body motions

As a consequence of LANS- $\alpha$ 's Taylor's frozen-in hypothesis closure, scales smaller than  $\alpha$  can phase-lock into coherent structures and be swept along by the larger scales (see, e.g., [109]). If we assume, formally, that this "frozen-in turbulence" takes the form of "rigid bodies" in the smoothed velocity field (no stretching), we arrive at a much different spectrum than  $k^{-1}$ , Eq. (5.18). All scales smaller than  $\alpha$  are subject to the frozen-in hypothesis and we expect to find such rigid bodies at these scales. We note that collections of "rigid" portions of the flow (rotating or non-rotating) reduce the total degrees of freedom (*dof*) and make physical sense with LANS- $\alpha$ 's relation to second-grade fluids: these rigid bodies can be envisioned as polymerized portions of the fluid. As a matter of fact, in such structures all internal *dof* are frozen. These "rigid bodies" follow as well from the consideration of LANS- $\alpha$  as an initial value problem in



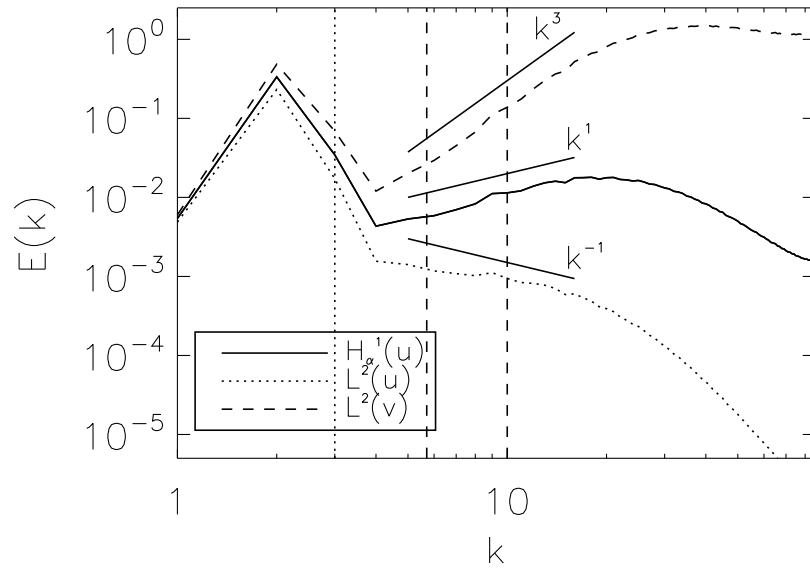


Figure 5.2: Spectral energy density,  $E(k)$ , versus wavenumber,  $k$ , for large- $\alpha$  LANS- $\alpha$  solution. Here forcing ( $k_0 = 1$ ) and  $\alpha$  ( $k_\alpha = 3$ , vertical dotted line) are set at the largest scales to increase the number of scales for which  $k\alpha > 1$ . Spectra are plotted for three norms:  $H_\alpha^1(u)$  norm (solid line),  $L^2(u)$  norm (dotted line), and the  $L^2(v)$  norm (dashed line). As these last two norms are not quadratic invariants of LANS- $\alpha$ , we employ the  $H_\alpha^1$  norm for all following results. All three spectra correspond to that derived from the assumption of rigid bodies in the smoothed velocity  $\mathbf{u}$ , Eq. (5.20). The vertical dashed lines are at the same scales as those in Fig. 5.1.

Fourier space, for which we have  $\hat{\mathbf{u}}(k) = \hat{\mathbf{v}}(k)/(1 + \alpha^2 k^2)$ . In the limit as  $\alpha$  approaches infinity, all wavenumber (and spatial) dependence for  $\bar{\mathbf{v}}$  is eliminated and the entire flow is advected with by an uniform velocity field (rigid body motion).

For a rigid body there can be no stretching and, therefore, all the longitudinal velocity increments,  $\delta u_{\parallel}$ , must be identically zero ( $\delta \mathbf{u}(\mathbf{l}) = \mathbf{\Omega} \times \mathbf{l}$  from basic mechanics with  $\mathbf{\Omega}$  the rotation vector and, hence,  $\delta u_{\parallel}(\mathbf{l}) = \delta \mathbf{u}(\mathbf{l}) \cdot \mathbf{l}/l = 0$ ). Note that in LANS- $\alpha$  Eq. (5.3) the  $v_j \partial_i u_j$  term contributes only a rotation and not a stretching of  $\mathbf{u}$ . Such polymerization would have two consequences. Firstly, since there is no stretching, these rigid bodies would not contribute to the turbulent energy cascade,

$$\langle (\delta u_{\parallel}(\mathbf{l}))^3 \rangle = 0. \quad (5.19)$$

Secondly, the energy spectrum from dimensional analysis ( $u^2 \sim \text{const}$ , for large  $\alpha/l$ :  $u = (1 + \alpha^2/l^2)^{-1}v \sim l^2v$ , and  $E_{\alpha}(k)k \sim uv \sim k^2$ ) is

$$E_{\alpha}(k) \sim k. \quad (5.20)$$

This is, in fact, the observed LANS- $\alpha$  spectrum for  $k\alpha \gg 1$  as is shown in Fig. 5.2. We verified that the spectrum is not the result of under-resolved runs, as is the case, e.g., in the  $k^2$  spectrum observed in truncated Euler systems [62] or in extremely under-resolved spectral simulations of the Navier-Stokes equations. Indeed, equipartition of the energy among all modes in a truncated Euler- $\alpha$  system should also lead to a  $k^2$  spectrum. Along with several experiments with different viscosities and also with statistically homogeneous and isotropic forcing (not shown here), these are assurances that the observed spectrum is not a result of inadequate numerical resolution. It should be noted that this is the same computation for which the third-order structure function is shown in Fig. 5.1. The third-order structure function is consistent with a  $l^3$  scaling (corresponding to a  $k^{-1}$  energy spectrum) while the spectrum itself is  $k^1$ . (Also shown in Fig. 5.2 are the  $L^2(u) \equiv \langle u^2 \rangle/2$  and the  $L^2(v) \equiv \langle v^2 \rangle/2$  norms which (through  $u \sim$

$\alpha^2\nu/k^2$  for  $k\alpha \gg 1$ ) correspond to  $k^{-1}$  and  $k^3$  spectra, respectively. Since the analytical properties of the LANS- $\alpha$  solution are based on the energy balance,  $dE_\alpha/dt = -2\nu\Omega_\alpha$ , in the  $H_\alpha^1(u)$  norm, we employ this norm for all following results.) These two different scalings,  $l^3$  and  $k^1$ , are consistent with a picture where a fluid has both rigid-body portions at scales smaller than  $\alpha$  (wherein there is no turbulent cascade) and spatial regions between these where the cascade does take place. For the structure functions, a non-cascading rigid body does not contribute to the scaling and consequently the cascading contribution, Eq. (5.16), dominates. The energy spectrum, however, for the limit of  $k$  very large, is dominated by the  $k^{+1}$  term, and hence the  $k^{-1}$  component is subdominant.

We further explore the validity of this picture by examining the spatial variation of the cubed longitudinal increment,  $(\delta v_\parallel(l))^3$  in DNS, and  $(\delta u_\parallel(l))^3$  in LANS- $\alpha$  for  $\alpha/l \gg 1$ , which in each case is proportional to the energy flux across a fixed scale  $l$ . (The presence of the hypothesized “rigid bodies” should be evident as significant portions of the flow where there is no energy flux.) In Fig. 5.3 we show visualizations of these quantities corresponding to  $l = 2\pi/10$  ( $k = 10$ ) for both the large- $\alpha$  LANS- $\alpha$  simulation and a highly turbulent DNS ( $k_0 = 2$ ,  $\nu = 3 \cdot 10^{-4}$ ). The scale ( $k = 10$ ) is chosen as it is in the inertial ranges of both flows. We note that for LANS- $\alpha$ , a significant portion of the flow is not contributing to the flux of energy to smaller scales (the filling factor for  $(\delta u_\parallel(2\pi/10))^3 < 10^{-2}$  is 0.67 as compared to 0.26 for the Navier-Stokes case). These regions can be identified as “polymerized” or “rigid bodies” in  $\mathbf{u}$  and their locations are found to be robust when the  $l$  used for  $(\delta u_\parallel(l))^3$  is varied over a factor of 2. Moreover, this is highlighted in the probability distribution functions (*pdfs*), see Fig. 5.4, where we see the LANS- $\alpha$  *pdf* is more strongly concentrated around zero than the DNS. This is consistent with the idea that the internal *dof* of large portions of the flow (at scales smaller than  $\alpha$ ) are frozen. We point out that this comparison is not a LES validation, but, rather, a comparison between the dynamics of two different

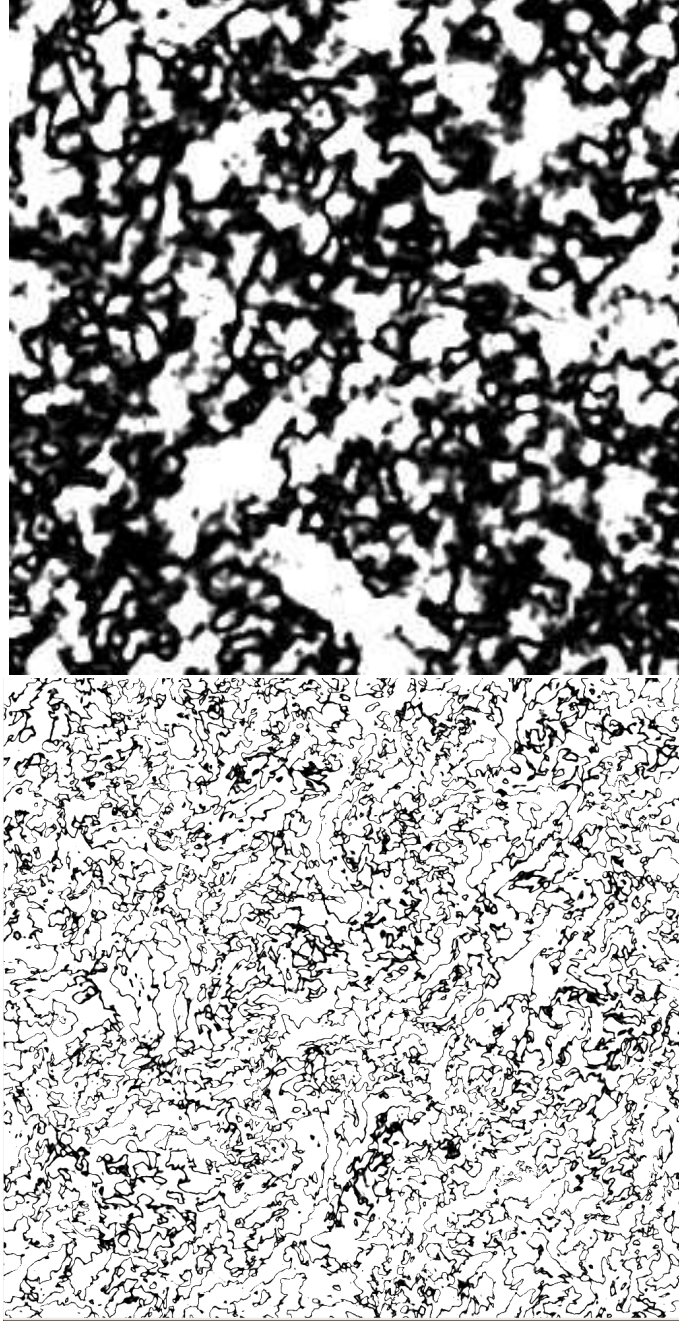


Figure 5.3: Two-dimensional slice of the cubed longitudinal increment  $(\delta u_{\parallel}(2\pi/10))^3$  for LANS- $\alpha$  and  $(\delta v_{\parallel}(2\pi/10))^3$  for DNS. For all black pixels, the cubed longitudinal increment is less than  $10^{-2}$  (approximately consistent with rigid bodies). On the top is the large- $\alpha$  simulation ( $k_0 = 1$ ,  $k_{\alpha} = 3$ ,  $\nu = 1.2 \cdot 10^{-4}$ ) where the filling factor (computed over the entire 3D domain) is 0.67. On the bottom is a DNS of Navier-Stokes ( $k_0 = 2$ ,  $\nu = 3 \cdot 10^{-4}$ ) where the filling factor is 0.26. Thus, a much greater portion of the flow is consistent with collections of rigid bodies for the large- $\alpha$  simulation.

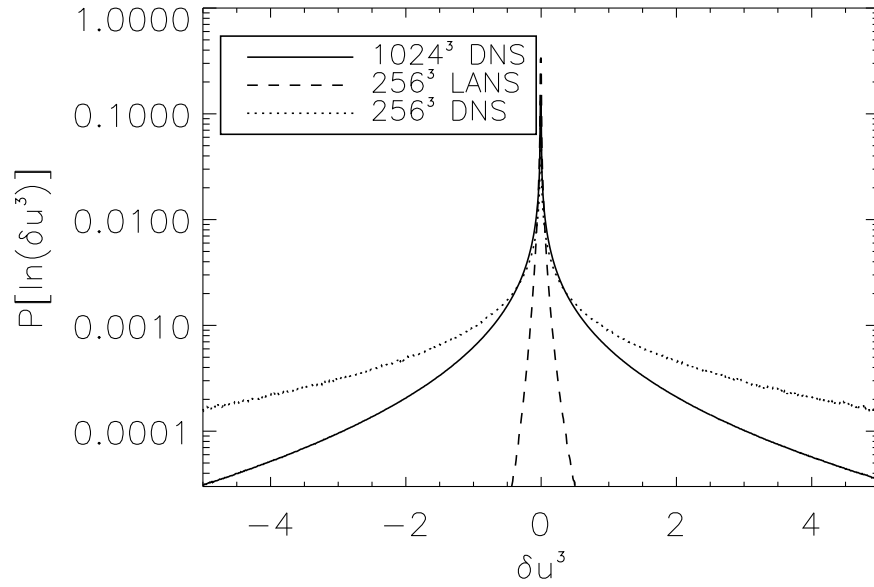


Figure 5.4: Pdfs of  $(\delta v_{\parallel}(2\pi/10))^3$  for DNS ( $N = 1024$ , solid line), and of  $(\delta u_{\parallel}(2\pi/10))^3$  for LANS- $\alpha$  ( $N = 256$ , dashed line), and of the DNS downgraded to lower resolution ( $N = 256$ , dotted line). See Fig. 5.3 for simulation parameters. Note that both *pdfs* have a slight positive asymmetry consistent with a positive dissipation rate  $\varepsilon_{(\alpha)}$ . The LANS- $\alpha$  *pdf* is more strongly concentrated around zero consistent with the idea that portions of the flow (at scales smaller than  $\alpha$ ) are acting as rigid bodies.

fluids at similar Reynolds numbers. One flow is a well-resolved numerical solution of the Navier-Stokes equations, and the other is a well-resolved solution of the LANS- $\alpha$  equations with large  $\alpha$ . For this reason a reduced resolution ( $N = 256$ ) representation for the DNS (for which  $N = 1024$ ) is not depicted in Fig. 5.3. We have performed such a down-sampling, however, and find the filling factor is reduced even more, to 0.14, and the tails of the *pdf* increase over the full-resolution analysis (dotted line in Fig. 5.4). No inverse Helmholtz filtering,  $\mathcal{H}^{-1}$  is applied to the DNS data. Note that this would amount to computing  $(\delta u_{\parallel}(l))^3$  in the DNS, which has no meaning in the dynamics of the Navier-Stokes equations (the energy flux is proportional to  $(\delta v_{\parallel}(l))^3$ ).

We end this section with further evidence of coexistent energy spectra,  $k^{-1}$  and  $k^1$ , in separate spatial portions of the flow. We mask out all portions of the flow that we identify with rigid bodies  $((\delta u_{\parallel}(2\pi/10))^3 < 10^{-2})$ , a 2D slice of which is shown in Fig. 5.3). The energy spectrum of the remaining portion of the flow is shown in Fig. 5.5 as a dashed line to be compared with the spectrum of the entire flow shown as a solid line. The operation of spatially filtering the flow before computing the spectrum serves to “smear out” the energy spectrum by convolving it with the spectrum of the filter. Deconvolution in 3D with  $N = 256$  is intractable and we are, therefore, unable to remove this “smearing” of the energy spectrum of the cascading portions of the flow. Nonetheless, after conducting what tests we could with the filtering process (not shown here), we conclude that the power law of the energy spectrum of these portions is negative and, thus, distinctly different from that of the rigid bodies.

#### 5.4 Resolution requirements for grid-independent LANS- $\alpha$ solutions: Size of attractor

It is useful to make a distinction between the quality of a subgrid model and effects arising from nonlinear interactions with discretization errors at marginal spatial resolutions (which are more characteristic of the discretization employed than of the

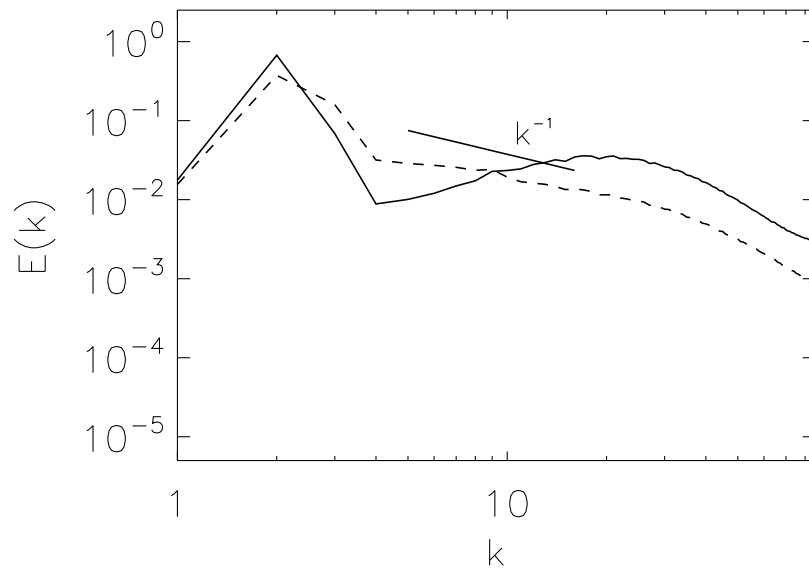


Figure 5.5: Spectral energy density,  $E(k)$ , versus wavenumber,  $k$ , for large- $\alpha$  LANS- $\alpha$  solution. The solid line indicates the spectrum as given in Fig. 5.2 but for a single snapshot (the same as selected for Fig. 5.3). The dashed line indicates the spectrum wherein all portions of the flow associated with “rigid bodies” (a 2D slice of which is shown in Fig. 5.3) are removed. This provides further evidence that the flow spatially in between the “rigid bodies” possesses a negative power law energy spectrum (the predicted  $k^{-1}$  power law is shown as a thick solid line).

subgrid model) [86, 163, 90]. Before doing this, we require an estimate for the total degrees of freedom for the LANS- $\alpha$  attractor which as we show, unlike for the 2D case (see [153]), for the 3D case is reduced compared to Navier-Stokes. The subdominant  $l^3$  scaling is associated with the flux of energy to small scales and thus must be used to estimate the degrees of freedom of the LANS- $\alpha$  attractor,  $dof_\alpha$ . For dissipation the large wavenumbers dominate and, therefore, combining the LANS- $\alpha$  energy balance, Eq. (5.5), with its sub-filter scale energy spectrum, Eq. (5.18), allows us to implicitly specify its dissipation wavenumber,  $k_\eta^\alpha$ , by

$$\frac{\varepsilon_\alpha}{\nu} \sim \int^{k_\eta^\alpha} k^2 E_\alpha(k) dk \sim \int^{k_\eta^\alpha} k^2 \varepsilon_\alpha^{2/3} \alpha^{2/3} k^{-1} dk \sim \varepsilon_\alpha^{2/3} \alpha^{2/3} (k_\eta^\alpha)^2. \quad (5.21)$$

Then we have,

$$k_\eta^\alpha \sim \frac{\varepsilon_\alpha^{1/6}}{\nu^{1/2} \alpha^{1/3}}. \quad (5.22)$$

Using that the linear numerical resolution,  $N$ , must be proportional to the dissipation wavenumber ( $N \geq 3k_\eta^\alpha$ ) and that  $Re \sim \nu^{-1}$ , we arrive at

$$N = C_0 k_\alpha^{1/3} Re^{1/2}, \quad (5.23)$$

or, equivalently,

$$dof_\alpha = \frac{C_0^3}{27\alpha} Re^{3/2}, \quad (5.24)$$

where  $C_0$  is an unknown constant (for further details see [77]). We verify this prediction and determine the constant  $C_0$  through the use of a database stemming from studies in which both the free parameter,  $\alpha$  (or, equivalently,  $k_\alpha$ ) and the linear resolution,  $N$ , for a set of DNS flows with  $Re \approx 500, 670, 1300$ , and  $3300$  are varied. In so doing, we establish the necessary numerical resolution for convergence to a grid-independent solution.

Convergence to the grid-independent solution is determined by comparison of the energy spectrum,  $E_\alpha(k)$ , between runs with a constant filter and varying resolution. In Fig. 5.6(a), we make such a comparison for  $Re \approx 500$  ( $N = 256$  for DNS) and  $k_\alpha = 14$



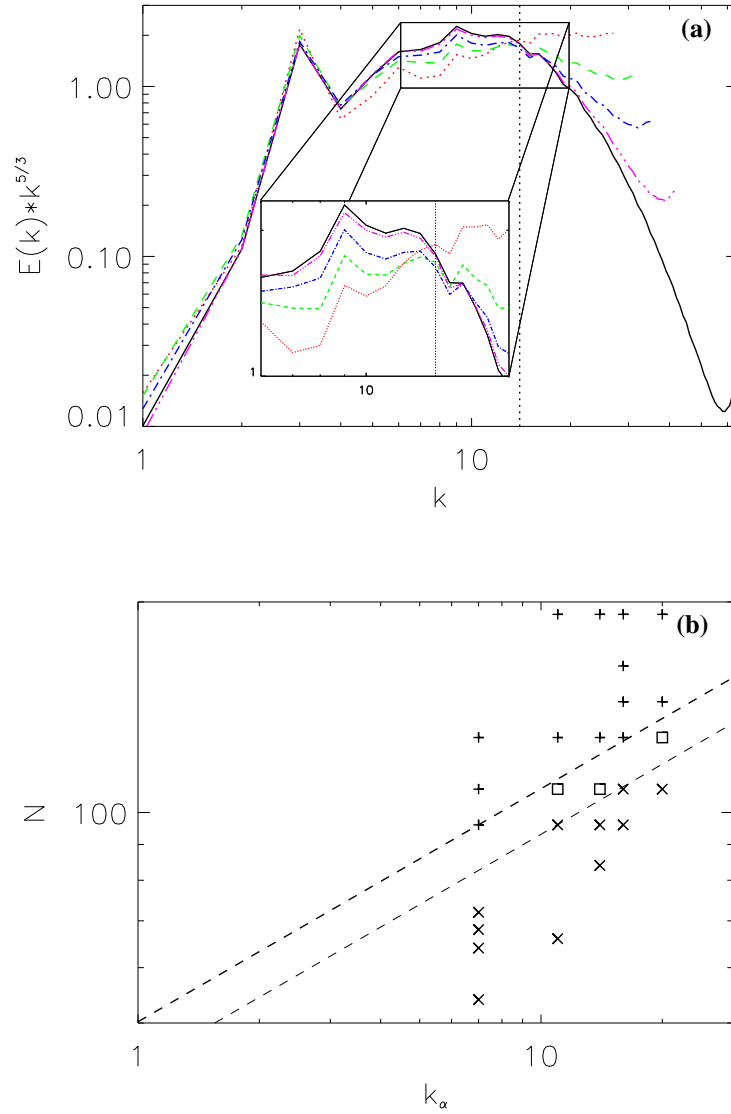


Figure 5.6: Plots for  $Re \approx 500$  simulations demonstrating convergence to the grid-independent LANS- $\alpha$  solution. **(a)** Average energy spectra ( $t \in [20, 33]$ ,  $t$  is time in units of eddy turn-over time) compensated by K41 for LANS- $\alpha$  simulations,  $k_\alpha \equiv 2\pi/\alpha = 14$ :  $192^3$  (black solid),  $84^3$  (red dotted),  $96^3$  (green dashed),  $108^3$  (blue dash-dotted), and  $128^3$  (pink dash-triple-dot). The vertical dashed line denotes  $k_\alpha$ . Inset is a blow-up near  $k_\alpha$  where convergence can be clearly seen. LANS- $\alpha$  at a linear resolution of  $128^3$  is approximately converged to the grid-independent solution while resolutions of  $96^3$  and less are clearly not. **(b)** The linear resolution of  $\alpha$ -model simulations,  $N$ , is plotted versus  $k_\alpha$ . Simulations with inadequate resolution are plotted as X's, those with approximately grid-independent solutions as +'s, and experiments that are neither clearly resolved nor clearly unresolved as boxes. The dashed lines represent  $N = Ck_\alpha^{1/3}$  indicating that a constant in the range  $43.2 < C < 50.2$  agrees with our data. This partially confirms the prediction of Eq. (5.23) and provides a reliable method to determine the needed resolution for a grid-independent LANS- $\alpha$  solution at a fixed  $Re$ .

( $N = 84, 96, 108, 128$ , and  $192$  for LANS- $\alpha$ ). We plot energy spectra compensated by  $k^{5/3}$  so that a K41  $k^{-5/3}$  spectrum would be flat. We see, based on comparing the energy spectra at wavenumbers smaller than  $k_\alpha$  to the  $192^3$  LANS- $\alpha$  spectrum, that simulations at resolutions of  $96^3$  and less are not converged while the one at  $128^3$  is. That is, except for the very small scales at the end of the dissipative range, there is very little difference between the spectra at  $128^3$  and at  $192^3$  (i.e., the solution is “grid-independent”). Meanwhile, for resolutions of  $96^3$  and less the spectra vary greatly with resolution (i.e., they are “unresolved”). In Fig. 5.6(b), we collect all the results of similar studies ( $Re \approx 500$ ) in a plot of resolution,  $N$ , versus inverse filter width,  $k_\alpha$ . (We change  $N$  for a given  $\alpha$ , then change  $\alpha$  and iterate.) Pluses correspond to grid-independent solutions, X’s to under-resolved solutions, and squares to “undecided” runs (i.e., that are neither clearly resolved nor clearly under-resolved). The dashed lines represent Eq. (5.23) with the minimal and maximal choice of  $C$  (where  $C_0 = CRe^{1/2}$ ), that agrees with our results (i.e.,  $43.2 < C < 50.2$ ). In Fig. 5.7 we conduct similar studies for  $Re \approx 670$ . We find  $49.5 < C < 51.4$  and again validate the predictive power of Eq. (5.23) for the necessary numerical resolution for grid-independent solutions.

The greatest utility of the prediction, however, is due to the single constant  $C_0$  which is independent of Reynolds number. A determination of this constant can cheaply be achieved repeating this process for several runs for low and moderate  $Re$ , and determines the resolution requirement for the highest  $Re$  attainable. The ranges of acceptable constants,  $C = C_0Re^{1/2}$ , for the four Reynolds number flows studied are plotted versus  $Re$  in Fig. 5.8. A power law  $C = C_0Re^\gamma$  fits our data with  $\gamma = 0.54 \pm 0.14$  demonstrating the final validation of the prediction,  $\gamma = 0.5$ , Eq. (5.23). The value of the constant is found to be  $C_0 = 2.0 \pm 0.2$ . We made one study for the maximally-helical ABC forcing at  $Re \approx 1600$  and  $\alpha = 2\pi/25$ . It is consistent with a value of  $C_0 = 1.8 \pm 0.1$ . We therefore conclude that the constant  $C_0$  is not a strong function of the forcing employed or of the scale at which the system is forced. As a result, and unlike

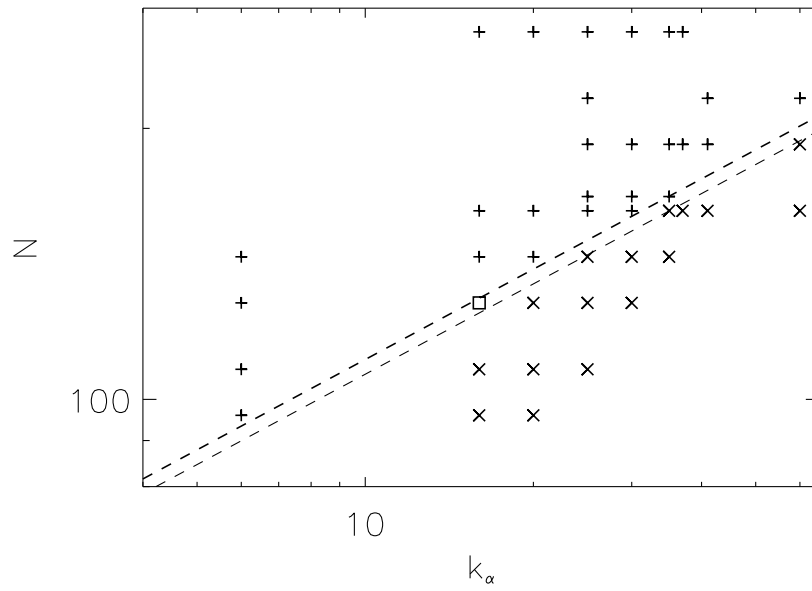


Figure 5.7: As Fig. 5.6(b) but for  $Re \approx 670$  simulations. The dashed lines represent  $N = Ck_\alpha^{1/3}$  indicating that a constant in the range  $49.5 < C < 51.4$  agrees with our data. Note also that any power law,  $N \propto k_\alpha^\beta$ , with  $0.30 < \beta < 0.46$  also agrees with the data.

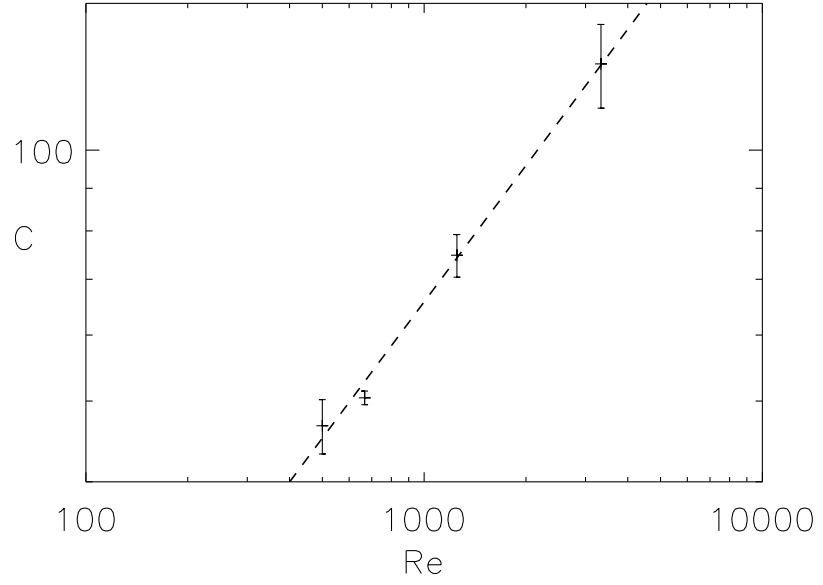


Figure 5.8: Acceptable choices of  $C = C_0 Re^{1/2}$ , versus Reynolds number,  $Re$ , for grid-independent LANS- $\alpha$ . Error bars are not confidence levels, but depict the range of values consistent with our database ( $N = Ck_\alpha^{1/3}$ ) at the four Reynolds numbers we tested. The dashed line depicts the least-squares fit with slope  $0.54 \pm 0.14$ . This completes the validation of Eq. (5.23) which predicts 0.5.

in 2D LANS- $\alpha$  [153], we verify that the size of the attractor in 3D LANS- $\alpha$  is smaller than that in Navier-Stokes, which is a promising result if the LANS- $\alpha$  equation is going to be used as an LES. However, before doing this, an assessment of the truncation errors introduced in discretized systems (as used to solve the equations numerically) and a study of the optimal choice for  $\alpha$  to capture the properties of a DNS is needed. We consider these problems in the following section.

### 5.5 Can LANS- $\alpha$ be considered as a Large Eddy Simulation?

In this section, we consider the LANS- $\alpha$  equations as a means to an end, and consider the solutions to their discretized equations as approximations to the Navier-Stokes solutions. We seek numerical approximations of LANS- $\alpha$  that minimize the difference to a fully resolved or direct numerical solution (DNS) of Navier-Stokes (i.e., we analyze the behavior of LANS- $\alpha$  solutions in the LES framework, and call here the model a “LANS- $\alpha$  LES”, or in short “ $\alpha$ -LES”). In the LES framework, LANS- $\alpha$ ’s turbulent stress tensor,  $\bar{\tau}_{ij}^\alpha$ , is given by (see, e.g., [114])

$$\bar{\tau}_{ij}^\alpha = \mathcal{H}^{-1} \alpha^2 (\partial_k u_i \partial_k u_j + \partial_k u_i \partial_j u_k - \partial_i u_k \partial_j u_k). \quad (5.25)$$

Previous studies have not made the distinction between grid-independent LANS- $\alpha$  and LANS- $\alpha$  LES, though one did study convergence to grid-independent solutions at moderate  $Re$  [90]. We find, however, a definite difference between the two approaches. We show in this section that, in fact, LANS- $\alpha$  combined with truncation error yields a better fit to DNS than grid-independent LANS- $\alpha$ . The resolution that yields an optimal  $\alpha$ -LES (a terminology to be defined below) is also found to follow Eq. (5.23). In the Section 5.5.1, we then address the quality and usability of the predictions of the LANS- $\alpha$  model viewed as an LES.

A remark about nomenclature may be in order at this point. Traditionally, and for good reasons, LES attempt at capturing the large-scale properties of a flow with a

huge Reynolds number, as found, e.g., in the atmosphere. In that case, the wavenumber at which the DNS is truncated is, at best, in the inertial range and it might even be in the energy-containing range, as for the atmospheric boundary layer with a Taylor Reynolds number  $R_\lambda \sim 10^4$ . Of a different nature are the modeling methods sometimes called quasi-DNS. Here, the idea is to model a flow at a given, moderate Reynolds number but with an expense in computing resources lesser than if performing a DNS. Under-resolved DNS fall in that category; in that case, the large-scales are presumably well reproduced but the small scales are noisy. It is in that spirit that we now examine the properties of the LANS- $\alpha$  model. We thus qualify a model as optimal in the sense of being optimal for the class of LANS- $\alpha$  models examined herein; in order to avoid repetition, we also use the terminology of alpha-optimal.

In Fig. 5.9 with  $k_\alpha = 41$ , we plot the  $Re \approx 670$  DNS spectrum (solid black line) and LANS- $\alpha$  spectra at three different resolutions. We observe that, while the  $N = 162$  solution (dotted red line) is not converged, it is a better approximation to the DNS than the grid-independent LANS- $\alpha$  solution. For all simulations we studied, the grid-independent LANS- $\alpha$  solution is not the best approximation to the DNS. Another example is given in Fig. 5.10 where we plot the mean square spectral error normalized to make fair comparisons between large and small  $k_\alpha$  results,

$$E_{sq} = \frac{1}{n} \sum_{k=k_F}^{k_\alpha} \frac{(E_\alpha(k) - E(k))^2}{E^2(k)}, \quad (5.26)$$

where  $k_F$  is the wavenumber for the forcing scale,  $E(k)$  is the DNS spectrum (in the  $L^2(v)$  norm),  $E_\alpha(k)$  is the LANS- $\alpha$  spectrum (in the  $H_\alpha^1(u)$  norm), and  $n$  is the number of terms in the sum. These errors are calculated for spectra averaged over turbulent steady-state solutions:  $t \in [16, 19]$  for  $Re \approx 670$ . We see that for a given filter or a given simulation resolution, there is a local minimum in the error. This minimum is a balance between truncation errors and the approximation error due to using LANS- $\alpha$  instead of the full Navier-Stokes equations. Due to these errors being, in some sense,

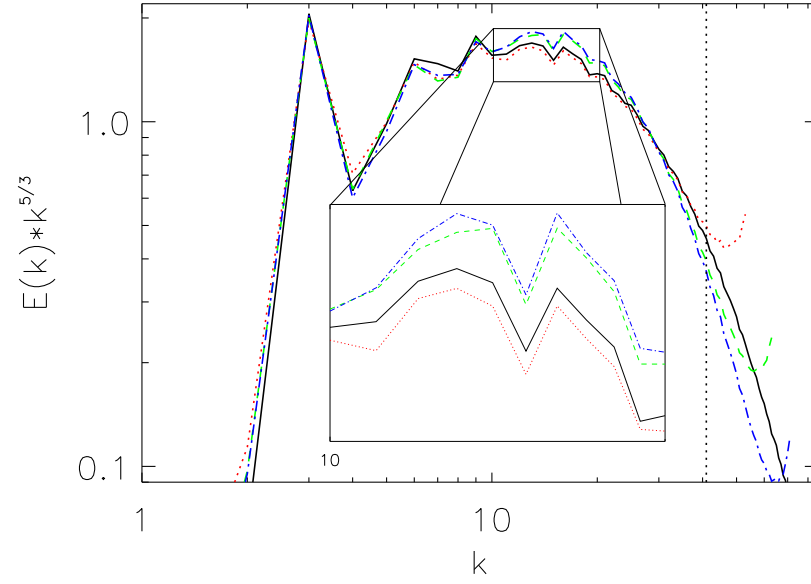


Figure 5.9: Plot of  $Re \approx 670$  simulations. Average compensated energy spectra: DNS (solid black line) and LANS- $\alpha$  simulations,  $k_\alpha = 41$ :  $N = 162$  (red dotted),  $N = 192$  (green dashed), and  $N = 216$  (blue dash-dotted). LANS- $\alpha$  at a linear resolution of 192 is approximately converged to the grid-independent solution while a resolution of 162 is not.  $N = 162$  does correspond, however, more closely to the DNS spectrum. We observe, in general, that a combination of LANS- $\alpha$  and truncation error yields the optimal  $\alpha$ -LES.

in opposition, the optimal  $\alpha$ -LES solution is found at a lower resolution than the grid-independent solution. Indeed, we see by examining Fig. 5.10 (a) that for a given filter the combination of truncation error and the LANS- $\alpha$  solution is a better approximation to the DNS. For fixed resolution, Fig. 5.10 (b), the optimal value for  $\alpha$  is not zero but has some finite value. This local minimum error shown in the figure keeps  $\alpha$  from going to zero ( $k_\alpha \rightarrow \infty$ ) in dynamical models [263]. We note, also, that the error is low for a finite range of  $N$  and  $k_\alpha$  near the minimum, indicating that an  $\alpha$ -LES solution may perform well for a range of parameters near the optimal ones. We find the resolution for an optimal  $\alpha$ -LES is also predicted by Eq. (5.23) (with  $C \approx 47$  for  $Re \approx 670$ , or  $C_0 \approx 1.8$ ). That is, optimal  $\alpha$ -LES resolution is just below that for grid-independent LANS- $\alpha$  solutions. Having demonstrated the predictability of the resolution for grid-independent LANS- $\alpha$  and of LANS- $\alpha$  LES given a Reynolds number and a filter, in the following section we seek to determine sufficient conditions on the free parameter  $\alpha$  for LANS- $\alpha$  to be a successful LES.

### 5.5.1 Free parameter $\alpha$ and quality of the $\alpha$ -LES

In this section, we make an analysis of the LES potential of LANS- $\alpha$  by considering only the grid-independent LANS- $\alpha$  solutions identified using Eq. (5.23). Note that from the results discussed in the previous section, we expect LANS- $\alpha$  optimal grid-dependent  $\alpha$ -LES approximations to have better performance. In the limit of  $\alpha$  going to zero, LANS- $\alpha$  Eq. (5.3) recovers the Navier-Stokes equations, Eqs. (5.2), but the question we address now is how small must  $\alpha$  be for LANS- $\alpha$  solutions to be good approximations to Navier-Stokes solutions. There are several length scales that  $\alpha$  could be related to: the forcing scale  $l_F$ , the integral scale  $L = 2\pi \int_0^\infty E(k)k^{-1}dk / \int_0^\infty E(k)dk$ , the Taylor microscale  $\lambda$ , or the Kolmogorov dissipation scale  $\eta_K$ . Plots of the mean square spectral errors to DNS (see Eq. (5.26)) versus these scales are shown in Fig. 5.11. While the general trend of errors decreasing with  $\alpha$  is apparent in all cases, in Fig.



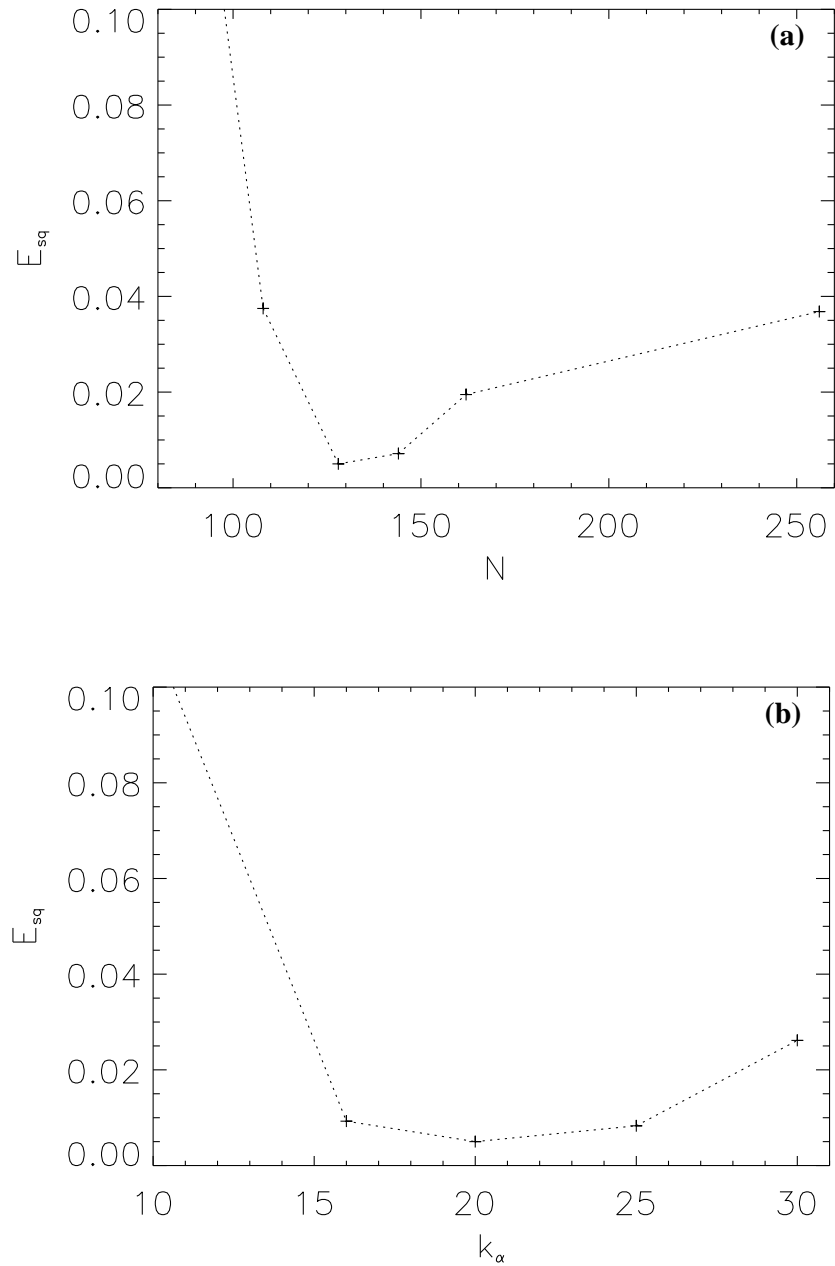


Figure 5.10: Plots for  $Re \approx 670$  simulations. **(a)** Average error (see Eq. (5.26)) versus simulation resolution for  $k_\alpha = 20$ . The optimal (grid-dependent) LES is for a resolution of  $N \approx 128$  and has a much smaller error compared to the DNS than the grid-independent LANS- $\alpha$  solution at higher resolution. **(b)** Average error versus  $k_\alpha$  for  $N = 128$ . At a given resolution the optimal value for  $\alpha$  is not zero but occurs at a local minimal error. Any  $k_\alpha \in [15, 25]$  has an error near the minimum indicating that an LES solution may perform well for a range of parameters near the optimal ones. A constant of  $C = C_0 Re^{1/2} \approx 47$  in Eq. (5.23) is found to correspond with optimal  $\alpha$ -LES approximations.

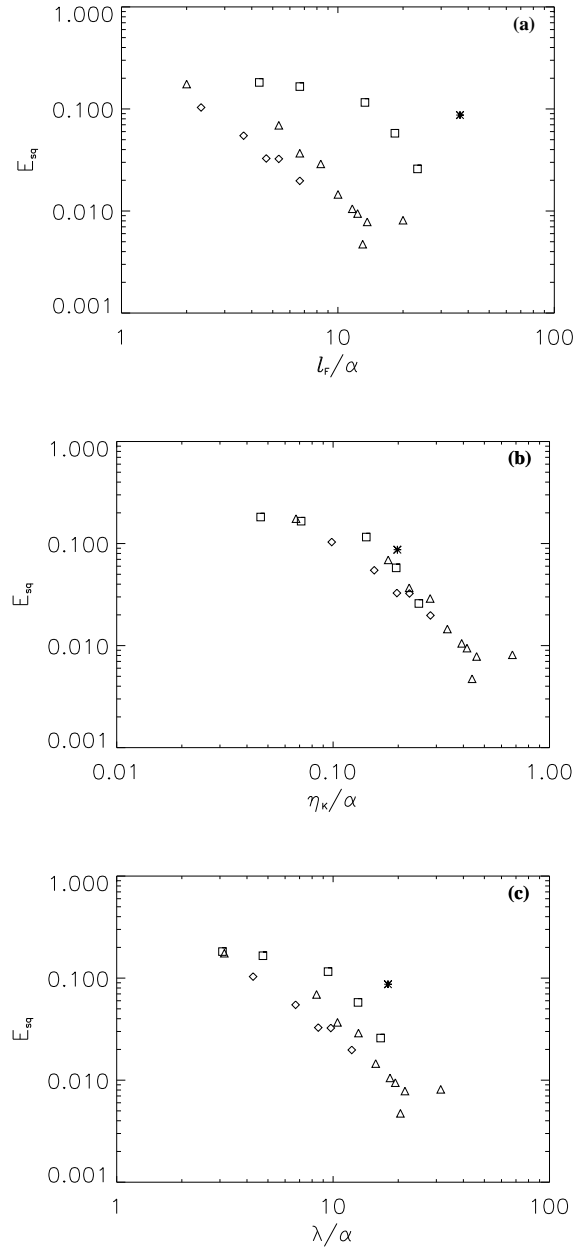


Figure 5.11: Plot of errors, Eq. (5.26), of grid-independent solutions compared to DNS. Asterisks are for  $Re \approx 8300$ , squares for  $Re \approx 3300$ , triangles for  $Re \approx 670$ , and diamonds for  $Re \approx 500$ . The single right-most triangle in all plots corresponds to a value of  $\alpha$  in the dissipative range ( $k_\alpha = 60$ ). The norm we employ to measure the error, Eq. (5.26), is no longer a good norm when dissipative scales are considered. **(a)** Errors versus  $l_f/\alpha$ . No clear correlation between LES quality and the ratio of the forcing scale to  $\alpha$  holds independently of Reynolds numbers. **(b)** Errors versus ratio of dissipative scale,  $\eta_K$ , to  $\alpha$ . The quality of the LES appears to be closely tied to this ratio. **(c)** Errors versus ratio of Taylor wavenumber,  $\lambda$ , to  $\alpha$ . The  $Re \approx 8300$  experiment (asterisk) indicates that the quality of the  $\alpha$ -LES is not tied to the Taylor scale.

5.11(a) we see a large difference between errors at varying Reynolds numbers and similar ratios of  $\alpha$  to the forcing scale,  $l_F$ . For a linear least-squares fit, the goodness-of-fit,  $\chi^2 \equiv \sum (E_{sq}^{actual} - E_{sq}^{fit})^2$ , was found to be  $\chi^2 = 6.2 \cdot 10^{-2}$ . The errors for  $Re \approx 3300$  are much larger than for the same ratio  $l_F/\alpha$  as results at both  $Re \approx 500$  and  $Re \approx 670$ . This is also the case for the integral scale. However, the quality of the  $\alpha$ -LES appears to be closely tied to the ratio of  $\alpha$  to the Kolmogorov dissipation scale. In Fig. 5.11(b) the errors are plotted versus the ratio of the dissipation scale,  $\eta_K$ , to  $\alpha$ . We see a very strong dependence ( $\chi^2 = 2.5 \cdot 10^{-2}$ ) between errors for several runs with four different Reynolds numbers indicating that the quality of the LANS- $\alpha$  LES approximation is a function of the ratio of  $\alpha$  to the dissipative scale. Finally, in Fig. 5.11(c) the errors are plotted versus the ratio of the Taylor Scale,  $\lambda$ , to  $\alpha$ . We find  $\chi^2 = 3.1 \cdot 10^{-2}$  for a linear least-squares fit. We note that a single experiment conducted at  $Re \approx 8300$  (the asterisks) confirms that the maximal value of  $\alpha$  is tied to the dissipation scale and not the Taylor scale.<sup>5</sup> This is more clearly demonstrated in Fig. 5.12 where we plot compensated energy spectra for a nearly constant ratio  $\lambda/\alpha$  at three Reynolds numbers. We see that the maximum deviation from the DNS spectrum increases with  $Re$ . As  $\lambda/\alpha$  is the same in all cases, the optimal  $\alpha$  is not dependent on the Taylor scale.

These findings were not accessible at lower Reynolds numbers due to inadequate separation of scales. For example, we give in Fig. 5.13(a) spectral flux for DNS at  $Re \approx 500$ , 670, and 3300 respectively.

We define the kinetic energy transfer function,  $T(k)$ , in Fourier space as  $T(k) = -\int \hat{\mathbf{v}}_k \cdot (\widehat{\boldsymbol{\omega} \times \mathbf{v}}) dV$ , where  $(\hat{\cdot})$  represents the Fourier transform. For LANS- $\alpha$  we have  $T_\alpha(k) = -\int \tilde{\mathbf{u}}_k \cdot (\widehat{\boldsymbol{\omega} \times \mathbf{u}}) dV$  where  $\boldsymbol{\omega} = \nabla \times \mathbf{v}$ . The flux is defined as usual from the transfer function as

$$\Pi_{(\alpha)}(k) = \int_0^k T_{(\alpha)}(k') dk'. \quad (5.27)$$

---

<sup>5</sup> For the  $Re \approx 8300$  LANS- $\alpha$  run, one turnover time took 45 minutes on 128 Opteron 2.2 GHz processors.

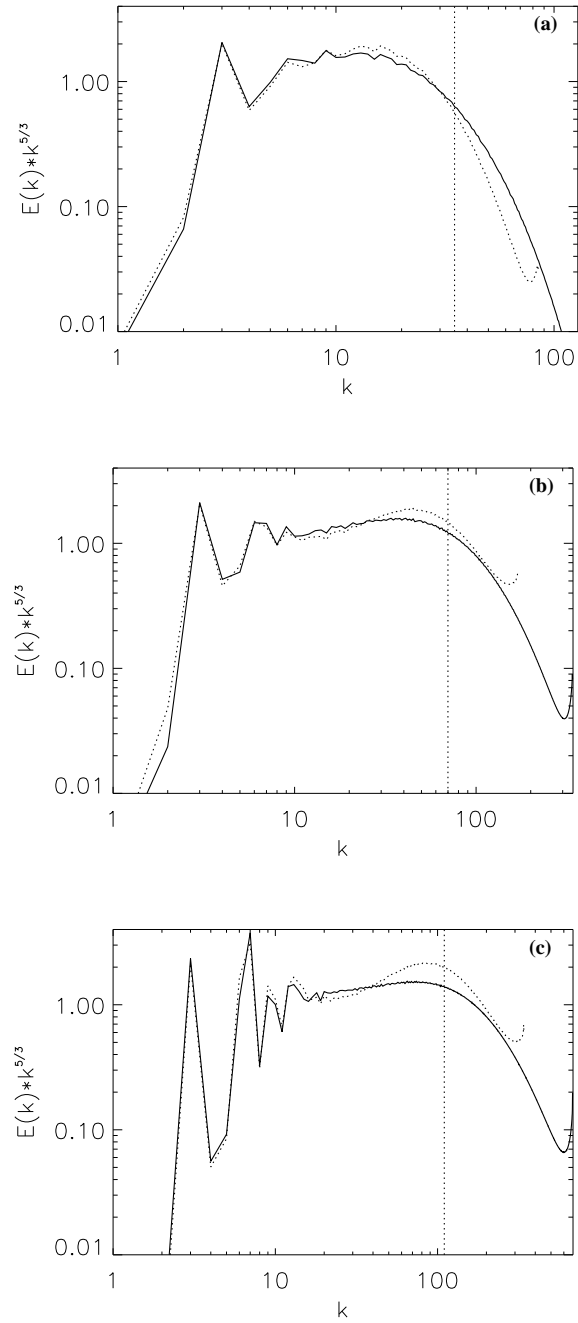


Figure 5.12: Compensated averaged grid-independent energy spectra for DNS (solid) and LANS- $\alpha$  (dotted) holding the ratio of Taylor scale  $\lambda$  to  $\alpha$  nearly constant. Vertical dotted lines indicate  $k_\alpha$ . **(a)**  $Re \approx 670$  and  $k_\alpha = 35$  ( $\lambda/\alpha = 18$ ). **(b)**  $Re \approx 3300$  and  $k_\alpha = 70$  ( $\lambda/\alpha = 17$ ). **(c)**  $Re \approx 8300$  and  $k_\alpha = 110$  ( $\lambda/\alpha = 17$ ). We see that the maximum deviation from the DNS increases with  $Re$ . This is due to the greater distance between  $\alpha$  and the dissipative scale  $\eta_K$ . (Note that scales larger than  $k = 3$  are affected by numerical truncation issues.)

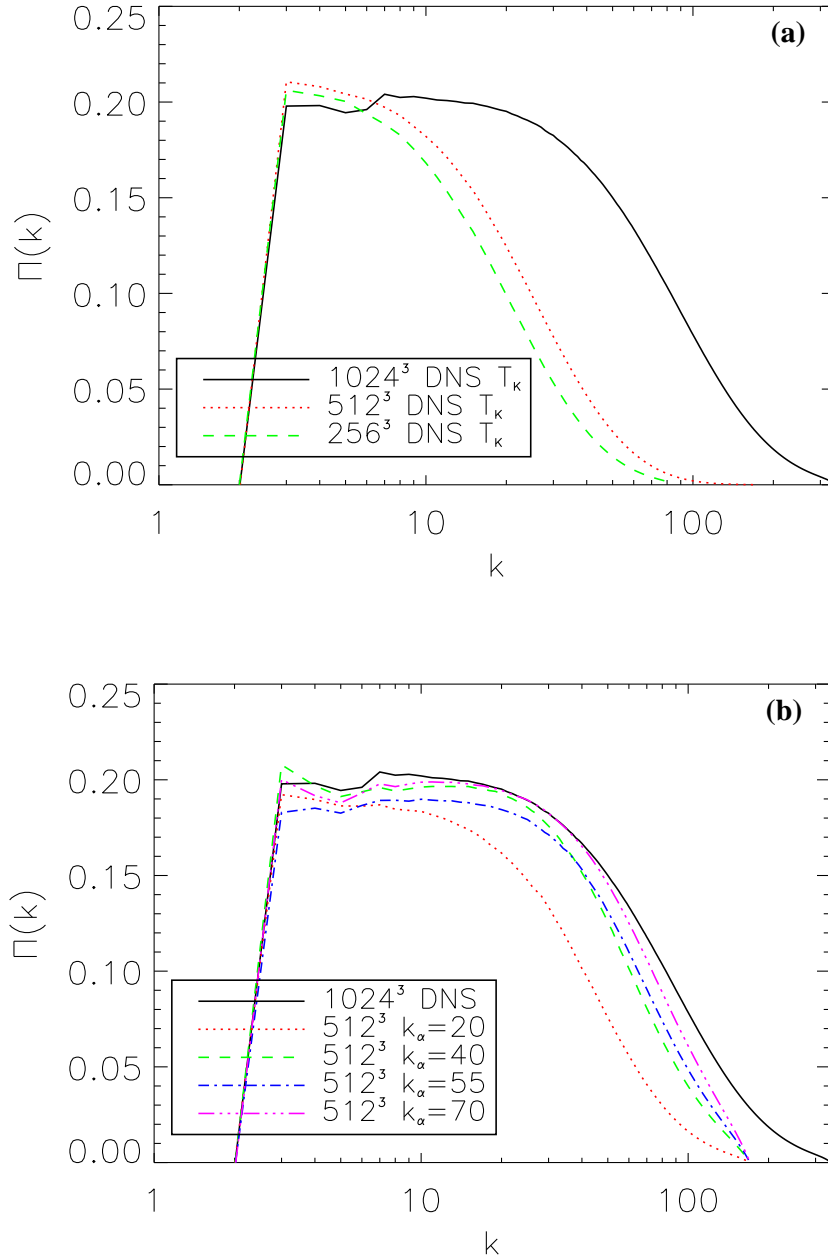


Figure 5.13: **(a)** Energy flux, Eq. (5.27), for three DNS with  $Re \approx 3300$  (black, solid),  $Re \approx 670$  (red, dotted), and  $Re \approx 500$  (green, dashed). No inertial range is discernible on the flux functions except for the highest Reynolds number case. The initial plateau followed by a bump and another plateau (for the case at the highest Reynolds number) is a result of the forcing employed. **(b)** Energy flux at  $Re \approx 3300$  for both DNS and  $\alpha$ -model runs; DNS is the black, solid line. See inset for LANS- $\alpha$  parameters. LANS- $\alpha$  gives a reduced flux which is linked to the significant pile-up of energy at high wavenumber as visible in the energy spectrum (see Fig 5.14). Plots of  $\varepsilon_\alpha$  versus  $t$  (not shown) also show that flux decreases (on average, at long times) with increasing  $\alpha$ .

Only  $Re \approx 3300$  (and  $Re \approx 8300$  not pictured here) demonstrates a range of nearly constant flux (a well-defined inertial range) before the dissipation scales. Following the scaling arguments in Ref. [77], one effect of the  $\alpha$ -model is to increase the time scale for the cascade of energy to small scales. This reduces the flux as  $\alpha$  increases ( $k_\alpha$  decreases) as do the hypothesized “rigid bodies”; this can be seen in Fig. 5.13(b). (Note that in DNS at high resolution, 80% of the flux is from local interactions which is strongly suppressed at scales smaller than  $\alpha$  [2].) As dissipation dominates the flux for low and moderate Reynolds number, the reduced flux of the  $\alpha$ -model has little consequence for these simulations. With a substantial inertial range, however, this reduced flux results in a pile-up of energy for scales larger than the dissipative scale and the spectrum approaches the  $k^1$  spectrum discussed in Section 5.3. As a consequence of the integral conservation of energy ( $E_\alpha = \int \mathbf{u} \cdot \mathbf{v}$ ) there is a corresponding decrease of energy at large scales. Consequently, as the inertial range increases,  $\alpha$  must be moved to smaller and smaller scales in order for LANS- $\alpha$  not to alter scales larger than  $\alpha$ . In summary, the  $\alpha$ -model’s reduced flux of energy to small scales is more crucial when the dissipation scale is farther away from  $\alpha$ .

### 5.5.2 Numerical savings from employing LANS- $\alpha$

If  $\alpha$  must be directly proportional to the Kolmogorov dissipation scale, we can estimate the LES computational savings of the LANS- $\alpha$  model. For the Navier-Stokes equations we have  $dof_{NS} \propto Re^{9/4}$  and, as we verified in Section 5.4, for LANS- $\alpha$  we have  $dof_\alpha = C_0^3 k_\alpha Re^{3/2}/27$ . If  $k_\alpha$  is directly proportional to the Navier-Stokes dissipation wavenumber,  $k_\eta$ , we arrive at

$$k_\alpha \approx \frac{1}{4} k_\eta \propto Re^{3/4}, \quad (5.28)$$

and, consequently,

$$dof_\alpha^{LES} \propto Re^{9/4}. \quad (5.29)$$

Note that for free  $\alpha$ ,  $dof_\alpha$  ( $dof$  of LANS- $\alpha$ ) is much smaller than  $dof_{NS}$ . But, to obtain an optimal LES,  $\alpha$  is tied to  $k_\eta$ ; then the resolution requirements ( $dof_\alpha^{LES}$ ) are different and the decrease in necessary computational resolution from employing LANS- $\alpha$  is fixed. In fact, for the forcing and boundary conditions employed, we find

$$dof_\alpha^{LES} \approx \frac{1}{12} dof_{NS}. \quad (5.30)$$

We note that Eq. (5.29) is consistent with theoretical predictions given in Ref. [91]. Other LES such as the similarity model [8] and the nonlinear (or gradient) model [143, 63] have also exhibited the characteristic that they achieve only moderate reductions in resolution and are, therefore, frequently used in mixed models with a Smagorinsky term (see, e.g., [162]). That such additional terms will be required for LANS- $\alpha$  to reproduce the energy spectrum of high  $Re$  flows, may not be a significant factor in its usability. Note that the usual addition of extra dissipative subgrid-stress terms (as in the Smagorinsky model) also introduces a stronger dependence of the system of equations with the spatial resolution, since the filter width in such models is often associated to the maximum wavenumber in the box,  $k_{max}$ . In that case, it can make more sense to use grid-dependent solutions of LANS- $\alpha$  (discussed at the beginning of Section 5.5) which give an optimal LANS- $\alpha$  LES, and can as a result give an extra gain in the computational costs.

We also conclude that, with the scale  $\alpha$  being tied to the dissipation scale  $\eta_K$ , the model LANS- $\alpha$  behaves more like a quasi-DNS by opposition to a traditional LES. Note however that a factor of  $\approx 2.3$  in resolution gain translates into a factor 27 in CPU and a factor 12 in memory savings, still a substantial gain.

## 5.6 LANS- $\alpha$ at very high Reynolds number

In this section, we compare and contrast LANS- $\alpha$  and Navier-Stokes solutions at high Reynolds number. Using results of previous sections for optimal resolution and

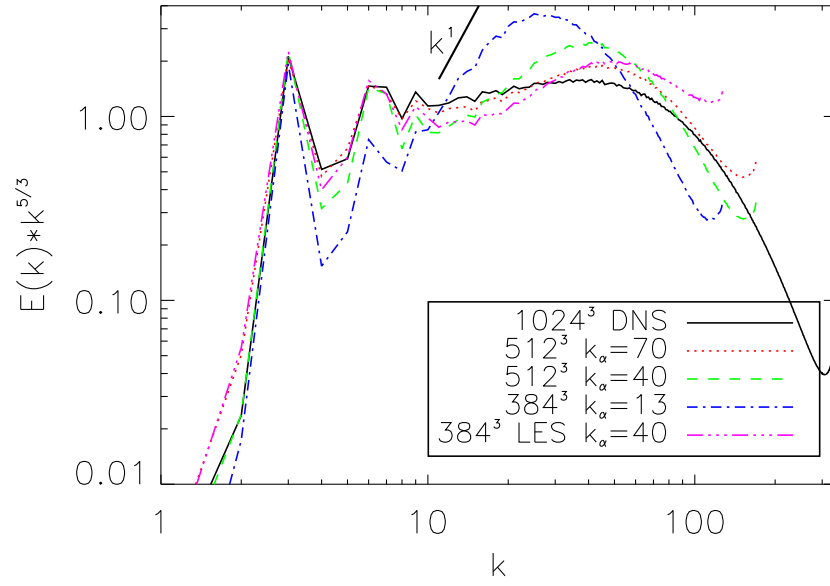


Figure 5.14: Compensated energy spectra averaged over  $t \in [8, 9]$ ,  $Re \approx 3300$ . DNS is the solid black line and grid-independent LANS- $\alpha$  solutions are shown as (red online) dotted ( $k_\alpha = 70$ ), (green) dashed ( $k_\alpha = 40$ ), and (blue) dash-dotted ( $k_\alpha = 13$ ) lines, respectively. A single LANS- $\alpha$  LES is shown as a (pink) dash-triple-dotted line ( $k_\alpha = 40$ ,  $N = 384$ ). The LES is seen to better approximate the DNS spectrum than the grid-independent solution for the same value of  $\alpha$  ( $2\pi/40$ ). As  $\alpha$  is increased the energy spectrum approaches the  $k^1$  spectrum discussed in Section 5.3.2.



the necessary value of  $\alpha$  to approximate DNS, we now evaluate both grid-independent LANS- $\alpha$  solutions and a single LANS- $\alpha$  LES for a highly turbulent flow ( $Re \approx 3300$ ,  $R_\lambda \approx 790$ ). We calculate grid-independent solutions for  $k_\alpha = 70$  ( $N = 512$ ), for  $k_\alpha = 40$  ( $N = 512$ ),<sup>6</sup> and for  $k_\alpha = 13$  ( $N = 384$ ). A LANS- $\alpha$  LES solution is computed for  $k_\alpha = 40$  ( $N = 384$ ).<sup>7</sup> Averaged compensated energy spectra are shown in Fig. 5.14. We see that the optimal LANS- $\alpha$  LES is a better approximation of the DNS spectra than the grid-independent LANS- $\alpha$  for the same value of  $\alpha$  ( $2\pi/40$ ). We also see that if  $\alpha$  is increased further, the energy spectrum approaches the  $k^1$  spectrum discussed in Section 5.3.2.

Fig 5.15 is a perspective volume rendering of the enstrophy density  $\omega^2$  ( $\omega \cdot \bar{\omega}$  for LANS- $\alpha$ ) for the DNS,  $k_\alpha = 70$  LANS- $\alpha$ , and  $k_\alpha = 13$  LANS- $\alpha$ . Due to the late time depicted here ( $t = 9$ , longer than a Lyapunov time) there can be no point-by-point comparison between the simulations. However, we note that the helical structure of the vortex tubes is preserved by the  $\alpha$ -model but that the tubes themselves are shorter and somewhat thicker for large values of  $\alpha$ . As was noted for moderate Reynolds numbers, this is due to LANS- $\alpha$  suppressing vortex stretching dynamics without changing its qualitative features [58]. This is in contrast to 2D LANS- $\alpha$  where the vorticity structures are seen to get thinner as  $\alpha$  increases [153]. This could also be related to the scaling differences between 2D and 3D LANS- $\alpha$ . It has been claimed that the development of helical structures in turbulent flows can lead to the depletion of nonlinearity and the quenching of local interactions [176, 233]. The depletion of energy transfer due to local interactions at some cutoff in wavenumber is also believed to bring about the bottleneck effect [106, 151, 154, 169]. Consistent with these results, in 2D LANS- $\alpha$  (where the vorticity structures are more fine than Navier-Stokes) the spectrum is steeper and in

---

<sup>6</sup> For the  $N = 512$  LANS- $\alpha$  runs, one turnover time took 70 minutes on 96 Opteron 2.2 GHz processors.

<sup>7</sup> For the  $N = 384$  LANS- $\alpha$  runs, one turnover time took 60 minutes on 32 Opteron 2.2 GHz processors.

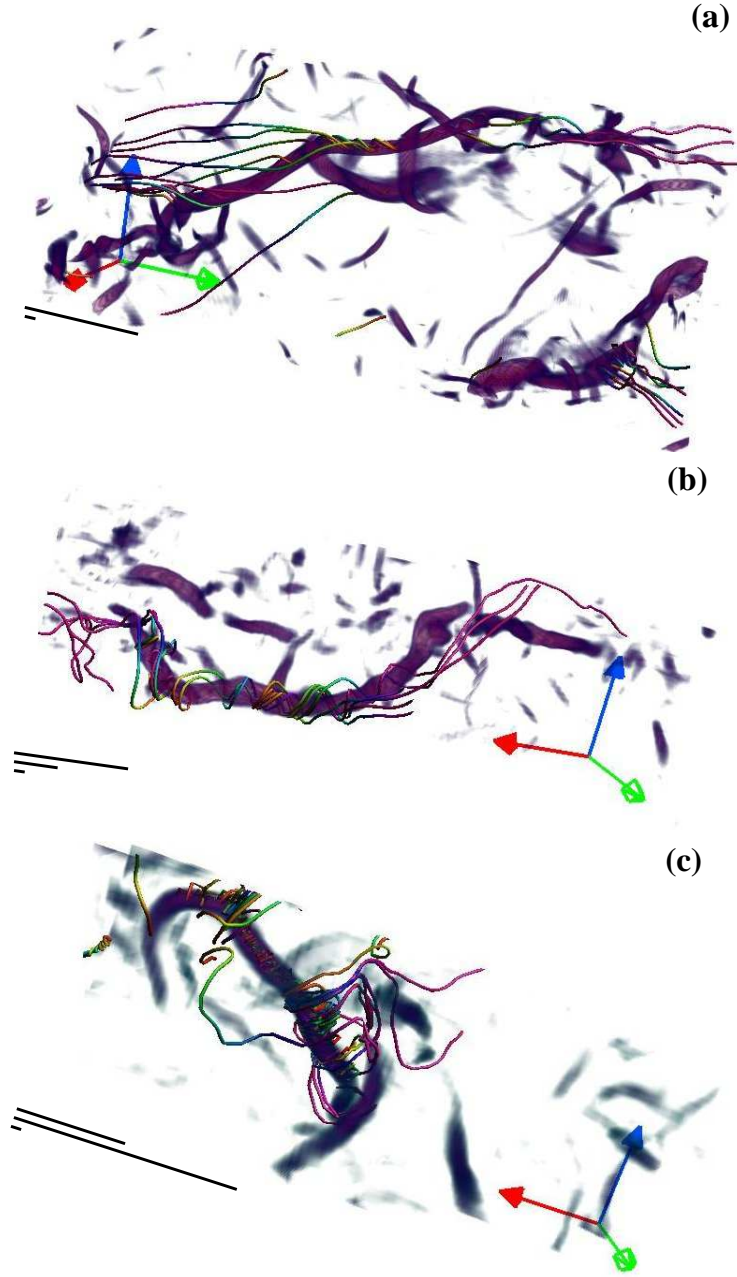


Figure 5.15: Rendering of enstrophy density  $\omega^2$  ( $\omega \cdot \bar{\omega}$  for LANS- $\alpha$ ). Due to the late time depicted here ( $t = 9$ , longer than a Lyapunov time) there can be no point-by-point comparison between the simulations. Instead, regions with approximately the same dimensions are selected around vortex tubes. Velocity  $\mathbf{v}$  field lines are also shown illustrating the helical nature of the tubes which is seen to be captured by LANS- $\alpha$ . (a) DNS. The thick bars represent, from top to bottom, the Taylor scale  $\lambda$  and the dissipative scale  $\eta_K$ , respectively. For LANS- $\alpha$  results the scale  $\alpha$  is depicted between these two. (b)  $k_\alpha = 70$ ,  $N = 512$ . (c)  $k_\alpha = 13$ ,  $N = 384$ . We see that, for large values of  $\alpha$ , the vortex tubes become shorter and somewhat thicker.

3D LANS- $\alpha$  (where the vorticity structures are shorter but fatter than Navier-Stokes) the spectrum is shallower.

Figure 5.16 shows the third-order (mixed) structure functions corresponding to the Kármán-Howarth theorems versus length  $l$ . For the DNS, we show  $\mathfrak{S}_3$  and  $\langle(\delta u)^2 \delta v\rangle$  for LANS- $\alpha$ . The dotted vertical lines indicate the various  $\alpha$ 's. A small inertial range for the DNS near  $l = 1$  is reproduced by all LANS- $\alpha$  results. The largest  $\alpha$  ( $2\pi/13$ ) exhibits a second inertial range at scales just smaller than  $\alpha$  ( $\langle(\delta u)^2 \delta v\rangle \sim l$  is consistent with Eq. (5.16)). We note this is the first demonstration of third-order structure functions in LANS- $\alpha$  consistent with a K41 inertial range followed by an  $\alpha$  inertial range and finally a dissipative range. Next, we observe the scaling of the longitudinal structure functions,

$$S_p(l) \equiv \langle |\delta v_{\parallel}|^p \rangle, \quad (5.31)$$

where we again replace the  $H_{\alpha}^1$  norm for the  $L^2$  norm in the case of LANS- $\alpha$ ,

$$S_p^{\alpha}(l) \equiv \langle |\delta u_{\parallel} \delta v_{\parallel}|^{p/2} \rangle. \quad (5.32)$$

We utilize the extended self-similarity (ESS) hypothesis [14, 15, 13] which proposes the scaling

$$S_p(l) \propto S_3(l)^{\xi_p} \quad (5.33)$$

or, for LANS- $\alpha$ ,

$$S_p^{\alpha}(l) \propto \langle (\delta u)^2 \delta v \rangle^{\xi_p}. \quad (5.34)$$

We display our results in Fig. 5.17(a). We note that for LANS- $\alpha$ , the third-order exponent is not equal to unity, contrary to the Navier-Stokes case. The Kármán-Howarth theorem implies  $\langle(\delta u)^2 \delta v\rangle \sim l$ , not  $S_3^{\alpha}(l) \sim l$ . We measured the deviation from linearity for each experiment (see Fig. 5.17(b)) and found that LANS- $\alpha$  becomes more intermittent as  $\alpha$  increases ( $k_{\alpha} = 13$  is slightly more intermittent than the DNS). As artificially dropping local small-scale interactions gives enhanced intermittency [142, 69],

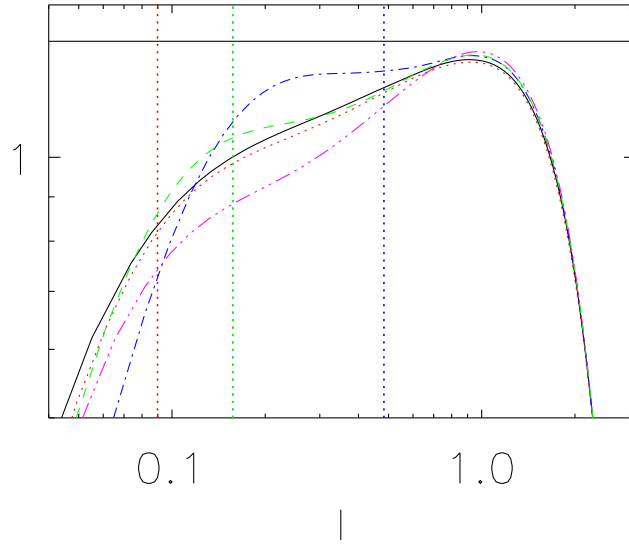


Figure 5.16: Compensated 3rd-order structure function versus length  $l$  (a horizontal line scales with  $l$ ). Structure functions corresponding to the Kármán-Howarth theorem are depicted ( $\mathfrak{S}_3$  for DNS,  $\langle(\delta u)^2\delta v\rangle$  for LANS- $\alpha$ ). Labels are as in Fig. 5.14. The dotted vertical lines indicate the various  $\alpha$ 's. A small inertial range for the DNS near  $l = 1$  is reproduced by LANS- $\alpha$ . The largest  $\alpha$  ( $2\pi/13$ ) exhibits a second inertial range at scales just smaller than  $\alpha$  ( $\langle(\delta u)^2\delta v\rangle \sim l$  is consistent with Eq. (5.16)).

this increased intermittency is the expected result of LANS- $\alpha$  reducing interactions at scales smaller than  $\alpha$ . We note, however, that even with such a large filter, LANS- $\alpha$  is a good approximation to the intermittency properties of the DNS. This is surprising given its energy spectrum and reduced flux in the inertial range. It is probably linked to the fact that LANS- $\alpha$  preserves global properties (in an  $H^1$  sense) of the Navier-Stokes equations and that these properties are important to the dynamics of small scales as measured by high-order structure functions.

## 5.7 Conclusions

We computed solutions of the Lagrangian-Averaged Navier-Stokes  $\alpha$ -model (LANS- $\alpha$ ) in three dimensions for significantly higher Reynolds numbers (up to  $Re \approx 8300$ ) than have previously been accomplished and performed numerous forced turbulence simulations of LANS- $\alpha$  to study their equilibrium states. The results were compared to DNS for  $Re \approx 500, 670, 3300$ , and  $8300$ , the last performed on a grid of  $2048^3$  points. We note that there are two ways to view the LANS- $\alpha$  simulations: as converged or “grid-independent” solutions of the LANS- $\alpha$  equations or as large-eddy simulations ( $\alpha$ -LES) which include grid effects. We found a definite difference between the two approaches in that the fully-converged grid-independent LANS- $\alpha$  is not the best approximation to a DNS of Navier-Stokes. Instead, the minimum error is a balance between truncation errors and the approximation error due to using LANS- $\alpha$  instead of the full Navier-Stokes equations. Due to these errors being, in some sense, in opposition, the optimal  $\alpha$ -LES solution was found at a lower resolution than the grid-independent solution (the error was low for a finite range of  $N$  and  $\alpha$  near the minimum, indicating that a LANS- $\alpha$  viewed as an LES solution may perform well for a range of parameters). Unlike the 2D case [153], 3D LANS- $\alpha$  has been shown to be a subgrid model (i.e., it reduces the resolution requirements of a given computation). This difference between 2D and 3D LANS- $\alpha$  indicates that other  $\alpha$ -models (as the LAMHD- $\alpha$  Eqs. [197, 196]

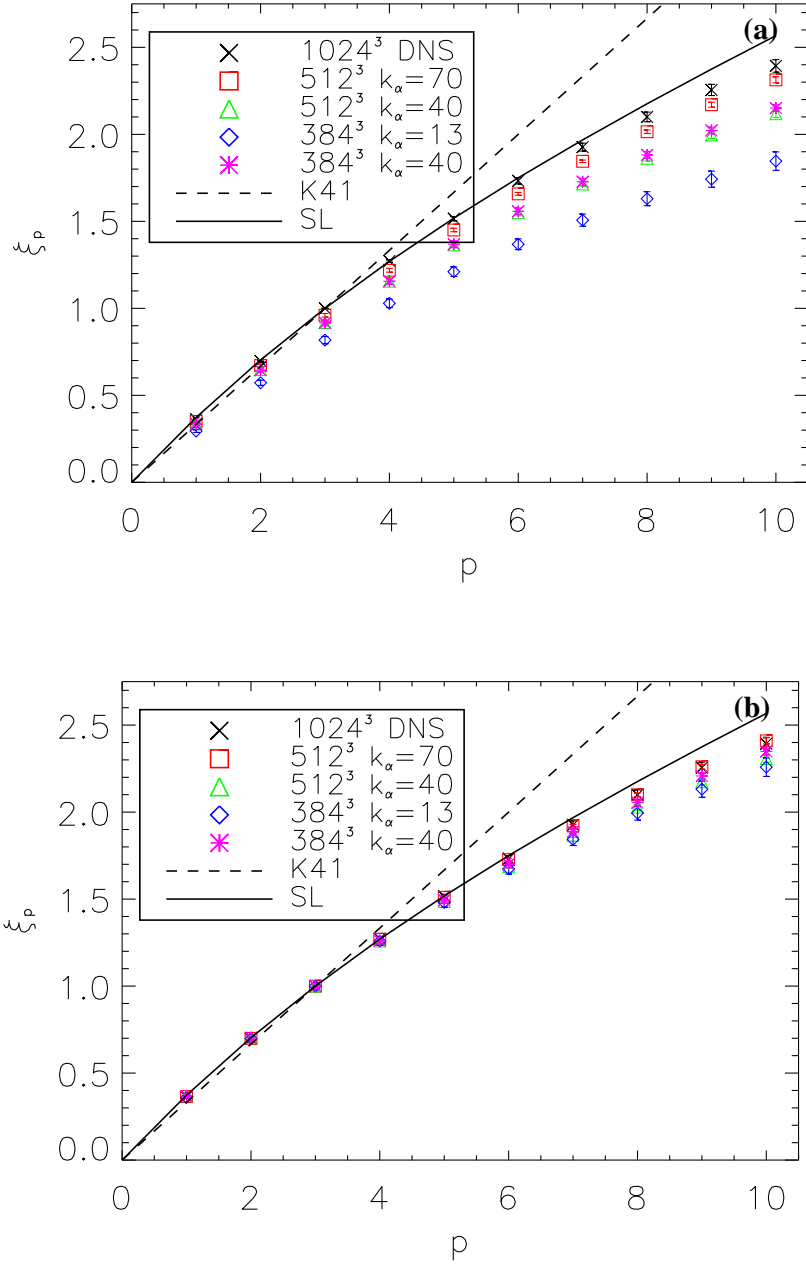


Figure 5.17: **(a)** Structure function scaling exponent  $\xi_p$  versus order  $p$ . Black X's are shown for the DNS. Grid-independent LANS- $\alpha$  are shown as (red) boxes ( $k_\alpha = 70$ ), as (green) triangles ( $k_\alpha = 40$ ), as (blue) diamonds ( $k_\alpha = 13$ ). LANS- $\alpha$  LES ( $k_\alpha = 40$ ,  $N = 384$ ) is shown as (pink) asterisks. The dashed line indicates K41 scaling and the solid line the She-Lévêque formula [214]. **(b)** Scaling exponents normalized to compare deviations from linearity.  $k_\alpha = 13$  is more intermittent than the DNS.

or the BV- $\alpha$  Eqs. [114]) may behave differently and studies of these systems at high resolution may be required.

We confirm the presence of the theoretically predicted  $l^3$  scaling of the third-order structure function (corresponding to a  $k^{-1}$  scaling of the energy spectrum) [77, 42, 60] through its bound on the number of degrees of freedom for LANS- $\alpha$  [77], in the structure functions of the smoothed velocity in simulations with large  $\alpha$ , and in the spectrum of specific spatial portions of the flow. In so doing, we have validated the predictive power of the bound  $dof_\alpha < C\alpha^{-1}Re^{3/2}$ , for the numerical resolution for grid-independent LANS- $\alpha$  solutions and for optimal LANS- $\alpha$  LES (with a separate constant of proportionality). The great utility of the prediction is that the single constant can cheaply be determined at low and moderate Reynolds number and predicts the resolution requirement for the highest Reynolds numbers attainable. We further found no great change in this single constant when employing the non-helical Taylor-Green or the maximally-helical ABC forcings.

However, the small scale ( $k\alpha \gg 1$ ) LANS- $\alpha$  spectrum was observed to be  $k^{+1}$ . We attribute this to the frozen-in-turbulence closure employed in deriving the  $\alpha$ -model. For scales smaller than  $\alpha$ , portions of the smoothed flow  $\mathbf{u}$  are locked into “rigid bodies.” By “rigid bodies,” we mean the internal degrees of freedom are frozen and these portions give no contribution to the energy cascade. This is consistent both with the observed  $k^{+1}$  spectrum and with field increments  $\delta u_\parallel$  being observed to be approximately zero over a large portion (compared to Navier-Stokes) of the flow. The turbulent energy cascade occurs in the space between these “rigid” portions. While the  $k^{-1}$  portions are subdominant to the  $k^{+1}$  portions in the energy spectrum, they prevail in the cascade and hence both the structure functions and the degrees of freedom of the LANS- $\alpha$  attractor.

We find that both of these scalings ( $k^{+1}$  and  $k^{-1}$ ) contribute to a reduction of flux at constant energy (i.e., the dissipation is reduced as has previously been observed

in 2D calculations [22]). This leads to a shallower (or even growing) energy spectrum as  $\alpha$  increases. Thus, for LANS- $\alpha$  viewed as an LES to reproduce the Navier-Stokes energy spectrum it is necessary that  $\alpha$  be not much larger than the dissipation scale ( $\alpha \lesssim 4\eta_K$  independent of Reynolds number); in that sense, it can be considered as a quasi-DNS as opposed to a traditional LES, substantially larger Reynolds numbers being modeled in the latter case, leading to substantially larger gain in resolution. As a consequence, the computational savings of LANS- $\alpha$  is fixed and not a function of Reynolds number. (However, and unlike the 2D case, the 3D  $\alpha$ -model does give a computational saving when used as a LES.) This result was *not accessible at lower Reynolds numbers due to inadequate separation of scales*. However, in one previous study for decaying turbulence with energy initially mostly at low wavenumbers ( $k = 3$ ), it was evident that as time evolved and energy moved to smaller scales, the resolution requirements of LANS- $\alpha$  increased [177]. Other LES such as the similarity model [8] and the nonlinear (or gradient) model [143, 63] have also exhibited the characteristic that resolution may be decreased only modestly and are, therefore, frequently used in mixed models with a Smagorinsky term (see e.g., [162]). That such additional terms will be required for LANS- $\alpha$  to reproduce the energy spectrum of high  $Re$  flows, may not be a significant factor in its usability.

We compared and contrasted LANS- $\alpha$  to a DNS at  $Re \approx 3300$  considering both structures and high-order statistics such as the longitudinal structure functions which are related with intermittency. With an appropriate choice of  $\alpha$  we were able to observe a Navier-Stokes inertial range followed by LANS- $\alpha$  inertial range at scales smaller than  $\alpha$ . For this second inertial range we again observed a  $k^{+1}$  energy spectrum. As  $\alpha$  increased, we noted a change in the aspect ratio of vortex tubes (they became shorter and fatter). This can be related to quenching of local small-scale interactions at scales smaller than  $\alpha$  and, thus, to the shallower spectrum for 3D LANS- $\alpha$  [176, 233, 106, 151, 154, 169]. Therefore, in 2D LANS- $\alpha$  (where the vorticity structures are more fine than



Navier-Stokes) the spectrum is steeper [153] and in 3D LANS- $\alpha$  (where the vorticity structures are shorter but fatter than Navier-Stokes) the spectrum is shallower. Finally, an examination of the longitudinal structure functions indicate that intermittency is increased as the parameter  $\alpha$  is increased consistent with the suppression of local small-scale interactions at scales smaller than  $\alpha$  [142, 69].

The elimination of the faster and faster interactions among smaller and smaller scales through the modified nonlinearity in LANS- $\alpha$  (together with the discrepancy between its solutions and Navier-Stokes solutions) highlights the importance of these interactions down to scales only slightly larger than the dissipative scale. That is, by removing these interactions anywhere in the inertial range (e.g.,  $\alpha \gtrsim 4\eta_K$ ), the resulting energy spectrum was found to differ from the DNS at scales larger than  $\alpha$ . The intermittency properties of the DNS, however, were well reproduced even with large filters. Noting this, if LANS- $\alpha$ 's  $k^1$  energy spectrum is not important for a given application, much greater reductions in resolution can be achieved. Future work should address whether this may be remedied in a LANS- $\alpha$  LES by the inclusion of another (dissipative) model for these interactions, or (in the case of magneto-hydrodynamics [197, 196] whether this problem is less significant because of the presence of greater spectral nonlocality [3, 168, 4]. The effect of LANS- $\alpha$  on the detailed scale-by-scale energy transfer should also be investigated as our results indicate that a model for local small-scale interactions would improve the  $\alpha$ -model. Another direction of future research is to explore other reduced LANS- $\alpha$  models, Clark- $\alpha$  and Leray- $\alpha$ , which break the frozen-in-turbulence closure and, also, the conservation of circulation. This we do in the following chapter. Finally, note that because of its greater mathematical tractability, LANS- $\alpha$  possibly allows for a better understanding of multi-scale interactions in turbulent flows thus modeled; therefore, detailed studies such as the one presented here may, *in fine*, allow for a better understanding of turbulence itself.

## Chapter 6

### Three regularization models of Navier-Stokes

In this chapter we test three regularizations of the Navier-Stokes equations, the Lagrangian-Averaged Navier-Stokes  $\alpha$ -model (LANS- $\alpha$ ), Leray- $\alpha$ , and Clark- $\alpha$ , as sub-grid-scale (SGS) models for large-eddy simulation (LES) by comparison with a direct numerical simulation (DNS) on a regular grid of  $1024^3$  points at a Reynolds number  $Re \approx 3300$  and a Taylor Reynolds number of  $R_\lambda \approx 790$ ; we use a Taylor-Green forcing which corresponds to a von Kármán flow as used in several laboratory experiments [228, 186, 28]. We first derive the Kármán-Howarth equation for both the Clark- $\alpha$  and Leray- $\alpha$  models. We confirm one of two possible scalings resulting from this equation for Clark- $\alpha$  as well as its associated  $k^{-1}$  energy spectrum. Clark- $\alpha$  reproduces the total dissipation and the time to reach a statistical turbulent steady-state of the DNS. For small values of the filter width ( $\alpha = 2\pi/40$ ) it reproduces as well the large-scale energy spectrum and intermittency properties of the DNS. For larger values ( $\alpha = 2\pi/13$ ), it exhibits increased intermittency. We find that for the Leray- $\alpha$  model, as  $\alpha$  increases the nonlinearity (and hence the effective Reynolds number) is decreased substantially. Therefore even for the smallest value studied ( $\alpha = 2\pi/40$ ) it was inadequate as an LES at high  $Re$ . The LANS- $\alpha$  energy spectrum  $\sim k^1$ , consistent with its so-called “rigid bodies,” precludes a reproduction of the energy spectrum of the DNS. We find, however, that this same feature reduces its intermittency compared to Clark- $\alpha$  (which shares a similar Kármán-Howarth equation) and is, thus, a better

approximation to the DNS in this regard for larger values of  $\alpha$ . Clark- $\alpha$  is found to be the best approximation for reproducing the super-filter scale energy spectrum and the total dissipation rate, whereas intermittency properties for larger values of  $\alpha$  are best reproduced by LANS- $\alpha$ .

## 6.1 Introduction

We compare three regularizations (Clark- $\alpha$ , Leray- $\alpha$ , and LANS- $\alpha$ ), which are related via truncation of sub-filter stresses (see Section 3.2), at high Reynolds number. One goal is to test if the differing predicted energy spectra at sub-filter scales influences their intermittency properties. As intermittency is believed to take place at small scales, it can be expected to influence the predicted energy spectra at small scales. For LANS- $\alpha$ , the predicted small-scale spectra is  $\sim k^{-1}$  [77]. This scaling has been observed to subdominant to a  $k^1$  energy spectrum corresponding to “rigid bodies” or “polymerized” portions of the fluid (see Chapter 5). The sub-filter scaling of the third-order structure function corresponded to a  $k^{-1}$  scaling of the energy spectrum. However, a spatial analysis of the cubed velocity increment revealed that for an enhanced portion of the flow there was an absence of stretching in the sub-filter scales. For a rigid body there can be no stretching and these portions have zero velocity increment and no contribution to the structure functions of all orders. As the energy spectrum is the Fourier transform of the second-order structure function, it follows that these portions of the flow contribute a  $k^1$  scaling for the energy spectrum in the  $H_\alpha^1(u)$  norm. For Clark- $\alpha$ , the correct time scale for vortex stretching is hard to determine and the spectrum can be between  $\sim k^{-1}$  and  $\sim k^{-7/3}$  (see Section 3.2.1.3). Leray- $\alpha$  has the same difficulty and the spectrum can be between  $\sim k^{-1/3}$  and  $\sim k^{-5/3}$  (see Section 3.2.2.2).

A second goal is to determine empirically what the actual sub-filter scale spectra are. In Section 6.2, we derive the Kármán-Howarth equation for Clark- $\alpha$  and Leray. To compare the three regularizations as subgrid models, we compute a fully resolved

DNS of the Navier-Stokes equations at a resolution of  $1024^3$  ( $\nu = 3 \cdot 10^{-4}$ ,  $Re \approx 3300$ , and  $R_\lambda \approx 790$ )<sup>1</sup> and model runs with the exact same conditions at a resolution of  $384^3$  in Section 6.3.<sup>2</sup> We utilize two filter widths, a choice guided by Chapter 5. Specifically, we take  $\alpha$  to be either 1/40th the box size which was found to produce an optimal  $\alpha$ -LES or  $\alpha$  of 1/13th the box size which was large enough to exhibit both Navier-Stokes and sub-filter-scale LANS- $\alpha$  dynamics (see Chapter 5). The larger filter case is important because it gives insight into the behavior of the models at scales much smaller than the filter width without requiring higher resolution than is feasible. In Section 6.4, we review bounds on the size of the attractors and comment on the computational savings of the three regularizations viewed as LES. Finally, in Section 6.5 we summarize our results, present our conclusions, and propose future directions of investigation.

## 6.2 Three regularization models

### 6.2.1 Kármán-Howarth equation for Clark- $\alpha$

The relevance of the Kármán-Howarth theorem (see Section 2.4) for the study of turbulence cannot be underestimated: as a corollary, rigorous scaling laws in the inertial range can be deduced. In this section we derive these results for the Clark- $\alpha$  case.

For the sake of simplicity, we consider the case  $\nu = 0$ , the dissipative terms can be added at any point in the derivation. We denote  $\mathbf{u}' \equiv \mathbf{u}(\mathbf{x}', t)$  and begin our investigation of the correlation dynamics by computing the ingredients of the partial derivative  $\partial_t(v_i u'_j)$ . Eq. (3.50) may be rewritten as:

$$\partial_t v_i + \partial_m (v_i u^m + u_i v^m - u_i u^m + p \delta_i^m - \alpha^2 \partial_n u_i \partial_n u^m) = 0. \quad (6.1)$$

---

<sup>1</sup> One turnover time took 15 hours on 256 IBM POWER4 processors and the code sustained 0.12 TFLOPS.

<sup>2</sup> The model runs were carried out on 32 Opteron 2.2 GHz processors. One turnover time took 60 minutes for the LANS- $\alpha$  runs, 90 minutes for the Leray- $\alpha$  runs, and 120 minutes for the Clark- $\alpha$  runs.

Combining Eqs. (3.1) and (3.53), we arrive at

$$\partial_t u'_j + \partial'_m (u'_j u'^m + \bar{\pi}' \delta_j^m + \alpha^2 g_\alpha \otimes \tau^{C'm}_j) = 0, \quad (6.2)$$

where  $\bar{\tau}_{ij}^C \equiv \mathcal{H}^{-1} \alpha^2 \tau^{Cj}_i$ . Multiplying Eq. (6.1) by  $u'_j$ , Eq. (6.2) by  $v_i$  and adding the result, yields

$$\begin{aligned} \partial_t \langle v_i u'_j \rangle &= \frac{\partial}{\partial r^m} \langle (v_i u^m + u_i v^m - u_i u^m - \alpha^2 \partial_n u_i \partial_n u^m) u'_j \rangle + \frac{\partial}{\partial r^m} \langle p u'_j \delta_i^m - \bar{\pi}' v_i \delta_j^m \rangle \\ &\quad - \frac{\partial}{\partial r^m} \langle (u'_j u'^m + \alpha^2 g_\alpha \otimes \tau^{C'm}_j) v_i \rangle, \end{aligned} \quad (6.3)$$

where we used homogeneity (see Section 2.4)

$$\frac{\partial}{\partial r^m} \langle \cdot \rangle = \frac{\partial}{\partial x'^m} \langle \cdot \rangle = -\frac{\partial}{\partial x^m} \langle \cdot \rangle. \quad (6.4)$$

Now, we can make the equation symmetric in the indices  $i, j$  adding the equation for  $\partial_t \langle v_j u'_i \rangle$ . We use homogeneity (see Section 2.4)

$$\langle v_i u'_j u'^m + v_j u'_i u'^m \rangle = -\langle v'_i u_j u^m + v'_j u_i u^m \rangle, \quad (6.5)$$

and define the tensors

$$\mathcal{Q}^C_{ij} = \langle v_i u'_j + v_j u'_i \rangle, \quad (6.6)$$

$$\mathcal{T}^{Cm}_{ij} = \langle (v_i u'_j + v_j u'_i + v'_i u_j + v'_j u_i - u_i u'_j - u_j u'_i) u^m + (u_i u'_j + u_j u'_i) v^m \rangle, \quad (6.7)$$

$$\Pi^{Cm}_{ij} = \langle (p u'_j - \bar{\pi}' v_j) \delta_i^m + (p u'_i - \bar{\pi}' v_i) \delta_j^m \rangle, \quad (6.8)$$

$$\mathcal{S}^{Cm}_{ij} = \left\langle (\partial_n u_i \partial_n u^m) u'_j + (\partial_n u_j \partial_n u^m) u'_i + g_\alpha \otimes \tau^{C'm}_j v_i + g_\alpha \otimes \tau^{C'm}_i v_j \right\rangle. \quad (6.9)$$

We can drop  $\Pi^{Cm}_{ij}$  because the terms with the pressures  $p$  and  $\bar{\pi}'$  vanish everywhere, as follows from the arguments of isotropy [68]. Finally, we obtain

$$\partial_t \mathcal{Q}^C_{ij} = \frac{\partial}{\partial r^m} \left( \mathcal{T}^{Cm}_{ij} - \alpha^2 \mathcal{S}^{Cm}_{ij} \right). \quad (6.10)$$

This is the Kármán-Howarth equation for Clark- $\alpha$  (compare to Eq. (3.113) in Section 3.2.3.2 for LANS- $\alpha$ ).

By dimensional analysis in Eq. (6.10) we arrive at

$$\varepsilon_\alpha^C \sim \frac{1}{l}(vu^2 + u^3 + \frac{\alpha^2}{l^2}u^3). \quad (6.11)$$

For large scales ( $l \gg \alpha$ ), we recover the Navier-Stokes scaling known as the four-fifths law,  $\langle (\delta v_\parallel(l))^3 \rangle \sim \varepsilon l$  (see Section 2.5). Here,  $\delta v_\parallel(l) \equiv [\mathbf{v}(\mathbf{x} + \mathbf{l}) - \mathbf{v}(\mathbf{x})] \cdot \mathbf{l}/l$  is the longitudinal increment of  $\mathbf{v}$ . The four-fifths law expresses that the third-order longitudinal structure function of  $\mathbf{v}$ ,  $S_3^v \equiv \langle (\delta v_\parallel)^3 \rangle$ , is given in the inertial range in terms of the mean energy dissipation per unit mass  $\varepsilon$  by

$$S_3^v = -\frac{4}{5}\varepsilon l, \quad (6.12)$$

or, equivalently, that the flux of energy across scales in the inertial range is constant.

We also recover the K41 energy spectrum,  $E(k)k \sim v^2 \sim \varepsilon^{2/3}l^{2/3}$  or, equivalently,

$$E(k) \sim \varepsilon^{2/3}k^{-5/3}. \quad (6.13)$$

For sub-filter scales ( $l \ll \alpha$ ), we have  $u \sim vl^2/\alpha^2$  and the first and third right-hand terms in Eq. (6.11) are equivalent. In this case, we are left with two different possible scalings depending on the prefactors in Eq. (6.11). If the first (and third) right-hand term is dominant, our scaling law becomes

$$\langle (\delta u_\parallel(l))^2 (\delta v_\parallel(l)) \rangle \sim \varepsilon_\alpha^C l. \quad (6.14)$$

For our small scale energy spectrum we would then have  $E_\alpha^C(k)k \sim uv \sim (\varepsilon_\alpha^C)^{2/3}\alpha^{2/3}$ , or, equivalently,

$$E_\alpha^C(k) \sim (\varepsilon_\alpha^C)^{2/3}\alpha^{2/3}k^{-1}. \quad (6.15)$$

This result is the same as for the  $\alpha$ -model [77]. If, however, the second right-hand term in Eq. (6.11) is dominant, we re-obtain the K41 results with  $\mathbf{u}$  substituted for  $\mathbf{v}$ . Consequently, we would find

$$E_\alpha^C(k) \sim k^{1/3}. \quad (6.16)$$

In comparison, based on phenomenological arguments (see Section 3.2.1.3) we can only constrain the Clark- $\alpha$  sub-filter scale spectrum to be between  $k^{-1}$  and  $k^{-7/3}$ .

### 6.2.2 Kármán-Howarth equation for Leray- $\alpha$

In this section we derive the Kármán-Howarth equation for the Leray- $\alpha$  case. Following Section 6.2.1, we begin our investigation of the correlation dynamics by computing the ingredients of the partial derivative  $\partial_t(v_i v'_j)$ . Eq. (3.92) may be rewritten as:

$$\partial_t v_i + \partial_m (v_i u^m + P \delta_i^m) = 0. \quad (6.17)$$

Multiplying Eq. (6.17) by  $v'_j$  yields

$$\partial_t \langle v_i v'_j \rangle = \frac{\partial}{\partial r^m} \langle v_i u^m v'_j \rangle + \frac{\partial}{\partial r^m} \langle P v'_j \delta_i^m \rangle. \quad (6.18)$$

Now, we can make the equation symmetric in the indices  $i, j$  adding the equation for  $\partial_t \langle v_j v'_i \rangle$ . We define the tensors

$$\mathcal{Q}^L_{ij} = \langle v_i v'_j + v_j v'_i \rangle, \quad (6.19)$$

$$\mathcal{T}^{Lm}_{ij} = \langle (v_i v'_j + v_j v'_i) u^m \rangle, \quad (6.20)$$

$$\Pi^{Lm}_{ij} = \langle P v'_j \delta_i^m + P v'_i \delta_j^m \rangle. \quad (6.21)$$

Again, we can drop  $\Pi^{Lm}_{ij}$  because the terms with the pressure  $P$  vanish everywhere and obtain

$$\partial_t \mathcal{Q}^L_{ij} = \frac{\partial}{\partial r^m} \mathcal{T}^{Lm}_{ij}. \quad (6.22)$$

This is the Kármán-Howarth equation for Leray- $\alpha$ .

The energy dissipation rate for Leray- $\alpha$ ,  $\varepsilon^L$ , satisfies  $\varepsilon^L \propto \partial_t \mathcal{Q}^L_{ij}$ . By dimensional analysis in Eq. (6.22) we arrive at

$$\varepsilon^L \sim \frac{1}{l} v^2 u. \quad (6.23)$$

For large scales ( $l \gg \alpha$ ), we recover the Navier-Stokes scaling, Eqs. (6.12) and (6.13).

For sub-filter scales ( $l \ll \alpha$ ) our scaling law becomes

$$\langle (\delta v_{\parallel}(l))^2 (\delta u_{\parallel}(l)) \rangle \sim \varepsilon^L l. \quad (6.24)$$

For our small scale energy spectrum we would then have  $E^L(k)k \sim v^2 \sim (\varepsilon^L)^{2/3} \alpha^{4/3} k^{2/3}$  (where we employed  $u \sim vl^2/\alpha^2$ ), or, equivalently,

$$E^L(k) \sim (\varepsilon^L)^{2/3} \alpha^{4/3} k^{-1/3}. \quad (6.25)$$

In comparison, based on phenomenological arguments (see Section 3.2.2.2) we can only constrain the Leray- $\alpha$  sub-filter scale spectrum to be between  $k^{-1/3}$  and  $k^{-5/3}$ .

### 6.2.3 LANS- $\alpha$

We summarize here the dimensional analysis argument for the LANS- $\alpha$  inertial range scaling that follows from the Kármán-Howarth theorem for LANS- $\alpha$ , beginning from Eq. (3.113) in Section 3.2.3.2:

$$\partial_t \mathcal{Q}^{\alpha}_{ij} = \frac{\partial}{\partial r^m} (\mathcal{T}^{\alpha m}_{ij} - \alpha^2 \mathcal{S}^{\alpha m}_{ij}). \quad (6.26)$$

The trace of this equation is the Fourier transform of the detailed energy balance for LANS- $\alpha$ ;

$$\mathcal{Q}^{\alpha}_{ij} = \langle v_i u'_j + v_j u'_i \rangle \quad (6.27)$$

is the second-order correlation tensor while

$$\mathcal{T}^{\alpha m}_{ij} = \langle (v_i u'_j + v_j u'_i + v'_i u_j + v'_j u_i) u^m \rangle, \quad (6.28)$$

and

$$\mathcal{S}^{\alpha m}_{ij} = \langle (\partial_m u_l \partial_i u_l) u'_j + (\partial_m u_l \partial_j u_l) u'_i + (g_\alpha \otimes \tau^{\alpha m}_j) v_i + (g_\alpha \otimes \tau^{\alpha m}_i) v_j \rangle, \quad (6.29)$$

are the third-order correlation tensors for LANS- $\alpha$  and  $\bar{\tau}^{\alpha}_{ij} = \mathcal{H}^{-1} \alpha^2 \tau^{\alpha j}_i$  is the sub-filter scale stress tensor. The energy dissipation rate for LANS- $\alpha$ ,  $\varepsilon_\alpha$ , satisfies  $\varepsilon_\alpha \propto \partial_t \mathcal{Q}^{\alpha}_{ij}$ . By dimensional analysis in Eq. (6.26) we arrive at

$$\varepsilon_\alpha \sim \frac{1}{l} (v u^2 + \frac{\alpha^2}{l^2} u^3). \quad (6.30)$$



For large scales ( $l \gg \alpha$ ), we recover the Navier-Stokes scaling Eqs. (6.12) and (6.13). For sub-filter scales ( $l \ll \alpha$ ) our scaling law becomes Eq. (6.14) and our sub-filter scale spectra is given by

$$E_\alpha(k) \sim \varepsilon_\alpha^{2/3} \alpha^{2/3} k^{-1}. \quad (6.31)$$

In this case, in the phenomenological arguments, we know that eddies of size  $k^{-1}$  are advected by the smoothed velocity, Eq. (3.84). This scaling is confirmed in Chapter 5 but coexists with a  $k^1$  energy spectrum corresponding to “rigid bodies” or “polymerized” portions of fluid which do not contribute to the turbulent energy cascade.

### 6.3 Numerical study

We compute numerical solutions to Eqs. (2.5), (3.50), (3.92), and (3.104) in a three-dimensional (3D) cube with periodic boundary conditions using a parallel pseudospectral code [81, 93]. We employ a Taylor-Green forcing [228] as in Chapter 5 (see Section ).

To compare the three regularizations (Clark- $\alpha$ , Leray- $\alpha$ , and LANS- $\alpha$ ) we compute a fully resolved DNS of the Navier-Stokes equations at a resolution of  $1024^3$  ( $\nu = 3 \cdot 10^{-4}$ ,  $Re \approx 3300$ ) and model runs with the exact same conditions at a resolution of  $384^3$ . The details of the flow dynamics of the DNS have already been given [2, 169]. In particular, the Reynolds number based on the integral scale  $\mathfrak{L} \equiv 2\pi \int E(k)k^{-1}dk/E \approx 1.2$  (where  $E$  is the total energy) is  $Re_{\mathfrak{L}} = U\mathfrak{L}/\nu \approx 3900$ , where  $U$  is the *r.m.s.* velocity and the Reynolds number based on the Taylor scale is  $R_\lambda \approx 790$ . The DNS was run for nine turnover times ( $\mathfrak{L}/U$ ) (in the following results, time  $t$  is in units of the turnover time). We employ two different filter widths for our comparisons,  $\alpha = 2\pi/40$  corresponding to an optimal  $\alpha$ -LES at this resolution and  $\alpha = 2\pi/13$  for which LANS- $\alpha$  exhibits both Navier-Stokes and LANS- $\alpha$  inertial ranges in the third-order structure function (see Chapter 5). From these we hope to obtain both the behavior of the models

for scales much smaller than  $\alpha$  and an indication of their LES potential. Note that the value of  $\alpha$  has been optimized for neither Clark- $\alpha$  nor Leray- $\alpha$ ; as a consequence, these models could perform better than indicated in this study.

In Fig. 6.1 we present the time evolution of the enstrophy,  $\langle \omega^2 \rangle$  ( $\langle \omega \cdot \bar{\omega} \rangle$  for LANS- $\alpha$  and Clark- $\alpha$ ), which is proportional to the dissipation,  $\varepsilon = \nu \langle \omega^2 \rangle$  ( $\varepsilon_\alpha = \nu \langle \omega \cdot \bar{\omega} \rangle$ ). Fig. 6.1 (a) is the result for  $k_\alpha \equiv 2\pi/\alpha = 40$  along with an under-resolved Navier-Stokes solution at a resolution of  $384^3$  ( $\nu = 3 \cdot 10^{-4}$ , pink dash-triple-dotted line). We see that both LANS- $\alpha$  and Clark- $\alpha$  reproduce the amount of dissipation and are within 10% of the DNS time to reach a statistical turbulent steady-state. As has been observed before, Leray- $\alpha$  is under-dissipative [90]. We also note that its time-scale to reach a steady-state is increased. In Fig. 6.1 (b), we plot a similar study for the large filter case ( $k_\alpha = 13$ ) along with a  $512^3$  DNS of a less turbulent flow ( $\nu = 1.5 \cdot 10^{-3}$ ,  $Re \approx 1300$ ,  $R_\lambda \approx 490$ , cyan long-dashed line). Here each run is calculated only until it reaches a statistical steady-state. We see that, for Leray- $\alpha$ , the dissipation is further reduced and the time-scale is increased when compared to the smaller  $\alpha$  case. We see by comparison with the  $Re \approx 1300$  DNS, that both these features also result from a reduced Reynolds number. For LANS- $\alpha$ , the dissipation is also decreased as  $\alpha$  is increased (the time to reach steady-state is not increased) which is likely related to its rigid bodies which would have no internal dissipation. Of the three models, Clark- $\alpha$  best reproduces the total dissipation for a large range of  $\alpha$ . Indeed, as it is the order  $\alpha^2$  approximation of Navier-Stokes, this should remain true until  $\alpha$  is very large.

The sub-filter scale spectra can be observed in Fig. 6.2 (b). The energy spectra are calculated as follows,

$$E(k) = \sum_{k_{eff} \geq k - \frac{1}{2}}^{k_{eff} < k + \frac{1}{2}} v_x^2(k_{eff}) + v_y^2(k_{eff}) + v_z^2(k_{eff}) \quad (6.32)$$

where  $k_{eff} = \sqrt{k_x^2 + k_y^2 + k_z^2}$  (the  $H_1^\alpha(u)$  norm is employed for Clark- $\alpha$  and LANS- $\alpha$ ). The length scale  $\alpha$  is indicated by a vertical dashed line and the plotted energy spectra

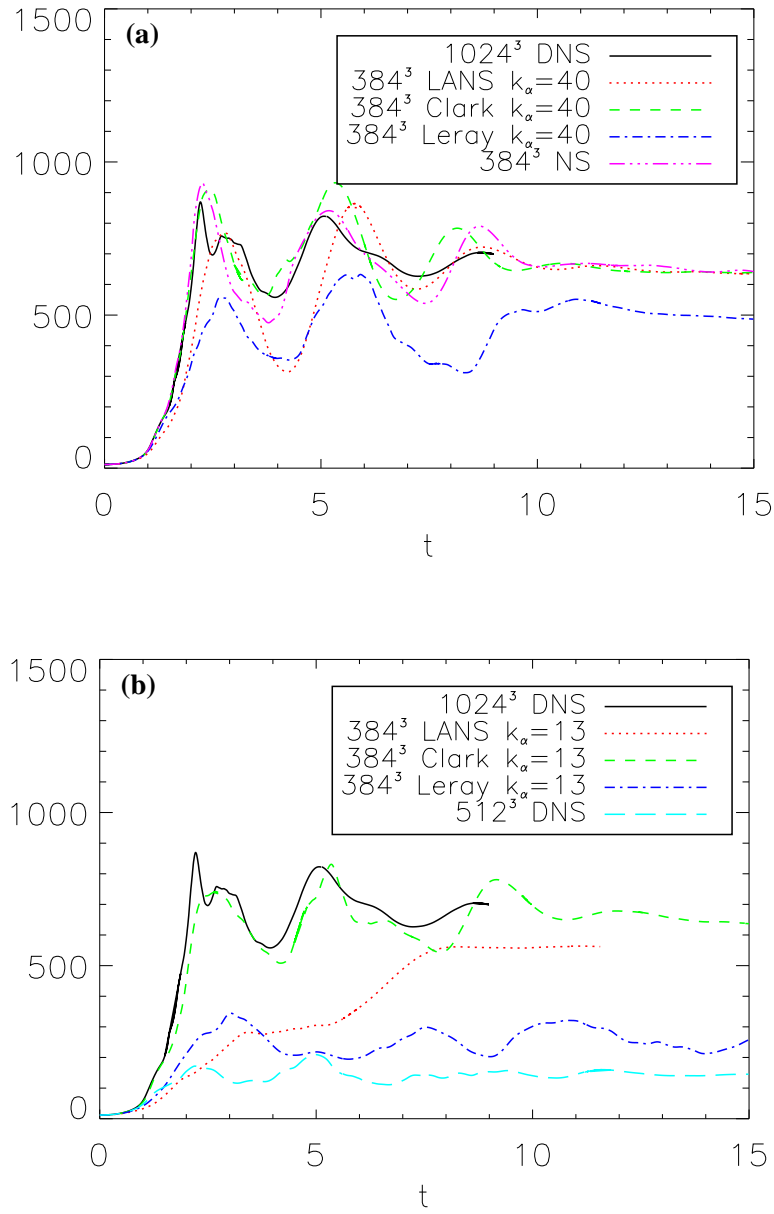


Figure 6.1: Time evolution of  $\langle \omega^2 \rangle$  ( $\langle \boldsymbol{\omega} \cdot \overline{\boldsymbol{\omega}} \rangle$ ) for LANS- $\alpha$  and Clark- $\alpha$ . DNS ( $Re \approx 3300$ ) is shown as solid black lines, LANS- $\alpha$  as dotted red, Clark- $\alpha$  as dashed green, and Leray- $\alpha$  as blue dash-dotted. **(a)**  $k_\alpha = 40$ . An under-resolved ( $384^3$ ) Navier-Stokes run is shown as a pink dash-triple-dotted line. **(b)**  $k_\alpha = 13$ . The cyan long-dashed line represents a  $512^3$  DNS ( $Re \approx 1300$ ,  $R_\lambda \approx 490$ ). Here each run is calculated only until it reaches a statistical steady-state. Leray- $\alpha$  reduces the dissipation,  $\varepsilon = \nu \langle \omega^2 \rangle$ , and increases the time scale to reach a statistical turbulent steady-state. Both effects are greater as  $\alpha$  is increased. By comparison with the  $Re \approx 1300$  run, we see that these two effects are consistent with a reduced effective Reynolds number. A smaller reduction in flux (but not an increase in time to steady-state) is also observed for LANS- $\alpha$  and is likely related to its rigid bodies.

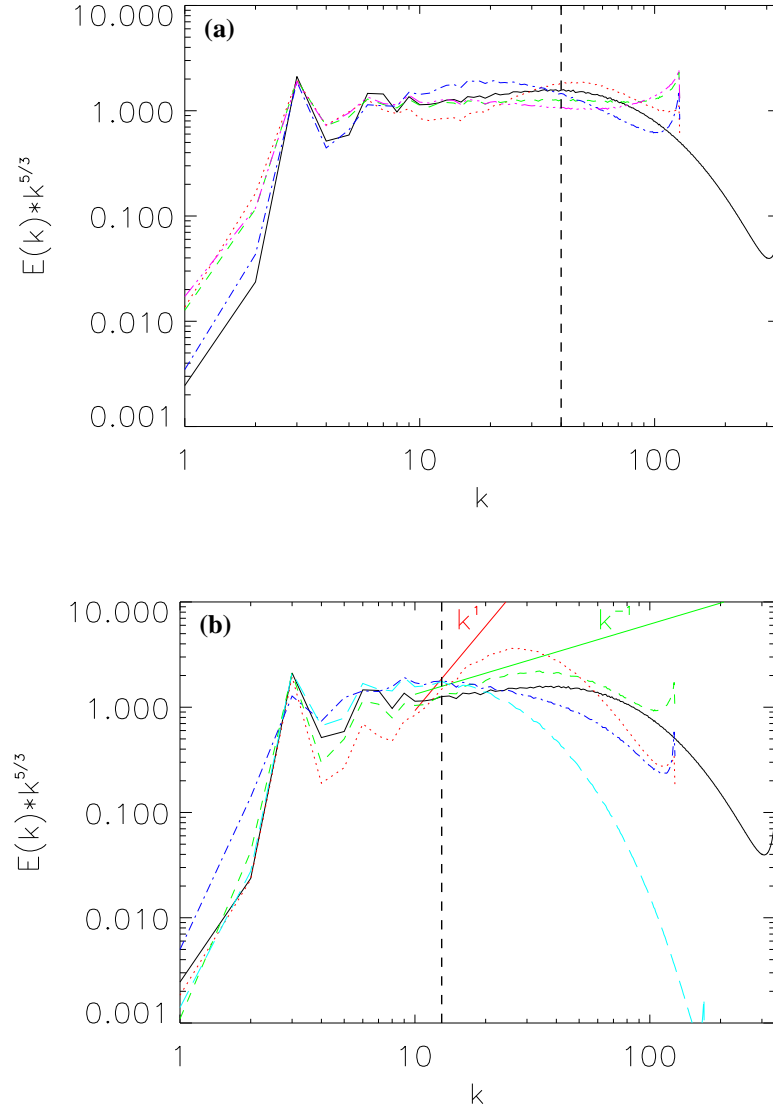


Figure 6.2: Spectra compensated by K41 for  $1024^3$  DNS averaged over  $t = [8.25, 9]$ . Labels are as in Fig. 6.1. **(a)**  $k_\alpha = 40$  (vertical dashed line).  $384^3$  simulations are averaged over  $t \in [15, 20]$ . Note that to make a comparison for most wavenumbers, the spectra must be averaged within a turbulent steady-state. Therefore, as the subgrid models are averaged over a different time interval, there is no meaningful comparison to the DNS for  $k < 3$ . Even though the value of  $\alpha$  is not optimized for Clark- $\alpha$ , this model does very well at reproducing the large-scale energy spectrum. Leray- $\alpha$ 's performance is the poorest **(b)**  $k_\alpha = 13$  (vertical dashed line). Compensated spectra for  $384^3$  LANS- $\alpha$  averaged over  $t \in [10.8, 11.6]$ , for  $384^3$  Clark- $\alpha$  over  $t \in [11.8, 12.6]$ , for  $384^3$  Leray- $\alpha$  over  $t \in [26.3, 27]$ , and for the  $Re \approx 1300$  DNS over  $t \in [18.1, 18.9]$ . Due to the large disparity in times to reach a turbulent steady-state, the time intervals chosen to average over also differ greatly. Clark- $\alpha$  exhibits the predicted  $k^{-1}$  spectrum, Eq. (6.15), and not  $k^{1/3}$ , Eq. (6.16), nor another possible spectrum, Eq. (3.89). The spectrum of Leray- $\alpha$  is very similar (for  $k \in [5, 20]$ ) to that of the  $Re \approx 1300$  DNS.

are compensated by  $k^{5/3}$  (i.e., leading to a flat K41  $k^{-5/3}$  spectrum). Clark- $\alpha$  is close to the predicted  $k^{-1}$  spectrum (and not the  $k^{1/3}$  Eq. (6.16) nor another possible spectrum, Eq. (3.89)) while LANS- $\alpha$  is close to its  $k^1$  spectrum (see Chapter 5). Leray- $\alpha$ , on the other hand, possesses a very steep sub-filter scale spectrum as well as enhanced large-scale energy as has been previously observed [90]. We note that its spectrum for  $k \in [5, 20]$  much better approximates the  $Re \approx 1300$  flow, but this may be an effect of the influence, e.g., through resonance mode coupling, of the large-scale forcing at  $k_0 = 3$ . This as well as the increased time scale and reduced dissipation, implies that the Leray- $\alpha$  model is operating at a much lower effective Reynolds number. This may be due to a further reduced nonlinearity in Leray- $\alpha$  as compared to, for instance, LANS- $\alpha$ . The advection term in LANS- $\alpha$ , Eq. (3.104), may be rewritten as  $\partial_t v + \boldsymbol{\omega} \times \mathbf{u}$  while the same term for Leray- $\alpha$ , Eq. (3.92), is  $\partial_t v + \mathbf{u} \cdot \nabla \mathbf{v}$ . Recall that the difference between  $\boldsymbol{\omega} \times \mathbf{v}$  and  $\mathbf{v} \cdot \nabla \mathbf{v}$  is the gradient of the energy,  $\nabla v^2/2$ , acting as a turbulent pressure. While this difference is usually absorbed into the modified pressure (especially for periodic boundary conditions), it is clearly nonlinear. Furthermore, it is an order-one term and (with its absence) the nonlinearity in Leray- $\alpha$  is significantly reduced compared to LANS- $\alpha$ . Hence, the effective Reynolds number (a ratio of the nonlinearity to the dissipation) is also reduced. Due to the nature of the derivation of Clark- $\alpha$ , however, its nonlinearity cannot be reduced (to order  $\alpha^2$ ) which is consistent with the results shown here.

Compensated spectra averaged over several eddy turn-over times are shown for the subgrid-model case (i.e.,  $k_\alpha = 40$ ) in Fig. 6.2 (a). Note that as the subgrid models are averaged over a different time interval, there is no meaningful comparison to the DNS for  $k < 3$ . Even without an optimal choice for the value of  $\alpha$ , Clark- $\alpha$  best reproduces the DNS spectrum for scales larger than  $\alpha$ . We compute the mean square

spectral error normalized to make fair comparisons between large and small  $k_\alpha$  results,

$$E_{sq} = \frac{1}{n} \sum_{k=k_F}^{k_\alpha} \frac{(E_{model}(k) - E(k))^2}{E^2(k)}, \quad (6.33)$$

where  $k_F$  is the wavenumber for the forcing scale,  $E(k)$  is the DNS spectrum (in the  $L^2(v)$  norm),  $E_{model}(k)$  is the subgrid model spectrum (in the appropriate norm), and  $n$  is the number of terms in the sum. We find (in decreasing order)  $E_{sq} = 0.077$  for the under-resolved  $384^3$ , 0.059 for Leray- $\alpha$ , 0.053 for LANS- $\alpha$ , and 0.031 for Clark- $\alpha$ . If we compute, instead the mean spectral error

$$E_{mean} = \frac{1}{n} \sum_{k=k_F}^{k_\alpha} \frac{|E_{model}(k) - E(k)|}{E(k)}, \quad (6.34)$$

we have in decreasing order,  $E_{mean} = 0.20$  for Leray- $\alpha$ , 0.19 for the under-resolved  $384^3$ , 0.19 for LANS- $\alpha$ , and 0.15 for Clark- $\alpha$ . We see that only Clark- $\alpha$  improves the estimate of the power spectrum at this resolution for both error measures. Leray- $\alpha$  performs the poorest of the three regularization models, but is also likely not optimized. As previously argued, its effective Reynolds number is too low to accurately model the DNS flow. Either a decrease in the viscosity  $\nu$ , or a decrease in the filter size  $\alpha$  (and, hence, an increase in the nonlinearity), or both would likely result in a more accurate SGS model. Due to the frozen-in rigid bodies, the LANS- $\alpha$  model cannot reproduce the DNS spectrum unless  $\alpha$  is less than a few times larger than the dissipation scale (see Chapter 5).

Another measure of the success of a subgrid model is the reproduction of structures in the flow. In Figure 6.3 we have 3D volume rendering of the enstrophy density  $\omega^2$  ( $\omega \cdot \bar{\omega}$  for LANS- $\alpha$  and Clark- $\alpha$ ) for the DNS, the three subgrid-model simulations ( $k_\alpha = 40$ ), the  $384^3$  under-resolved Navier-Stokes solution, all at a Reynolds number of  $\approx 3300$ , and the  $Re \approx 1300$  DNS. Due to the late times depicted (longer than a Lyapunov time) there can be no point-by-point comparison between the simulations. Instead, we note that there are four horizontal bands where the forcing causes a maximum shear. This large-scale feature of the flow is missing only from Leray- $\alpha$  and

the  $Re \approx 1300$  run. The three other runs reproduce this feature well (note that the apparently thicker tubes present in Clark- $\alpha$  are vortex tube mergers). The results lead again to the conclusion that the under-resolved, Clark- $\alpha$ , and LANS- $\alpha$  models are acceptable subgrid models and that Leray- $\alpha$  has a reduced effective  $Re$ .

Validation of the Kármán-Howarth equation scalings, Eqs. (6.14) and (6.24), enables us to measure scaling laws in the inertial range and, thus, compare the intermittency properties of the models. The third-order correlations involved in the theorems, namely

$$L^\alpha(l) \equiv \langle (\delta u_\parallel(l))^2 (\delta v_\parallel(l)) \rangle \quad (6.35)$$

for Clark- $\alpha$  and LANS- $\alpha$ ,

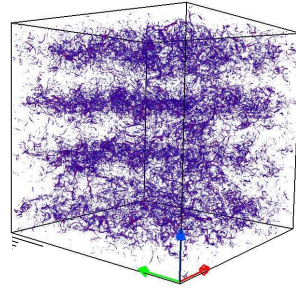
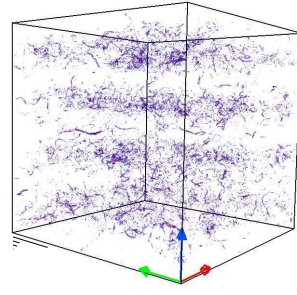
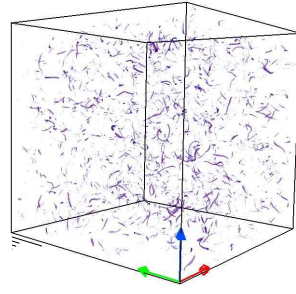
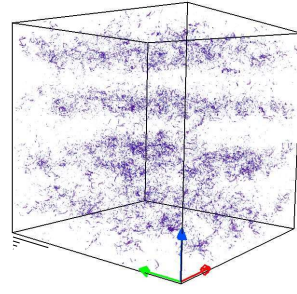
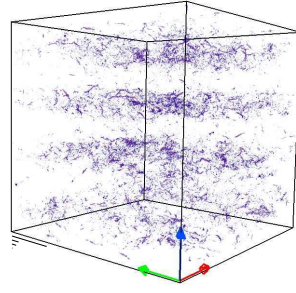
$$L^L(l) \equiv \langle (\delta v_\parallel(l))^2 (\delta u_\parallel(l)) \rangle \quad (6.36)$$

for Leray- $\alpha$ , and  $L(l) \equiv S_3^v$  for Navier-Stokes, are plotted versus  $l$  in Fig. 6.4. For the subgrid models, shown in Fig. 6.4 (a), the predicted  $l^1$  scaling (solid line) is well-reproduced by all models and the under-resolved run at scales larger than  $\alpha$  (vertical dashed line). The  $k_\alpha = 13$  results are shown in Fig. 6.4 (b) where we can see validation of the Kármán-Howarth scaling for scales smaller than  $\alpha$  for both LANS- $\alpha$  and Clark- $\alpha$ . In particular, we note the observed scaling for Clark- $\alpha$  verifies the  $vu^2 \sim l$  scaling and not the (theoretically possible)  $vu^2 \sim l^{-1}$  ( $u^3 \sim l$ ) scaling. The predicted scaling is not observed in Leray due to the reduced effective Reynolds number. With these scalings in hand, we may proceed to observe the scaling of the longitudinal structure functions,

$$S_p^v(l) \equiv \langle (\delta v_\parallel)^{p/2} \rangle, \quad (6.37)$$

where we again replace the  $H_\alpha^1$  norm,  $\langle |\delta v_\parallel| |\delta u_\parallel| \rangle$ , for the  $L^2$  norm,  $\langle (\delta v_\parallel)^2 \rangle$ , in the case of Clark- $\alpha$  and LANS- $\alpha$ . We utilize the extended self-similarity (ESS) hypothesis [14, 15, 13] which proposes the scaling

$$S_p^v(l) \propto \left( L^{(\alpha, L)}(l) \right)^{\xi_p},$$

(a)  $Re \approx 3300$  DNS(b) Clark- $\alpha$ (c) Leray- $\alpha$ (d) LANS- $\alpha$ 

(e) Under-resolved Navier-Stokes

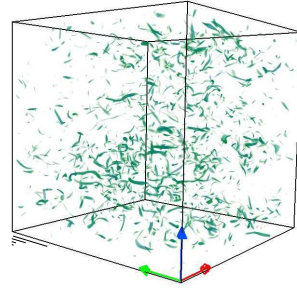
(f)  $Re \approx 1300$  DNS

Figure 6.3: Volume rendering of the enstrophy density  $\omega^2$  ( $\omega \cdot \bar{\omega}$  for LANS- $\alpha$  and Clark- $\alpha$ ). The four lengths depicted are integral length scale  $\mathcal{L}$ , Taylor scale  $\lambda$ , filter width  $\alpha$ , and dissipative scale  $\eta_K$  as calculated separately for each simulation. For (a)  $Re \approx 3300$  DNS, (b) Clark- $\alpha$ , (d) LANS- $\alpha$ , and (e) under-resolved Navier-Stokes the snapshot is for  $t = 9$ . For (c) Leray- $\alpha$  it is for  $t = 16$  and for (d)  $Re \approx 1300$  DNS it is for  $t = 19$  corresponding to their slower development of turbulence. For Leray- $\alpha$  the location of vortex tubes are consistent with a lower  $Re$  flow while the other models (including under-resolving) reproduce the large-scale pattern of the flow well. The color scale indicates the strength of the enstrophy density with purple stronger than green.



and normalize the results by  $\xi_3$  to better visualize the deviation from linearity (which serves as a measure of intermittency). The results are displayed in Fig. 6.5.

In Fig. 6.5 (b), we may more clearly observe the intermittency properties of the models at sub-filter scales. We note a reduced intermittency for both Leray- $\alpha$  and the  $Re \approx 1300$  DNS. This is consistent with the smoother, more laminar fields (due to reduced effective  $Re$ ) possessed by both. Interestingly, though LANS- $\alpha$  and Clark- $\alpha$  both possess the same cascade scaling, Eq. (6.14), as confirmed in Fig. 6.4 (b), Clark- $\alpha$  is markedly more intermittent. As artificially dropping local small-scale interactions gives enhanced intermittency [142, 69], this increased intermittency is the expected result of truncation of the higher-order terms in the sub-filter stress tensor. And, if LANS- $\alpha$ 's  $k^1$  spectrum is indeed associated with rigid bodies, these would serve to decrease the intermittency (no fluctuations inside a given rigid body) which is consistent with the results shown here. Due to this effect LANS- $\alpha$  of the three regularization models best reproduces the intermittency of the DNS for larger values of  $\alpha$ . In Fig. 6.5 (a), we display the SGS model intermittency results where all models reproduce the intermittency up to the tenth-order moment within the error bars (there is a small decrease in intermittency for Leray- $\alpha$ ). Thus, we conclude that with adequately chosen values of  $\alpha$  (and of  $\nu$  for Leray- $\alpha$ ), all three models can reproduce the intermittency of the DNS (to within the error bars).

## 6.4 Discussion of computational gains

The rationale behind doing LES is that it leads to adequate solutions with a reduced computational cost, through a lesser number of *dof*; indeed, for an LES, the ratio of Navier-Stokes's *dof* to the model's *dof*, a prediction for memory savings and hence computation time savings for numerical simulation, is a crucial factor. In this regard, analytical bounds on the size of the attractors for regularization subgrid models

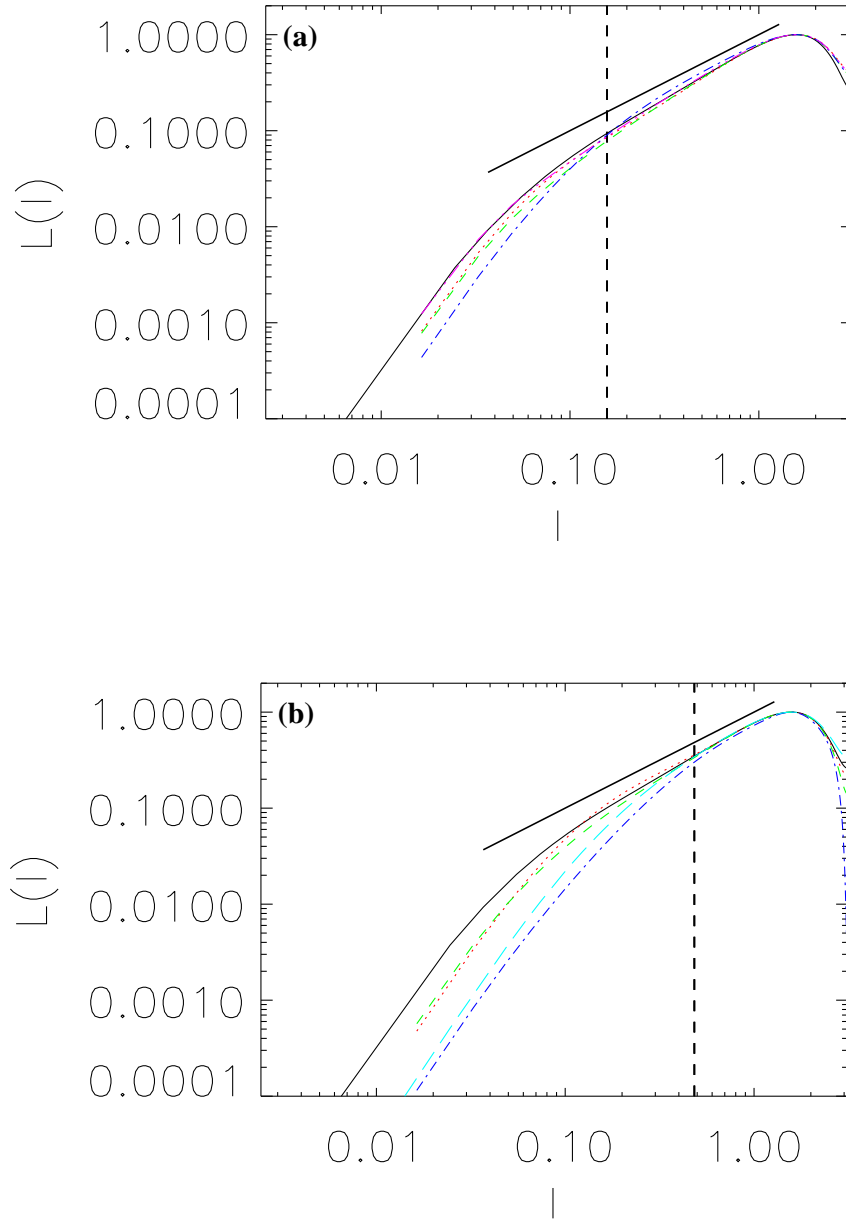


Figure 6.4: Third-order structure function associated with the Kármán-Howarth equation,  $L^{(\alpha, L)}(l)$ , versus length,  $l$ . Labels are as in Fig. 6.1. The vertical dashed lines indicate the lengths  $\alpha$ . **(a)**  $k_\alpha = 40$  **(b)**  $k_\alpha = 13$  The Clark- $\alpha$  result is consistent with a  $u^2v \sim l^1$  scaling, Eq. (6.14), and clearly inconsistent with a  $u^2v \sim l^{-1}$  ( $u^3 \sim l$ ) scaling as would arise from the middle term in Eq. (6.11). The truncation has very little effect on the scaling for the  $384^3$  under-resolved DNS. The results for Leray- $\alpha$  are again consistent with a reduced effective  $Re$ .

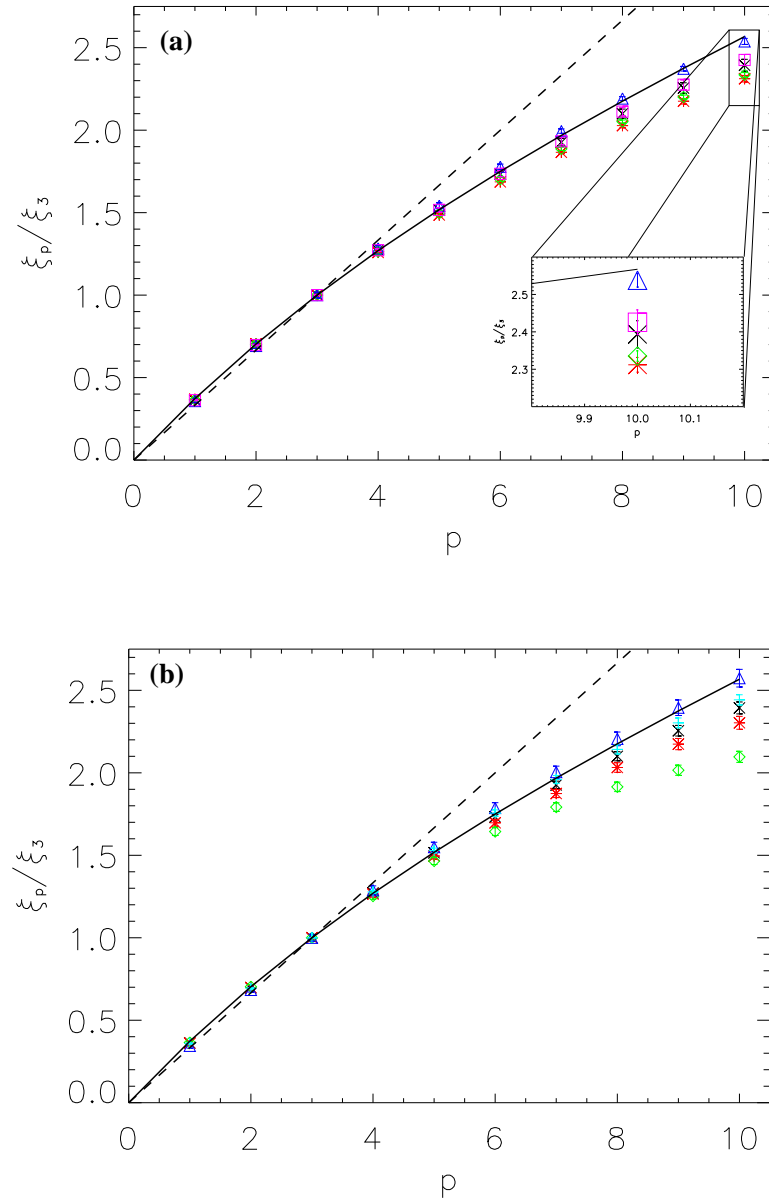


Figure 6.5: Normalized structure function scaling exponent  $\xi_p/\xi_3$  versus order  $p$ . The dashed line indicates K41 scaling and the solid line the She-Lévêque formula. The DNS results are indicated by black X's. **(a)**  $k_\alpha = 40$ , red asterisks for LANS- $\alpha$ , green diamonds for Clark- $\alpha$ , blue triangles for Leray- $\alpha$ , and pink boxes for the under-resolved Navier-Stokes run. With a small enough filter-width,  $\alpha$ , the intermittency properties of the DNS can be reproduced with all three models. **(b)**  $k_\alpha = 13$ : The  $Re \approx 1300$  DNS results are shown by cyan pluses. Leray- $\alpha$  is less intermittent consistent with the smoother field produced by a lower  $Re$  flow. Clark- $\alpha$  is more intermittent than Navier-Stokes at sub-filter scales. LANS- $\alpha$  is less intermittent than Clark- $\alpha$ , likely due to the influence of its rigid bodies (see text).

can be useful. The *dof* for LANS- $\alpha$  is derived in [77] and confirmed in Chapter 5,

$$dof_\alpha \propto \frac{L}{\alpha} Re^{3/2}, \quad (6.38)$$

where  $L$  is the integral scale (or domain size). We may compare this to the *dof* for Navier Stokes,

$$dof_{NS} \sim \left( \frac{L}{\eta_K} \right)^3 \sim Re^{9/4}, \quad (6.39)$$

which immediately yields

$$\frac{dof_{NS}}{dof_\alpha} \sim \left( \frac{\alpha}{L} \right) Re^{3/4}. \quad (6.40)$$

It was found, however, that to reproduce the energy spectrum of an equivalent DNS, the filter-width  $\alpha$  must be no larger than a few times the dissipation scale,  $\eta_K$  (see Chapter 5). With this added constraint it follows that the reduction in *dof* is independent of  $Re$  (and a factor of about 10). Our study here illustrates that the high-order structure functions can be reproduced for much larger values of  $\alpha$ . Therefore, in applications where the  $k^1$  rigid-body spectrum is not of great concern, much greater reduction in numerical resolution would be feasible.

For Clark- $\alpha$  there is an upper bound on the Hausdorff,  $d_H$ , and fractal,  $d_F$ , dimensions of the attractor,

$$d_H \leq d_F \leq C \left( \frac{L}{\eta_K^C} \right)^3 \left( \frac{L}{\alpha} \right)^{3/4}, \quad (6.41)$$

where  $\eta_K^C$  is the Kolmogorov dissipation length scale corresponding to the Clark- $\alpha$  model [42]. From its observed  $k^{-1}$  spectrum, we may estimate  $\eta_K^C$  or, equivalently,  $k_\eta^C \sim 1/\eta_K^C$ . For dissipation the large wavenumbers dominate and, therefore, combining the Clark- $\alpha$  energy balance Eq. (5.5) with its sub-filter scale energy spectrum Eq. (6.15) allows us to implicitly specify its dissipation wavenumber,  $k_\eta^C$ , by

$$\frac{\varepsilon_\alpha^C}{\nu} \sim \int^{k_\eta^C} k^2 E_\alpha^C(k) dk \sim \int^{k_\eta^C} k^2 (\varepsilon_\alpha^C)^{2/3} \alpha^{2/3} k^{-1} dk \sim (\varepsilon_\alpha^C)^{2/3} \alpha^{2/3} (k_\eta^C)^2. \quad (6.42)$$

Then we have,

$$k_\eta^C \sim \frac{(\varepsilon_\alpha^C)^{1/6}}{\nu^{1/2} \alpha^{1/3}}. \quad (6.43)$$

It follows that

$$\frac{dof_{NS}}{dof_{Clark}} \sim Re^{3/4} \left(\frac{\alpha}{L}\right)^{3/4} \alpha^{-1}. \quad (6.44)$$

This is similar to the prediction for LANS- $\alpha$ , but as energy spectra are more easily reproduced for larger values of  $\alpha$  than LANS- $\alpha$  (but not, necessarily, intermittency properties), it may be the case that  $\alpha$  is not tied to the Kolmogorov dissipation scale  $\eta_K$ . If so, then the computational saving might increase as  $Re^{3/4}$  which is promising for use as a LES. As the results in Section 6.3 for  $k_\alpha = 40$  ( $\alpha \approx 7\eta_K$ ) are acceptable, this may, indeed, be the case. If not, this is still a greater reduction in  $dof$  (a factor of 20) than for LANS- $\alpha$  (see Chapter 5).

For the Hausdorff,  $d_H$ , and fractal dimensions,  $d_F$ , of the global attractor, we have an upper bound for Leray- $\alpha$

$$d_H \leq d_F \leq c \left(\frac{L}{\eta_K^L}\right)^{12/7} \left(1 + \frac{L}{\alpha}\right)^{9/14} \quad (6.45)$$

where  $\eta_K^L$  is the dissipation length scale for Leray- $\alpha$  [60]. Again, we estimate the dissipation wavenumber for Leray- $\alpha$   $k_\eta^L \sim 1/\eta_K^L$ . From Eqs. (3.97) and (6.25), that is, assuming the  $k^{-1/3}$  spectrum resulting from the Kármán-Howarth equation, we find

$$\frac{\varepsilon^L}{\nu_L} \sim \int^{k_\eta^L} k^2 E^L(k) dk \sim \int^{k_\eta^L} k^2 (\varepsilon^L)^{2/3} \alpha^{4/3} k^{-1/3} dk \sim (\varepsilon^L)^{2/3} \alpha^{4/3} (k_\eta^L)^{8/3}. \quad (6.46)$$

Then we have,

$$k_\eta^L \sim \frac{(\varepsilon^L)^{1/8}}{\nu_L^{3/8} \alpha^{1/2}}. \quad (6.47)$$

It follows that

$$\frac{dof_{NS}}{dof_{Leray}} \sim \frac{L^{9/7} \nu^{-9/4}}{\nu_L^{-9/14} \alpha^{-6/7} (1 + \frac{L}{\alpha})^{9/14}}. \quad (6.48)$$

Our results suggest that for an effective LES  $\nu_L$  must be chosen *smaller* than  $\nu$ . This leads to an upper bound on the computational savings for Leray- $\alpha$ ,

$$\frac{dof_{NS}}{dof_{Leray}} < C \frac{Re^{45/28} \alpha^{6/7}}{(1 + \frac{L}{\alpha})^{9/14}}. \quad (6.49)$$

If we further assume that  $\alpha$  is directly proportional to the dissipative scale  $\eta_K$ , we arrive at

$$\frac{dof_{NS}}{dof_{Leray}} < C Re^{27/56} \quad (6.50)$$

which is not exceedingly promising for use as a LES. All such estimates are, however, purely conjectural until the proper choice of  $\alpha$  and  $\nu_L$  are determined.

## 6.5 Conclusions

We derived the Kármán-Howarth equations for the Leray- $\alpha$  and Clark- $\alpha$  models. These two models may be viewed as successive truncations of the sub-filter scale stress of the Lagrangian-Averaged Navier-Stokes  $\alpha$ -model (LANS- $\alpha$ ). In the case of Clark- $\alpha$  two different inertial range scalings follow from the dimensional analysis of this equation. The case of Leray- $\alpha$  is simpler as a single scaling is predicted (this is the case for Navier-Stokes and LANS- $\alpha$  as well). We computed solutions for a  $1024^3$  DNS under periodic boundary conditions ( $\nu = 3 \cdot 10^{-4}$ ,  $Re \approx 3300$ ) and at  $384^3$  resolution under the same exact conditions for LANS- $\alpha$ , Leray- $\alpha$ , Clark- $\alpha$ , and an under-resolved  $384^3$  solution of the Navier-Stokes equations. We employed two different filter widths  $\alpha$ . The first  $\alpha = 2\pi/40$  was employed to test the LES potential of the models and the second  $\alpha = 2\pi/13$  to test sub-filter scale predictions. We found that for Leray- $\alpha$ , as  $\alpha$  increases, the nonlinearity (and hence the effective Reynolds number  $Re$ ) is decreased substantially. For this reason, we were unable to confirm either the inertial range scaling from its Kármán-Howarth equation or its sub-filter scale energy spectrum. For Clark- $\alpha$  we were able to determine the dominant Kármán-Howarth inertial range scaling to be  $u^2 v \sim l$  and to confirm the associated  $k^{-1}$  energy spectrum.

The performance of the three regularizations as subgrid models (for a resolution of  $384^3$  and  $k_\alpha = 40$ ) was comparable to that of the under-resolved Navier-Stokes solution in reproducing the DNS energy spectrum. Only Clark- $\alpha$  showed a clear improvement in approximating the spectrum. From 3D volume rendering of enstrophy density we found Clark- $\alpha$  and LANS- $\alpha$  comparable to the under-resolved solution. Even at  $\alpha = 2\pi/40$ , Leray- $\alpha$ 's 3D spatial structures are more consistent with a significantly reduced  $Re$  flow (we compared to  $Re \approx 1300$ ). We note that the value of  $\alpha$  was chosen optimally for LANS- $\alpha$  at a resolution of  $384^3$  and that for Clark- $\alpha$  (and especially for Leray- $\alpha$ ) smaller resolutions may have comparable results for this value. That is, their performance should perhaps be compared to an even less well-resolved Navier-Stokes solution. Such a comparison is beyond the scope of this present work.

Though LANS- $\alpha$  and Clark- $\alpha$  exhibit the same inertial range scaling resulting from similarities in their Kármán-Howarth equations, Clark- $\alpha$  is decidedly more intermittent than the DNS for large values of  $\alpha$  (e.g.,  $\alpha = 2\pi/13$ ). At the same time, LANS- $\alpha$  is only slightly more intermittent than the DNS. These results are consistent with artificially dropping spectrally local small-scale interactions as the result of truncating the SGS stress tensor. This effect is reduced for LANS- $\alpha$  by its “rigid bodies” which can possess no internal fluctuations. For Leray- $\alpha$ , the observed reduced intermittency is related to its smoother, more laminar fields as a result of its reduced effective  $Re$ . Thus, its true sub-filter scale intermittency properties were also inaccessible.

Finally, we commented on the reduced *dof* of the models compared to Navier-Stokes (and, hence, their LES potential for computational savings). We note that as LANS- $\alpha$  reproduces the intermittency properties of a DNS well even for larger values of  $\alpha$ , a greater reduction in numerical saving can be achieved than previously predicted (see Chapter 5) if its  $k^1$  rigid-body energy spectrum is not important for a given application. As Clark- $\alpha$  possesses a similar reduction in *dof* to LANS- $\alpha$ , its LES potential is tied to the optimal value of  $\alpha$  for LES. Our study indicates that Clark- $\alpha$  may be applicable

(especially with regards to the energy spectrum) for larger values of  $\alpha$  than LANS- $\alpha$ . In fact, if its optimal value is not a function of  $Re$ , the computational resolution savings increases as  $Re^{3/4}$  for Clark- $\alpha$ . For the case of Leray- $\alpha$ , the prediction is complicated by the effective reduction in  $Re$  as  $\alpha$  increases. Prediction of optimized values of  $\alpha$  and of effective dissipation  $\nu_L$  are required to assess its LES potential. Future work should include such a study for both Leray- $\alpha$  and Clark- $\alpha$ .

All three regularizations are shown to be successful in that the control of the gradient reduces the degrees of freedom and saves computation while preserving a properly defined Reynolds number (albeit for Leray- $\alpha$  that definition is not yet determined). Clark- $\alpha$  reproduces well the total dissipation, the time scale to obtain a turbulent statistical steady-state, and the large-scale energy spectrum of a DNS. These results follow from Clark- $\alpha$  being an order  $\alpha^2$  approximation of Navier-Stokes. We have shown that Leray- $\alpha$  reduces the effective Reynolds number of the flow. Last of the three models, LANS- $\alpha$  restores Kelvin's circulation theorem (advected by a smoothed velocity) and the conservation of some form of helicity. Using spectra as a measure of the success of a subgrid model, LANS- $\alpha$  is a poor model due to its  $k^1$  sub-filter scale spectrum. Other measures of the success of a subgrid model are possible: for example, in regard to intermittency, LANS- $\alpha$  may be considered the superior model. For Clark- $\alpha$ , intermittency may be a function of filter width while for LANS- $\alpha$ , intermittency does not vary much with  $\alpha$ .



## Chapter 7

### Conclusion and future research problems

The efforts of a child trying to dam a small stream flowing in the street, and his surprise at the strange way the water works its way out, has its analog in our attempts over the years to understand the flow of fluids. We have tried to dam the water by getting the laws and equations . . . but the water has broken through the dam and escaped our attempt to understand it.

-Richard Feynman, *Lectures on Physics*

#### 7.1 Review of key results

This dissertation made some of the first inroads to practical application of regularizations as subgrid models for highly turbulent flows. Through careful examination of the limitations of these models, we begin to understand both how to employ them and how to interpret the results of their use. We have not demonstrated achievement of the ambitious goal of LES (which themselves have so far been *a posteriori* tested only on moderate  $Re$  flows) by reducing the degrees of freedom necessary to model high  $Re$  flows by orders of magnitude. But, rather, we have demonstrated the capability of reducing the resolution requirements by moderate amounts for such flows while still recovering the high-order statistics of the flow. This brings into reach the more reasonable goal of the detailed scientific study of high  $Re$  flows years before the computational resources become available for fully resolved simulations. Again, it is of great import to understand the limitations of the models and to differentiate the failings of the models from their reliable predictions.

The main conclusions of the dissertation are:

- The LAMHD- $\alpha$  model employed as a LES can reproduce the intermittency and other scalings (such as the cancellation exponent) of MHD DNS in *a posteriori* tests. The model does not corrupt the super-filter scale in these stringent tests for LES. This is an encouraging result for the model as a generally applicable MHD LES. It is also of interest to point out that the  $k^1$  energy spectrum which reduces the usefulness of LANS- $\alpha$  is absent from the LAMHD- $\alpha$  results. This could be due to the hyperdiffusivity in its induction equation. It may also be linked to the higher degree of nonlocality (in Fourier space) of nonlinear interactions in MHD (see [3, 168]).
- By achieving sufficient separation between scales, it was possible to numerically observe a Navier-Stokes inertial range followed by a LANS- $\alpha$  inertial range. This is an important result in that it validates theoretical developments of the LANS- $\alpha$  model and their associated predictions and demonstrates that multiple scaling ranges (dependent on the balances between different terms) are possible in turbulence.
- The LANS- $\alpha$  Kármán-Howarth scaling,  $u^2v \sim l$  ( $u^3 \sim l^3$ ), at *sub-filter scales* was confirmed. Further confirmation was provided by the associated  $k^{-1}$  energy spectrum observed for the regions between the rigid bodies introduced by LANS- $\alpha$  and by validation of the resulting prediction for the size of the LANS- $\alpha$  attractor. This provides a methodology for achieving either grid-independent LANS- $\alpha$  solutions or optimal  $\alpha$ -LES. It therefore reduces the number of free parameters for applying the model to only one, namely, the length scale  $\alpha$ .
- The sub-filter energy spectrum of LANS- $\alpha$ ,  $E(k) \sim k^1$ , was discovered and

associated with a “polymerization” of the fluid (behaving as rigid bodies with no internal degrees of freedom), due to the frozen-in-turbulence approximation employed in the derivation of the model. Because of this spectrum, LANS- $\alpha$  only approximates the DNS spectrum when  $\alpha \lesssim 4\eta_K$  where  $\eta_K$  is the Kolmogorov dissipation scale. This fixes the final free parameter fully specifying the application of the model. Consequently, the reduction in degrees of freedom is a factor of about one-twelfth (the reduction in computation cost including time stepping is a factor of one-twenty-seventh). These rigid bodies decrease the flux of energy to small scales as they possess no internal stretching motions. They also serve to decrease intermittency (resulting in a better approximation of the DNS intermittency), likely due to the conservation of circulation.

- The Kármán-Howarth equation for Clark- $\alpha$  was derived and confirmed (by determination of its leading factor) as was the associated  $k^{-1}$  energy spectrum *at sub-filter scales*. As the theory was unable to differentiate between the possible scalings, this result makes possible the use of theoretical predictions by specifying which one is applicable (at least for the forcing and boundary conditions employed). Clark- $\alpha$  was observed to exhibit an enhanced sub-filter scale intermittency but a similar sub-filter scale dissipation rate as compared to Navier-Stokes. This is an interesting result as Clark- $\alpha$  is the order  $\alpha^2$  Taylor approximation of the turbulent stress tensor. It shows that intermittency is reduced by higher order terms, or, perhaps by the conservation of circulation which is restored by LANS- $\alpha$  through the addition of other order  $\alpha^2$  cross terms not present in a Taylor expansion.
- The effect of increasing the filter width  $\alpha$  in the Leray- $\alpha$  model is to reduce the nonlinearity. Hence, the effective Reynolds number is smaller than  $v_{rms}L/\nu$ . For this reason, despite a derivation of the Kármán-Howarth equation for Leray- $\alpha$ ,

it was not possible to obtain numerical confirmation. This greatly reduces the LES potential of the Leray- $\alpha$  model inasmuch as a low  $Re$  flow does not model a high  $Re$  flow. Prior to this study, Leray- $\alpha$  was believed to have the greatest LES potential of the three Navier-Stokes regularizations presented.

## 7.2 Future research

This dissertation opens up several opportunities for further research and it has not touched upon several other important topics. The most important are outlined in this section.

**MHD:** As subgrid modeling for MHD is a relatively new field, much remains to be done:

- 3D studies of LAMHD- $\alpha$  would provide even smaller errors for the anomalous scaling though at increased computational expense.
- In a manner similar to Clark- $\alpha$  and Leray- $\alpha$  being truncations of LANS- $\alpha$ , simplifications could possibly be devised for LAMHD- $\alpha$ . As longer scaling ranges are computationally possible for 2D MHD than for 3D Navier-Stokes, this may be an approach at learning about the sub-filter scale properties of Leray- $\alpha$ .
- A detailed study of the scaling, as presented in Chapter 5 for LANS- $\alpha$ , should be done as well for LAMHD- $\alpha$ . Of particular interest is if LAMHD- $\alpha$  retains the intermittency properties without the rigid body energy spectrum, due to its hyperdiffusivity. It is also of great interest to learn if larger computational savings can be realized with LAMHD- $\alpha$  than with LANS- $\alpha$  due to this feature.
- Application of LAMHD- $\alpha$  to more realistic problems in geophysics and astrophysics, such as the dynamo problem at large magnetic Prandtl number ( $\nu \gg \eta$ )

as encountered in the interstellar medium or turbulent convection at low magnetic Prandtl number as encountered in the solar convection zone.

**Navier-Stokes:** A vast amount of work has already been accomplished for Navier-Stokes by several teams in the world, but work still remains to be done and a few new opportunities have been found in this dissertation:

- The hypothesized “rigid bodies” for LANS- $\alpha$  open several avenues for exploration:
  - \* Such rigid bodies should also be visible in the flow via other diagnostics (considered at the appropriate scale): the rotation vector (vorticity) should be orthogonal to the vector velocity increments and the Jacobian of the velocity field should be found to have a single real eigenvector, which is parallel to the vorticity.
  - \* The size of rigid bodies in LANS- $\alpha$  should be determined as well as the dependence of the size and the filling factor on  $\alpha$ . Visualization of their time evolution should also be carried out.
  - \* The intermittency properties of LANS- $\alpha$  in between the rigid bodies should be investigated. If the spectrum and intermittency of these portions of the flow are a reasonable model for Navier-Stokes, LANS- $\alpha$  may have wider application with greater computational saving.
  - \* Since Taylor’s frozen-in-turbulence hypothesis does not apply to Leray- $\alpha$  and Clark- $\alpha$ , we expect them not to show “polymerization” of the flow. This should be tested.
- As LANS- $\alpha$  has reduced sub-filter scale dissipation, its combination with a dissipative model may provide a promising LES. Both eddy-viscosity and hyperviscosity (perhaps similar to the hyperdiffusivity in LAMHD- $\alpha$ ) could be

tried.

- The universality of the scaling results for Clark- $\alpha$  should be investigated: do they change with the forcing and boundary conditions?
- A detailed study of the scaling, as presented in Chapter 5 for LANS- $\alpha$ , should be done as well for Clark- $\alpha$  and Leray- $\alpha$ . In the case of Clark- $\alpha$ , it is of interest to learn how large  $\alpha$  may be and the consequence this has on the computational savings achievable. Conversely, for Leray- $\alpha$  it is of interest to learn how small the filter width must be for Leray- $\alpha$  to begin to become a good model of high  $Re$  flows and to what extent  $\nu_L$  can be tuned to achieve this goal. This dissertation has shown the previous expectations of Leray- $\alpha$  were overly optimistic and it would be important to determine just how well it can perform as a LES.
- Turbulence has memory in that future behavior can exhibit a time-lag dependence on the field at previous times. This has been previously exploited for LES (see, e.g., [162]) and it would be of interest to learn if regularizations that incorporate previous evolution of the large-scale fields could be developed.
- Now that the sub-filter scale energy spectrum and intermittency properties are known for LANS- $\alpha$  and Clark- $\alpha$ , it remains to be seen how these properties affect application of the models to realistic flows at high  $Re$ .

**Analysis:** As pointed out in Chapter 1, the existence and uniqueness of smooth solutions to Navier-Stokes has remained an open problem for well over one hundred years. Leray was unable to prove the existence of *smooth* solutions with the Leray model. It would be of interest to see if any further progress could be made with the LANS- $\alpha$  or Clark- $\alpha$  regularizations as both of these capture more of the nonlinear behavior of Navier-Stokes than does the Leray model.

### 7.3 Final remarks

In this work we have answered several practical questions about regularizations as subgrid models for turbulent flows. We have demonstrated that properties of the nonlinear problem of fluid turbulence, such as the fundamental property of intermittency, can be preserved under careful modification of the nonlinearity (for instance, by preserving the symmetries: conservations laws, circulation, Kármán-Howarth theorem, etc.). The models so devised can be used to answer scientific questions about flows (especially when the shortcomings, as demonstrated here, are kept in mind) at a reduced computational cost. We have seen evidence that small-scale circulation (as preserved by the  $\alpha$ -model) is an important component for the closure problem. Helicity may reduce the small-scale nonlinear local interactions (the nonlinearity is zero spatially whenever velocity and vorticity are aligned) and this favors the importance of nonlocal interactions which lead to intermittency. At the same time, local interactions may only be entirely removed in the dissipative range. To do otherwise results in a reduction of spectral flux and an incorrect turbulent energy spectrum (as is the case for LANS- $\alpha$ ). Thus, the solution to the closure problem (either for subgrid modeling or for analysis) should include the proper balance between local and nonlocal interactions, which is different in different ranges of scales.

## Bibliography

- [1] O. Agullo, W.-C. Müller, B. Knaepen, and D. Carati. Large eddy simulation of decaying magnetohydrodynamic turbulence with dynamic subgrid-modeling. Physics of Plasmas, 8:3502–3505, July 2001.
- [2] A. Alexakis, P. D. Mininni, and A. Pouquet. Imprint of Large-Scale Flows on Turbulence. Physical Review Letters, 95(26):264503–+, December 2005.
- [3] A. Alexakis, P. D. Mininni, and A. Pouquet. Shell-to-shell energy transfer in magnetohydrodynamics. I. Steady state turbulence. Phys. Rev. E, 72(4):046301–+, October 2005.
- [4] A. Alexakis, P. D. Mininni, and A. Pouquet. On the Inverse Cascade of Magnetic Helicity. ApJ, 640:335–343, March 2006.
- [5] D. G. Andrews and M. E. McIntyre. An exact theory of nonlinear waves on a Lagrangian-mean flow. J. Fluid Mech., 89:609–646, 1978.
- [6] R. A. Antonia, M. Ould-Rouis, F. Anselmet, and Y. Zhu. Analogy between predictions of Kolmogorov and Yaglom. Journal of Fluid Mechanics, 332:395–409, February 1997.
- [7] Gregory L. Baker and Jerry P. Gollub. Chaotic Dynamics: an introduction. Cambridge University Press, Cambridge, 1990.
- [8] J. Bardina, J. H. Ferziger, and W. C. Reynolds, editors. Improved subgrid-scale models for large-eddy simulation, July 1980.
- [9] C. Basdevant, B. Legras, R. Sadourny, and M. Béland. A Study of Barotropic Model Flows: Intermittency, Waves and Predictability. Journal of Atmospheric Sciences, 38:2305–2326, November 1981.
- [10] G. K. Batchelor. On the Spontaneous Magnetic Field in a Conducting Liquid in Turbulent Motion. Proceedings of the Royal Society of London. Series A, Mathematical and Physical Sciences, 201(1066):405–416, 1950.
- [11] G. K. Batchelor. An Introduction to Fluid Dynamics. Cambridge University Press, Cambridge, 1967.
- [12] R. Benzi, L. Biferale, S. Ciliberto, M. V. Struglia, and R. Tripiccone. Generalized scaling in fully developed turbulence. Physica D, 1996.



- [13] R. Benzi, L. Biferale, S. Ciliberto, M. V. Struglia, and R. Tripiccone. Scaling property of turbulent flows. Phys. Rev. E, 53:R3025–+, April 1996.
- [14] R. Benzi, S. Ciliberto, C. Baudet, G. Ruiz Chavarria, and R. Tripiccone. Extended self-similarity in the dissipation range of fully developed turbulence. Europhysics Letters, 24:275–+, November 1993.
- [15] R. Benzi, S. Ciliberto, R. Tripiccone, C. Baudet, F. Massaioli, and S. Succi. Extended self-similarity in turbulent flows. Phys. Rev. E, 48:R29–+, July 1993.
- [16] D. Bernard, G. Boffetta, A. Celani, and G. Falkovich. Conformal invariance in two-dimensional turbulence. Nature Physics, 2:124–128, February 2006.
- [17] L. Berselli, G. Galdi, T. Iliescu, and W. Layton. Mathematical analysis for the rational large eddy simulation model. Math. Models and Methods in App. Sci., 12:1131, 2002.
- [18] A. Bershadskii and K. R. Sreenivasan. Intermittency and the Passive Nature of the Magnitude of the Magnetic Field. Physical Review Letters, 93(6):064501–+, August 2004.
- [19] H. S. Bhat, R. C. Fetecau, J. E. Marsden, and K. Mohseni. Lagrangian Averaging for Compressible Fluids. 2003. [arXiv:physics/0311086](https://arxiv.org/abs/physics/0311086).
- [20] J. Birn and M. Hesse. Details of current disruption and diversion in simulations of magnetotail dynamics. J. Geophys. Res., 101:15345–15358, July 1996.
- [21] D. Biskamp and W.-C. Müller. Scaling properties of three-dimensional isotropic magnetohydrodynamic turbulence. Physics of Plasmas, 7:4889–4900, December 2000.
- [22] D. Biskamp and E. Schwarz. On two-dimensional magnetohydrodynamic turbulence. Physics of Plasmas, 8(7):3282–3292, 2001.
- [23] D. Biskamp, E. Schwarz, and A. Celani. Nonlocal Bottleneck Effect in Two-Dimensional Turbulence. Physical Review Letters, 81:4855–4858, November 1998.
- [24] D. Biskamp and H. Welter. Dynamics of decaying two-dimensional magnetohydrodynamic turbulence. Physics of Fluids B, 1:1964–1979, October 1989.
- [25] Mary L. Boas. Mathematical Methods in the Physical Sciences. John Wiley & Sons, New York, 2nd edition, 1983.
- [26] S. Boldyrev, J. Mason, and F. Cattaneo. Dynamic Alignment and Exact Scaling Laws in MHD Turbulence. ArXiv Astrophysics e-prints, May 2006.
- [27] V. Borue and S. A. Orszag. Self-similar decay of three-dimensional homogeneous turbulence with hyperviscosity. Phys. Rev. E, 51:856–+, February 1995.
- [28] M. Bourgoïn, L. Marié, F. Pétrélis, C. Gasquet, A. Guigon, J.-B. Luciani, M. Moulin, F. Namer, J. Burguete, A. Chiffaudel, F. Daviaud, S. Fauve, P. Odier, and J.-F. Pinton. Magnetohydrodynamics measurements in the von Kármán sodium experiment. Physics of Fluids, 14:3046–3058, September 2002.

- [29] J. Boussinesq. Théorie de l' Écoulement Tourbillant. Mem. Présentés par Divers Savants Acad. Sci. Inst. Fr., 23:46–50, 1877.
- [30] M. Brachet. The geometry of small-scale structures in a Taylor-Green vortex. Academie des Sciences Paris Comptes Rendus Serie Sciences Mathematiques, 311:775–780, September 1990.
- [31] A. Brandenburg. The Case for a Distributed Solar Dynamo Shaped by Near-Surface Shear. ApJ, 625:539–547, May 2005.
- [32] A. Brandenburg and W. Dobler. Hydromagnetic turbulence in computer simulations. Computer Physics Communications, 147:471–475, August 2002.
- [33] A. Brandenburg and G. R. Sarson. Effect of Hyperdiffusivity on Turbulent Dynamos with Helicity. Physical Review Letters, 88(5):055003–+, February 2002.
- [34] A. Brandenburg and K. Subramanian. Astrophysical magnetic fields and nonlinear dynamo theory. Phys. Rep., 417:1–4, October 2005.
- [35] J. W. Brault and O. R. White. The Analysis and Restoration of Astronomical Data via the Fast Fourier Transform. Astron. & Astrophys., 13:169–+, July 1971.
- [36] M. K. Browning, M. S. Miesch, A. S. Brun, and J. Toomre. Dynamo Action in the Solar Convection Zone and Tachocline: Pumping and Organization of Toroidal Fields. ApJ, 648:L157–L160, September 2006.
- [37] A. S. Brun, M. S. Miesch, and J. Toomre. Global-Scale Turbulent Convection and Magnetic Dynamo Action in the Solar Envelope. ApJ, 614:1073–1098, October 2004.
- [38] A. S. Brun and J. Toomre. Turbulent Convection under the Influence of Rotation: Sustaining a Strong Differential Rotation. ApJ, 570:865–885, May 2002.
- [39] J. M. Burgers. A mathematical model illustrating the theory of turbulence. Advances in Applied Mechanics, 1:171–199, 1948.
- [40] Roberto Camassa and Darryl D. Holm. An Integrable Shallow Water Equation with Peaked Solutions. Physical Review Letters, 71(11):1661–1664, 1993.
- [41] Claudio Canuto, M. Yousuff Hussaini, Alfio Quarteroni, and Thomas A. Zang. Spectral Methods in Fluid Dynamics. Springer-Verlag, New York, 1988.
- [42] C. Cao, D. D. Holm, and E. S. Titi. On the Clark  $\alpha$  model of turbulence: global regularity and long-time dynamics. Journal of Turbulence, 6:19–+, 2005.
- [43] D. Carati, G. S. Winckelmans, and H. Jeanmart. On the modelling of the subgrid-scale and filtered-scale stress tensors in large-eddy simulation. Journal of Fluid Mechanics, 441:119–138, August 2001.
- [44] V. Carbone and R. Bruno. Sign Singularity of the Magnetic Helicity from In Situ Solar Wind Observations. ApJ, 488:482–+, October 1997.

- [45] F. Cattaneo. On the Origin of Magnetic Fields in the Quiet Photosphere. ApJ, 515:L39–L42, April 1999.
- [46] S. Cerutti and C. Meneveau. Intermittency and relative scaling of subgrid-scale energy dissipation in isotropic turbulence. Physics of Fluids, 10:928–937, April 1998.
- [47] CFD-Wiki. Center for computational fluid dynamics-wiki, 2007. [Online; accessed 4-June-2007].
- [48] F. H. Champagne. The fine-scale structure of the turbulent velocity field. Journal of Fluid Mechanics, 86:67–108, May 1978.
- [49] S. Chandrasekhar. The Theory of Axisymmetric Turbulence. Philosophical Transactions of the Royal Society of London. Series A, Mathematical and Physical Sciences, 242(855):557–577, 1950.
- [50] S. Chandrasekhar. The Invariant Theory of Isotropic Turbulence in Magneto-Hydrodynamics. Proceedings of the Royal Society of London. Series A, Mathematical and Physical Sciences, 204(1079):435–449, 1951.
- [51] S. Chandrasekhar. The Invariant Theory of Isotropic Turbulence in Magneto-Hydrodynamics. II. Proceedings of the Royal Society of London. Series A, Mathematical and Physical Sciences, 207(1090):301–306, 1951.
- [52] S. Chandrasekhar and P. C. Kendall. On Force-Free Magnetic Fields. ApJ, 126:457–+, September 1957.
- [53] P. Charbonneau. Multiperiodicity, Chaos, and Intermittency in a Reduced Model of the Solar Cycle. Sol. Phys., 199:385–404, April 2001.
- [54] P. Charbonneau, G. Blais-Laurier, and C. St-Jean. Intermittency and Phase Persistence in a Babcock-Leighton Model of the Solar Cycle. ApJ, 616:L183–L186, December 2004.
- [55] S. Chen, C. Foias, D. D. Holm, E. Olson, E. S. Titi, and S. Wynne. Camassa-Holm Equations as a Closure Model for Turbulent Channel and Pipe Flow. Physical Review Letters, 81:5338–5341, December 1998.
- [56] S. Chen, C. Foias, D. D. Holm, E. Olson, E. S. Titi, and S. Wynne. A connection between the Camassa-Holm equations and turbulent flows in channels and pipes. Physics of Fluids, 11:2343–2353, August 1999.
- [57] S. Chen, C. Foias, D. D. Holm, E. Olson, E. S. Titi, and S. Wynne. The Camassa-Holm equations and turbulence. Physica D Nonlinear Phenomena, 133:49–65, 1999.
- [58] S. Chen, D. D. Holm, L. G. Margolin, and R. Zhang. Direct numerical simulations of the Navier-Stokes alpha model. Physica D Nonlinear Phenomena, 133:66–83, 1999.

- [59] A. Cheskidov. Turbulent Boundary Layer Equations. C.R. Acad. Ser. I, 334:423, 2002.
- [60] Alexey Cheskidov, Darryl D. Holm, Eric Olson, and Edriss S. Titi. On a Leray– $\alpha$  model of turbulence. Proceedings of the Royal Society of London, A461:629–649, 2005.
- [61] J.-P. Chollet and M. Lesieur. Parameterization of Small Scales of Three-Dimensional Isotropic Turbulence Utilizing Spectral Closures. Journal of Atmospheric Sciences, 38:2747–2757, December 1981.
- [62] C. Cichowlas, P. Bonaïti, F. Debbasch, and M. Brachet. Effective Dissipation and Turbulence in Spectrally Truncated Euler Flows. Physical Review Letters, 95(26):264502–+, December 2005.
- [63] R. A. Clark, J. H. Ferziger, and W. C. Reynolds. Evaluation of subgrid-scale models using an accurately simulated turbulent flow. Journal of Fluid Mechanics, 91:1–16, March 1979.
- [64] T. C. Clune, J. R. Elliott, M. Miesch, J. Toomre, and G. A. Glatzmaier. Computational aspects of a code to study rotating turbulent convection in spherical shells. Parallel Computing, 25:361–390, 1999.
- [65] P. Constantin, E. Weinan, and E. S. Titi. Onsager’s conjecture on the energy conservation for solutions of Euler’s equation. Communications in Mathematical Physics, 165:207–209, October 1994.
- [66] P. A. Davidson. An Introduction to Magnetohydrodynamics. Cambridge University Press, Cambridge, UK, March 2001.
- [67] M. A. de Avillez and D. Breitschwerdt. Global dynamical evolution of the ISM in star forming galaxies. I. High resolution 3D simulations: Effect of the magnetic field. A&A, 436:585–600, June 2005.
- [68] Theodore de Kármán and Leslie Howarth. On the Statistical Theory of Isotropic Turbulence. Proceedings of the Royal Society of London, A164:192–215, 1938.
- [69] B. Dubrulle, J.-P. Laval, S. Nazarenko, and O. Zaboronski. A model for rapid stochastic distortions of small-scale turbulence. Journal of Fluid Mechanics, 520:1–21, December 2004.
- [70] S. Dyachenko, A. C. Newell, A. Pushkarev, and V. E. Zakharov. Optical turbulence: weak turbulence, condensates and collapsing filaments in the nonlinear Schrödinger equation. Physica D Nonlinear Phenomena, 57:96–160, June 1992.
- [71] Robert Ecke. The Turbulence Problem: An Experimentalist’s Perspective. Los Alamos Science, (29):124–141, 2005.
- [72] J. R. Elliott, M. S. Miesch, and J. Toomre. Turbulent Solar Convection and Its Coupling with Rotation: The Effect of Prandtl Number and Thermal Boundary Conditions on the Resulting Differential Rotation. ApJ, 533:546–556, April 2000.

- [73] G. L. Eyink. Local 4/5-law and energy dissipation anomaly in turbulence . Nonlinearity, 16:137–145, January 2003.
- [74] G.L. Eyink. Exact results on stationary turbulence in 2D: consequences of vorticity conservation. Physica D Nonlinear Phenomena, 91:97–142, 1996.
- [75] B. R. Fabijonas and D. D. Holm. Mean Effects of Turbulence on Elliptic Instability in Fluids. Physical Review Letters, 90(12):124501–+, March 2003.
- [76] Raffaele Ferrari and Glenn R. Flierl. Turbulence in geophysical systems. <http://ocw.mit.edu/OcwWeb/Earth-Atmospheric-and-Planetary-Sciences/12-820Spring-2005/CourseHome/index.htm>.
- [77] C. Foias, D. D. Holm, and E. S. Titi. The Navier-Stokes-alpha model of fluid turbulence. Physica D Nonlinear Phenomena, 152-153:505–519, May 2001.
- [78] C. Foias, D. D. Holm, and E. S. Titi. The three dimensional viscous camassa-holm equations, and thier relation to the navier-stokes equations and turbulence theory. Journal of Dynamics and Differential Equations, 14(1):1–35, January 2002.
- [79] Matteo Frigo and Steven G. Johnson. FFTW: An adaptive software architecture for the FFT. In Proc. 1998 IEEE Intl. Conf. Acoustics Speech and Signal Processing, volume 3, pages 1381–1384. IEEE, 1998.
- [80] Uriel Frisch. Turbulence, The Legacy of A. N. Kolmogorov. Cambridge University Press, Cambridge, UK, 1995.
- [81] D. O. Gómez, P. D. Mininni, and P. Dmitruk. Parallel Simulations in Turbulent MHD”. Physica Scripta, page 123, 2005.
- [82] S. Galtier, S. V. Nazarenko, A. C. Newell, and A. Pouquet. A weak turbulence theory for incompressible magnetohydrodynamics. Journal of Plasma Physics, 63:447–488, June 2000.
- [83] S. Galtier and A. Pouquet. Solar Flare Statistics with a One-Dimensional MHD Model. Sol. Phys., 179:141–165, 1998.
- [84] M. Germano. Turbulence - The filtering approach. Journal of Fluid Mechanics, 238:325–336, May 1992.
- [85] M. Germano, U. Piomelli, P. Moin, and W. H. Cabot. A dynamic subgrid-scale eddy viscosity model. Physics of Fluids, 3:1760–1765, July 1991.
- [86] B. J. Geurts and J. Fröhlich. A framework for predicting accuracy limitations in large-eddy simulation. Physics of Fluids, 14:L41–L44, June 2002.
- [87] B. J. Geurts and D. D. Holm. Alpha-Modeling Strategy for LES of Turbulent Mixing. In D. Drikakis and B. J. Geurts, editors, Turbulent Flow Computation, pages 237+, London, 2002. Kluwer Academic Publishers.
- [88] B. J. Geurts and D. D. Holm. Leray Simulation of Turbulent Shear Layers. In J. P. Castro and P. E. Hancock, editors, Advances in Turbulence IX: Proceedings of the Ninth European Turbulence Conference, pages 337+, Barcelona, 2002. CIMNE.

- [89] B. J. Geurts and D. D. Holm. Regularization modeling for large-eddy simulation. Physics of Fluids, 15:L13–L16, January 2003.
- [90] Bernard J. Geurts and Darryl D. Holm. Leray and LANS- $\alpha$  modelling of turbulent mixing. Journal of Turbulence, 7(10):1–33, 2006.
- [91] J. D. Gibbon and D. D. Holm. Length-scale estimates for the LANS- $\alpha$  equations in terms of the Reynolds number. Physica D Nonlinear Phenomena, 220:69–78, August 2006.
- [92] G. A. Glatzmaier and J. Toomre. Global-Scale Solar Turbulent Convection and its Coupling to Rotation. In R. K. Ulrich, E. J. Rhodes, Jr., and W. Dappen, editors, ASP Conf. Ser. 76: GONG 1994. Helio- and Astro-Seismology from the Earth and Space, pages 200–+, 1995.
- [93] D. O. Gómez, P. D. Mininni, and P. Dmitruk. MHD simulations and astrophysical applications. Advances in Space Research, 35:899–907, 2005.
- [94] T. Gomez, H. Politano, and A. Pouquet. On the validity of a nonlocal approach for MHD turbulence. Physics of Fluids, 11:2298–2306, August 1999.
- [95] J. T. Gosling, J. Birn, and M. Hesse. Three-dimensional magnetic reconnection and the magnetic topology of coronal mass ejection events. Geophys. Res. Lett., 22:869–872, April 1995.
- [96] David Gottlieb and Steven A. Orszag. Numerical Analysis of Spectral Methods: Theory and Applications. J.W. Arrowsmith Ltd., Bristol, UK, 1977.
- [97] H. L. Grant, R. W. Stewart, and A. Moilliet. Turbulence spectra from a tidal channel. Journal of Fluid Mechanics, 12:241–268, 1962.
- [98] R. Grauer, J. Krug, and C. Marliani. Scaling of high-order structure functions in magnetohydrodynamic turbulence. Physics Letters A, 195:335–338, December 1994.
- [99] R. J. Greatbatch and B. T. Nadiga. Four Gyre Circulation in a Barotropic Model with Double Gyre Wind Forcing. J. Phys. Oceanogr., 30:1461, 2000.
- [100] Ronald B. Guenther and John W. Lee. Partial Differential Equations of Mathematical Physics and Integral Equations. Dover Publications, Inc., New York, 1996.
- [101] N. E. Haugen and A. Brandenburg. Inertial range scaling in numerical turbulence with hyperviscosity. Phys. Rev. E, 70(2):026405–+, August 2004.
- [102] N. E. Haugen, A. Brandenburg, and W. Dobler. Simulations of nonhelical hydro-magnetic turbulence. Phys. Rev. E, 70(1):016308–+, July 2004.
- [103] N. E. L. Haugen and A. Brandenburg. Hydrodynamic and hydromagnetic energy spectra from large eddy simulations. Physics of Fluids, 18:5106–+, July 2006.
- [104] Stephen Hawking, editor. Stephen Hawking’s A brief history of time : a reader’s companion. Bantam Books, New York, 1992.

- [105] G. Heinemann. On the consideration of mesoscale transports in climate modelling. Theoretical and Applied Climatology, 83:35–50, January 2006.
- [106] J. R. Herring, D. Schertzer, M. Lesieur, G. R. Newman, J. P. Chollet, and M. Larcheveque. A comparative assessment of spectral closures as applied to passive scalar diffusion. Journal of Fluid Mechanics, 124:411–437, 1982.
- [107] D. D. Holm. Fluctuation Effects on 3D Lagrangian Mean and Eulerian Mean Fluid Motion. Physica D Nonlinear Phenomena, 133:215+, 1999.
- [108] D. D. Holm. Averaged Lagrangians and the mean effects of fluctuations in ideal fluid dynamics. Physica D Nonlinear Phenomena, 170:253–286, September 2002.
- [109] D. D. Holm. Kármán Howarth theorem for the Lagrangian-averaged Navier Stokes alpha model of turbulence. Journal of Fluid Mechanics, 467:205–214, September 2002.
- [110] D. D. Holm. Lagrangian averages, averaged Lagrangians, and the mean effects of fluctuations in fluid dynamics. Chaos, 12:518–530, 2002.
- [111] D. D. Holm and R. Kerr. Transient Vortex Events in the Initial Value Problem for Turbulence. Physical Review Letters, 88(24):244501–+, June 2002.
- [112] D. D. Holm, J. E. Marsden, and T. S. Ratiu. Euler-Poincaré Models of Ideal Fluids with Nonlinear Dispersion. Physical Review Letters, 80:4173–4176, May 1998.
- [113] D. D. Holm, J. E. Marsden, and T. S. Ratiu. The Euler-Poincaré Equations and Semidirect Products with Applications to Continuum Theories. Adv. in Math., 137:1–81, 1998.
- [114] D. D. Holm and B. Nadiga. Modeling Mesoscale Turbulence in the Barotropic Double Gyre Circulation. J. Phys. Oceanogr., 33:2355, 2003.
- [115] D. D. Holm, V. Putkaradze, P. D. Weidman, and B. A. Wingate. Boundary Effects on Exact Solutions of the Lagrangian-Averaged Navier-Stokes- $\alpha$  Equations. J. Stat. Phys., 113:841, 2003.
- [116] D. D. Holm and B. A. Wingate. Baroclinic instabilities of the two-layer quasi-geostrophic alpha model. J. Phys. Oceanogr., 35:1287–1296, 2005.
- [117] Darryl D. Holm. Modified speziale model for les turbulence. private communication, 2003.
- [118] Darryl D. Holm. Taylor’s Hypothesis, Hamilton’s Principle, and the LANS- $\alpha$  Model for Computing Turbulence. Los Alamos Science, (29):172–180, 2005.
- [119] Darryl D. Holm, Chris Jeffery, Susan Kurien, Daniel Livescu, Mark A. Taylor, and Beth A. Wingate. The LANS- $\alpha$  Model for Computing Turbulence: Origins, Results, and Open Problems. Los Alamos Science, (29):152–171, 2005.
- [120] P. Hoyng. Helicity fluctuations in mean field theory: an explanation for the variability of the solar cycle? A&A, 272:321–+, May 1993.



- [121] P. Hoyng, M. A. J. H. Ossendrijver, and D. Schmitt. The geodynamo as a bistable oscillator. Geophysical and Astrophysical Fluid Dynamics, 94:263–+, 2001.
- [122] P. Hoyng, D. Schmitt, and M. A. J. H. Ossendrijver. A theoretical analysis of the observed variability of the geomagnetic dipole field. Physics of the Earth and Planetary Interiors, 130:143–157, April 2002.
- [123] John K. Hunter and Bruno Nachtergaele. Applied Analysis. World Scientific Publishing Co. Pte. Ltd., New Jersey, 2001.
- [124] A. A. Ilyin, E. M. Lunasin, and E. S. Titi. A modified-Leray- $\alpha$  subgrid scale model of turbulence. Nonlinearity, 19:879–897, April 2006.
- [125] P. S. Iroshnikov. Turbulence of a Conducting Fluid in a Strong Magnetic Field. Soviet Astronomy, 7:566–+, February 1964.
- [126] Y. Kaneda, T. Ishihara, M. Yokokawa, K. Itakura, and A. Uno. Energy dissipation rate and energy spectrum in high resolution direct numerical simulations of turbulence in a periodic box. Physics of Fluids, 15:L21–L24, February 2003.
- [127] H. S. Kang, S. Chester, and C. Meneveau. Decaying turbulence in an active-grid-generated flow and comparisons with large-eddy simulation. Journal of Fluid Mechanics, 480:129–160, April 2003.
- [128] B. Knaepen and P. Moin. Large-eddy simulation of conductive flows at low magnetic Reynolds number. Physics of Fluids, 16:1255–+, May 2004.
- [129] A. N. Kolmogorov. Dissipation of energy in locally isotropic turbulence. Dokl. Akad. Nauk SSSR, 32(1):16–18, 1941. Reprinted in *Proc. R. Soc. Lond. A (1991)* **434**, 15–17.
- [130] A. N. Kolmogorov. On degeneration (decay) of isotropic turbulence in an incompressible viscous liquid. Dokl. Akad. Nauk SSSR, 31:538–540, 1941.
- [131] A. N. Kolmogorov. The local structure of turbulence in incompressible viscous fluid for very large Reynolds numbers. Dokl. Akad. Nauk SSSR, 30(4):299–303, 1941. Reprinted in *Proc. R. Soc. Lond. A (1991)* **434**, 9–13.
- [132] A. N. Kolmogorov. A refinement of previous hypotheses concerning the local structure of turbulence in a viscous incompressible fluid at high Reynolds number. Journal of Fluid Mechanics, 13:82–85, 1962.
- [133] R. H. Kraichnan. Inertial-range spectrum of hydromagnetic turbulence. Physics of Fluids, 8:1385–1387, 1965.
- [134] R. H. Kraichnan. Inertial Ranges in Two-Dimensional Turbulence. Physics of Fluids, 10:1417–1423, 1967.
- [135] R. H. Kraichnan. Eddy viscosity in two and three dimensions. Journal of Atmospheric Sciences, 33:1521–1536, August 1976.
- [136] R. H. Kraichnan and S. Nagarajan. Growth of Turbulent Magnetic Fields. Physics of Fluids, 10:859–870, 1967.



- [137] J. R. Kulkarni, L. K. Sadani, and B. S. Murthy. Wavelet Analysis of Intermittent Turbulent Transport in the Atmospheric Surface Layer over a Monsoon Trough Region. Boundary-Layer Meteorology, 90:217–239, 1999.
- [138] Pijush K. Kundu. Fluid Mechanics. Academic Press, San Diego, 1990.
- [139] S. Kurien, M. A. Taylor, and T. Matsumoto. Cascade time scales for energy and helicity in homogeneous isotropic turbulence. Phys. Rev. E, 69(6):066313–+, June 2004.
- [140] Susan Kurien and Mark A. Taylor. Direct Numerical Simulations of Turbulence: Data Generation and Statistical Analysis. Los Alamos Science, (29):142–151, 2005.
- [141] E. L  v  que and C. R. Koudella. Finite-Mode Spectral Model of Homogeneous and Isotropic Navier-Stokes Turbulence: A Rapidly Depleted Energy Cascade. Physical Review Letters, 86:4033–4036, April 2001.
- [142] J.-P. Laval, B. Dubrulle, and S. Nazarenko. Nonlocality and intermittency in three-dimensional turbulence. Physics of Fluids, 13:1995–2012, July 2001.
- [143] A. Leonard. Energy cascade in large-eddy simulations of turbulent fluid flows. In Turbulent diffusion in environmental pollution; Proceedings of the Second Symposium, Charlottesville, Va., April 8-14, 1973. Volume A. (A75-30951 13-47) New York, Academic Press, Inc., 1974, p. 237-248. NASA-supported research., pages 237–248, 1974.
- [144] J. Leray. Essai sur le mouvement d’un fluide visqueux emplissant l’espace. Acta Math., (63):193–248, 1934.
- [145] M. Lesieur and O. Metais. New trends in large-eddy simulations of turbulence. Annual Review of Fluid Mechanics, 28:45–82, 1996.
- [146] Marcel Lesieur. Turbulence in Fluids. Kluwer Academic Publishers, Dordrecht, 3rd edition, 2000.
- [147] D. K. Lilly. The representation of small-scale turbulence in numerical simulation experiments. In Proc. IBM Scientific Computing Symp. Environ. Sci., page 195, 1967.
- [148] D. K. Lilly. A proposed modification of the Germano subgrid-scale closure method. Physics of Fluids, 4:633–635, March 1992.
- [149] J. S. Linshiz and E. S. Titi. Analytical Study of Certain Magnetohydrodynamic-alpha Models. ArXiv Mathematics e-prints, June 2006.
- [150] S. Liu, C. Meneveau, and J. Katz. On the properties of similarity subgrid-scale models as deduced from measurements in a turbulent jet. Journal of Fluid Mechanics, 275:83–119, 1994.
- [151] D. Lohse and A. M  ller-Groeling. Bottleneck Effects in Turbulence: Scaling Phenomena in  $r$  versus  $p$  Space. Physical Review Letters, 74:1747–1750, March 1995.

- [152] D. W. Longcope and R. N. Sudan. Renormalization group analysis of reduced magnetohydrodynamics with application to subgrid modeling. Physics of Fluids B, 3:1945–1962, August 1991.
- [153] E. Lunasin, S. Kurien, M. Taylor, and E. Titi. A study of the Navier-Stokes-alpha model for two-dimensional turbulence. ArXiv Physics e-prints, February 2007.
- [154] D. O. Martínez, S. Chen, G. D. Doolen, R. H. Kraichnan, L.-P. Wang, and Y. Zhou. Energy spectrum in the dissipation range of fluid turbulence. Journal of Plasma Physics, 57:195–201, January 1997.
- [155] J. Mason, F. Cattaneo, and S. Boldyrev. Dynamic Alignment in Driven Magnetohydrodynamic Turbulence. Physical Review Letters, 97(25):255002–+, December 2006.
- [156] P. J. Mason. Large-eddy simulation: A critical review of the technique. Quarterly Journal of the Royal Meteorological Society, 120:1–26, January 1994.
- [157] W. H. Matthaeus and M. L. Goldstein. Measurement of the rugged invariants of magnetohydrodynamic turbulence in the solar wind. J. Geophys. Res., 87:6011–6028, August 1982.
- [158] J. Maurer, P. Tabeling, and G. Zocchi. Statistics of turbulence between two counter-rotating disks in low temperature helium gas. Europhysics Letters, 26:31–36, 1994.
- [159] W. D. McComb. The physics of fluid turbulence. Oxford University Press, Oxford, December 1990.
- [160] J. C. McWilliams. The emergence of isolated coherent vortices in turbulent flow. Journal of Fluid Mechanics, 146:21–43, 1984.
- [161] M. Meneguzzi, U. Frisch, and A. Pouquet. Helical and nonhelical turbulent dynamos. Physical Review Letters, 47:1060–1064, October 1981.
- [162] C. Meneveau and J. Katz. Scale-Invariance and Turbulence Models for Large-Eddy Simulation. Annual Review of Fluid Mechanics, 32:1–32, 2000.
- [163] J. Meyers, B. J. Geurts, and M. Baelmans. Database analysis of errors in large-eddy simulation. Physics of Fluids, 15:2740–2755, September 2003.
- [164] M. S. Miesch. Large-Scale Dynamics of the Convection Zone and Tachocline. Living Reviews in Solar Physics, 2:1–+, April 2005.
- [165] M. S. Miesch, A. S. Brun, and J. Toomre. Solar Differential Rotation Influenced by Latitudinal Entropy Variations in the Tachocline. ApJ, 641:618–625, April 2006.
- [166] M. S. Miesch, J. R. Elliott, J. Toomre, T. L. Clune, G. A. Glatzmaier, and P. A. Gilman. Three-dimensional Spherical Simulations of Solar Convection. I. Differential Rotation and Pattern Evolution Achieved with Laminar and Turbulent States. ApJ, 532:593–615, March 2000.

- [167] M. S. Miesch, N. N. Mansour, and T. Hartlep. Subgrid-scale modeling in solar convection simulations. In Center for Turbulence Research, Proceedings of the Summer Program, page to appear, 2006.
- [168] P. Mininni, A. Alexakis, and A. Pouquet. Shell-to-shell energy transfer in magnetohydrodynamics. II. Kinematic dynamo. Phys. Rev. E, 72(4):046302–+, October 2005.
- [169] P. D. Mininni, A. Alexakis, and A. Pouquet. Large-scale flow effects, energy transfer, and self-similarity on turbulence. Phys. Rev. E, 74(1):016303–+, July 2006.
- [170] P. D. Mininni and D. O. Gómez. A new technique for comparing solar dynamo models and observations. A&A, 426:1065–1073, November 2004.
- [171] P. D. Mininni, D. O. Gómez, and G. B. Mindlin. Biorthogonal decomposition techniques unveil the nature of the irregularities observed in the solar cycle. Physical Review Letters, 89(10):109901–+, August 2002.
- [172] P. D. Mininni, D. C. Montgomery, and A. Pouquet. Numerical solutions of the three-dimensional magnetohydrodynamic  $\alpha$  model. Phys. Rev. E, 71(4):046304–+, April 2005.
- [173] P. D. Mininni, D. C. Montgomery, and A. G. Pouquet. A numerical study of the alpha model for two-dimensional magnetohydrodynamic turbulent flows. Physics of Fluids, 17:5112–+, March 2005.
- [174] P. D. Mininni, Y. Ponty, D. C. Montgomery, J.-F. Pinton, H. Politano, and A. Pouquet. Dynamo Regimes with a Nonhelical Forcing. ApJ, 626:853–863, June 2005.
- [175] H. K. Moffatt. The degree of knottedness of tangled vortex lines. Journal of Fluid Mechanics, 35:117–129, 1969.
- [176] H. K. Moffatt and A. Tsinober. Helicity in laminar and turbulent flow. Annual Review of Fluid Mechanics, 24:281–312, 1992.
- [177] K. Mohseni, B. Kosović, S. Shkoller, and J. E. Marsden. Numerical simulations of the Lagrangian averaged Navier-Stokes equations for homogeneous isotropic turbulence. Physics of Fluids, 15:524–544, February 2003.
- [178] K. Mohseni, S. Shkoller, B. Kosovic, and J. Marsden. Numerical simulations of the Lagrangian Averaged Navier-Stokes (LANS) equations for forced isotropic homogeneous turbulence. In Proceedings of the 15th AIAA Computational Fluid Dynamics Conference, Anaheim, CA, June 2001. AIAA paper 2001-2645.
- [179] K. Mohseni, S. Shkoller, B. Kosovic, J. Marsden, D. Carati, A. Wray, and B. Rogallo. Numerical simulations of homogeneous turbulence using Lagrangian averaged Navier-Stokes equations. In Proceedings of the 2000 Summer Program, pages 271–283. NASA Ames/Stanford University, 2000.
- [180] A. S. Monin and A. M. Yaglom. Statistical Fluid Mechanics, volume 2. MIT Press, Cambridge, MA, 1975.

- [181] D. C. Montgomery and A. Pouquet. An alternative interpretation for the Holm “alpha model”. Physics of Fluids, 14(9):3365–3366, 2002.
- [182] Gordon E. Moore. Cramming more components into integrated circuits. Electronics, 38(8), 1965.
- [183] J.-J. Moreau. Constants d’un ilot tour-billonnaire en fluide parfait barotrope. C. R. Acad. Sci. Paris, 252:2810–12, 1961.
- [184] R. H. Morf, S. A. Orszag, and U. Frisch. Spontaneous singularity in three-dimensional, inviscid, incompressible flow. Physical Review Letters, 44:572–575, March 1980.
- [185] W.-C. Müller and D. Carati. Dynamic gradient-diffusion subgrid models for incompressible magnetohydrodynamic turbulence. Physics of Plasmas, 9:824–834, March 2002.
- [186] V. Nayagam and F. A. Williams. Rotating Spiral Edge Flames in von Karman Swirling Flows. Physical Review Letters, 84:479–482, January 2000.
- [187] Alan Newell and Jerome Moloney. Nonlinear Optics. Westview Press, Boulder, 2004.
- [188] A. Noullez, G. Wallace, W. Lempert, R. B. Miles, and U. Frisch. Transverse velocity increments in turbulent flow using the RELIEF technique. Journal of Fluid Mechanics, 339:287–307, May 1997.
- [189] A. M. Obukhov. On the distribution of energy in the spectrum of turbulent flow. Dokl. Akad. Nauk SSSR, 32(1):22–24, 1941.
- [190] A. M. Obukhov. Spectral energy distribution in a turbulent flow. Izv. Akad. Nauk SSSR Ser. Geogr. Geofiz., 5(4), 1941.
- [191] A. J. H. Ossendrijver and P. Hoyng. Stochastic and nonlinear fluctuations in a mean field dynamo. A&A, 313:959–970, September 1996.
- [192] E. Ott, Y. Du, K. R. Sreenivasan, A. Juneja, and A. K. Suri. Sign-singular measures - Fast magnetic dynamos, and high-Reynolds-number fluid turbulence. Physical Review Letters, 69:2654–2657, November 1992.
- [193] T. Passot and A. Pouquet. Hyperviscosity for compressible flows using spectral methods. Journal of Computational Physics, 75:300–313, April 1988.
- [194] Hans L. Pécseli. Selected Topics in Plasma Physics. Universitetet i Oslo, compendium for course, 2003.
- [195] J. Pietarila Graham, D. Holm, P. Mininni, and A. Pouquet. Highly turbulent solutions of LANS-alpha and their LES potential. ArXiv e-prints, 2007. <http://arxiv.org/abs/0704.1928>.

- [196] J. Pietarila Graham, D. D. Holm, P. Mininni, and A. Pouquet. Inertial range scaling, Kármán-Howarth theorem, and intermittency for forced and decaying Lagrangian averaged magnetohydrodynamic equations in two dimensions. Physics of Fluids, 18:045106, April 2006.
- [197] J. Pietarila Graham, P. D. Mininni, and A. Pouquet. Cancellation exponent and multifractal structure in two-dimensional magnetohydrodynamics: Direct numerical simulations and Lagrangian averaged modeling. Phys. Rev. E, 72(4):045301(R)–+, October 2005.
- [198] U. Piomelli and T. A. Zang. Large-eddy simulation of transitional channel flow. Computer Physics Communications, 65:224–230, April 1991.
- [199] U. Piomelli, T. A. Zang, C. G. Speziale, and M. Y. Hussaini. On the large-eddy simulation of transitional wall-bounded flows. Physics of Fluids, 2:257–265, February 1990.
- [200] H. Politano and A. Pouquet. Model of intermittency in magnetohydrodynamic turbulence. Phys. Rev. E, 52:636–641, July 1995.
- [201] H. Politano and A. Pouquet. von Kármán-Howarth equation for magnetohydrodynamics and its consequences on third-order longitudinal structure and correlation functions. Physical Review E, 57(1):R21–R24, 1998.
- [202] H. Politano, A. Pouquet, and V. Carbone. Determination of anomalous exponents of structure functions in two-dimensional magnetohydrodynamic turbulence. Europhysics Letters, 43:516–521, September 1998.
- [203] H. Politano, A. Pouquet, and P. L. Sulem. Inertial ranges and resistive instabilities in two-dimensional magnetohydrodynamic turbulence. Physics of Fluids B, 1:2330–2339, December 1989.
- [204] Hélène Politano and Annick Pouquet. Dynamical length scales for turbulent magnetized flows. Geophysical Research Letters, 25(3):273–276, 1998.
- [205] Y. Ponty, P. D. Mininni, D. C. Montgomery, J.-F. Pinton, H. Politano, and A. Pouquet. Numerical Study of Dynamo Action at Low Magnetic Prandtl Numbers. Physical Review Letters, 94(16):164502–+, April 2005.
- [206] Y. Ponty, H. Politano, and J.-F. Pinton. Simulation of Induction at Low Magnetic Prandtl Number. Physical Review Letters, 92(14):144503–+, April 2004.
- [207] A. Pouquet, U. Frisch, and J. Leorat. Strong MHD helical turbulence and the nonlinear dynamo effect. Journal of Fluid Mechanics, 77:321–354, September 1976.
- [208] A. Pouquet, M. Lesieur, J. C. Andre, and C. Basdevant. Evolution of high Reynolds number two-dimensional turbulence. Journal of Fluid Mechanics, 72:305–319, November 1975.
- [209] V. Putkaradze and P. Weidman. Turbulent wake solutions of the Prandtl  $\alpha$  equations. Phys. Rev. E, 67(3):036304–+, March 2003.

- [210] Lewis Fry Richardson. Weather prediction by numerical process. Dover Publications, Inc., New York, 1965. out of print.
- [211] Pierre Sagaut. Large Eddy Simulation for Incompressible Flows, An Introduction. Springer, Berlin, 3rd edition, 1998.
- [212] J. Sánchez Almeida. The Magnetism of the Very Quiet Sun. In T. Sakurai and T. Sekii, editors, ASP Conf. Ser. 325: The Solar-B Mission and the Forefront of Solar Physics, pages 115–+, December 2004.
- [213] J. M. Schmidt and P. J. Cargill. Magnetic reconnection between a magnetic cloud and the solar wind magnetic field. Journal of Geophysical Research (Space Physics), 108:1023, January 2003.
- [214] Z. She and E. Leveque. Universal scaling laws in fully developed turbulence. Physical Review Letters, 72:336–339, January 1994.
- [215] L. F. G. Simmons, C. Salter, and G. I. Taylor. An Experimental Determination of the Spectrum of Turbulence. Proceedings of the Royal Society of London, A165(920):73–89, 1938.
- [216] J. Smagorinsky. General circulation experiments with the primitive equations. I: The basic experiment. Mon. Weather Rev., 91(3):99–165, 1963.
- [217] B. U. O. Sonnerup, G. Paschmann, I. Papamastorakis, N. Sckopke, G. Haerendel, S. J. Bame, J. R. Asbridge, J. T. Gosling, and C. T. Russell. Evidence for magnetic field reconnection at the earth’s magnetopause. J. Geophys. Res., 86:10049–10067, November 1981.
- [218] L. Sorriso-Valvo, V. Carbone, A. Noullez, H. Politano, A. Pouquet, and P. Veltri. Analysis of cancellation in two-dimensional magnetohydrodynamic turbulence. Physics of Plasmas, 9:89–95, January 2002.
- [219] L. Sorriso-Valvo, V. Carbone, P. Veltri, V. I. Abramenko, A. Noullez, H. Politano, A. Pouquet, and V. Yurchyshyn. Topological changes of the photospheric magnetic field inside active regions: A prelude to flares? Planet. Space Sci., 52:937–943, August 2004.
- [220] J. C. Sprott. Simplest dissipative chaotic flow. Physics Letters A, 228:271–274, February 1997.
- [221] B. Sreenivasan and C. A. Jones. Structure and dynamics of the polar vortex in the Earth’s core. Geophys. Res. Lett., 32:20301–+, October 2005.
- [222] K. R. Sreenivasan. On the scaling of the turbulence energy dissipation rate. Physics of Fluids, 27:1048–1051, May 1984.
- [223] James Stewart. Calculus. Brooks/Cole Publishing Company, Pacific Grove, California, 1987.
- [224] H. R. Strauss. Nonlinear, three-dimensional magnetohydrodynamics of noncircular tokamaks. Physics of Fluids, 19:134–140, January 1976.

- [225] P. Tabeling and O. Cardoso, editors. Turbulence, A Tentative Dictionary, volume 341 of B, New York, 1994. NATO ASI, Plenum Press.
- [226] G. I. Taylor. Statistical theory of turbulence. Proceedings of the Royal Society of London, A151:421–478, 1935.
- [227] G. I. Taylor. The Spectrum of Turbulence. Proceedings of the Royal Society of London, A164:476–490, 1938.
- [228] G. I. Taylor and A. E. Green. Mechanism of the Production of Small Eddies from Large Ones. Proceedings of the Royal Society of London, A158, 1937.
- [229] M. L. Theobald, P. A. Fox, and S. Sofia. A subgrid-scale resistivity for magneto-hydrodynamics. Physics of Plasmas, 1:3016–3032, September 1994.
- [230] D. J. Tritton. Physical fluid dynamics /2nd revised and enlarged edition/. Oxford, Clarendon Press, 1988, 536 p., 1988.
- [231] J. Trujillo Bueno, N. Shchukina, and A. Asensio Ramos. A substantial amount of hidden magnetic energy in the quiet Sun. Nature, 430:326–329, July 2004.
- [232] Jans Trulsen. Radiation. Universitetet i Oslo, compendium for course, 2003.
- [233] Arkady Tsinober. An Informal Introduction to Turbulence. Kluwer Academic Publishers, Dordrecht, 2001.
- [234] Y. Tsuji. Intermittency effect on energy spectrum in high-Reynolds number turbulence. Physics of Fluids, 16:L43+, May 2004.
- [235] S. I. Vainshtein, K. R. Sreenivasan, R. T. Pierrehumbert, V. Kashyap, and A. Juneja. Scaling exponents for turbulence and other random processes and their relationships with multifractal structure. Phys. Rev. E, 50:1823–1835, September 1994.
- [236] M. van Reeuwijk, H. J. J. Jonker, and K. Hanjalić. Incompressibility of the Leray– $\alpha$  model for wall-bounded flows. Physics of Fluids, 18:018103, 2006.
- [237] A. Vögler. Three-dimensional simulations of magneto-convection in the solar photosphere. PhD thesis, Göttingen University, 2003.
- [238] A. Vögler, J. H. M. J. Bruls, and M. Schüssler. Approximations for non-grey radiative transfer in numerical simulations of the solar photosphere. A&A, 421:741–754, July 2004.
- [239] A. Vögler, S. Shelyag, M. Schüssler, F. Cattaneo, T. Emonet, and T. Linde. Simulations of magneto-convection in the solar photosphere. Equations, methods, and results of the MURaM code. A&A, 429:335–351, January 2005.
- [240] B. Vreman, B. Geurts, and H. Kuerten. Large-eddy simulation of the turbulent mixing layer. Journal of Fluid Mechanics, 339:357–390, May 1997.
- [241] Wikipedia. Approximation — wikipedia, the free encyclopedia, 2007. [Online; accessed 17-July-2007].



- [242] Wikipedia. Clairaut's theorem — wikipedia, the free encyclopedia, 2007. [Online; accessed 28-June-2007].
- [243] Wikipedia. Claude-louis navier — wikipedia, the free encyclopedia, 2007. [Online; accessed 20-May-2007].
- [244] Wikipedia. Divergence theorem — wikipedia, the free encyclopedia, 2007. [Online; accessed 28-June-2007].
- [245] Wikipedia. Geoffrey ingram taylor — wikipedia, the free encyclopedia, 2007.
- [246] Wikipedia. George gabriel stokes — wikipedia, the free encyclopedia, 2007. [Online; accessed 20-May-2007].
- [247] Wikipedia. John strutt, 3rd baron rayleigh — wikipedia, the free encyclopedia, 2007. [Online; accessed 17-July-2007].
- [248] Wikipedia. Kelvin's circulation theorem — wikipedia, the free encyclopedia, 2007. [Online; accessed 29-June-2007].
- [249] Wikipedia. Levi-civita symbol — wikipedia, the free encyclopedia, 2007. [Online; accessed 22-May-2007].
- [250] Wikipedia. Linear — wikipedia, the free encyclopedia, 2007. [Online; accessed 28-June-2007].
- [251] Wikipedia. Magnetohydrodynamics — wikipedia, the free encyclopedia, 2007. [Online; accessed 20-May-2007].
- [252] Wikipedia. Navier-stokes equations — wikipedia, the free encyclopedia, 2007. [Online; accessed 20-May-2007].
- [253] Wikipedia. Nonlinearity — wikipedia, the free encyclopedia, 2007. [Online; accessed 28-June-2007].
- [254] Wikipedia. Robert strutt, 4th baron rayleigh — wikipedia, the free encyclopedia, 2007. [Online; accessed 17-July-2007].
- [255] Wikipedia. Turbulence — wikipedia, the free encyclopedia, 2007. [Online; accessed 28-June-2007].
- [256] G. S. Winckelmans, A. A. Wray, O. V. Vasilyev, and H. Jeanmart. Explicit-filtering large-eddy simulation using the tensor-diffusivity model supplemented by a dynamic Smagorinsky term. Physics of Fluids, 13:1385–1403, May 2001.
- [257] L. Woltjer. A Theorem on Force-Free Magnetic Fields. Proceedings of the National Academy of Sciences of the United States of America, 44(6):489–491, 1958.
- [258] L. Woltjer. Hydromagnetic equilibrium configurations. AJ, 63:312–+, 1958.
- [259] E. S. Wright. Modeling and Analysis of Aqueous Chemical Reactions in a Diffusive Environment. PhD thesis, University of Colorado, 2002.



- [260] A. M. Yaglom. O localnoi structuri polia temperatur b turbulentnom potoke. Dokl. Akad. Nauk SSSR, 69:743–746, 1949.
- [261] P. K. Yeung, D. A. Donzis, and K. R. Sreenivasan. High-Reynolds-number simulation of turbulent mixing. Physics of Fluids, 17:1703–+, August 2005.
- [262] A. Yoshizawa. Subgrid modeling for magnetohydrodynamic turbulent shear flows. Physics of Fluids, 30:1089–1095, April 1987.
- [263] Hongwu Zhao and Kamran Mohseni. A Dynamic model for the Lagrangian Averaged Navier-Stokes- $\alpha$  Equations. 2004. arXiv:physics/0408113.
- [264] Y. Zhou, O. Schilling, and S. Ghosh. Subgrid scale and backscatter model for magnetohydrodynamic turbulence based on closure theory: Theoretical formulation. Phys. Rev. E, 66(2):026309–+, August 2002.

## Appendix A

### Required identities

When the LES filter is taken to be the inverse of a Helmholtz operator,  $L = \mathcal{H}^{-1} = (1 - \alpha^2 \nabla^2)^{-1}$ , we have  $v_i = (1 - \alpha^2 \partial_{kk})u_i$ . Making use of this we have

$$\begin{aligned} v_j \partial_i u_j &= u_j \partial_i u_j - \alpha^2 (\partial_{kk} u_j) \partial_i u_j \\ &= \frac{1}{2} \partial_i u_j u_j - \alpha^2 (\partial_{kk} u_j) \partial_i u_j. \end{aligned} \quad (\text{A.1})$$

Integrating the last term by parts w.r.t  $k$  results in

$$(\partial_{kk} u_j) \partial_i u_j = \partial_k (\partial_i u_j \partial_k u_j) - \partial_k u_j \partial_k (\partial_i u_j). \quad (\text{A.2})$$

Now, we change the order of differentiation in this last term and follow that with integrating the last term by parts w.r.t  $i$  to find

$$\begin{aligned} \partial_k u_j \partial_i (\partial_k u_j) &= \partial_i (\partial_k u_j \partial_k u_j) - \partial_k u_j \partial_i (\partial_k u_j) \\ &= \frac{1}{2} \partial_i (\partial_k u_j \partial_k u_j). \end{aligned} \quad (\text{A.3})$$

Upon substituting (A.3) into (A.2) into (A.1), we find

$$v_j \partial_i u_j = \frac{1}{2} \partial_i [u_j u_j - \alpha^2 \partial_k u_j \partial_k u_j] - \alpha^2 \partial_k (\partial_i u_j \partial_k u_j). \quad (\text{A.4})$$

We can now group the pressure-like terms,  $\mathcal{P}^* \equiv \frac{1}{2} [u_j u_j - \alpha^2 \partial_k u_j \partial_k u_j]$ , and relabel the dummy indices in the remaining term to find

$$v_j \partial_i u_j = \partial_i \mathcal{P}^* - \alpha^2 \partial_j (\partial_i u_k \partial_j u_k). \quad (\text{A.5})$$

We begin, again, by making use of the definition of the smoothed velocity  $\mathbf{u}$ , and find

$$u_j \partial_j v_i = u_j \partial_j u_i - \alpha_2 u_j \partial_j \partial_{kk} u_i. \quad (\text{A.6})$$

We then integrate the last term by parts w.r.t.  $k$  to see

$$u_j \partial_k (\partial_j \partial_k u_i) = \partial_k (u_j \partial_j \partial_k u_i) - (\partial_j \partial_k u_i) \partial_k u_j. \quad (\text{A.7})$$

The chain rule yields,

$$\partial_j (\partial_k u_i \partial_k u_j) = \partial_k u_j (\partial_j \partial_k u_i) + \partial_k u_i (\partial_k 0), \quad (\text{A.8})$$

by using the incompressibility condition. Now, return to the first term of (A.7) and integrate by parts w.r.t.  $k$  again, finding

$$u_j \partial_k (\partial_j u_i) = \partial_k (u_j \partial_j u_i) - \partial_j u_i \partial_k u_j. \quad (\text{A.9})$$

Finally, substitution of (A.8) into (A.7), and (A.7) and (A.9) into (A.6) results in

$$u_j \partial_j v_i = u_j \partial_j u_i - \alpha_2 [\partial_{kk} (u_j \partial_j u_i) - \partial_k (\partial_j u_i \partial_k u_j) - \partial_j (\partial_k u_i \partial_k u_j)]. \quad (\text{A.10})$$

After grouping terms and changing dummy indices as needed, we arrive finally at

$$u_j \partial_j v_i = (1 - \alpha^2 \partial_{kk}) u_j \partial_j u_i + \alpha^2 \partial_j (\partial_k u_i \partial_j u_k + \partial_k u_i \partial_k u_j). \quad (\text{A.11})$$